ADVANCED FRACTURING TECHNOLOGY FOR TIGHT GAS: AN EAST TEXAS FIELD DEMONSTRATION

Final Report

October 1, 2001 – December 31, 2004

By

Mukul M. Sharma
Project Director

March 2005

Work Performed under Contract No. DE-FC26-01NT41326

Submitted by
The University of Texas at Austin
Petroleum & Geosystems Engineering
P.O. Box 7726
Austin, Texas 78713-7726

Tim Grant
Project Manager
U. S. Department of Energy
National Energy Technology Laboratory
Morgantown, West Virginia

DISCLAIMER

TABLE OF CONTENTS

EXECUTIVE SUMMARY

This DOE sponsored project at the University of Texas at Austin and Anadarko Petroleum Corporation conducted over the past 2 years has focused on strategies for improving productivity in the Bossier play in East Texas. The key to the successful application of successful fracture designs is the selection of a specific strategy and fracture design for a specific well based on an analysis of the well data. The development of 3-D hydraulic fracture models that are capable of accurately modeling proppant transport and fracture propagation is crucial to the successful selection of these strategies in tight gas formations over a broad cross-section of tight gas sand assets with widely varying stress regimes and formation properties.

Analysis of the production response from a large number of fracs in the Bossier sands indicates that traditional gel-fracs quite often perform poorly (and are more expensive to perform) compared to slick-water fracs. A likely cause of the poor performance of the gel-fracs is gel-plugging of the proppant pack. This has lead to the widespread use of slick-water fracs and variations of it (hybrid fracs). Two data wells were selected, APC Anderson #1 and APC Anderson #2, for conducting extensive analysis of petrophysical and other data to evaluate fracturing strategies. In addition 6 test wells were identified in the Dowdy Ranch field to evaluate fracturing treatments. Micro-seismic data collected from the Dowdy Ranch Test Wells indicate that hybrid fracture treatments resulted in created fracture lengths of 600 to 700 feet and effective fracture half lengths of 150 to 250 feet. It has been postulated that the small effective fracture lengths obtained are primarily the result of proppant settling in low viscosity fluids. The use of a smaller 40-70 mesh size proppant [as opposed to 20-40 mesh size] has also resulted in significant improvements to well productivity in most cases. However, in some fields, the application of hybrid fractures or the use of smaller proppant does not yield any significant benefits and may in fact cause a reduction in the productivity of the wells. No clear guidelines were available to an operator to indicate when a hybrid fracture would be warranted as opposed to a slick-water treatment, a gel frac or if other treatment designs should be considered. To develop better selection criteria for fracture designs, lab data and models for proppant placement in slick-water, hybrid-fracs and

other more complex fracture designs were developed as a part of this DOE sponsored study.

An experimental study was undertaken to investigate the impact of fracture width and fluid rheology on proppant transport (including particle settling and horizontal transport). Experiments were conducted in a fracture flow cell for Newtonian fluids as well as shear thinning fluids with varying viscosities. New models for proppant transport and settling in hydraulic fractures were developed and implemented in a 3-d hydraulic fracturing code. The proppant settling models developed account for changes in the settling velocities and rheology caused by fracture walls, proppant concentration, turbulence effects due to high fluid velocities and inertial effects associated with large relative velocities between the proppant and the fluid. Proppant velocity relative to the fluid in the direction of flow is affected by the fracture walls and can result in significant reduction in the proppant transport. A model was developed to estimate the proppant retardation (ratio of particle velocity to the fluid velocity) due to these effects. All these correlations have been incorporated into a fully 3-D hydraulic fracture code, UTFRAC-3D.

In addition to proppant settling, the use of slick water fracs also raises concerns about the loss of large volumes of water based fluids into low permeability, low water saturation sands. The loss of water-based fluid is well known to result in significant water-blocking problems and can retard the flow of gas back into the well. The use of slick-water fracs in some situations may, therefore, not be the optimum fracture treatment. Gel induced damage of the proppant pack versus water blocking of the tight gas matrix is a choice that may need to be made. One of the important lessons learnt from conducting core flow experiments, is that the removal of water blocks in tight gas sands occurs in two stages. The first stage is the displacement of water that occurs over a short time period [about 100 pore volumes]. Following this short duration recovery of frac fluid (usually only a small percentage of the fluid is recovered), the long term clean up of the gas well occurs primarily by vaporization of the water due to the flow of the gas which becomes under-saturated as its pressure decreases. Vaporization effects have not been considered in earlier studies of water-block clean up and have a profound effect on the productivity index of low permeability gas wells.

In summary, laboratory and modeling work conducted at University of Texas as well as field experience in Anadarko wells in the Bossier have resulted in improvements to our understating of proppant placement and fractured well productivity in tight gas sands. By conducting hydraulic fracture simulations that incorporate realistic models for proppant transport and fracture propagation, such as those developed here, the selection of an optimal fracturing strategy can be speeded up and performance predictions made with a greater degree of confidence. Without such detailed studies many of these strategies which may be very effective in some locations may prove to be completely ineffective in others.

Key Publications Resulting from this Project

1. Sharma, M. M.., P. B. Gadde, R. Sullivan, R. Sigal, R. Fielder, D. Copeland, L. Griffin and L. Weijers, "Slick Water and Hybrid Fracturing Treatments: Some Lessons Learnt", *Journal of Petroleum Technology,* March 2005.
2. Sharma, M.M., P. B. Gadde, D. Copeland, R. Sigal, R. Fielder, and R. B. Sullivan, "The Impact of Proppant Placement on the Productivity of Tight Gas Wells" *GasTIPS*, **9**, No. 4, 19-24, Fall 2003.
3. Liu, Y. and M. M. Sharma, "Effect of Fracture Width and Fluid Rheology on Proppant Settling and Retardation: An Experimental Study', SPE 96208 to be presented at the SPE Annual Technical Conference and Exhibition, Dallas, Texas, October 2005.
4. Gadde, P. B., Y. Liu, J. Norman, R. Bonnecaze, and M. M. Sharma, "Modeling Proppant Settling in Water-Fracs", SPE 89875 presented at the SPE Annual Technical Conference and Exhibition, Houston, Texas, 26-29 September 2004.
5. Gadde, P. B. and M. M. Sharma, "The Impact of Proppant Retardation on Propped Fracture Lengths", SPE 97106, to be presented at the SPE Annual Technical Conference and Exhibition, Dallas, Texas, October 2005.
6. Mahadevan, J. and M. M. Sharma, "Clean-up of Water Blocks in Low Permeability Formations," *SPE Journal*, September 2005.
7. Mahadevan, J., M. M. Sharma and Y.C. Yortsos, "Evaporative Clean-up of Water-Blocks in Gas Wells", SPE 94215, presented at the SPE Production Operations Symposium, April 2005.

CHAPTER 1. INTRODUCTION

The primary objective of this research was to improve completion and fracturing practices in gas reservoirs in marginal plays in the continental United States. The Bossier Play in East Texas, a very active tight gas play, was chosen as the site to develop and test the new strategies for completion and fracturing. Figure 1 provides a general location map for the Dowdy Ranch Field, where the wells involved in this study are located.

The Bossier and other tight gas formations in the continental Unites States are marginal plays in that they become uneconomical at gas prices below $2.00 MCF. It was, therefore, imperative that completion and fracturing practices be optimized so that these gas wells remain economically attractive. The economic viability of this play is strongly dependent on the cost and effectiveness of the hydraulic fracturing used in its well completions.

Water-fracs consisting of proppant pumped with un-gelled fluid is the type of stimulation used in many low permeability reservoirs in East Texas and throughout the United States. The use of low viscosity Newtonian fluids allows the creation of long narrow fractures in the reservoir, without the excessive height growth that is often seen with cross-linked fluids. These low viscosity fluids have poor proppant transport properties. Pressure transient tests run on several wells that have been water-fractured indicate a long effective fracture length with very low fracture conductivity even when large amounts of proppant are placed in the formation. A modification to the water-frac stimulation design was needed to transport proppant farther out into the fracture. This requires suspending the proppant until the fracture closes without generating excessive fracture height. A review of fracture diagnostic data collected from various wells in different areas (for conventional gel and water-fracs) suggests that effective propped lengths for the fracture treatments are sometimes significantly shorter than those predicted by fracture models.

There was no accepted optimal method for conducting hydraulic fracturing in the Bossier. Each operator used a different approach. Anadarko, the most active operator in the play, had tested at least four different kinds of fracture treatments. The ability to arrive at an optimal fracturing program was constrained by the lack of adequate fracture models to simulate the fracturing treatment, and an inability to completely understand the results obtained in previous fracturing programs. This research aimed at a combined theoretical, experimental and field-testing program to improve fracturing practices in the Bossier and other tight gas plays.

1.1 OBJECTIVES

Improvements to fracturing technologies and practices offer the best chance of improving the performance and economics of gas wells in marginal plays. This research aimed to improve the performance and reduce the cost of fracture treatments by acquiring and analyzing fracture treatment data from the Bossier play in East Texas. A comprehensive field data acquisition strategy was developed to help better understand the process of water fracturing. Specifically, the following technological issues were recognized to be important for enhancing the effectiveness of the fracture treatments.

- Better estimation of the dimensions of the created fracture
- Better estimates of propped lengths
- Optimizing fracture design (fluids, rates, pumping schedules, proppant concentrations etc.)

One of the objectives was to test job modifications that could help in optimizing fracture designs. Analysis of the data from fracture treatments was expected to help better understand the process of water fracturing and the conditions under which it can be applied and make recommendations to improve such fracture treatment designs.

Improved proppant transport models were needed to accurately model proppant transport when both ungelled and cross-linked fluids with proppant are used. An accurate proppant transport model that would allow engineers to customize treatment designs for individual wells in many different reservoirs was planned for development. The improvements to the fracture model included better models for proppant transport, fluid leakoff and fracture cleanup when low viscosity frac-fluids are pumped at high rates. The new proppant transport model would account for various factors like the turbulence, inertial effects, concentration effects and the effect of walls. The results of the improved fracture modeling program were planned to be backed up with laboratory and field test data.

The improved model was intended to be used to design a series of well completions for wells in the Bossier. Multiple methods such as micro-seismic imaging were to be used to determine the fracture geometry. At least one of the wells was planned to be cored and a complete core analysis including geo-mechanical and relative permeability was to be done. Tests were to be conducted to study proppant placement and formation and fracture cleanup. It was anticipated that the results of this research will result in an improvement in the productivity of fractured wells and/or a reduction in cost of completing and fracturing these wells.

Initial testing on Bossier core had indicated that some of the low permeability intervals might require a drawdown higher than the reservoir pressure to initiate flow after coming in contact with water. As a result, these low permeability intervals were not expected to contribute to production. An inexpensive fluid system was planned to be developed to prevent the formation of a waterblock in the low permeability intervals with very low irreducible water saturations. The development of this system was expected to result in gas production from zones that previously would not produce after fracturing and would have the largest impact on the re-stimulation of wells with depleted reservoir pressure.

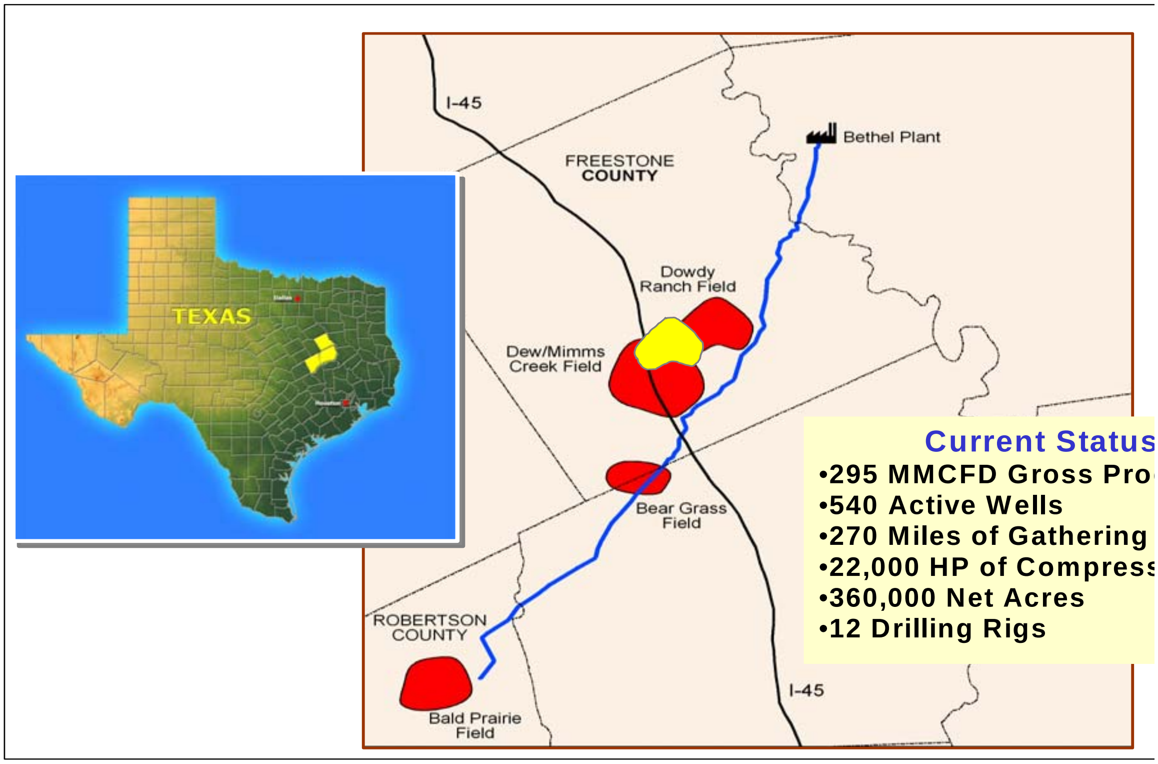

Figure 1: The Dowdy Ranch field in the East Texas Bossier trend

CHAPTER 2. BOSSIER BACKGROUND

The current Bossier play is located on the western flank of the East Texas Basin. Figures 1 provides a cross section for the Dowdy Ranch Field, where the wells involved in this study are located. Although gas has been produced from the Bossier interval from the 1970's, the current play began in 1996 and gained major attention with Anadarko's aggressive 1998 drilling program. Anadarko has drilled extensively in this area and no significant drilling problems have been encountered. Anadarko is the most active operator in the Bossier play with operators such as Cross Timbers and Pioneer also being very active.

Bossier wells generally produce dry gas with little or no water production from sands embedded in the Bossier. The water saturation in some sands has been measured at below 10%. This is consistent with a "basin bottom" gas column more than 3000 feet thick reported by Montgomery[1]. Most production is from over-pressured zones that are part of a regional overpressure cell that extends over the southern half of the East Texas basin (Montgomery and Karlewicz[2]). The Bossier sands are part of the upper Jurassic age Cotton valley group deposited in the East Texas basin. The Bossier interval, which lies immediately beneath the Cotton Valley sandstones, is a thick lithologically complex system containing black to gray-black shales interbedded with fine-grained argillaceous sandstones. The Cotton Valley group is underlain regionally by the Upper Jurassic Louark group, which includes other hydrocarbon bearing formations such as the Smackover carbonates and Haynesville/Cotton Valley limestones. Overlying the Cotton Valley group is the regionally productive lower cretaceous Travis peak and Petit formations.

Productive sands are found at depths ranging from 12,000 to 15,000 feet. A stratigraphic column (Montgomery and Karlewicz[2]) is shown in Figure 2. The Bossier is the time-equivalent of the fluvial-deltaic Cotton Valley sands that produce to the west. The Bossier sands were deposited in paleo-bathymetric lows formed by salt movement contemporaneous with Bossier deposition. Deposition was also influenced by carbonate buildups and shoals in the underlying Cotton Valley lime. The sand transport feeding the system came both from southwest and east-southeast trending channels.

The Bossier sands are generally classified as lowstand delta front and prodelta material. The sands occur in the top 500-600 feet of the Bossier shale. They are found as lenses, segregated pods, and channel trends. The areal extent of these sands range from hundreds of acres to several square miles, with thicknesses up to hundreds of feet. As drilling has continued on tighter spacing the heterogeneity of the sands has become more apparent. Five separate sand units (Taylor, Shelly, Moore, Bonner, and York) have been identified (see Figure 2). The hydrocarbons in the Bossier sands are believed to be sourced from the surrounding shale.

The upper three sands, Taylor, Shelly, and Moore, are generally of lower reservoir quality than the Bonner and York. They have reported porosities in the 6 to 15% range and permeabilities in the 0.001 to 1 md range. They generally have higher clay content than the Bonner. The porosity in the Bonner sand varies from 8 to 20%, with permeabilities in the range of sub-millidarcy to several millidarcies (normally less than 0.1 md). The sands are generally quartz arenites or subarkoses. They are moderately sorted with subangular to subrounded grains. In the productive zones the majority of the storage seems to be in lower permeability sands, which in part probably accounts for the observed hyperbolic decline curves. We primarily focused on the Bonner and York sands in this study, as those are the predominant pay zones in the Dowdy Ranch Area.

Bossier sand rock types include clean sandstones, argillaceous weakly laminated sandstones, dolomitic sandstones and argillaceous burrowed siltstones. Intergranular constituents are primary quartz overgrowths, diagenetic clays in the sands, and detrital clays found in both sand and silt. The clay fraction is predominantly grain coating chlorite and illite. Bossier sands also have a narrow range of grain size, typically from upper very fine to fine. The sands are medium to well sorted, while the silts are poorly sorted. Bossier sands also exhibit a significant diagenetic overprint, including mechanical compaction, cementation from quartz overgrowths, grain coating / pore lining clay development and grain dissolution.

Although the effective porosity in Bossier sands varies from 1% to 17%, the average porosity in the net sand ranges from 6% to 10%. Absolute permeability varies from 0.001md to 1 md in all the rock types, while average permeability in the reservoir rock ranges from 0.005 md to 0.05 md. Measured water saturation in the reservoir rock ranges from as low as 5% in most cases to as high as 50% in the lower-quality reservoir rock.

All producing wells drilled in the Bossier play are hydraulically fractured. The development of optimal fracturing procedures, therefore, has a big impact on the long-term economic viability of the play.

2.1 BOSSIER FRACTURE TREATMENTS

There have been several hundred jobs already pumped in the Bossier by Anadarko. Anadarko has tried five different fracturing methods in order to develop an effective treatment strategy (Figure 2).

Type I: Type I fracture treatments involved stimulating the wells with conventional cross-linked gel and sand treatments. On average, these wells produced 12,000 cubic feet of gas per day for each net foot of pay during the first six months on line. These jobs were expensive, falling into a range of $200,000 up to $350,000. A lower cost method was then sought out.

Type II: Type II fracture treatments were water fracs without proppant. The production rate for these wells was higher for the first month and later the rates dropped significantly as the fracture began to close. However, these treatments were inexpensive, ranging only $50,000 to $100,000 each and therefore improved the well economics significantly.

Type III: Type III frac-jobs were water fracs with 20/40-mesh sand used as proppant. These fracs cost between $100,000 and $150,000 each and the production rates for the wells increased.

Type IV: Type IV jobs involve pumping water with 40/70-mesh sand as proppant. The treatment involved pumping proppant and slick water in alternating stages. Typically, 200,000 pounds of sand was pumped in these types of treatments and they cost about the same or slightly more than the Type III jobs. The production rates for these treatments were significantly higher than the rest. These wells had long-term production rates of about 16,000 cu. ft. of gas per day per foot of net pay.

Type V: Type V treatments are hybrid fracs: In these fracture treatments, slick water is pumped first to generate length. This is followed by a cross-linked gel pad and then by the proppant stage with 20/40-mesh sand with cross-linked gel. Cost for these jobs typically range from $175,000 to $225,000. This is the type of treatment pumped on the wells in this study and what is currently pumped in the Dowdy Ranch area. These wells have long-term production rates of about 18,000 cu. ft. of gas per day per foot of net pay.

2.2 REFERENCES

1. Montgomery, S., East Texas Basin Bossier Gas Play, Petroleum Frontiers, 2001.
2. Montgomery, S. and Karlewicz R., Bossier Play has Room to Grow, Oil & Gas Journal, Jan. 29, 2001.

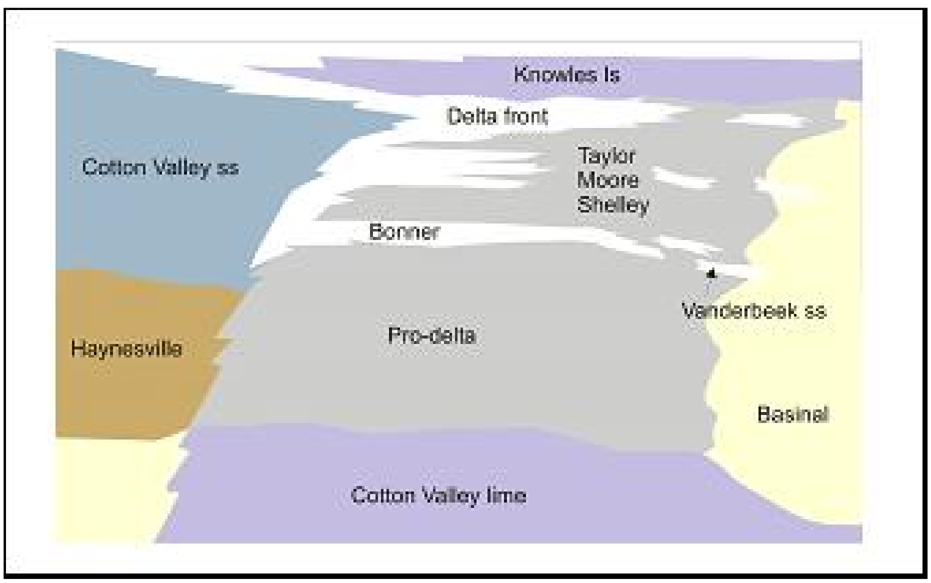

Figure 1: Productive sands are found at depths ranging from 12,000 ft to 15,000 ft

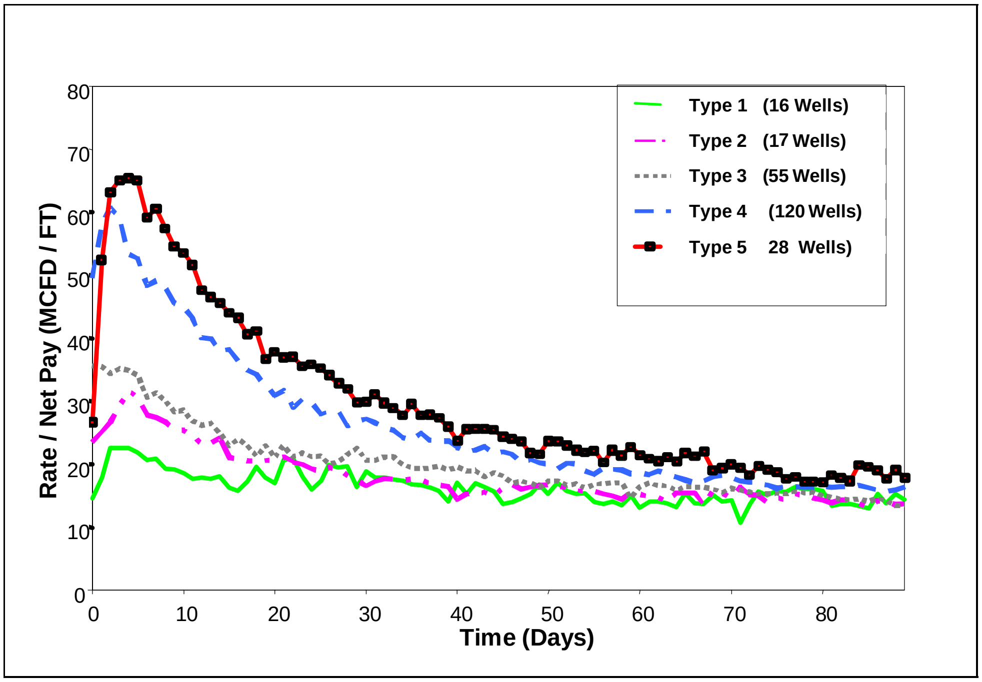

Figure 2: The different types of fracture treatments pumped in the Bossier

CHAPTER 3. DATA WELLS – SIX WELL STUDY

In order to better understand the process of fracturing tight gas sands, a comprehensive data set was gathered and analyzed for the Bossier formation in the Dowdy Ranch field. Six wells were chosen for an intensive study of the effectiveness of new fracturing protocols. Figure 1 shows the position of these wells. The dataset collected on the APC Anderson #2 well represents one of the most comprehensive datasets ever collected for a commercial gas well. Additional data was collected on five offset wells in the field. The wells considered in the study were

- APC Anderson #2 - Main data collection well
- APC Anderson #3
- APC Anderson #4
- Bowers A-2
- Burgher C-23
- Hunter Bonner A-2

The wells were cased and perforated in the Bossier. Table 1 shows the data collected for each of the wells. Initially, the wells in the area were drilled on 40-acre spacing, however several 20-acre spaced wells were also being drilled at the time the wells in this study were completed. The APC Anderson #2 and #1 (Figure 1) were drilled on 10-acre spacing for the purpose of having a close offset to compare and for using the APC Anderson #1 as an observation well for the micro-seismic work. Productive sands are found at depths ranging from 12,000 to 15,000 feet (Figure 2).

All of the wells in this study were completed with one or two hybrid fracture treatment stages down casing. The APC Anderson #1 was completed in one large stage, while the APC Anderson #2 was completed in two separate stages for comparison. After the production logging and buildup tests were performed and the wells cleaned up significantly, tubing and packer were run in each to aid in keeping the wells unloaded and to protect the casing

After the fracture treatment, the wells were put on production. When production of injected water from the fracture stimulation declined, a production log was run. The production log identified the gas production from the different intervals in the Bossier. A comparison of this information with the log and core data helped to determine if all of the intervals were effectively stimulated.

3.1 DATA COLLECTION IN APC ANDERSON #2

The maximum amount of data was collected on the APC Anderson #2. The entire interval was cored, and a complete set of core analysis was performed across the sands. A full suite of logs was run across the zones of interest. These included density, dipole sonic and resistivity logs. Prior to the stimulation on the APC Anderson #2, a stress test was conducted in the shale, determining the shale stress gradient at 0.82 psi/ft. The dipole sonic logs across the pay zone and in the shales were calibrated with stress tests. Figure 6 shows the stress profile. The frac jobs were micro-seismically monitored with downhole geophones and included breakdown and mini-frac stages. Post fracture data collection included pressure buildup testing, production logs with multiple passes, and tracer logs with multiple isotopes. The data collected in APC Anderson #2 includes

- 271 feet of Core
- Dipole Sonic log and cross-dipole sonic log
- Micro-seismic monitoring
- Bottomhole Temperature and Pressure during frac job
- Bottomhole Temperature and Pressure during first 2 days of flowback
- Spectral GR logs
- Production log
- Run one 14 day build-up
- Traced jobs with multiple isotopes

Advanced fracture diagnostics were used on these stimulations to monitor the impact of various fracture job parameters on fracture geometry. The following techniques were used to help determine the fracture geometry:

- Microseimic imaging (for length, height and azimuth)
- Radioactive tagging with multiple isotopes (for height)

- Recording of bottomhole treatment pressure (to calibrate fracture simulation models)
- Production logs (to evaluate effective propped fracture length and zonal coverage)

These techniques provided complimentary but independent data, which has enhanced the confidence in interpretations as well as given information on the usefulness of each technique in the Bossier

Radioactive isotopes were used to determine fracture height and proppant placement near the wellbore. A radioactive isotope was placed in the proppant stage that at the end of the treatment. A spectral GR log was run after the treatment to determine the fracture height at the wellbore and the placement of the different sand stages.

A pressure bomb will be placed in the bottom of the well to record the bottomhole treating pressure during the treatment. The bomb will record the data and be recovered after the treatment. This data can be used to calibrate numerical simulation of the water-fracture stimulation. The bottomhole pressure gauge information should more accurately reflect the actual bottomhole treating pressure. Because of the depth, high treatment rate and multiple fluids used during the job, it will be difficult to accurately estimate the bottomhole treating pressure from the surface treating pressure, hydrostatic and calculated fluid friction. This will also allow the service companies to improve the friction correlations for ungelled fluids with sand.

3.2 APC ANDERSON #2 FRACTURE TREATMENTS

For stage 1 in the York, a diagnostic injection was pumped first to determine the fracture closure stress (Figure 4). After that, a mini frac, a small acid stage and a Type V hybrid frac followed. A composite bridge plug was then set to isolate the York. The Bonner sand was perforated and another diagnostic injection and mini frac were conducted. Following a small acid injection the main hybrid frac was pumped in the Bonner. Both treatments were monitored with micro-seismic tools.

Figure 5 shows the treatment data collected during the York stage. The York has 89 feet of net pay in this well and therefore called for a sizeable job. The designed volume of the 300,000 lbs of 20/40 proppant was successfully placed using a 35# borate. This stage was pumped at an average injection rate of 35 bpm. The job shows a significant net pressure gain of about 1000 psi, suggesting confined fracture growth and increasing fracture complexity as the job progresses. This is similar to the mapping results that were obtained in an earlier mapping project. This conclusion is confirmed in direct growth observations using micro-seismic data for this stage (presented in chapter 7).

Figure 6 is a plot of the data collected on the Bonner stage. The 53 net feet of pay in the Bonner called for a smaller job, designed at 175,000 lbs of 20/40 proppant. Once again a 35# borate gel was used in the crosslinked stages and the net pressure gain was over 1000 psi. In comparison to the treatment in the York, most of the net pressure rise in this treatment comes almost immediately after proppant arrives on formation, indicating a possible near-wellbore width restriction in the fracture. The relatively steep pressure increase and the instantaneous reaction to proppant indicate that this is not a tip screen-out. With the risk of a screenout with bottomhole gauges in the hole, it was decided to call flush early placing only 135,000 lbs of the designed 175,000 lbs into the created fracture.

In addition to fluid leaking off via localized faulting, the low efficiency of these jobs can also be attributed to a strong pressure dependant permeability effect in the Bossier sands. Figure 7 shows the bottomhole temperature for the fracture treatment. Note that the fracture slurry is only heated up about 1.5°F per 1000 ft during most of the fracture treatment. The fluid heats up slowly after the stimulation is completed.

After the fracture treatment, the wells were put on production. When production of frac-water from the fracture stimulation declined, a production log was run in APC Anderson #2 wells. A comparison of this information with the core data helped to determine if all of the intervals were effectively stimulated (Figure 8).

A tracer log run after the frac treatment is shown in Figure 9. Results from the tracer log do not appear to be entirely consistent with the micro-seismic data. This, however, is not uncommon as the tracer logs only reflect the fracture geometry very close to the wellbore.

3.3 DATA COLLECTION IN OTHER 5 WELLS

The data collected in the five other wells include:

- Dipole sonic logs
- Downhole pressure and temperature data during frac jobs
- Hybrid fractured sands (included breakdown and minifrac stages)
- Tracer jobs with multiple isotopes
- Production logs (4 wells)

3.3.1 Bowers A-2

Figure 10 shows the fracture treatment for Bowers A-2. Figure 11 shows that the pressure increases steadily during the proppant stage. This has been observed across all the fracture treatments for this study.

3.3.2 APC Anderson #3

Figure 12 shows the fracture treatment for APC Anderson #3. The fracture was a single stage job. Figure 13 shows the steady pressure increase during the proppant stage. Figure 14 shows the radioactive tracer log. The production log is shown in Figure 15. Note that less than 1% of the production is coming from one of the best porosity zones. It is possible that the single stage fracture job did not effectively stimulate that zone.

3.3.3 APC Anderson #4

Figure 16 shows the fracture treatment for APC Anderson #4 for the York sand. Figure 17 shows the production log. APC Anderson #4 was stimulated through a 2-stage fracture treatment. It should be noted that unlike APC Anderson #3, all the layers are contributing effectively to the production.

3.3.4 Hunter Bonner A-2

Figures 18 and 20 show data from the fracture treatments in the York, Bonner and Moore sands. As observed in other wells, Figure 19 shows a steady increase in bottom-hole pressure during the proppant stage. Figure 21 shows the production log for the well. The Moore sand does not appear to be effectively stimulated. 88% of the production is coming from the Bonner and York sands even though they make up less than 40% of the net pay.

3.3.5 Burgher C-23

Figure 21 shows the fracture treatment in the York sand for Burgher C-23. Figure 23 shows the fracture treatment in the Bonner sand. Figures 22 and 24 show the steady increase in pressure during the proppant stage. Figure 25 shows the production log. Note that the 2-stage fracture job has stimulated both the sands effectively.

3.4 OBSERVATIONS AND CONCLUSIONS

- Rock properties over the majority of each zone are similar in wells studied indicating a good degree of homogeneity horizontally.
- Rock properties are much less homogeneous than they appear on the GR/porosity log vertically and there is considerable small-scale vertical variation.
- Fractures in Bossier sands have complicated geometry and fracture mechanics. This is, at least in part due, to small-scale layering and the presence of faults.
- Typically net pressure increases by 800 - 1700 psi during a frac job. An increase in the slope of the bottom-hole treatment pressure (BHTP) was observed in most of the jobs, as soon as the proppant reached the perforations.
- In the Bonner, a consistent 100 – 250 psi pressure increase was observed when the cross-linked gel reached the perforations. BHTP increased significantly in several wells when the 2.5 ppg proppant stage reached the perforations. This suggests the possibility of limited proppant bridging caused by inadequate fracture width.
- A high near wellbore pressure drop is observed in several treatments (greater than the expected perforation friction). This also suggests the possibility of near wellbore fracture constriction or reorientation.
- A majority of fracture length appears to be created during the slick-water stage.
- Fracture height appears to be less than expected based on BHTP (BHTP ≥ Stress of barriers + 1000 psi).

- Better production resulted from two-stage stimulations when compared with one-stage jobs. Increased initial rates and higher pseudo-steady state rates were observed several months after the treatments.
- Sands can be effectively stimulated at lower rates (yields lower average treating pressures & stimulation cost). However, the rates should be kept high enough to avoid excessive proppant bridging. The pressure buildup when the proppant reaches the perforations may be a good indicator of the extent of proppant bridging.
- Large variations in the frictional pressure drop when pumping slick-water and cross-linked fluids have been observed. Data collected from BHP gauges significantly increases the reliability of fracture models.
- The frac slurry only heats up about 1 to 1.5 ^{o}F per 1000 feet during the frac job. This has a significant effect on cross-linking kinetics. In many cases the fluid may not be cross-linked when it hits the perforations. Higher cross-linker concentrations should be used in these situations to speed up the cross linking reaction (at lower temperatures).

	Density/Neutron/ Induction/GR Logs	Dipole Sonic	Core	NMR	Shale Stress Test	Micro-Seismic	R/A Tracer	BHP During Frac	Build Up
APC Anderson #2	√	√	√	√	√	√	√	√	√
APC Anderson #3	√						√	√	√
APC Anderson #4	√	√					√		√
Burgher G-23	√	√					√		
Bower A-2	√						√	√	
Hunter Bonner A-2	√	√					√		√

Table 1: Data collected from the 6 data wells

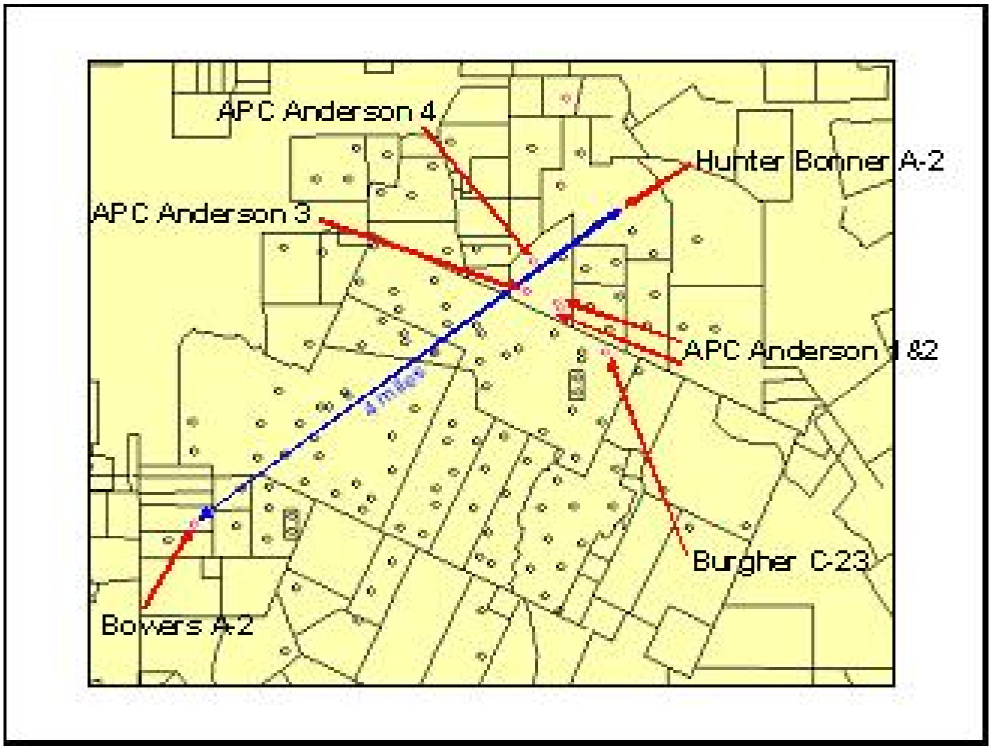

Figure 1: Six wells in the Dowdy Ranch field were chosen as data wells.

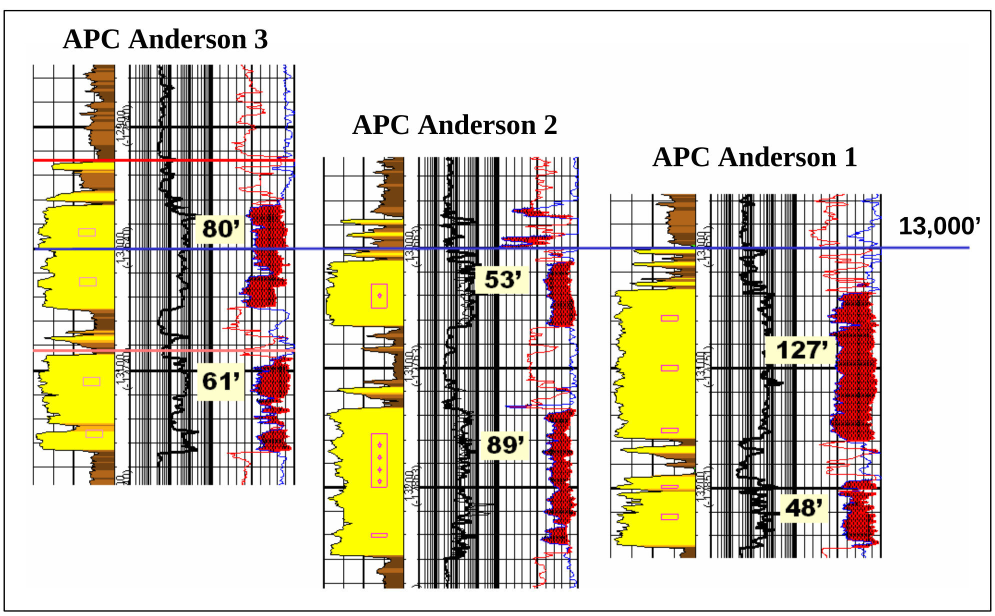

Figure 2: Productive sands are found at depths ranging from 12,000 ft to 15,000 ft

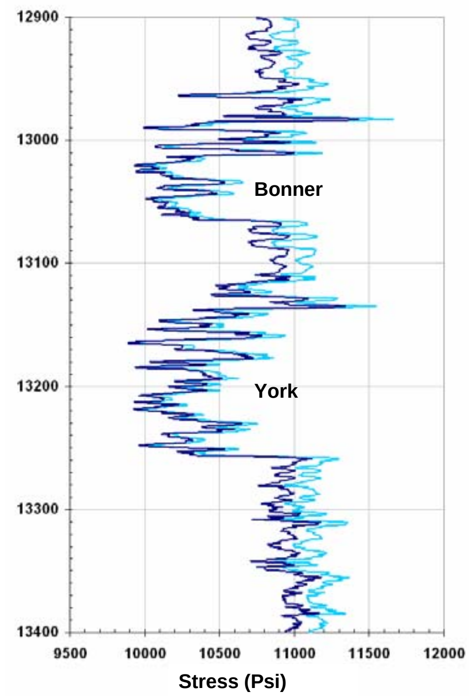

Figure 3: Measured and corrected stress profiles

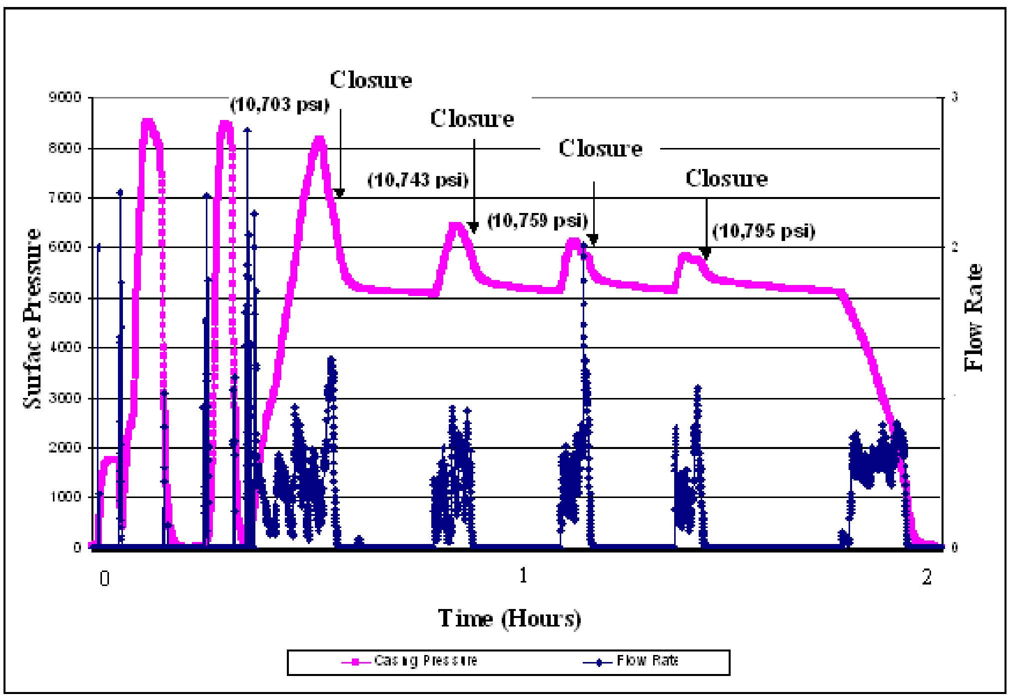

Figure 4: Mini-frac test for APC Anderson #2

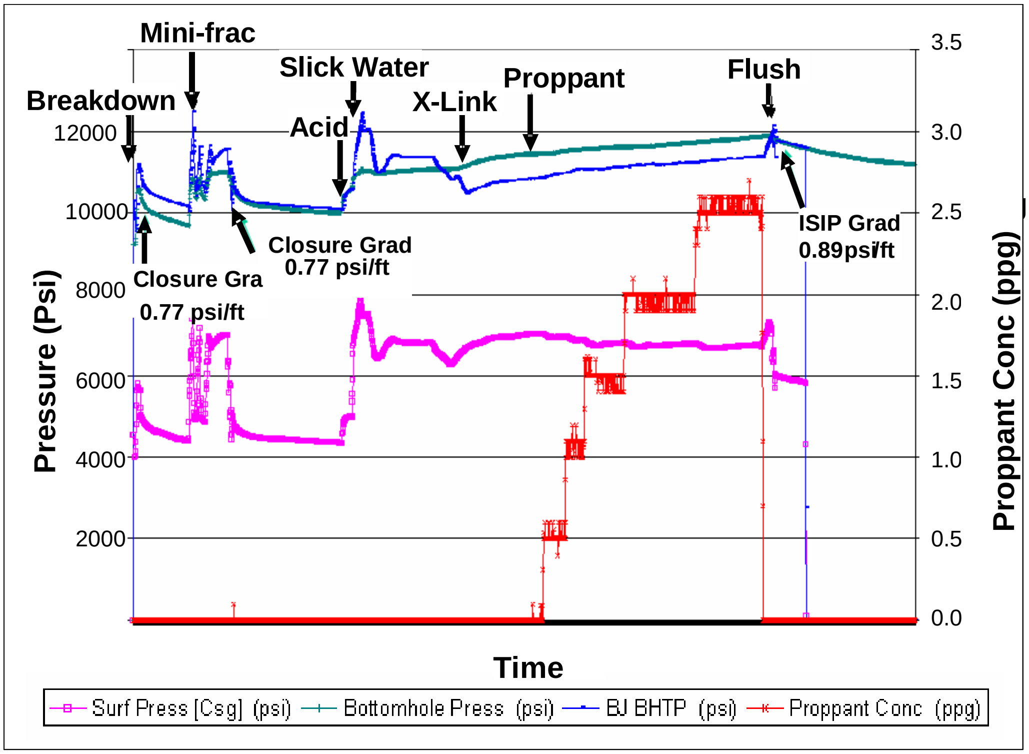

Figure 5: Fracture treatment in the York sand for APC Anderson #2

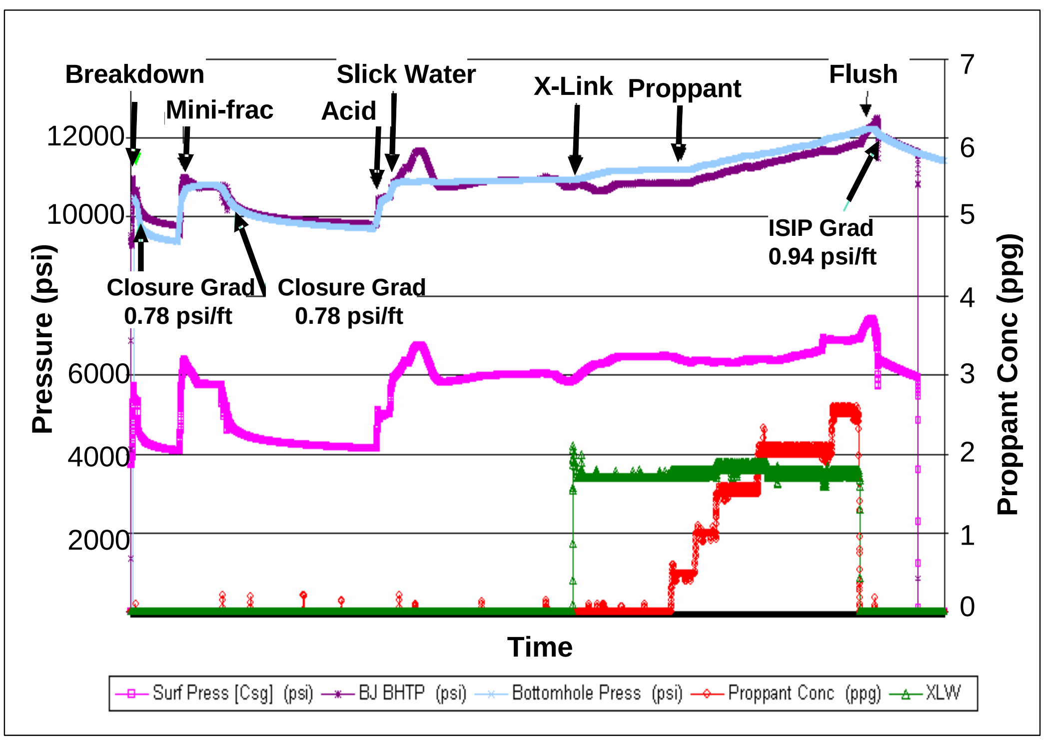

Figure 6: Fracture treatment in the Bonner sand for APC Anderson #2

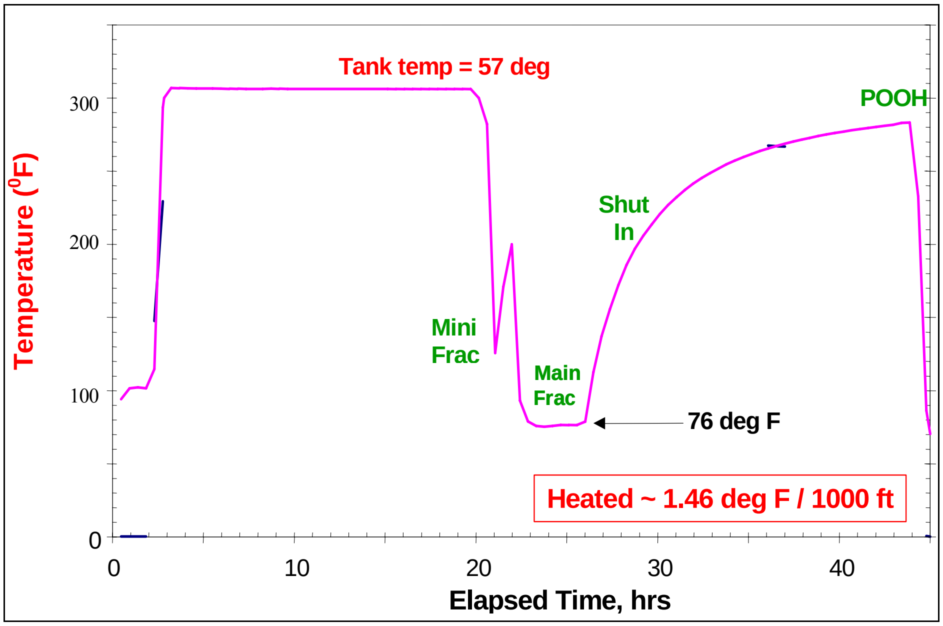

Figure 7: Bottomhole temperature during the fracture treatment for APC Anderson #2

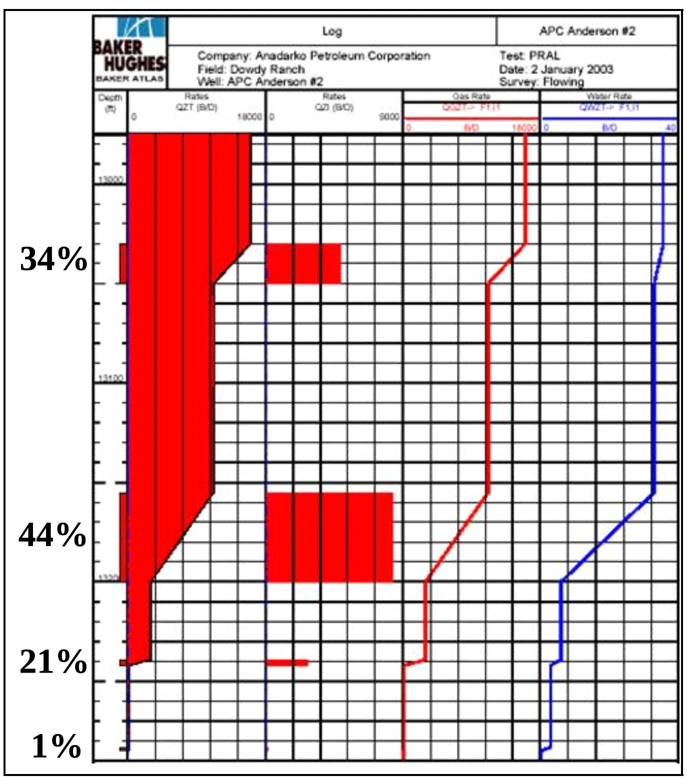

Figure 8: Production log for APC Anderson #2

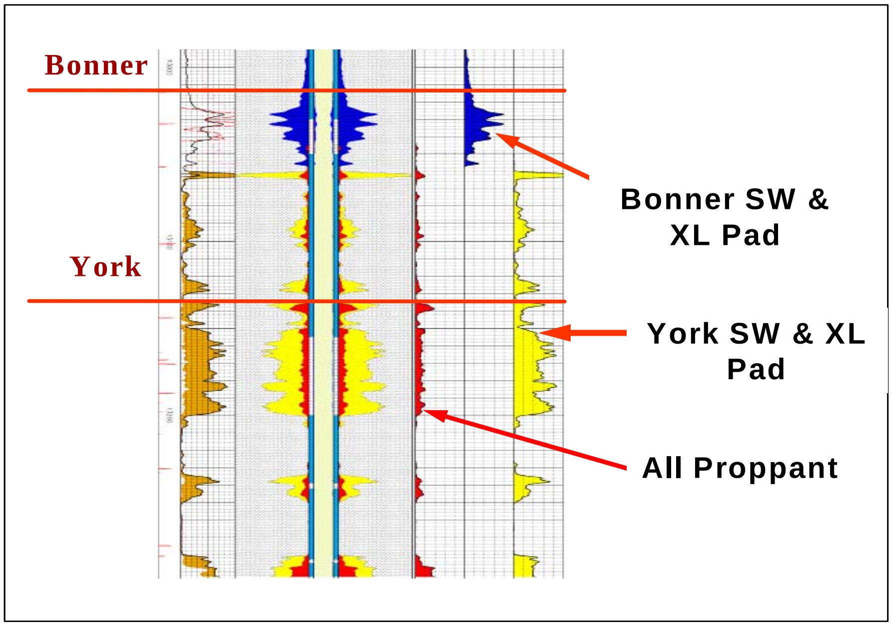

Figure 9: Tracer log for APC Anderson #2

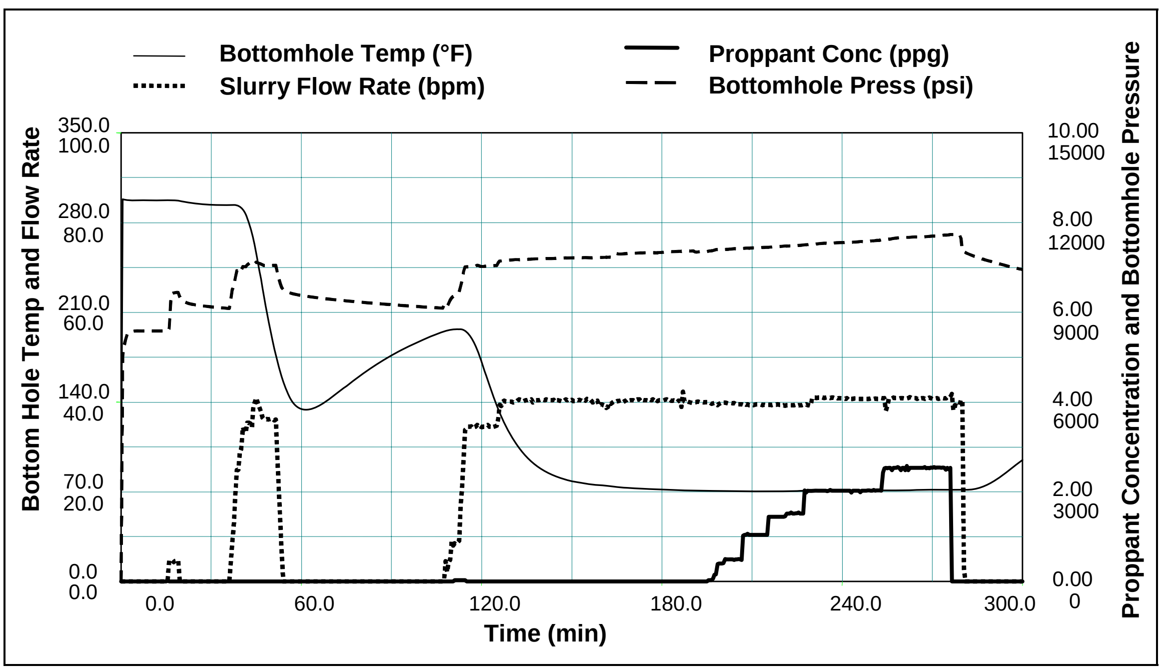

Figure 10: Fracture treatment for Bowers A-2

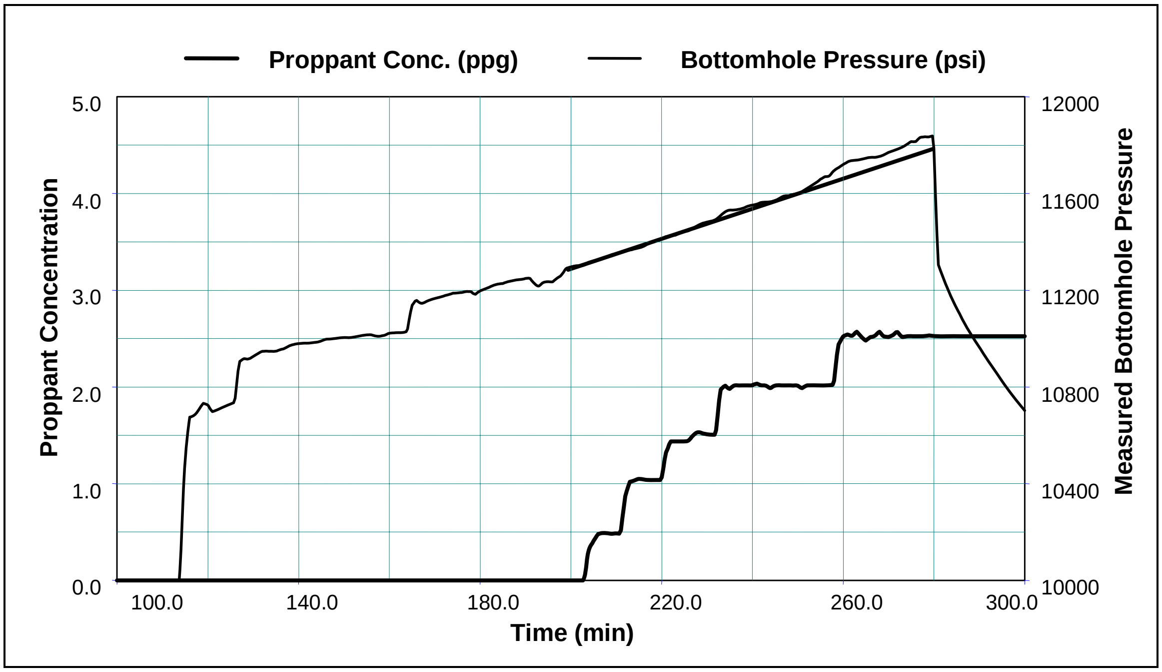

Figure 11: Steady increase in BHP during the proppant stage for Bowers A-2

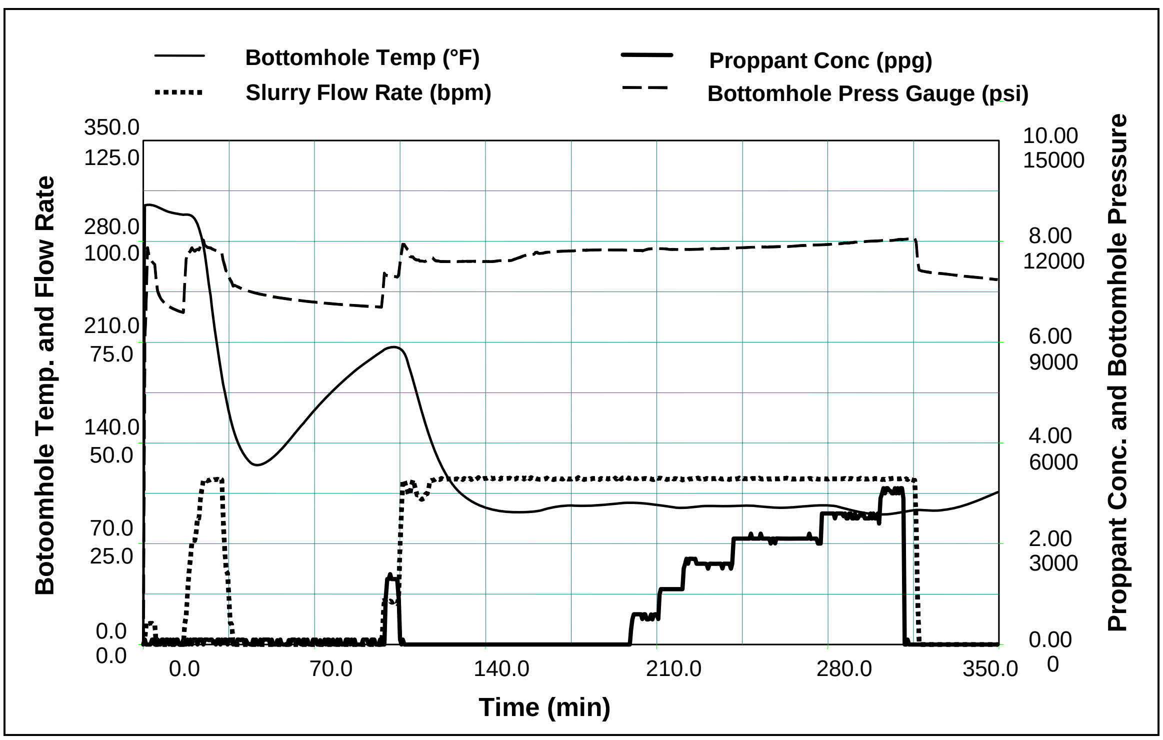

Figure 12: Fracture treatment for APC Anderson #3

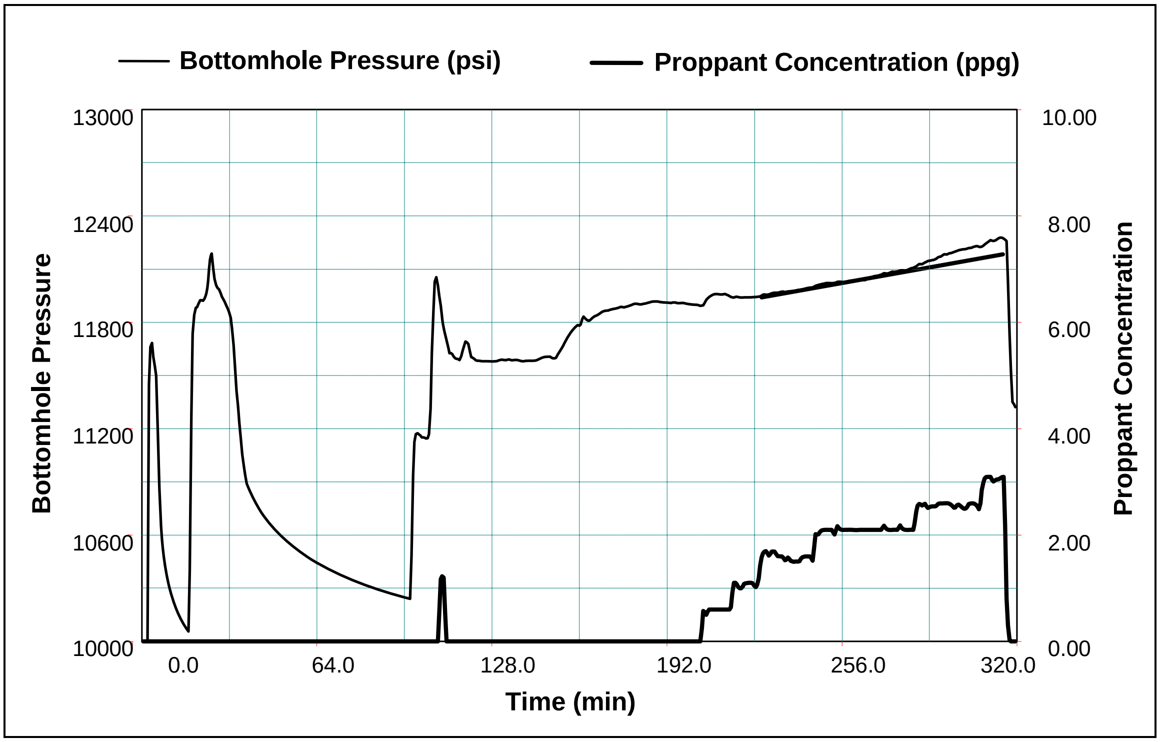

Figure 13: Steady increase in BHP during the proppant stage for APC Anderson #3

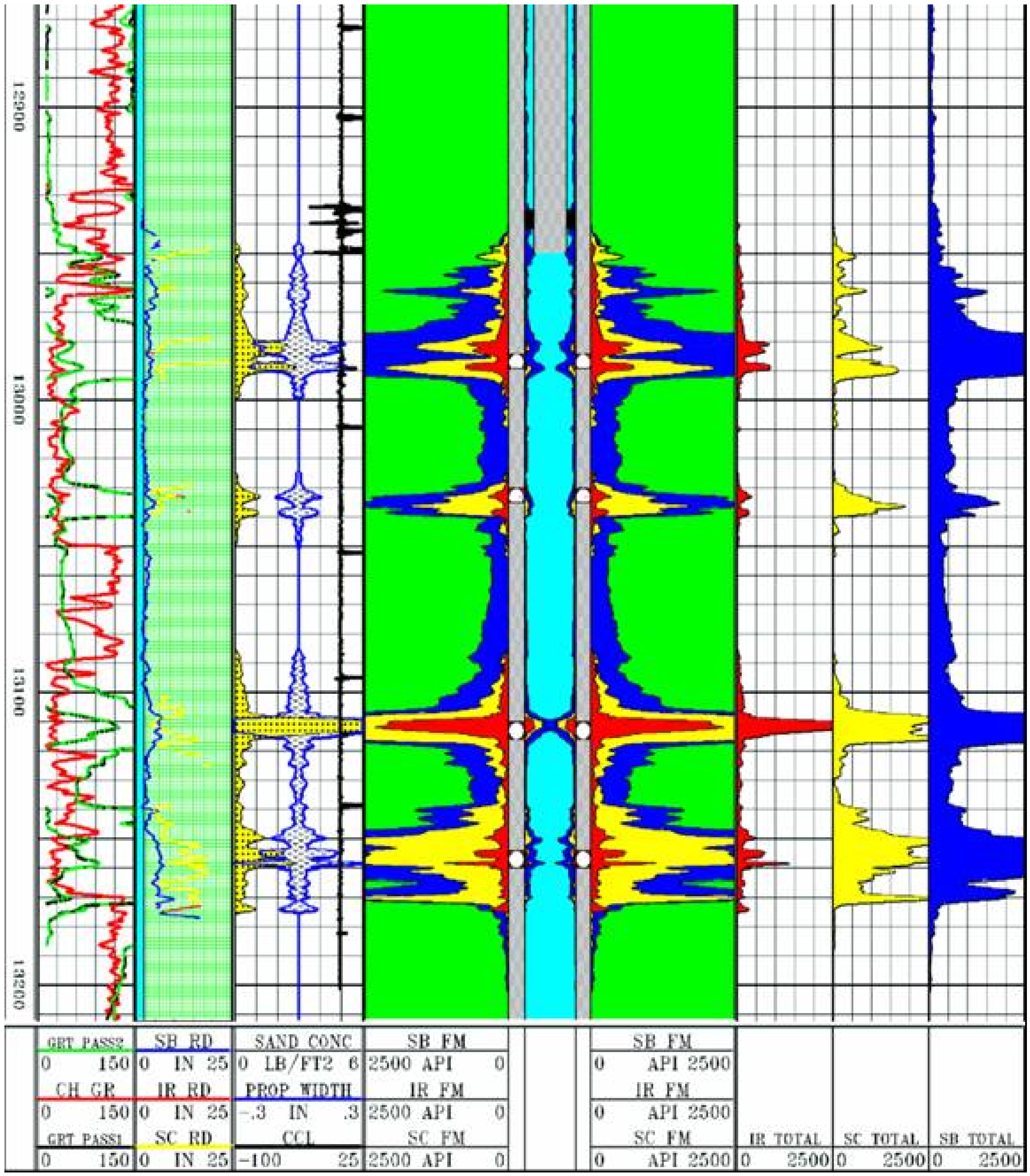

Figure 14: Radioactive tracer log for APC Anderson #3

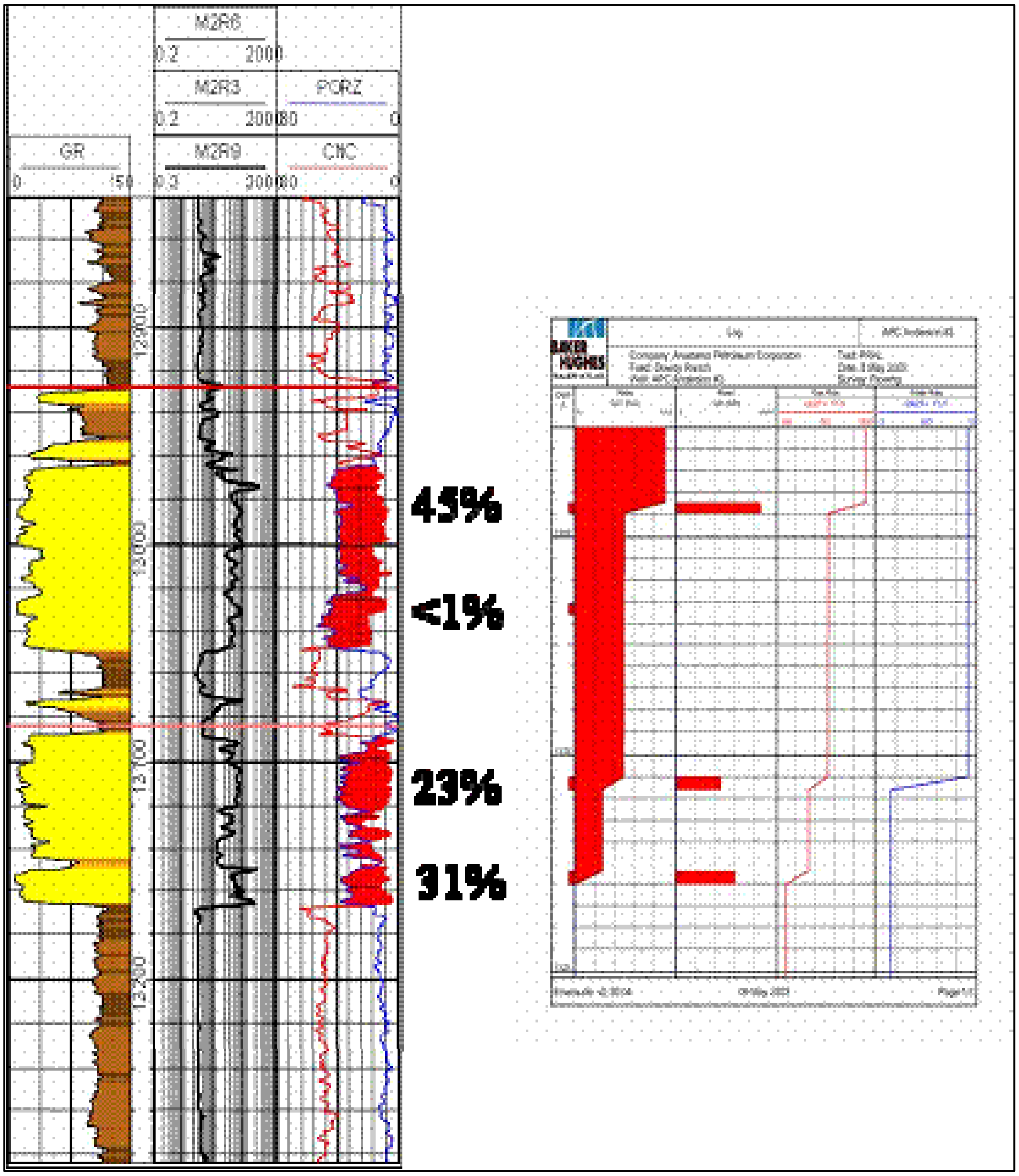

Figure 15:Production log for APC Anderson #3

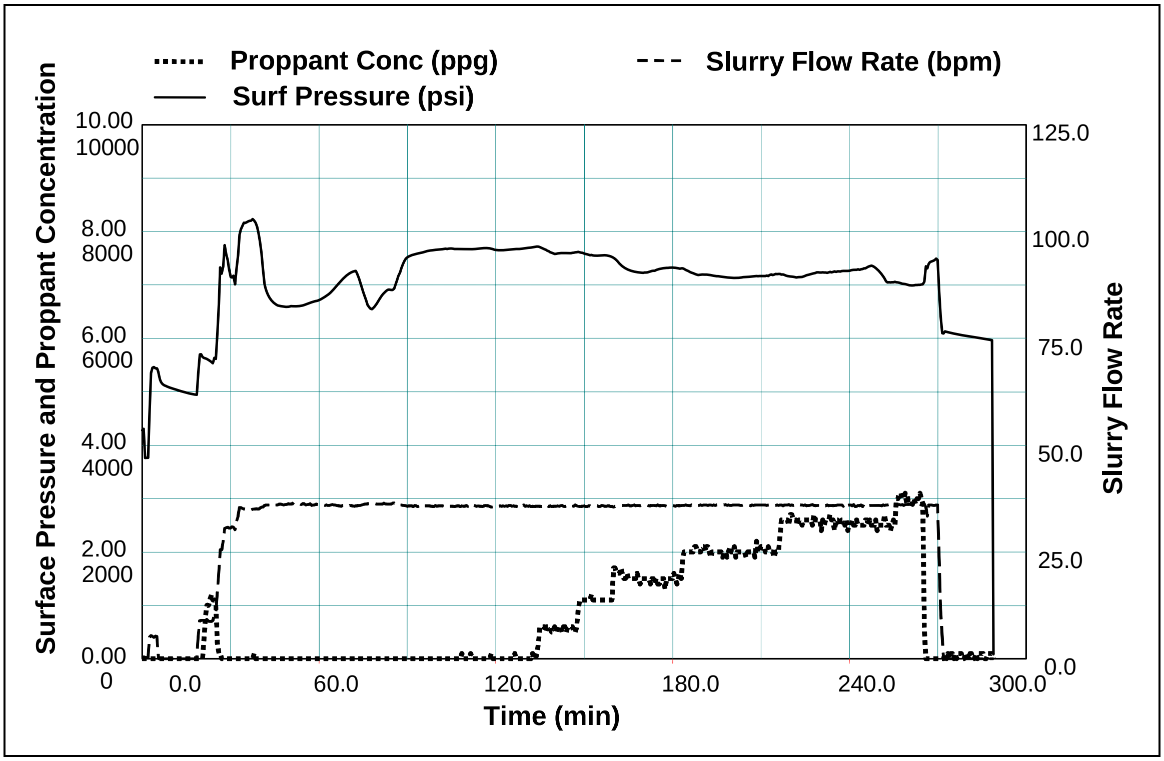

Figure 16: Fracture treatment for APC Anderson #4

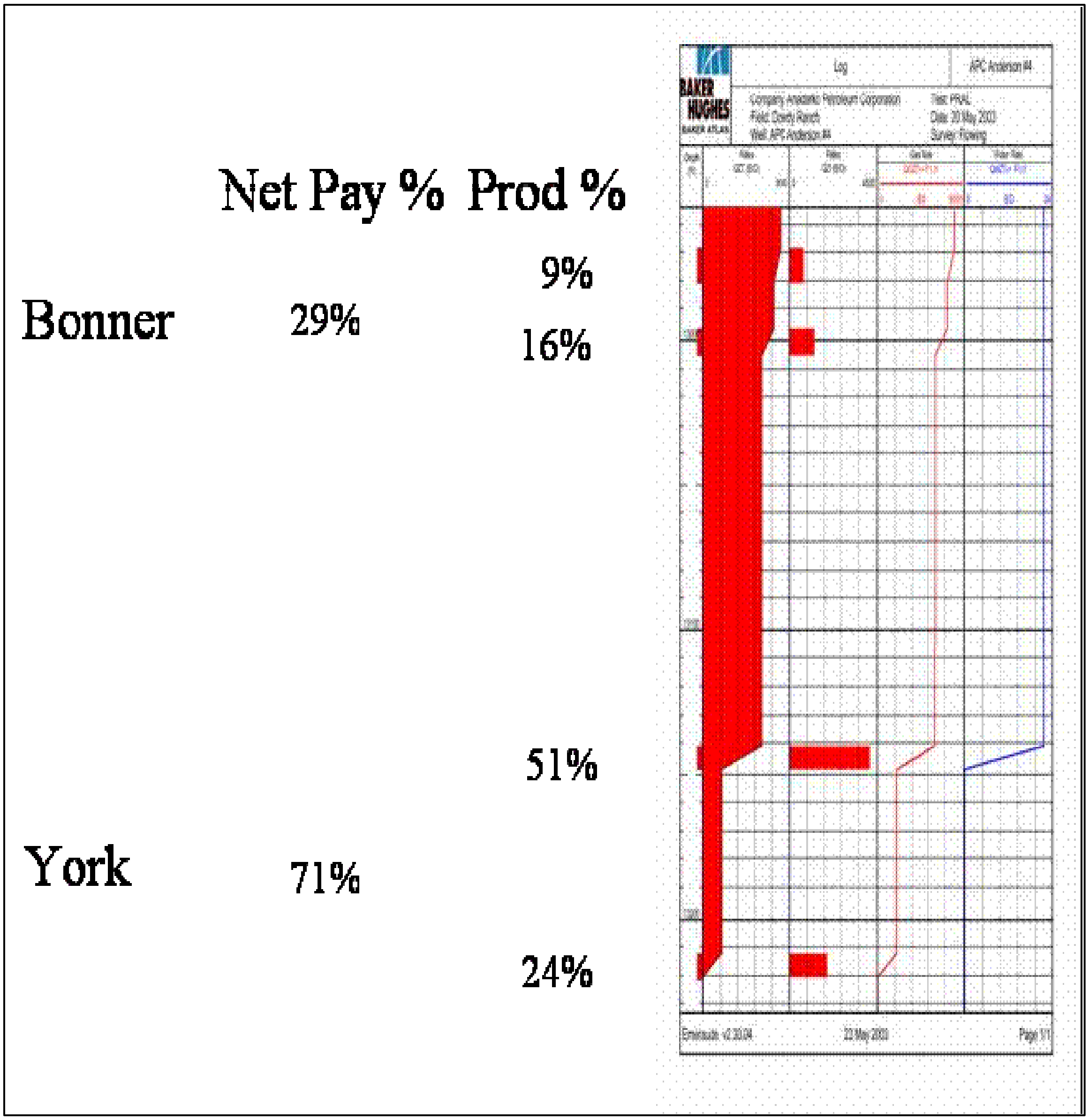

Figure 17: Production log for APC Anderson #4

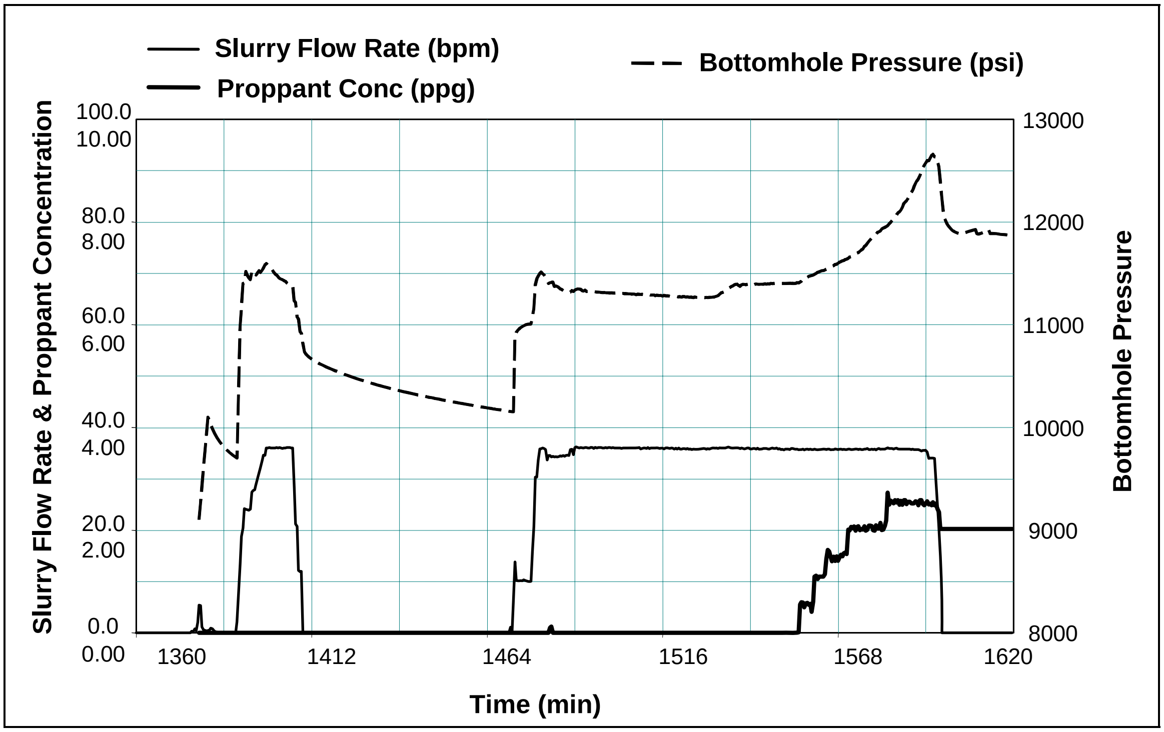

Figure 18: Fracture treatment for Hunter Bonner A-2 in York / Bonner sands

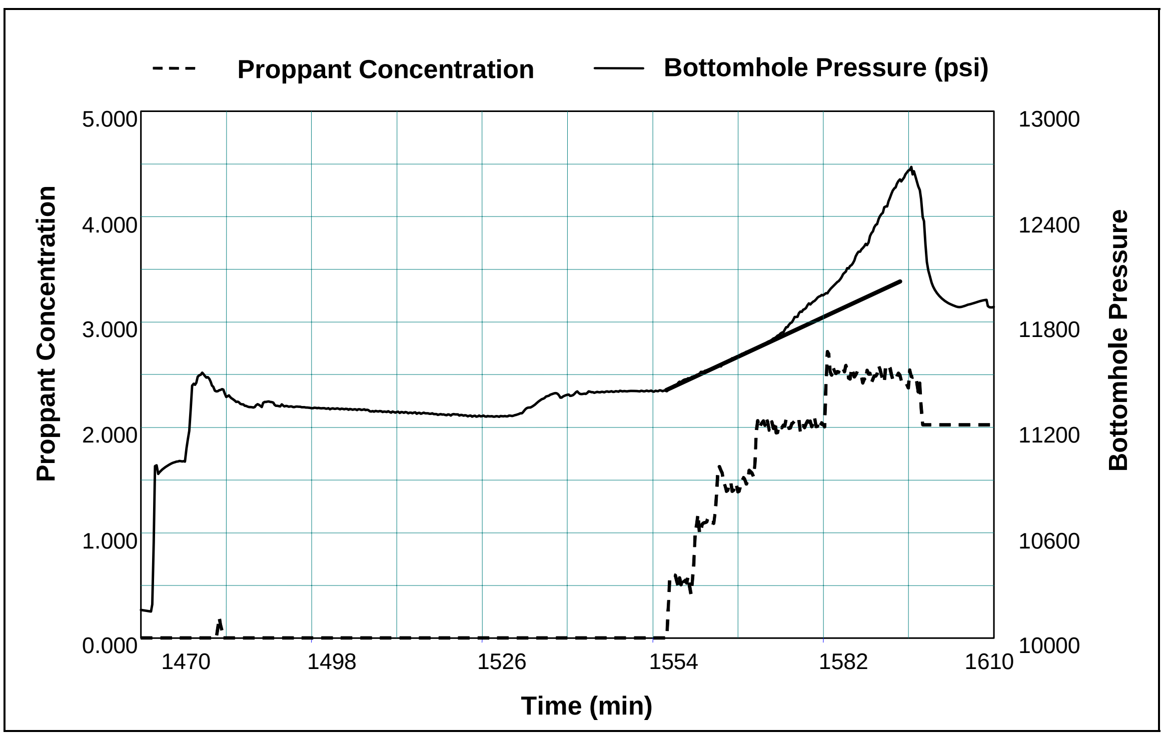

Figure 19: Steady increase in BHP during the proppant stage for Hunter Bonner A-2

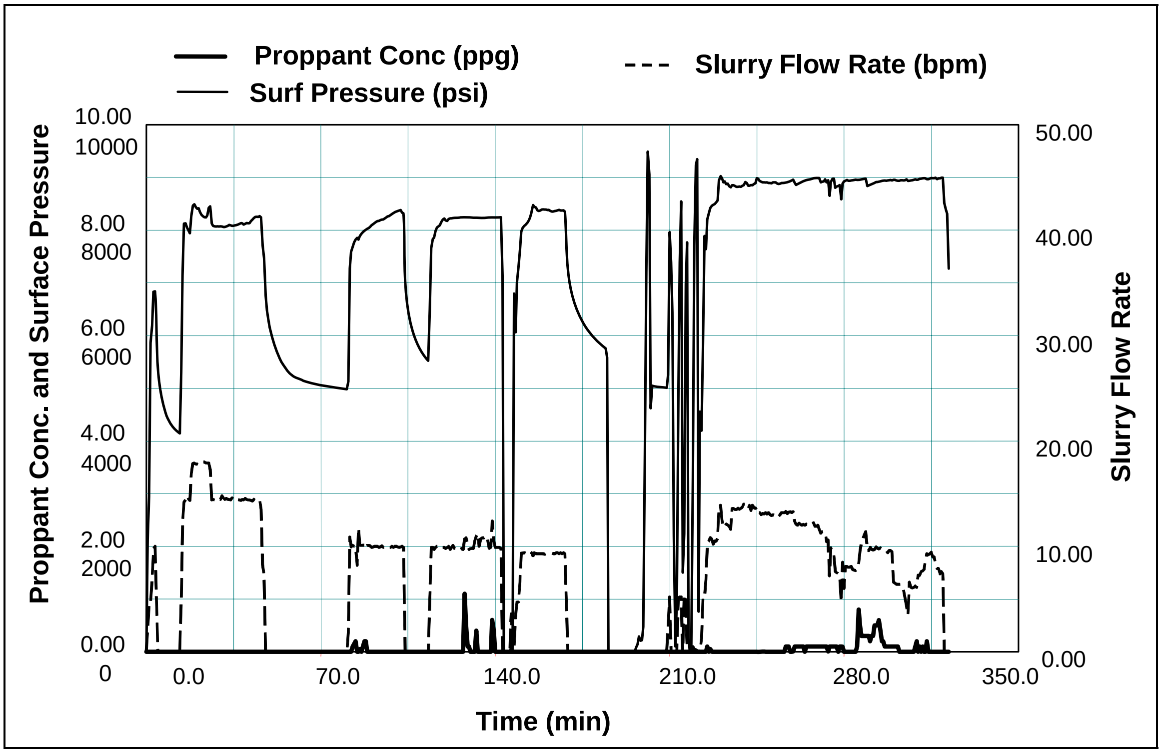

Figure 20: Fracture treatment for Hunter Bonner A-2 in Moore sand

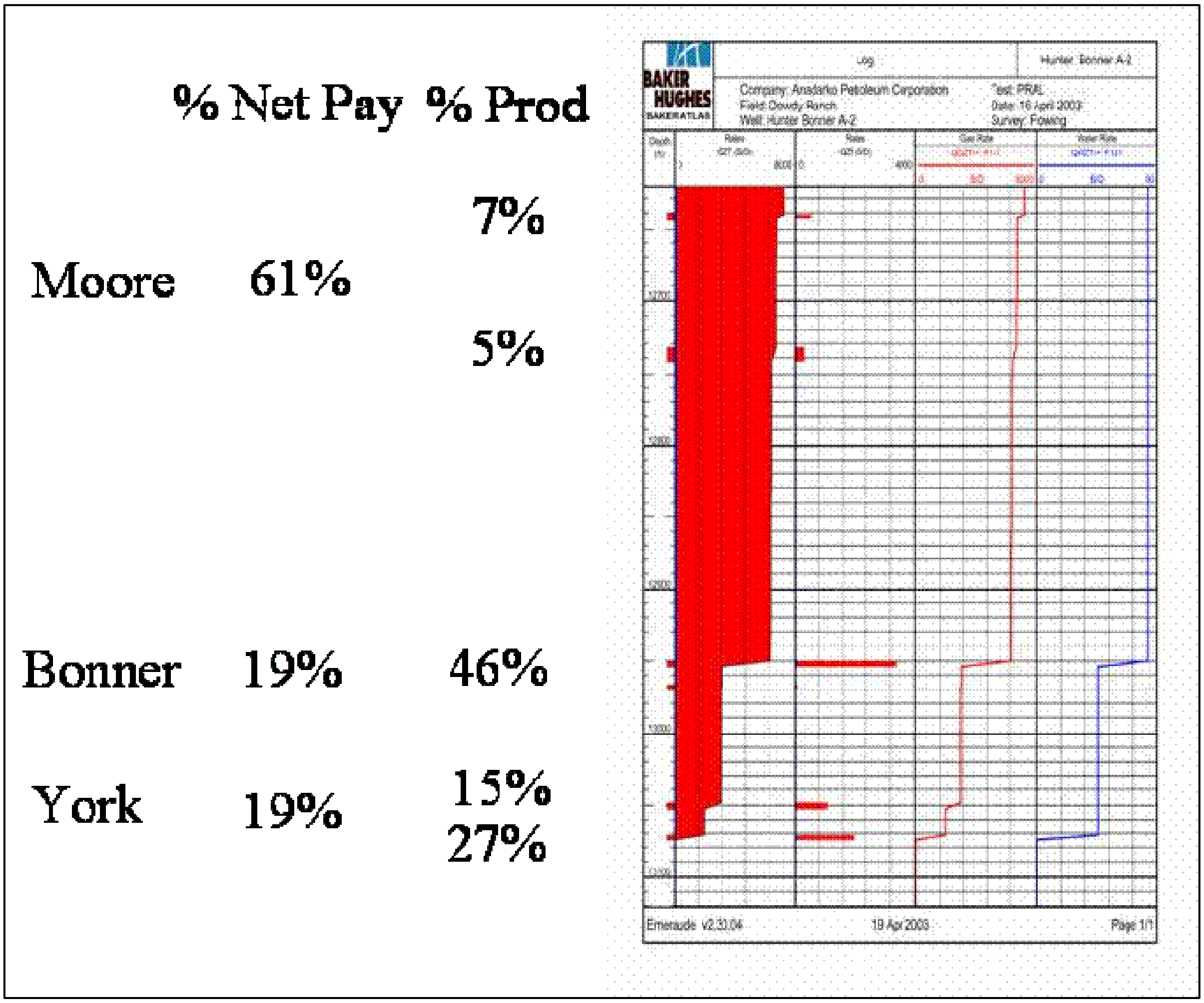

Figure 21: Production log for Hunter Bonner A-2

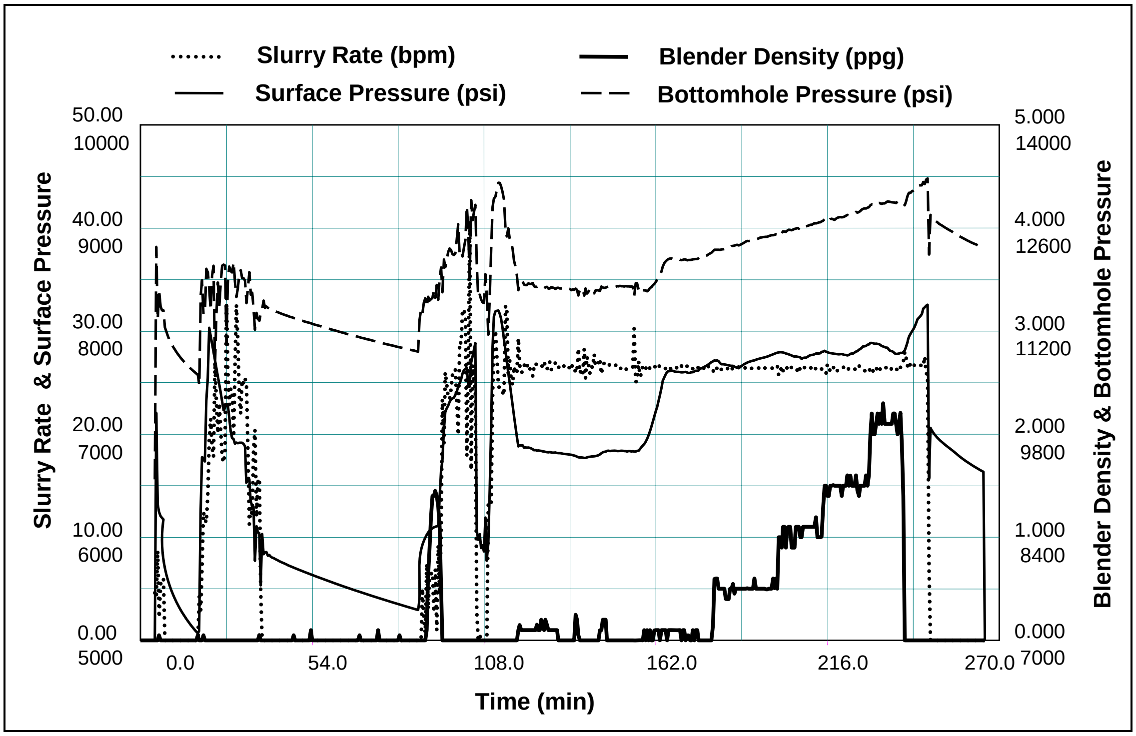

Figure 22: Fracture treatment for Burgher C-23 in York sand

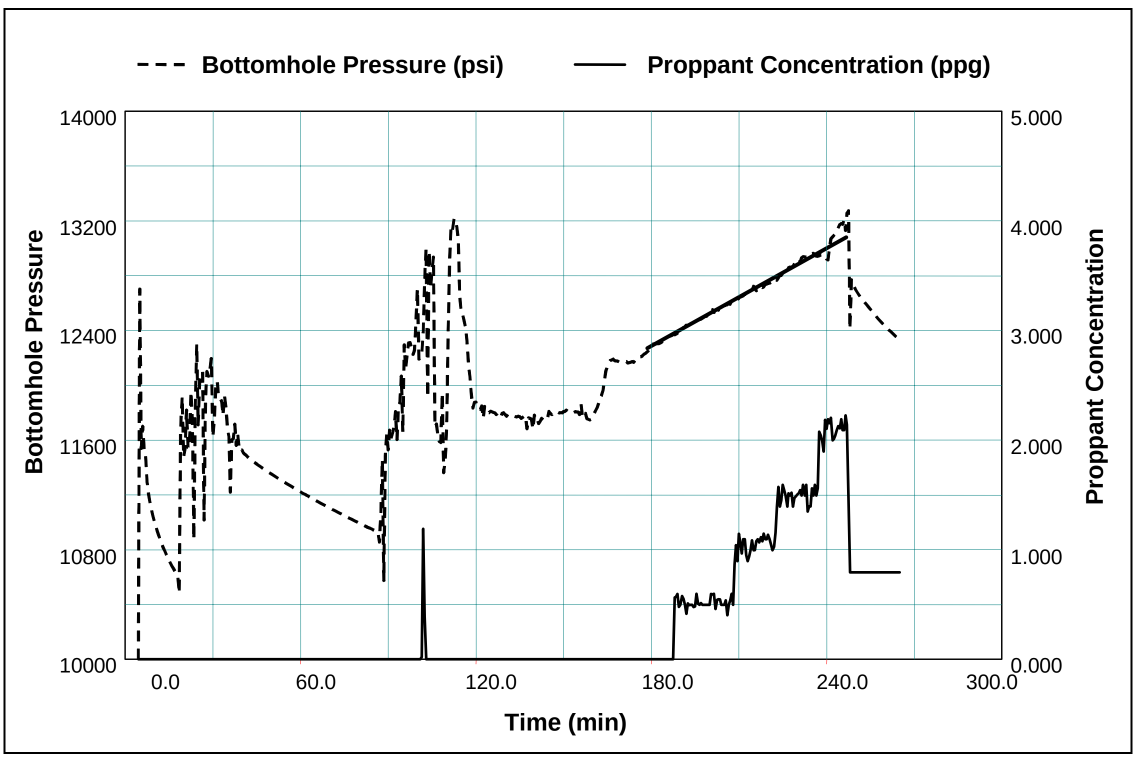

Figure 23: Steady increase in BHP during the proppant stage for Burgher C-23 in York

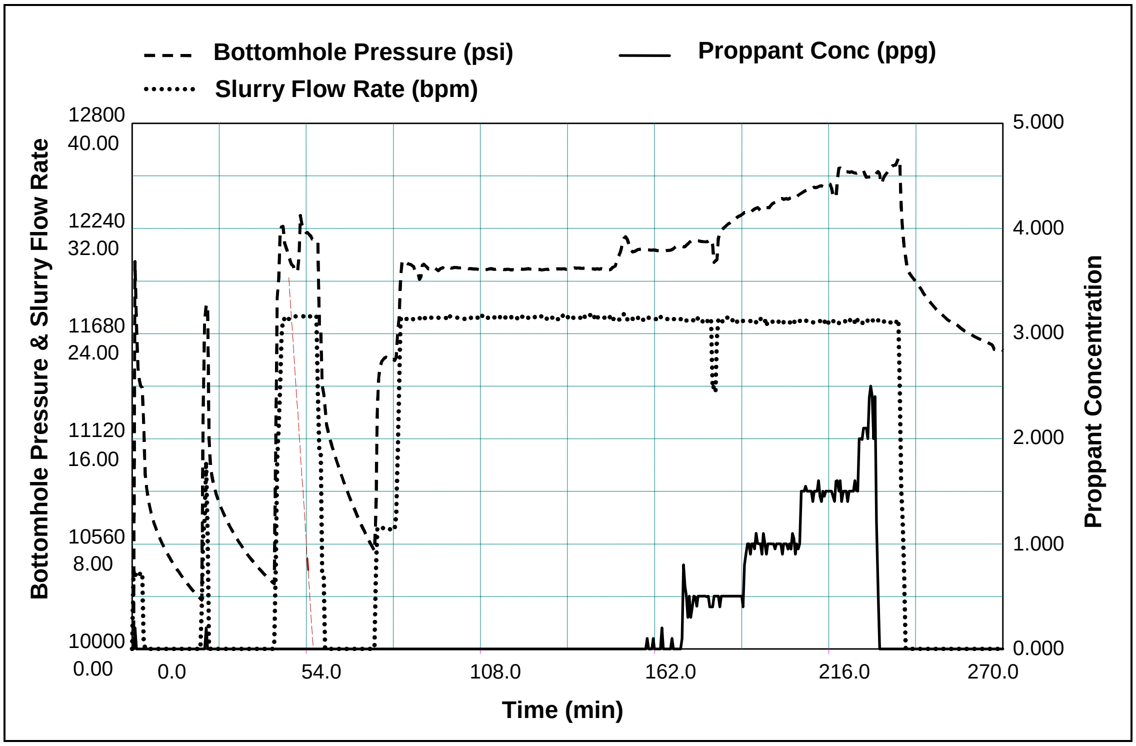

Figure 24: Fracture treatment for Burgher C-23 in Bonner sand

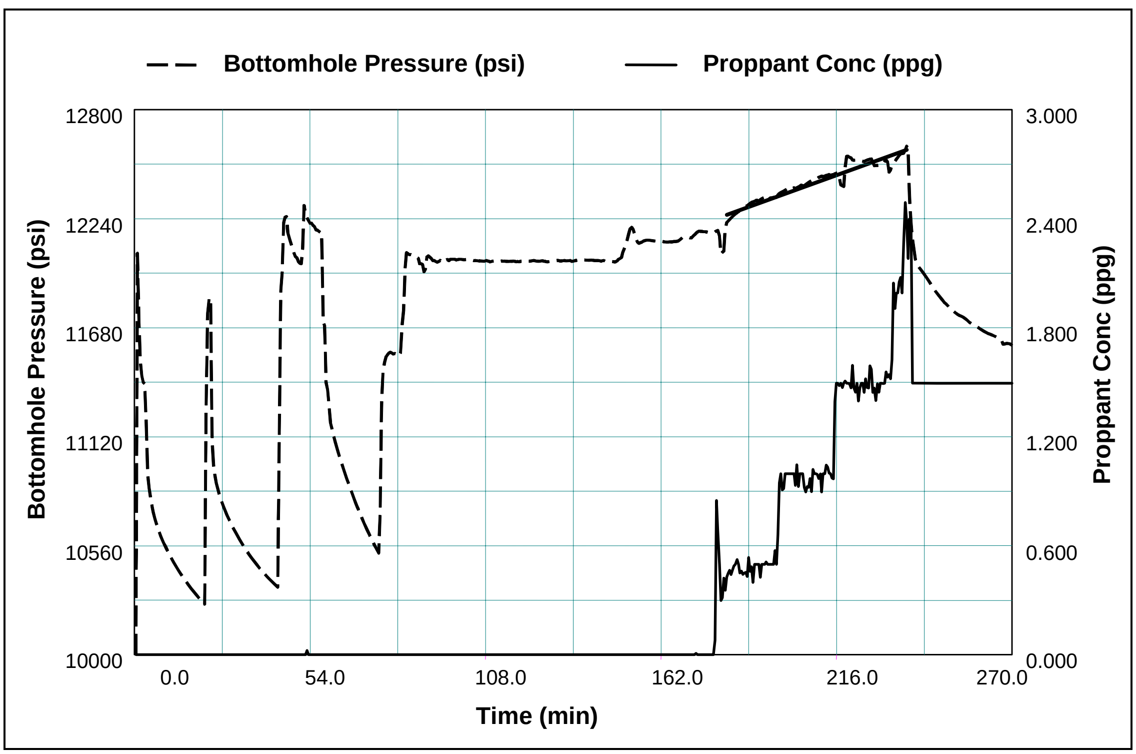

Figure 25: Steady increase in BHP during the proppant stage for Burgher C-23 in Bonner

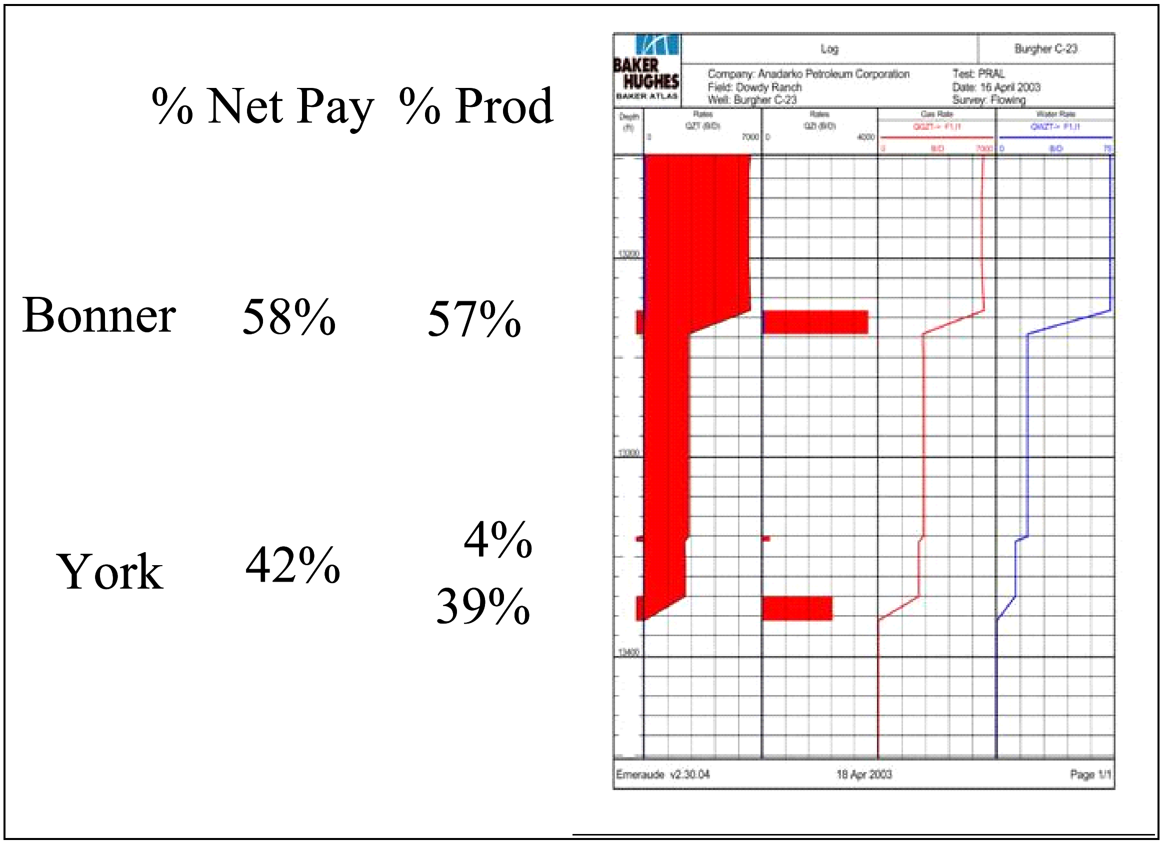

Figure 26: Production log for Burgher C-23

CHAPTER 4. FRACTURE TREATMENT AND MICRO-SEISMIC DATA ANALYSIS FOR APC ANDERSON #2

4.1 INTRODUCTION

In order to better understand the process of fracturing tight gas sands, a comprehensive data set was gathered and analyzed for the Bossier formation in the Dowdy Ranch field. The dataset collected on the APC Anderson #2 well represents one of the most comprehensive datasets ever collected for a commercial gas well. The entire interval was cored, and a complete set of core analysis was performed across the sands. Stress profiles derived from dipole sonic logs across the pay zone and in the shales below were calibrated with stress tests. The frac jobs were micro-seismically monitored with downhole geophones and included breakdown and mini-frac stages. Post fracture data collection included pressure buildup testing, production logs with multiple passes, and tracer logs with multiple isotopes. Additional data was collected on five offset wells in the field. Results from these wells were presented in Chapter 3.

The bottomhole treating pressures were found to be higher than expected based on the measured stress profiles. However, the higher treating pressures encountered did not result in excessive fracture height growth. This may be partially attributed to unexpected faulting providing a conduit for fluid leak-off, resulting in low efficiency and narrow fractures. Propped or effective fracture lengths derived from pressure buildup analysis and history matching production data were significantly shorter than designed frac lengths (or those predicted from uncalibrated frac models). The net pressure plots showed some evidence of proppant bridging even at low proppant concentrations, again indicating only limited fracture widths were being achieved. The data collected and analyzed provide valuable insight into the performance of water and hybrid fracs in tight gas formations. Recommendations for the design of future fracture treatments are made based on the findings.

This chapter focuses on the data acquired in the APC Anderson #2 well, summarizes our findings thus far and presents recommendations for better fracture treatments based on the lessons learnt. Some relevant results from the offset wells are also discussed here.

4.2 BACKGROUND

A review of fracture diagnostic data collected from various wells in different areas (for conventional gel and water-fracs) suggests that effective propped lengths for the fracture treatments are sometimes significantly shorter than those predicted by fracture models[1]. The calculated fracture half-lengths from post-production analyses suggest much shorter effective half-lengths than the original designs [2,3]. Barree et. al.[1] present cases from tight gas sands in the Rocky Mountain Region where half-lengths from gas production analyses are sometimes an order of magnitude lower than those predicted by fracture models. By accounting for the various mechanisms that reduce conductivity such as loss of proppant pack width, non-Darcy flow and multiphase flow in the fracture, they estimated the effective fracture length. Rushing and Sullivan[3] presented a comparison between water fracs and hybrid fracs. They concluded that hybrid fractures generate longer effective frac lengths than conventional water fracs. Pumping higher proppant concentrations in conventional water fracs does not lead to longer and more conductive fractures due to proppant settling. The effective conductivity for hybrid fracs was not consistently higher than for water fracs. Griffin et. al.[4] presented micro-seismic mapping results for two water fracs and one hybrid frac in the Bossier. The fractures were mostly contained in the sands. Fracture orientations were primarily East-West for all the three treatments they reported. A study[5] comparing about 50 water fracs with gel fracs found that the water fracs performed at least as well as gel fracs in low permeability gas formations. Also, pumping larger volumes led to higher production rates associated with longer fractures. Experiments[6] performed with fractured cores from the East Texas Cotton Valley sandstone show that fracture displacement was required to provide residual fracture conductivity in unpropped fractures and the conductivity may vary by at least two orders of magnitude depending on the formation properties and is difficult to predict. Use of even low concentrations of high strength proppant led to infinite-acting fracture conductivity. Although smaller proppant sizes achieve lower conductivity than larger proppant grain sizes, the deeper placement of smaller proppant can improve production performance[7].

A comprehensive field data acquisition strategy was developed to help better understand the process of water fracturing. Specifically, the following technological issues were recognized to be important for enhancing the effectiveness of the fracture treatments.

- Better estimation of the dimensions of the created fracture
- Better estimates of propped lengths
- Optimizing fracture design (fluids, rates, pumping schedules, proppant concentrations etc.)

4.3 DRILLING AND WELL COMPLETION

The APC Anderson #1 and #2 were drilled on 10-acre spacing for the purpose of having a close offset to compare and for using the #1 as an observation well for the micro-seismic work. The APC Anderson #1 was completed in one large stage, while the APC Anderson #2 was completed in two separate stages for comparison. Prior to the stimulation on the APC Anderson #2, a stress test was conducted in the shale, determining the shale stress gradient at 0.82 psi/ft. The greatest amount of data was collected on the APC Anderson #2, including the core and micro-seismic images.

4.4 CORE AND LOG DATA COLLECTED

A full suite of logs was run across the zones of interest. These included density, dipole sonic and resistivity logs. The dipole sonic logs across the pay zone and in the shales were calibrated with stress tests.

All petrophysical data collected for the Anderson APC #2 well is available electronically at the following website:

Website address: http://www.omnilabs.com/home

User Name: DOE

Password: UT

Whole core was recovered through the complete Bossier productive interval along with core from zones above the Bossier for APC Anderson #2. The coring program was designed based on the zone thicknesses from a neighboring well APC Anderson #1. However, the thickness of York changed significantly from the neighboring well leading to only partial recovery of the core from this layer. This core was completely characterized both geo-mechanical and petrophysically. The core testing program consisted of three parts: 1) fluid extraction, tracer detection and porosity on vertical plugs to provide in-situ brine saturation, 2) porosity and permeability at 800 and 2500 psi every foot along the core, and 3) geologic characterization. The geologic characterization consisted of photography and core description, and rock typing from thin section descriptions taken every foot. The thin section study parsed the rocks into nine rock types, the first five being essentially non-reservoir rocks, and the last four having visible porosity. The core estimates of S_w are in good agreement with preliminary log analysis. The tracer analysis showed low water saturations (in some cases as low as 4%) in reservoir sands. The reservoir zones range from 4% to 10% porosity and the permeability at 2500 psi confining stress ranges from 0.002 md to 0.1 md. The core analysis also included geo-mechanical measurements, Hg capillary pressure measurements, mineralogy, NMR, relative permeability, and electrical measurements.

In general the pore geometry inferred from the measurements is typical of that seen in other studies of tight gas sands. The high-pressure Hg capillary measurements show two similar rock types. Both have a sharp primary peak. They differ in the amount of small pores not accessed from the dominant pore throat. The NMR pore size distributions do not show distributions as sharp-peaked since the NMR spectra represent pore body sizes not pore throats.

Permeability measurements were performed with a minimum of two confining pressures. A subset was measured at five confining pressures. As is usual in tight gas sands there is noticeable decrease in permeability with confining pressure. Even after removing samples that appeared to be cracked, the decrease in permeability satisfies a Walsh type relationship. That is,

$$k^{1/3} = A - B \log(\nu)$$

where, k is the permeability, ν the confining pressure and A and B are free parameters. This relationship is predicted for flow through crack like apertures (Walsh, 1981). The average values of A and B can be used to predict the value of permeability at any confining pressure from a measurement at a single confining pressure. Both A and B must be determined on a case-by-case basis. The variation in permeability with effective stress has a direct impact on the leakoff calculations that need to be made in hydraulic fracture simulators. As shown by Settari et. al.[8] the stress dependent leakoff can have a large impact on predicted fracture lengths.

The Hg capillary pressure data, permeability, and NMR data are consistent with the main pore throats being crack like. Based on other tight gas cases this was probably produced by digenetic processes. There is no evidence of a dual porosity system or that natural fractures dominate the permeability

The above measurements provided the necessary data to perform rock typing, establish permeability predictors, and determine the appropriate moduli to use in the fracture modeling, and model production data. Measurements of both static moduli and dynamic moduli (velocities) were used to establish correlations that enable static moduli to be estimated from sonic logs which are needed as inputs into fracture models.

4.5 APC ANDERSON #2 FRACTURE TREATMENTS

For stage 1 in the York, a diagnostic injection was pumped first to determine the fracture closure stress. After that, a mini frac, a small acid stage and a Type V hybrid frac followed. A composite bridge plug was then set to isolate the York. The Bonner sand was perforated and another diagnostic injection and mini frac were conducted. Following a small acid injection the main hybrid frac was pumped in the Bonner. Both treatments were monitored with micro-seismic tools.

Figure 1 shows the treatment data collected during the York stage. The York has 89 feet of net pay in this well and therefore called for a sizeable job. The designed volume of the 300,000 lbs of 20/40 proppant was successfully placed using a 35# borate. This stage was pumped at an average injection rate of 35 bpm. Typical rates for the hybrid jobs in this area are 45 bpm, however, in this case the lower rate was used to attempt to keep the fracture better confined to the pay interval and to reduce horsepower charges. The job shows a significant net pressure gain of about 1000 psi, suggesting confined fracture growth and increasing fracture complexity as the job progresses. This is similar to the mapping results that were obtained in an earlier mapping project. This conclusion is confirmed in direct growth observations using micro-seismic data for this stage (Figures 12 & 13).

Figure 2 is a plot of the data collected on the Bonner stage. The 53 net feet of pay in the Bonner called for a smaller job, designed at 175,000 lbs of 20/40 proppant. Once again a 35# borate gel was used in the crosslinked stages and the net pressure gain was over 1000 psi. In comparison to the treatment in the York, most of the net pressure rise in this treatment comes almost immediately after proppant arrives on formation, indicating a possible near-wellbore width restriction in the fracture. The relatively steep pressure increase and the instantaneous reaction to proppant indicate that this is not a tip screen-out. With the risk of a screenout with bottomhole gauges in the hole, it was decided to call flush early placing only 135,000 lbs of the designed 175,000 lbs into the created fracture. In addition to fluid leaking off via localized faulting, the low efficiency of these jobs can also be attributed to a strong pressure dependant permeability effect in the bossier sands [8]. It was observed that the fracture slurry is only heated up about 1.5°F per 1000 ft during most of the fracture treatment. The fluid heats up slowly after the stimulation is completed.

4.6 FRACTURE DIAGNOSTICS IN APC ANDERSON #2

Various direct and indirect fracture diagnostics were used to monitor the fracture treatments including:

- Micro-seismic imaging (for length, height and azimuth)
- Radioactive tagging with multiple isotopes (for near-wellbore height)
- Recording of bottomhole treatment pressure (to improve fracture simulation)
- Production logs (to evaluate effective propped fracture length and zonal coverage)

Micro-seismic imaging was used to measure overall fracture growth in real-time. Microseisms are microearthquakes induced by the changes in stress and pressure associated with hydraulic fracturing[9]. These earthquakes are slippages that occur along pre-existing planes of weakness (e.g., natural fractures) and emit seismic energy that can be detected at nearby seismic receivers. With an array of tri-axial receivers situated at depth near the hydraulic fracture, compressional (primary or P) and shear (secondary or S) waves can be detected. The location of any individual microseism is deduced from arrival times of the P and S waves (provides distance and elevation) and from particle motion of the P-wave (provides azimuth from the receiver array to the event). In order to use the particle motion information, it is also necessary to orient the receivers and the orientation is typically performed by monitoring perforations, string shots, or other seismic sources in the treatment well or some other nearby well. Accurate location of the microseisms, and thus the fracture image, is strongly dependent on accurate information about the velocity structure. To improve the results for this project, cross-well velocity data was directly measured using a perforation-timing procedure[10].

This project utilized a single micro-seismic imaging well (APC Anderson #1) to monitor the APC Anderson #2 York and Bonner treatments. The observation well was located 495 feet from the treatment well. Since microseisms are extremely small, a sensitive and high rate telemetry system is required to obtain accurate results. To meet these requirements, a twelve-level, three-component retrievable geophone array was deployed using a fiber optic wireline unit. Once at depth, the receivers were clamped against the wellbore using mechanical arms. The tool string was configured for an aperture to adequately cover the target zones. The treatments were continuously monitored giving the capability of determining how the fractures grew with time, which proved critical for understanding the complex fracture growth.

The micro-seismic mapping results for the York Sand stimulation are shown in Figure 3 and Figure 4. The fracture orientation is N91°E with asymmetrical growth 550 feet to the west and 275 feet to the east. Events were observed in the Bonner indicating the treatment had grown out of zone. However, by looking at the fracture growth with time it was clear that the communication between the York and Bonner was at a single point approximately 300 feet out along the west wing of the fracture. From this point, the fracture grew up and extended both back to the wellbore and farther to the west in the Bonner sand. The communication based on this information appears to be through a fault. The main portion of the fracture treatment, except that attributed to the fault, was contained within the York Sand.

The Bonner stimulation mapping results are shown in Figure 5 and Figure 6. The Bonner fracture also grew east/west with an azimuth of N87°E. The fracture growth was asymmetrical with an east wing extending 475 feet and a west wing of 175 feet. The Bonner treatment was also observed to have communicated upward in to the Moore and Bossier Marker sands through a fault. For the Bonner stimulation a significant amount of the treatment appears to have gone out of zone.

Combined results from the micro-seismic surveys are shown in Figure 7 and Figure 8. It is clear that the orientation of the fractures is in the east/west direction. Two separate faults were identified. For the York, the closest fault to the wellbore appears to be non-communicating at the York Sand level; however, it still appears to have generated a significant amount of microseisms (flaws associated with the fault) near the fault along with attenuated micro-seismic signals that cross the fault from the far wing. The second fault is open during the stimulation and communicates upwards to the Bonner. The hydraulic fracture in the York sand continues to grow westward beyond the second fault intersection.

For the Bonner stimulation, the fault closest to the wellbore was open during the stimulation and is responsible for the upward communication to the Moore and Bossier Marker sands. Interestingly, this is the same fault that was observed to be non-communicating at the York level on the first stimulation. The westward growth of the fracture in the Bonner sand appears to have been arrested where it intersected the fault. The fracture in the Bonner does not extend to the second fault observed during the York stimulation.

Previous micro-seismic mapping in this area also observed fracture growth along faults resulting in communication between sands.[11] For both APC Anderson #2 treatments, the out of zone growth was not the result of conventional fracture height growth but communication through the faults. In the previous micro-seismic mapping work in this area, one dataset did indicate fracture height growth up though the bounding shales, clearly generating microseisms in the shale layers.

A tracer log was run after the frac treatment. Results from the tracer log do not appear to be entirely consistent with the micro-seismic data. This, however, is not uncommon as the tracer logs only reflect the fracture geometry very close to the wellbore.

A pressure bomb was placed at the bottom of the well to record the bottomhole treating pressure during the treatment. The bomb recorded the data and was recovered after the treatment. This data was used to help calibrate hydraulic fracture model for both sands. The bottomhole pressure gauge information more accurately reflected the actual bottomhole treating pressures. Because of the depth, high treatment rate and multiple fluids used during the job, it is difficult to accurately estimate the bottomhole treating pressure from the surface treating pressure, hydrostatic and calculated fluid friction. This also allowed for improving the friction correlations for non-gelled fluids with sand.

4.7 FRACTURE MODELING

Fracture growth modeling was conducted using calibrated model settings that were obtained from a previous micro-seismic mapping project[4] in nearby wells. Although the initial fracture confinement for early fracture growth in both the York and the Bonner propped fracture treatments could be modeled effectively using these calibrated models, leakage of large slurry volumes through the fault area and the associated growth in shallower zones was not predicted by the model.

In order to account for this rather unusual behavior, we assumed that approximately 50% of the total injection rate would be used to propagate the fracture in the main target zones, while the remaining 50% would leak away through the fault. Unfortunately, micro-seismic mapping does not provide a direct measurement of fracture volume, and it was therefore not possible to directly measure the volume distribution between the main fracture system and the fracture systems above the pay zone fed by fluid leakoff through the fault. Therefore, uncertainty about fracture volume in the pay zone is substantial.

When using this simplistic leakoff assumption, fracture growth in the main target interval is still similar to the fracture growth behavior that was observed in the previous mapping project. An advantage of this new project was that more input data was available through direct measurements, especially a wealth of new data for the Young's modulus and the fracture closure stress profile. These directly measured parameters (through stress and core tests) provided an opportunity to decrease the degrees of freedom in the calibrated model.

A calibrated model is the closest approximate solution of what the fracture will do given the best data that is available for a specific reservoir. Reducing the degrees of freedom provides a more unique solution to fracture geometry when matching net pressure with a calibrated model. Of course a "calibrated model" can still contain several degrees of freedom that need to be addressed by reasonable assumptions.

Despite these shortcomings in calibrated models, a fracture design using a calibrated model is still far better than any uncalibrated alternative. Calibrated models use an empirical approach to match the observed fracture dimensions. Obviously, the calibrated model becomes better as additional measured data is incorporated. For example, the degrees of freedom in calibrated models dramatically reduce by including stress and modulus data for various layers. The data acquired for the APC Anderson #2 provided the information needed to improve the calibration of the model.

By measuring the closure stress profile more accurately with injection tests at different depths and utilizing dipole sonic inferred fracture closure stresses, it was found that the stress contrast between shales and sands was typically higher than what was previously assumed. For example, a sand-shale stress gradient contrast of about 0.07 psi/ft was measured in the new well, while the previous assumption was to use a 0.05 psi/ft contrast. This higher closure stress contrast would result in less fracture height growth. To compensate for this the calibrated model's composite layering effect was decreased slightly.

Micro-seismic mapping clearly shows initial fracture growth confinement to the York and Bonner sands in both treatments. Directly after the diagnostic injections, growth was observed in layers above the main target, initiating at the position where a fault intersects the layer.

The fracture treatment data in the York sand is shown in Figure 1. Fracture half-length in the York treatment is about 425 ft and it shows asymmetry of about 100 ft due to the inability of the fracture to penetrate through a sealing fault. Net pressure (see Figure 9) during the fracture treatment increases right from the start, even before proppant is being pumped. This increase is a confirmation of the confined fracture height growth in this layer. As the net pressure rises even more quickly than would be expected just based on fracture growth confinement to the York, it is also expected the fracture growth becomes more complex as the treatment progresses. This complex fracture growth was also observed on previous treatments, and could be a potential explanation for the relatively low effective fracture half-length observed in long-term production data. The narrower fracture width associated with complex growth decrease fracture conductivity and may result in insufficient fluid clean-up near the fracture tip. Figure 10 shows the fracture geometry resulting from matching both the net pressure and the dimensions inferred from micro-seismic mapping.

The fracture treatment data for the Bonner sand is shown in Figure 2. Fracture half-length from the Bonner treatment is about 375 ft with significant asymmetry around the wellbore due to the faulting. Net pressure (see Figure 11) during the fracture increases throughout the treatment, but starts rising much quicker as proppant arrives downhole. This sudden increase when proppant arrives downhole is an indication of a width restriction in the vicinity of the wellbore. Figure 12 shows the fracture geometry resulting from matching both the net pressure and the dimensions inferred from micro-seismic mapping.

4.8 PRODUCTION RESPONSE AND WELL TESTING

After the fracture treatment, the wells were put on production. When production of frac-water from the fracture stimulation declined, a production log was run in APC Anderson #2 wells. A comparison of this information with the core data helped to determine if all of the intervals were effectively stimulated.

After flowing the well for a little more than a month, the production log was run in the APC Anderson #2. The flow surveys showed that 34% of the production was from the Bonner, and 65 % from the York. The shale interval stress tested was contributing the remaining 1%. These percentages matched up very closely to the percentages of net pay each zone had to the total stimulated interval, indicating we had effectively stimulated both sands.

The cumulative production of the APC Anderson #2 has been 30% greater than that from the APC Anderson #1, which had 19% more net pay (Figure 13). With all other factors being the same, it appears that stimulating the Bonner and York in two stages had a large impact on the effectiveness of the treatments, and thus the productivity of the well.

Downhole pressure gauges were run in APC Anderson #2 for a two-week pressure buildup test once the well's rate had dropped to about 1.5 million cubic feet per day, 7 ½ months after gas was put to sales. This data was used for pressure transient analysis as seen in Figure 14. The results from this analysis can be used to infer propped fracture half-length and a comparison made with those derived from micro-seismic images. Although, still much shorter than what models would predict for a hybrid job in this area, the calculated effective fracture half-length of about 220 ft is a significant improvement from what was achieved with previous types of fracs (water fracs or gel fracs). Clearly, the effective or propped half-length of 220 ft is shorter than the created frac half-length of 400-500 ft measured by micro-seismic imaging. The production response of the well is consistent with 200 ft long effective flowing fracture half-lengths.

4.9 LESSONS LEARNT

1. Bossier sands have rock properties that are more heterogeneous than they appear on the GR/porosity log (vertical variation). Vertical variation and layering is a partial cause for fracture height containment in Bossier treatments, where a modest sand-shale stress contrast and a composite layering effect result in effective in-zone fracture growth.
2. Two stage fracture jobs resulted in better production rates than single stage jobs because both the sands were effectively stimulated.
3. Micro-seismic data indicates created fracture half-lengths of 400 to 500 feet. Propped or effective fracture half-lengths derived from pressure buildup analysis and history matching production data were significantly shorter (220 ft) than designed frac half-lengths.
4. Propped frac half-lengths of 220 feet were obtained from pressure buildup and production data in this well. The effective propped half-lengths for hybrid fracs are longer than the propped frac half-lengths obtained from either cross-link gel or water frac treatments, which typically show effective frac half-lengths of 100-150 feet.
5. Faults can have significant impact on fracture growth. Out-of-zone fracture height growth in this area is primarily the result of faults. Contrary to popular belief, hydraulic fractures can grow through faults (faults are not necessarily barriers to hydraulic fracture growth), and this paper shows an example of both a “barrier” fault and a fault that acts as a leak.
6. Hydraulic fractures typically grow east/west in this area.
7. Calibrated fracture growth models can provide a more accurate representation of fracture growth. Detailed closure stress measurements and core tests can help to improve the quality of these calibrated models.

8. The bottomhole treating pressures were found to be higher than expected based on the measured stress profiles. Typically net pressure increased by 800 - 1700 psi during frac jobs. The continuously rising net pressures are an indication of fracture containment, and also of increasing fracture complexity.

9. Frac slurry only heats up only about 1-1.5 °F per 1000 feet during the frac job at the pump rates used in this study. This can have a significant effect on the cross-linking kinetics. Depending on the desired fluid rheology, adjustments to the fluid system need to account for a bottomhole temperature that is on the order 10 °F higher than the surface temperature.

10. Data collected from BHP gauges increases confidence for modeling, especially at these depths (12,000') and when fluids with dramatically different viscosities and friction properties are being used.

4.10 REFERENCES

1. Barree, R.D., Cox, S.A., Gilbert V.J. and Dobson, M.: "Closing the Gap: Fracture Half Length from Buildup and Production Analysis", SPE 84491, presented at the SPE Annual Technical Conference, Denver, Oct 2003.
2. Barree, R.D., Cox, S.A., Barree, V.L. and Conway, M.W.: "Realistic Assessment of Proppant Pack Conductivity for Material Selection", SPE 84306, presented at the SPE Annual Technical Conference, Denver, Oct 2003.
3. Rushing, J.A. and Sullivan, R.B.: "Evaluation of Hybrid Water-Frac Stimulation Technology in the Bossier Tight Gas Sand Play", SPE 84394, presented at the SPE Annual Technical Conference, Denver, Oct 2003.
4. Griffin, L.G., Sullivan, R.B., Wolhart, S., Waltman, C., Wright, C.A., Weijers, L., and Warpinski, N.R., "Hydraulic Fracture Mapping of the High-Temperature, High-Pressure Bossier Sands in East Texas," SPE 84489, SPE Annual Technical Conference & Exhibition, Denver, Colorado, October 5 – 8, 2003.
5. Mayerhofer, M.J. and Meehan, N.D.: "Waterfracs – Results from 50 Cotton Valley Wells", SPE 49104, presented at the SPE Annual Technical Conference, New Orleans, Sept. 1998.

6. Fred, C.N., McConnell, S.B., Boney, C.L. and England, K.W.: "Experimental Study of Hydraulic Fracture Conductivity Demonstrates the Benefits of Using Proppants" SPE 60326, presented at the SPE Rocky Mountain Regional/Low Permeability Reservoirs Symposium, Denver, March 2000.
7. Mack, D.J, and Myers, R.R.: "Proppants: Is Bigger Better or is Placement the Key", SPE 72381, presented at the SPE Eastern Regional Meeting, Canton, October 2001.
8. Settari, A and Sullivan, R.B.: "The Modeling of the Effect of Water Blockage and Geomechanics in Waterfracs", SPE 77600, presented at the SPE Annual Technical Conference, San Antonio, Oct 2002.
9. Warpinski, N. R., Wolhart, S. L, and Wright, C. A., "Analysis and Prediction of Micro-seismicity Induced by Hydraulic Fracturing," SPE 71649, SPE Annual Technical Conference & Exhibition, New Orleans, LA, Sept 30 –October 3, 2001.
10. Warpinski, N.R, Sullivan, R.B, Uhl, J.E., Waltman, C.K., and Machovoe, S.R., "Improved Micro-seismic Fracture Mapping Using Perforation Timing Measurements for Velocity Calibration," SPE 84488, SPE Annual Technical Conference & Exhibition, Denver, Colorado, October 5 – 8, 2003.

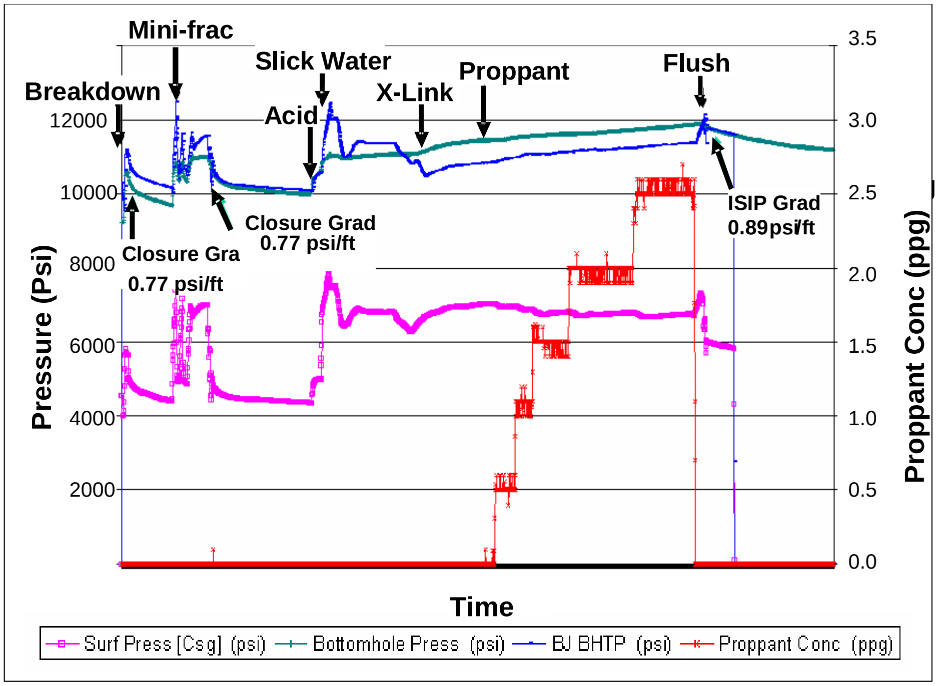

Figure 1: Fracture treatment in the York sand

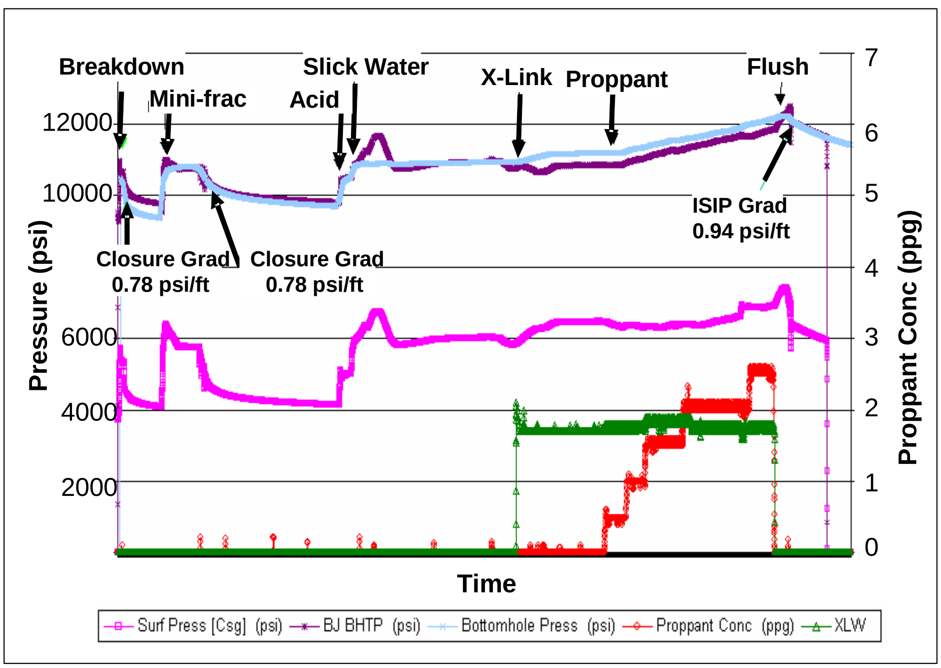

Figure 2: Fracture treatment in the Bonner sand

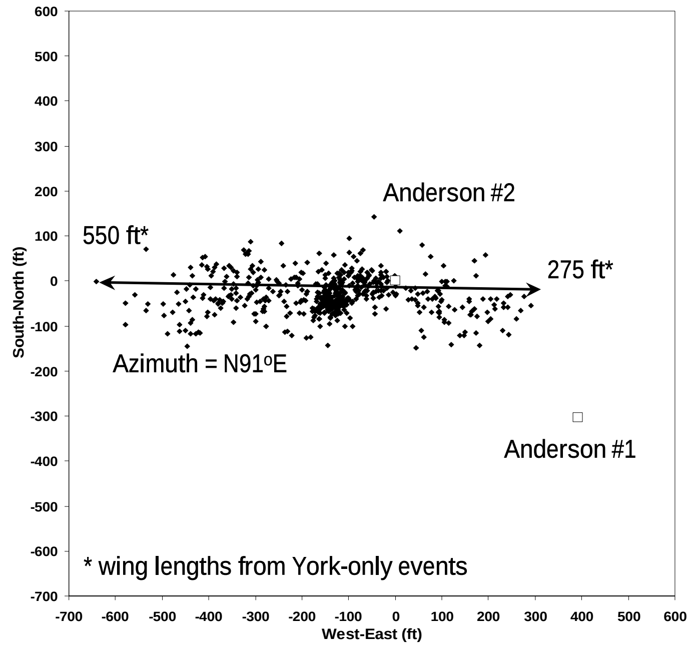

Figure 3: APC Anderson #2 York Stimulation, Micro-seismic Data Plan View

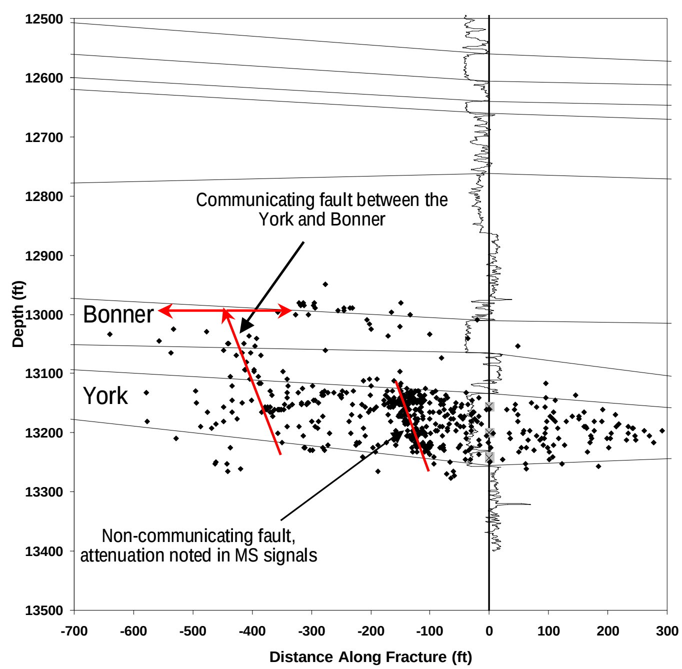

Figure 4: APC Anderson #2 York Stimulation, Micro-seismic Data Side View

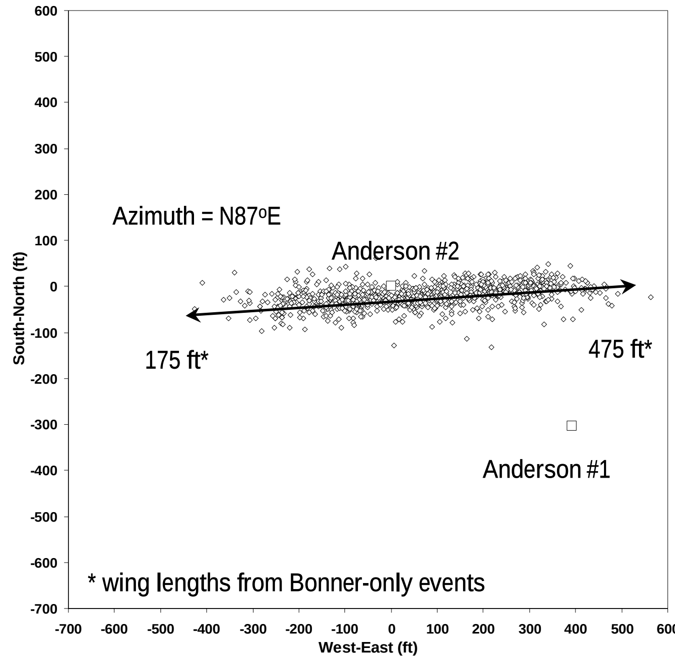

Figure 5: APC Anderson #2 Bonner Stimulation, Micro-seismic Data Plan View

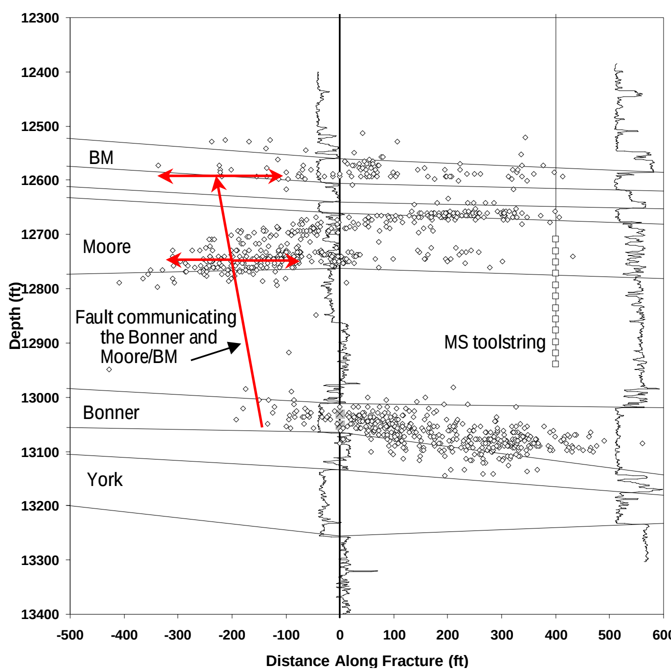

Figure 6: APC Anderson #2 Bonner Stimulation, Micro-seismic Data Side View

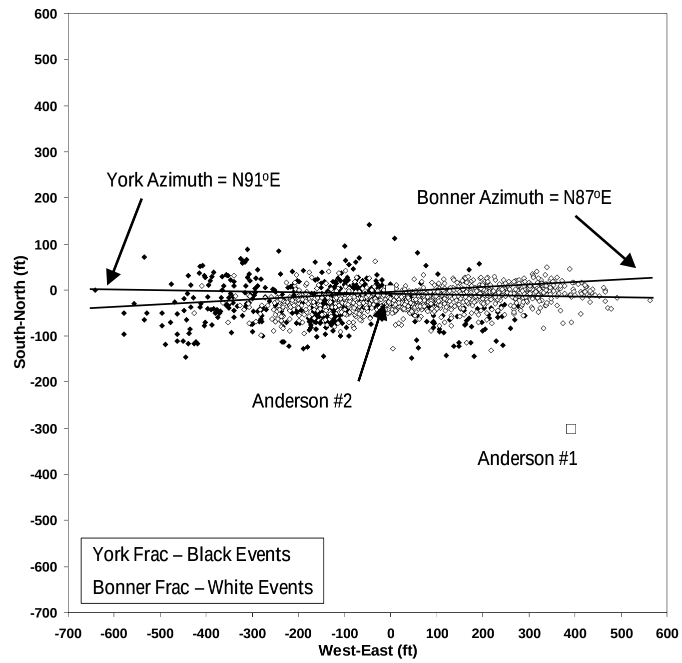

Figure 7: APC Anderson #2 Combined Results, Micro-seismic Data Plan View

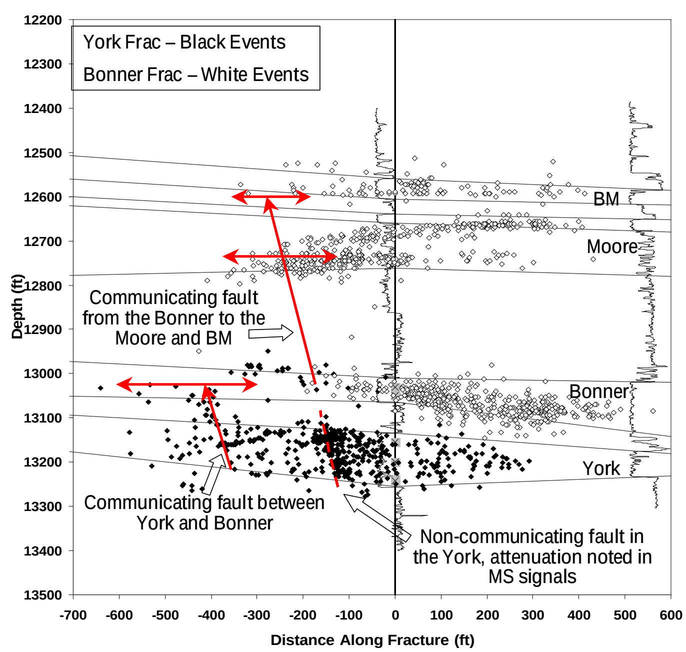

Figure 8: APC Anderson #2 Combined Results, Micro-seismic Data Side View

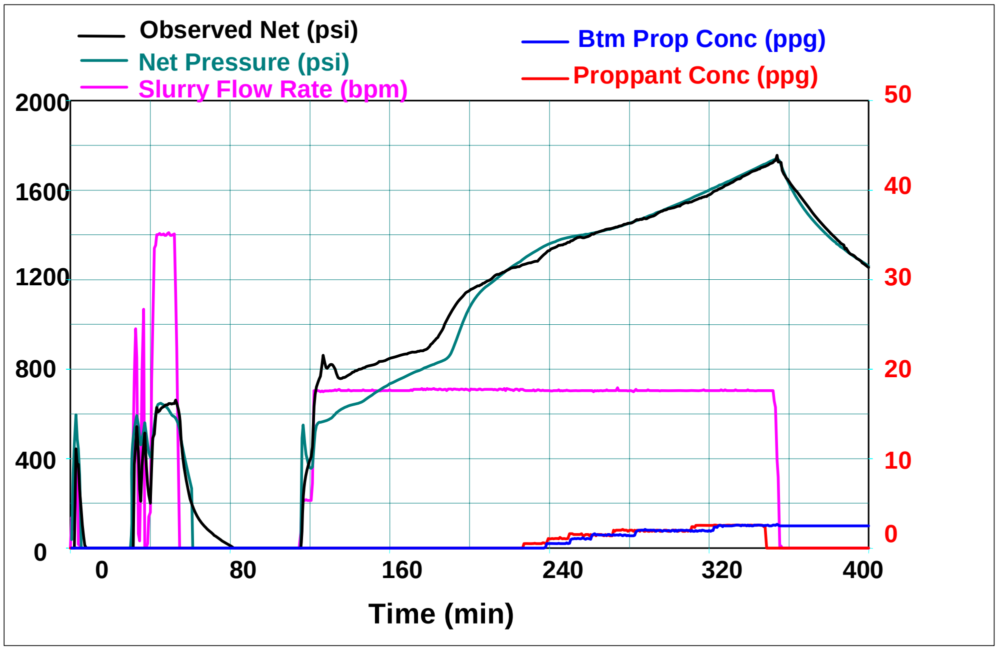

Figure 9: APC Anderson #2 York Stimulation, Net Pressure Match

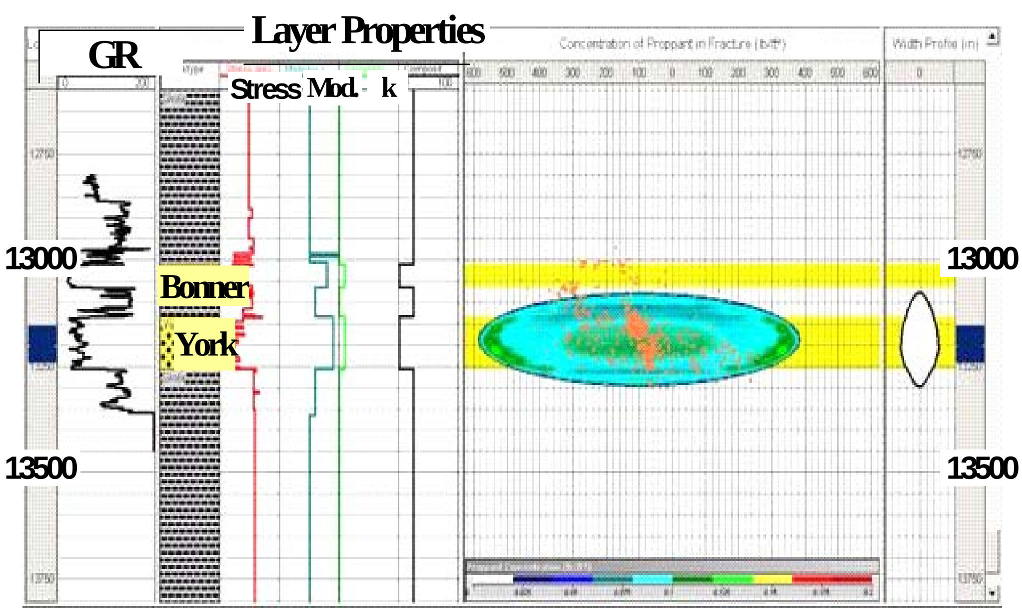

Figure 10: APC Anderson #2 York Stimulation, Fracture Profile and MS (orange dots) events

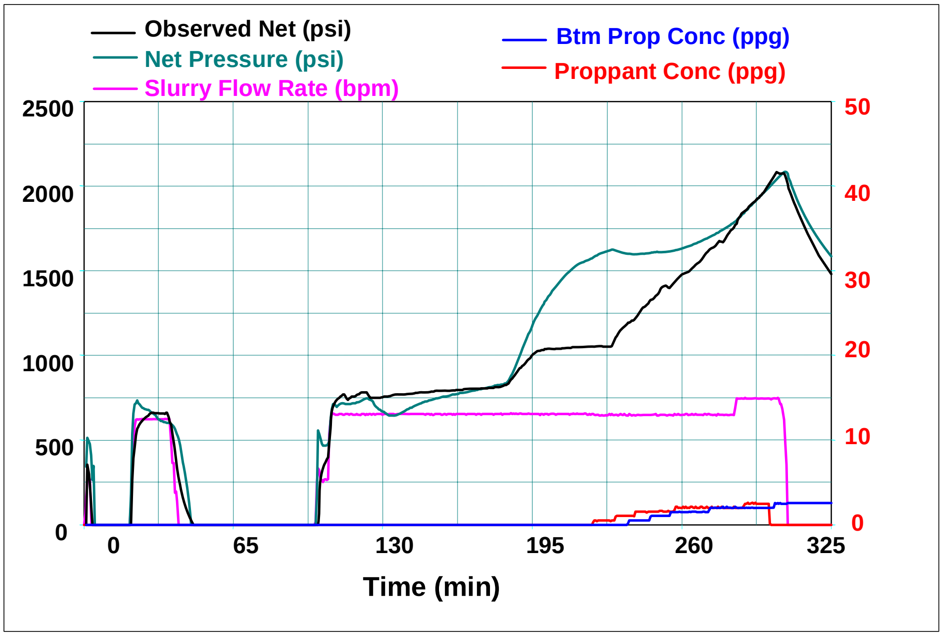

Figure 11: APC Anderson #2 Bonner Stimulation, Net Pressure Match

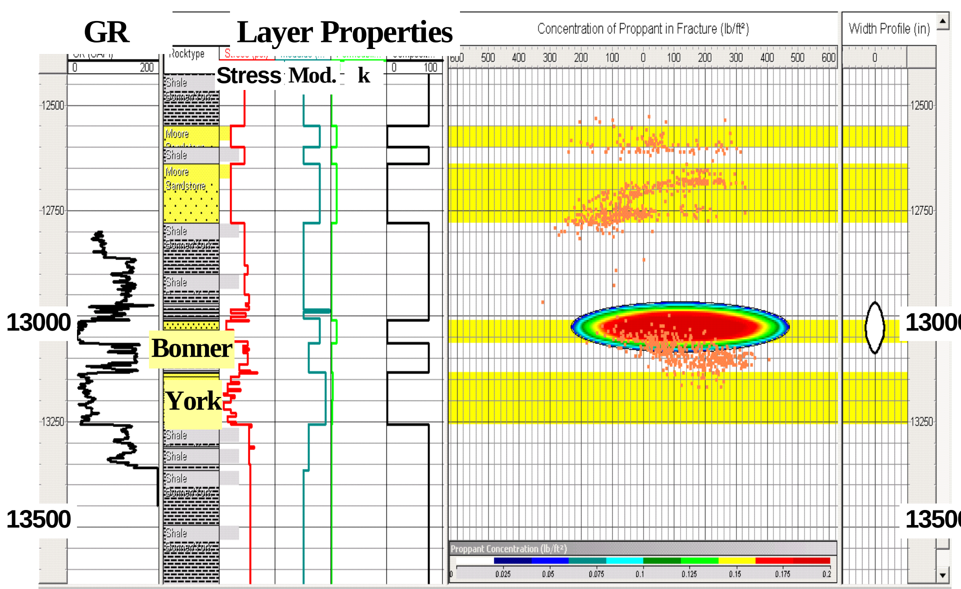

Figure 12: APC Anderson #2 Bonner Stimulation, Fracture Profile and MS (orange dots) events

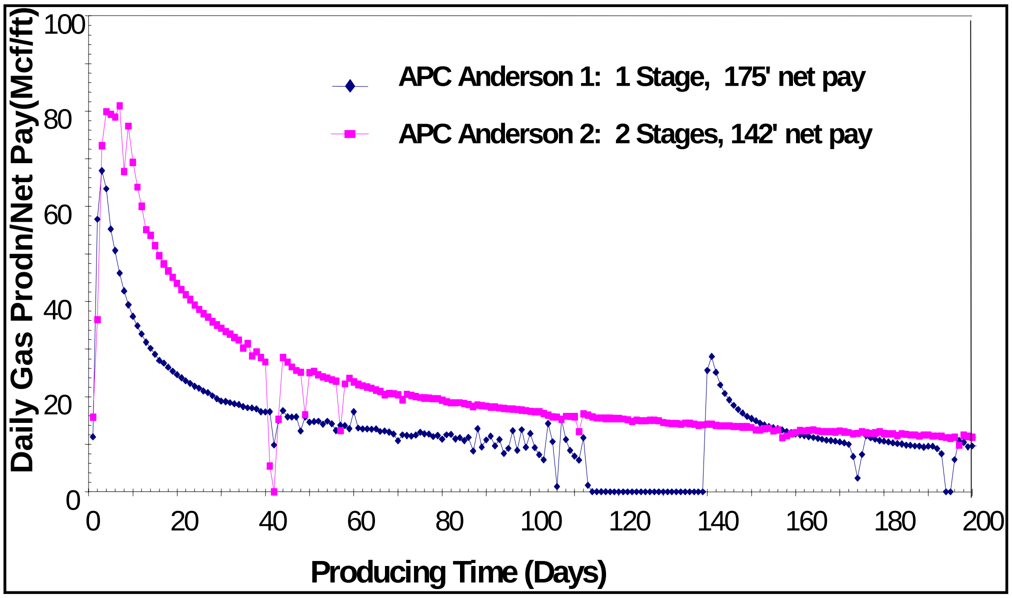

Figure 13: Comparison of gas production per foot of pay for 1 stage and 2 stage fracture treatments

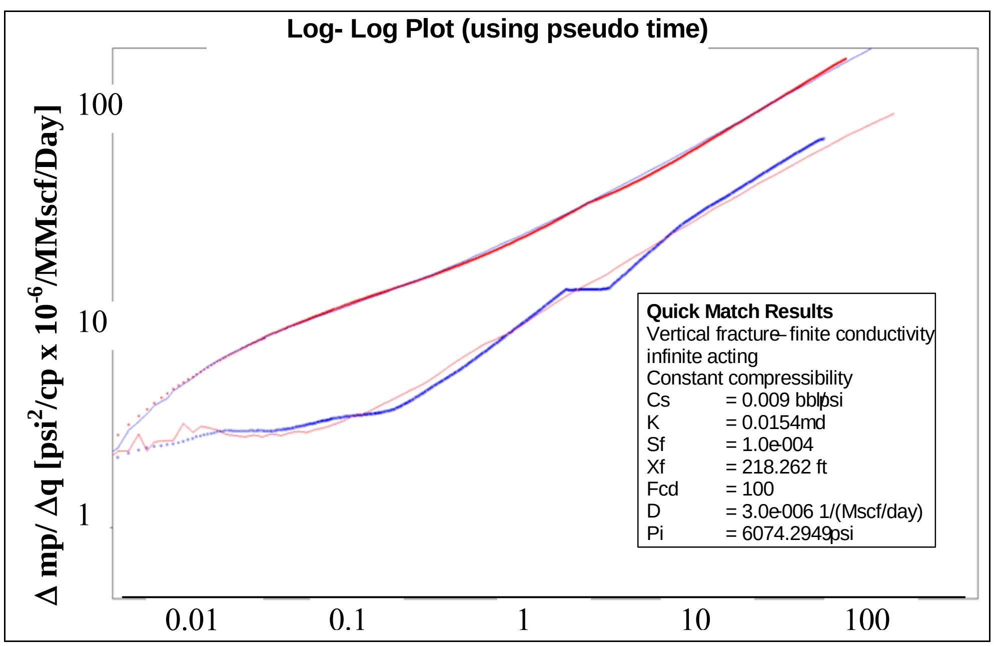

Figure 14: The calculated effective half-lengths and conductivity

CHAPTER 5. MODELING PROPPANT SETTLING IN WATER-FRACS

5.1 ABSTRACT

Water-fracs, consisting of proppant pumped with un-gelled fluid are the type of stimulation used in many low-permeability reservoirs throughout the United States. The use of low viscosity, Newtonian, fluids allows the creation of long narrow fractures in the reservoir without the excessive height growth often seen with cross-linked fluids. Proppant transport is a central issue in all these treatments because of the low viscosity of the fracturing fluid.

New models for proppant transport and settling in hydraulic fractures were developed and implemented in a 3-dimensional hydraulic fracturing code. It is shown that a simple Stokes' settling model is grossly inadequate. The proppant settling models developed in this paper account for the effects of fracture walls, changes in settling velocities and rheology caused by changes in proppant concentration, turbulence effects due to high fluid velocities and inertial effects associated with large relative velocities between the proppant and the fluid. Narrower fractures, higher proppant concentration and smaller proppant size reduce settling whereas turbulence leads to an increase in settling. Results are presented to show how the settling velocities are impacted by fluid velocity, proppant size, fluid rheology and fracture width. In most instances settling velocities differ significantly from the Stokes' settling velocity.

The new proppant settling model was incorporated into a 3-D hydraulic fracture simulator (UTFRAC-3D). Simulation results show that when settling is accounted for, significantly shorter propped lengths are obtained. The narrow fractures associated with water-fracs alter settling and thereby alter the proppant placement significantly. Although increasing fluid viscosity can reduce settling rates, increased height growth reduces the distance to which proppant can be placed. This clearly suggests a need to optimize fluid rheology. The improved fracture simulator can be used to better design fracture treatments (fluid rheology, injection rates, proppant concentration and size) for better proppant placement under a given set of in-situ stress conditions.

5.2 INTRODUCTION

Water-fracs are commonly applied in low permeability gas reservoirs. These treatments involve pumping low viscosity un-gelled fracture fluids. The low viscosity of the slick water leads to long created fracture lengths. However, due to high settling velocities of the proppant in the low viscosity fluid, the propped lengths achieved can be very small. Modifications to the water-frac stimulation design are needed to transport proppant further out into the fracture. This requires suspending the proppant until the fracture closes without generating excessive fracture height. Proppant transport clearly is a central issue in all these treatments. An improved proppant transport model is presented that can accurately model proppant transport when either un-gelled or cross-linked fluids are used to place the proppant. The use of this proppant transport model will allow engineers to customize treatment designs for individual wells.

The complete model for proppant transport in hydraulic fractures was incorporated into UTFRAC-3D, a fully three-dimensional hydraulic fracture simulator. The proppant transport equations were solved on an adaptive finite element mesh. The settling of the proppant was modeled taking into account the change in settling velocities and rheology due to changes in proppant concentration, turbulence effects due to high fluid velocities, and inertial effects associated with large relative velocities between the proppant and the fluid.

Inertial effects become significant at high settling velocities ($Re_p>2$) and are discussed in the next section. The effects of particle concentration, fracture width and turbulence are discussed in the following sections. An example calculation is shown to demonstrate the importance of each of the correlation factors applied to the Stokes' settling velocity. Finally, the settling correlations are incorporated into a proppant transport model in a fully 3-D fracture simulator (UTFRAC-3D). Results from the model are discussed in the last section.

5.3 INERTIAL EFFECTS IN PROPPANT SETTLING

A particle in a quiescent, unbounded fluid will accelerate until a balance is reached between the opposing forces of buoyancy and drag. When these forces are in balance, the terminal velocity (or Stokes' settling velocity) can be determined. This Stokes' settling velocity is valid for small particle Reynolds numbers ($Re_p < 2$) when wall effects are not important[1,2] and can be expressed as:

$$V_s = \frac{(\rho_p - \rho_f) g d_p^2}{18\mu} \qquad (1)$$

where, V_s (cm/s) is the Stokes' settling velocity of a single particle, ρ_p (g/cm^3) and ρ_f (g/cm^3) are the density of the particle and the suspending fluid, respectively, d_p (cm) is the diameter of the particle, g (980 cm/s^2) is acceleration due to gravity and μ (poise) is the viscosity of the liquid.

However, when the particle Reynolds number is large, the settling velocity is affected by the turbulent wakes created behind the particle. Many correlations are available to account for this change in velocity, but the following is used for this analysis and is valid for $2 < Re_p < 500$ [2]

$$\frac{1}{6}\pi {d_p}^3 (\rho_p - \rho_f) g = C_D \pi \left(\frac{d_p}{2}\right)^2 \frac{\rho_f {V_{Re}}^2}{2} \qquad (2)$$

$$C_D = \frac{18.5}{{N_{Re}}^{0.6}} \qquad (3)$$

$$V_{Re} = \frac{20.34(\rho_p - \rho_f)^{0.71} d_p^{1.14}}{\rho_f^{0.29} \mu^{0.43}} \qquad (4)$$

This can be represented in a more convenient form in terms of the corrected Stokes' velocity:

$$V_{Re} = V_s f(Re_p) \qquad (5)$$

Figures 1 to 3 show graphical representations of the Stokes' Equation (Eqn. 1) and the correlation for corrected terminal velocity (Eqn. 5). The parameters used to construct the Figure are listed in Table 1. It is clear that inertial effects slow down the settling rate of proppant particles significantly. This is particularly true at high particle Reynolds numbers (Re_p>5).

5.4 EFFECT OF PROPPANT CONCENTRATION ON SETTLING VELOCITIES

The behavior of a single particle is of little interest for fracturing. This section examines the effect of concentration on the terminal settling velocity. First, several correlations are introduced, evaluated and compared graphically. Finally, an empirical correlation is presented that captures the important effect of solids concentration and approaches the correct limit of zero settling velocity at maximum packing. All of the correlations presented in this section are valid for unbounded flows.

In a system with no fluid motion (a sedimentation process), Govier and Aziz developed the following expression for terminal velocity, which accounts for particle concentration[5]

$$\ln\left(V_\phi / V_s\right) = -5.9\phi \qquad (6)$$

In this equation, V_ϕ is the settling rate of the particles at a volume fraction, ϕ, and V_s is the settling velocity of a single particle in an unbounded fluid.

Nolte gives another simple expression for the effect of solids concentration effect on the terminal velocity[5, 6]

$$V_\phi = V_s\left(1 + 6.88\phi\right)^{-1} \qquad (7)$$

Again, V_ϕ is the corrected terminal velocity and ϕ is the volume fraction of the particles.

Daneshy[7] proposed the following equation:

$$V_\phi = V_s\left[\left(1-\phi\right)/10^{1.82\phi}\right] \qquad (8)$$

Like the previous two expressions, this correlation is a simple correction to the Stokes' terminal velocity and is a function of the particle concentration.

Richardson and Zaki[6] present the following expression for the terminal velocity as a function of concentration[6,9] where $F_\phi = 6\pi u a V_\phi \beta_t$ (F_ϕ is the drag force) and β_t is the coefficient due to particle concentration. A force balance on the particle requires:

$$\frac{4}{3}\pi a^3 \left(\rho_p - \rho_f\right) g = 6\pi\mu a V_\phi \beta_t \qquad (9)$$

$$V_\phi = \frac{\left(\rho_p - \rho_f\right) g d_p^2}{18\mu}\beta_t \qquad (10)$$

$$\beta_t = \left(1-\phi\right)^{4.65} \qquad (11)$$

$$V_\phi = V_s\left[(1-\phi)^{4.65}\right] \qquad (12)$$

Maude and Whitmore generalized a correlation for various flow regimes by introducing an experimentally determined parameter β [9]:

$$V_\phi = V_s\left[(1-\phi)^{\beta}\right] \qquad (13)$$

Where, β is approximately 5 for mono-dispersed spheres in creeping flow, and β is between 2 and 4 in turbulent flow.

Many, more complicated expressions for the effect of concentration exist. For example, the Zigrang-Sylvester[23] equation is given below:

$$V_\phi = \gamma - \sqrt{\gamma^2 - \alpha^2} \qquad (14)$$

Where

$$\gamma = \frac{\left(2\alpha + \delta^2\right)}{2} \qquad (15)$$

$$\alpha = \frac{2}{0.63\sqrt{3}}\left[\frac{(\rho_p - \rho_f)gd_p(1-\phi)}{\rho_f(1-\phi)^{1/3}}\right]^{1/2} \qquad (16)$$

$$\delta = \frac{4.8}{0.63}\left[\mu \exp\left(\frac{5\phi}{3(1-\phi)}\right)\Big/\rho_f d_p\right]^{1/2} \qquad (17)$$

The first five correlations are compared in Figure 4. Except for the Nolte equation, all of the correlations predict very similar results.

Ideally, a simple relationship that captures the trends presented in Figure 4 and, also, predicts a zero terminal velocity as the suspension approaches maximum packing is desired. To capture these trends, we fit a curve (Figure 4) to the correlations. The resulting polynomial follows:

$$V_\phi = V_s(2.37\phi^2 - 3.08\phi + 1) \qquad (18)$$

This empirical correlation that incorporates the concentration effect on settling rate agrees well with experimental data available in the literature[6] (Figure 5).

5.5 EFFECT OF FRACTURE WIDTH ON SETTLING VELOCITIES

The previous sections considered unbound flow and ignored the effect of the fracture walls. This section introduces expressions that modify the terminal velocity in the presence of impermeable confining walls. Furthermore, averaged expressions are presented to account for the presence of walls. We recognize that fracture walls will be permeable. Corrections for fluid leak-off are currently being investigated and will be discussed in a later publication.

Consider the system described by Figure 6. Lorentz[12] derived the following expression for a sphere moving parallel to a vertical wall. The force on the particle is expressed as follows:

$$\frac{F}{6\pi\mu aV}=1+\frac{9}{16}\left(\frac{a}{l_i}\right)+o\left(\frac{a}{l_i}\right)^2 \quad (i=1,2) \qquad (19)$$

In this expression, a is the radius of the sphere, l_1 is the distance to the wall 1, l_2 is the distance to wall 2 and V is the instantaneous velocity of the sphere. When the ratio of a/l_i is small, the higher order terms of Eqn. (19) can be ignored. Using this notation, the effect of the two parallel walls on the settling velocity of a sphere is given by the following simplified expression:

$$\frac{F}{6\pi\mu aV}=1+\frac{9}{16}\left(\frac{a}{l_1}+\frac{a}{l_2}\right)+o\left[\left(\frac{a}{l_1}\right)^2+\left(\frac{a}{l_2}\right)^2\right] \qquad (20)$$

or

$$\frac{F}{6\pi\mu aV}=1+\frac{9}{16}\frac{a}{l}\left(\frac{l}{l_1}+\frac{l}{l_2}\right) \qquad (21)$$

Where l represents half the distance between the walls and F is the modified drag force acting on the sphere in the presence of the walls.

When the ratio a/l is small, Eqn. (21) can be expressed as follows:

$$\frac{F}{6\pi uaV}=\left[1-\frac{9}{16}\left(\frac{a}{l_1}+\frac{a}{l_2}\right)\right]^{-1} \qquad (22)$$

Let l_1 = x, the position of the particle. Therefore, Eqn. (22) can be expressed as follows:

$$\frac{F}{6\pi uaV}=\left[1-\frac{9}{16}\left(\frac{a}{x}+\frac{a}{2l-x}\right)\right]^{-1} \qquad (23)$$

Balancing the viscous and gravity forces results in the following corrected settling velocity of a single sphere near a wall.

$$V_w=V_s\left[1-\frac{9a}{16}\left(\frac{1}{x}+\frac{1}{2l-x}\right)\right] \qquad (24)$$

For a small ratio of a/l Eqn. (24) predicts the following trends as shown in the figures (Figure 7 represent a ratio $a/2l = 0.1$ and Figure 8 represents a ratio $a/2l = 0.01$).

As noted in these figures, the velocity is attenuated near the walls, and this effect is more pronounced at larger values of $a/2l$.

To obtain a more useful solution, the velocity is averaged over the width of the fracture. The average velocity of a sphere between the walls is expressed as follows:

$$\bar{V}_w = \int_a^{2l-a} V_w P(x)dx \qquad (25)$$

Where $P(x)$ is the probability of finding a particle at a distance x from the wall. The probability function will in general depend in a complex way on the fluid velocity distribution and on the leakoff rate. For simplicity, $P(x)$ is assumed to be constant for all values of x, a < x < 2l-a.

$$\int_a^{2l-a} P(x)dx = 1 \qquad (26)$$

Therefore,

$$P(x) = \frac{1}{2l - 2a} \qquad (27)$$

Integrating the velocity results in the following expression for the average velocity of a particle bounded by walls:

$$\bar{V}_w = V_s\left[1 - \frac{9}{16}\left(\frac{m}{1-m}\right)\ln\left(\frac{2-m}{m}\right)\right] \quad (28)$$

where $m = a/l$. As noted, the average settling velocity is a function of Stokes' settling velocity and the ratio of the radius of the particle to the width of the slot.

$$V_w = V_s\left[0.563\left(\frac{a}{l}\right)^2 - 1.563\left(\frac{a}{l}\right) + 1\right] \quad (29)$$

Figure 9 compares the average corrected velocity given by the averaged equation presented above. It is important to reiterate that this expression is strictly valid when the ratio of *a/l* is much less than 1. Alternatively a polynomial correlation that matches Eqn. 28 and approaches the correct limits can be used. We propose the following correlation.

Figure 10 shows a comparison between Eqns. 28 and 29. Experiments are currently underway to test the validity of Eqn. (28) and the curve fitted correlation.

5.6 EFFECT OF TURBULENCE ON SETTLING VELOCITIES

It is well known that the turbulent motion of the suspending fluid will affect the settling velocity of particles in a suspension. However, several different effects have been observed. For instance, Brucato et al. [4] observed a decrease in settling velocity for a Couette-Taylor flow field. Using a novel experimental technique, they were able to extract a correlation for the drag coefficient that accurately predicts an increase in the drag (compared to a quiescent fluid).

$$\frac{C_d - C_{d_o}}{C_{d_o}} = 8.76x10^{-4}\left(\frac{d_p}{\varsigma}\right)^3 \quad (30)$$

Where

$$\varsigma = \left(\frac{\nu^3}{\varepsilon}\right)^{\frac{1}{4}} \quad (31)$$

Here, ν is the kinematic viscosity and ε is the energy dissipation. Another correlation that predicts a reduction in terminal velocity for a single sphere in turbulence is given by the following model proposed by Clark et al.[5].

$$V_t = 1.74\left(\frac{2a(\rho_p - \rho_f)g}{\rho_f}\right)^{\frac{1}{2}} \quad (32)$$

Similar to the Brucato et al.[4] formulation, this empirical correlation results in an increased drag (decreased settling velocity). However, numerical analysis suggests that some flow configurations, including turbulent channel and pipe flows, result in an increase in the settling velocity. Several recent numerical investigations have studied this phenomenon and identified several important flow parameters. Very few experimental studies are presently available.

Maxey[14] conducted extensive numerical modeling of particle deposition in turbulent flows. He used direct numerical simulations (DNS) to investigate the settling of aerosol particles in homogenous turbulence and noted a 10 percent increase in the settling velocities of the aerosol. He suggested that a relationship between the 'inertial response' of the particle and the energy dissipation spectrum accounted for this effect. Later investigations by Wang and Maxey[21] concluded that the particle settling velocity could increase by as much as fifty percent. Again, they used DNS to model the problem. They attribute the increased settling velocity to 'inertial bias' and determined that the Kolmogorov scale (small scale) fluctuations were the most important in determining the velocity increase. In a more recent publication, Maxey et al.[14], these results were confirmed. However, there has been some debate over the importance of different time scales. Yang and Lei[22] agree that the Kolmogorov time scale is important but also believe large-scale fluctuations affect velocity and concentration profiles[22]. Finally, numerical analysis by Mei et al.[16] revealed that non-linear drag attenuates the increased settling velocity caused by turbulence in the suspending fluid. The purpose of this section is to incorporate the available theoretical analysis into a correlation that will capture the change in particle settling rates.

5.6.1 The Governing Parameters

In summary, numerical analysis has revealed the important effect of turbulence on settling velocity if the ratio of the particle-time-scale and the Kolmogorov- time -scale is near unity. A particle response time for the system is defined as follows:

$$\tau_p = \frac{2(\rho_p - \rho_f)a^2}{9\rho_f \nu} \qquad (33)$$

The Kolmogorov time scale is defined in terms of the viscosity and the energy dissipation spectrum as follows:

$$\tau_k = \left(\frac{\nu}{\varepsilon}\right)^{\frac{1}{2}} \qquad (34)$$

An important result of the numerical studies is that the settling velocity increases to a maximum when the ratio of the relaxation time of the particle and the Kolmogorov time scale approaches unity.

$$\lambda = \frac{\tau_p}{\tau_k} \approx o(1) \qquad (35)$$

Wang and Maxey[21] provide numerical data revealing the importance of this parameter. Data from this study used for our analysis is presented in Figure 11.

These results show the change in settling velocity (relative to a quiescent fluid) as a function of the ratio of the two time scales. The above results are normalized by the Kolmogorov velocity, which is equivalent to the Stokes' settling velocity. As indicated graphically, the ratio of the time scales extends from 0 to 3.5 and indicates a maximum near unity (more specifically, 0.75). Furthermore, this graph indicates a change in the maximum at various Reynolds numbers (the change in settling velocity increases with increasing Re numbers).

Unfortunately, these results are difficult to generalize and involve parameters that are often impractical to measure. However, Wang and Maxey's results reveal that the important parameters governing the phenomena of increased settling velocity are the ratio of time scales and the experimentally measured Reynolds number based on the average fluid velocity. Such a correlation has been developed and implemented in the UTFRAC-3D to properly account for the turbulence effects in proppant settling. Figure 12 presents the correlations at various Reynold's Numbers as a function of the ratio of the time scales (λ). Figure 13 presents the correlation with data extracted from Maxey and Wang's numerical simulations.

5.7 PROPPANT TRANSPORT MODEL IN UTFRAC-3D

To demonstrate the importance of settling in the prediction of propped fracture lengths, a model for proppant transport was incorporated into UTFRAC-3D, a fully three-dimensional hydraulic fracture simulator. The proppant transport equations are solved on an adaptive finite element mesh[25,26]. The settling of the proppant is modeled taking into account the important factors discussed above that affect settling.

Mass conservation for the slurry in two dimensions can be expressed as

$$\frac{\partial(\rho w)}{\partial t} + \nabla.(\rho \vec{q}) = -\rho_f q_l \qquad (36)$$

where ρ is the slurry density, w is the fracture width, q is the slurry velocity, ρ_f is the fluid density and q_l is the leak-off.

Mass conservation for the particles can be expressed as

$$\frac{\partial(c\rho_p w)}{\partial t} + \nabla.(c\rho_p \overrightarrow{q_p}) = 0 \qquad (37)$$

where c is the proppant concentration, ρ_p is the proppant density, w is the fracture width and q_p is the proppant velocity.

The velocity vector for the proppant can be expressed as

$$\bar{q}_p = \bar{q} + \hat{k} V_t \qquad (38)$$

where q is the velocity of the slurry, V_t is the corrected settling velocity of the proppant and $\hat{k}$ is a unit vector in the y direction.

The fracture mechanics, fluid flow in the fracture and the proppant concentration yield three systems of equations for three unknowns – width, pressure and concentration. A Galerkin finite element method is employed to obtain an approximation to concentration c. For the moving boundary problem, an unstructured mesh is employed in order to discretize the irregular domain. The unstructured mesh associated with the Delunay Triangualtion aids in convection of nodal points and the insertion of new nodes inside the domain as the fracture propagates. The mesh consists of triangular and quadrilateral elements. The same mesh is used for all variables – pressure, width and concentration. The proppant transport equations are partially decoupled from the fracture mechanics equations by basing the rheology[27,28] of the proppant slurry on the proppant concentration from the previous time step.

5.8 IMPACT OF PROPPANT SETTLING ON PROPPED FRACTURE LENGTH

Effective fracture lengths in water fracs where the proppant is pumped with slick water are much shorter than the created frac lengths. Modeling proppant transport is critical to improving the propped fracture lengths of these wells. Developing an accurate model for proppant transport is the first step in designing the optimum rheology for proppant placement under a given set of reservoir conditions. UTFRAC-3D is a fully 3-D easy to use model for the design for water and hybrid fracs.

Figure 14a shows the proppant concentration distribution in the fracture when ungelled slick water (1 cp) is used to place the proppant without considering proppant settling. Figures 14b and 14c show the proppant concentration distributions when Stoke's settling (without any corrections) is considered and when corrected Stoke's settling is modeled. Note that when Stoke's settling is considered, the settling of the proppant is very significant leading to very short propped lengths. When the various effects such as turbulence, fracture walls etc., are considered, the settling velocities obtained are significantly smaller, therefore, the proppant is carried further into the fracture.

Figure 15a shows the proppant concentration distribution in the fracture when a 100 cp fluid is used to place the proppant without considering proppant settling. Figures 15b and 15c show the proppant concentration distributions when Stoke's settling (without any corrections) and the corrected settling is considered. Due to the higher viscosity, the proppant settling velocity is much lower and therefore, the proppant placement is much better compared to slick water.

Figures 16 and 17 show the proppant concentration distributions (with corrected settling) for 1cp and 100 cp fluids for a case where the created fracture lengths are long. Note that for the 1cp case, due to the higher settling velocities, the proppant does not reach the end of the created fracture resulting in short propped length. For the 100 cp case, the proppant is carried much further into the fracture resulting in longer propped fracture.

5.9 CONCLUSIONS

Correlations are presented for modeling proppant settling in water fracs. These correlations allow fracture models to account for inertial effects, proppant concentration, fracture width and turbulence for the first time. These correlations have been incorporated into a fully 3-D fracture simulator. Results from the simulator clearly show the importance of accounting for the settling correlations when modeling proppant transport in water fracs. The effective fracture lengths obtained when correcting for proppant settling effects with the appropriate correlations can vary significantly from similar simulations conducted with Stoke's settling or assuming no settling at all. This model can find use in the design of water fracs and will help in designing fracture treatments for maximum propped lengths.

NOMENCLATURE:

a	Radius of particle (cm);
d_p	Diameter of particle (cm);
ρ_p	Density of proppant (gm/cc);
ρ_f	Density of fluid (gm/cc)
g	Acceleration (980cm/s^2);
μ	Viscosity (poise);
V_s	Settling rate of particle in Stokes' flow (cm/s);
V_{Re}	Settling rate of particle with high particle Renolds Number (cm/s);
$f(Re_p)$	High particle Renolds Number correction coefficient

ϕ Proppant concentration (volume of solid / volume of mixture)

$f(\phi)$ Concentration correction coefficient;

$f(W)$ Wall correction coefficient;

V_ϕ Settling rate of concentrated particles (cm/s);

V_w Settling rate corrected for presence of walls (cm/s);

$\bar{V}_w$ Average settling rate corrected for presence of walls (cm/s);

V Instantaneous settling rate of particle (cm/s);

P(x) Probability function of V_w distribution;

l_1 Distance from center of particle to wall 1 (cm);

l_2 Distance from center of particle to wall 2 (cm);

5.10 REFERENCES

1. McCabe, W. L., "Unit Operations of Chemical Engineering", McGraw-Hill Book Co. Inc., 1956.
2. Asmolov, E. S., "The inertial lift on a small particle in weak-shear parabolic flow", Physics of Fluids, v. 14, No. 1, pp. 15, 2002.
3. Biswas, G. and Eswaran, V., "Turbulent Flows: Fundamentals, Experiments and Modeling", CRC Press, Boca Raton, 2002.
4. Brucato, A. et al., "Particle drag coefficients in turbulent fluids", Chemical Engineering Science, v. 52, n 18, pp. 3295, 1998.
5. Clark, P. and Quadir, J., "Prop Transport in Hydraulic Fracturing: A Critical Review of Particle Settling Velocity Equations", SPE/DOE 9866, 1981.
6. J. F. Richardson and W. N. Zaki, "The Sedimentation of a Suspension of Uniform Spheres Under Conditions of Viscous Flow", Chemical Engineering Science, 1954, Vol.3 pp.65 to 73
7. Daneshy, A. A.: "Numerical Simulation of Sand Transport in Hydraulic Fracturing", Journal of Petroleum Technology, pp. 132-140, Jan. 1978.
8. Ganatos, P., Pfeffer, R. and Weinbaum, S., J. of Fluid Mech., v. 99, pt. 4, pp. 755-783, 1980.

9. Happel J., and Brenner H., “Low Reynolds Number Hydrodynamics”, Prentice Hall, Englewood Cliffs, N. J., pp. 412, 1965.
10. Jasberg, A., et al., "Hydrodynamical Forces Acting on Particles in a Two-Dimensional Flow Near a Solid Wall", Computer Physics Communication, v. 129, pp. 196, 2000.
11. Libby, A., "Introduction to Turbulence", Taylor and Francis, 1996.
12. Lorentz H. and A. Abh., Theory. Phys., 1 23, 1907.
13. Maxey, M. R., "The gravitational settling if aerosol particles in homogeneous turbulence and random flow fields", J. Fluid Mech., v. 174, pp. 441, 1987.
14. Maxey, M. R. et al., "Simulations of dispersed turbulent multiphase flow", Fluid Dynamics Research, v. 20, pp. 143, 1997.
15. Acharya, A., “Particle Transport in Viscous and Viscoelastic Fracturing Fluids”, SPE 13179, 1986.
16. Mei, R. "An approximate expression for the shear lift force on a spherical particle at finite Reynolds number", Int. J. Multiphase Flow, v. 18, No. 1, pp. 145, 1992.
17. Mei, R. et al., "Turbulent Dispersion of Heavy Particles with Nonlinear Drag", Trans ASME, v. 119, pp. 170, 1997.
18. Patankar, N. A., Haung, P. Y., Ko, T. and Joseph, D. D., "Lift-off of a single particle in Newtonian and Viscoelastic fluids by direct numerical simulation", J. Fluid Mech., v. 438, pp. 67, 2001.
19. Saffman, P.G., "The lift on a small sphere in a slow shear flow", J. of Fluid Mech., v. 22, pt. 2, pp. 385, 1965.
20. Segre G. and Silberberg A. Journal of Fluid Mechanics, v. 14, pp. 115, 1962.
21. Wang, L. P. and Maxey, M. R., " Settling velocity and concentration distribution of heavy particles in homogeneous isotropic turbulence", J. Fluid Mech., v. 256, pp. 27, 1993.
22. Yang, C. and Lei, U., "The Role of the Turbulent Scales in the Settling Velocity of Heavy Particles in Homogenous Isotropic Turbulence", J Fluid Mech., v. 371, pp. 179, 1998.
23. Zigrang D. J., and Sylvester N. D., “An Explicit Equation for Particle Settling Velocities in Solid-Liquid Systems”, AICHE J28 (3), pp. 514-515, 1982.
24. R. Byron Bird, Warren E. Stewart and Edwin N. Lightfoot. “Transport Phenomena”,

First Version(1960), P192.

25. Ouyang, S., “Propagation of Hydraulically Induced Fractures with Proppant Transport”, Ph.D. Dissertation, The University of Texas at Austin, May 1994.
26. Gu, H.R. and Yew, C.H., “Finite Element Solution of a Boundary Integral Equation for Mode I Embedded Three-Dimensional Fractures”, International Journal for Numerical Methods in Engineering, 1988, 26, pp. 1525-1540
27. Shah, S.N., “Rheological Characterization of Hydraulic Fracturing Slurries”, SPE 22839, presented at the SPE Annual Technical Conference, Dallas, 1991
28. Shah, S.N., “Proppant Settling Correlations for Non-Newtonian Fluids”, SPE Production Engineering, November 1989, pp. 446-448

ρ_f	1.0 g/ml
ρ_p	2.5 g/ml
μ	1.0 cP
a	0~0.1 cm

Table 1: Default system properties used in figures below (a is radius of particles).

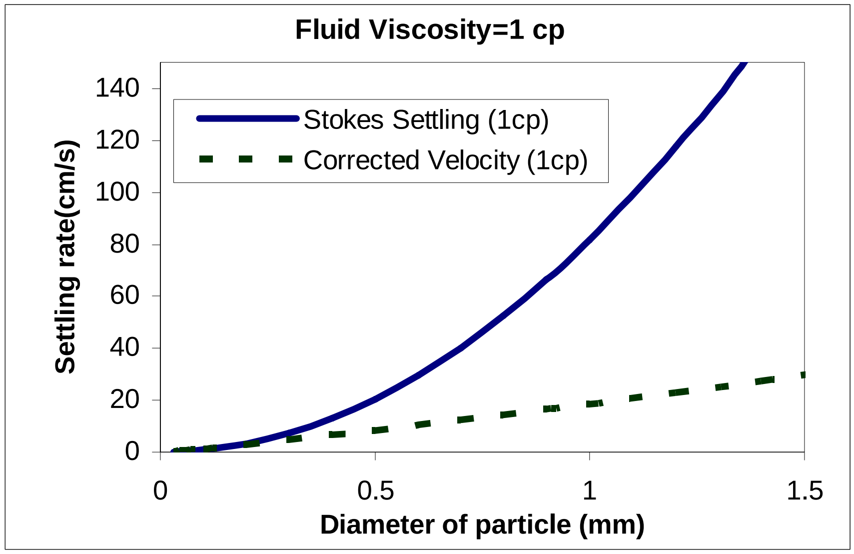

Figure 1: Terminal velocity of different size particles predicted by Stoke's equation and corrected for inertial effects.

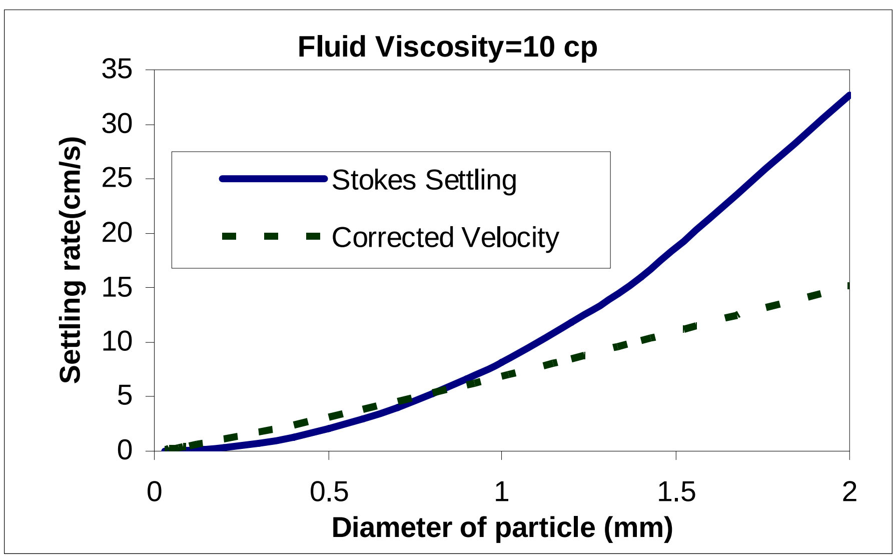

Figure 2: Settling velocity predicted by Stoke's equation and corrected for inertial effect in 10 cp fluid.

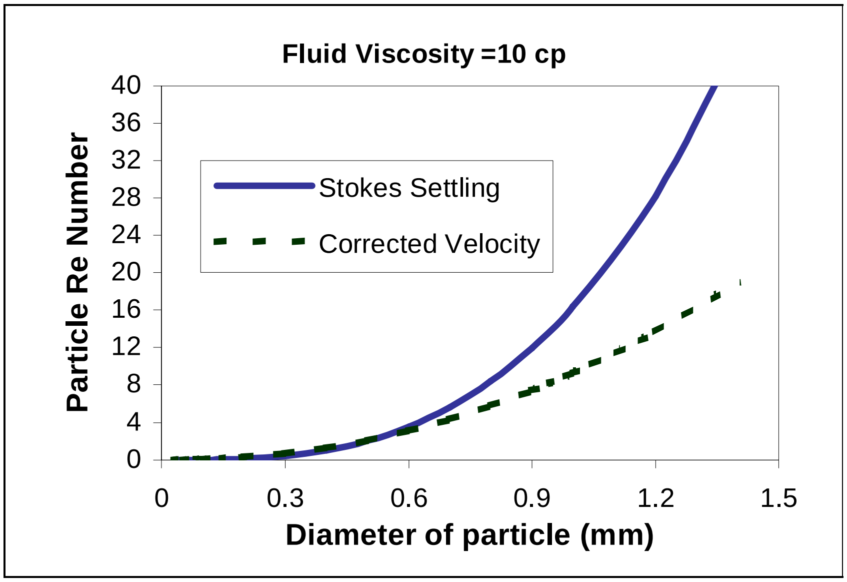

Figure 3: Particle Reynolds number as a function of radius.

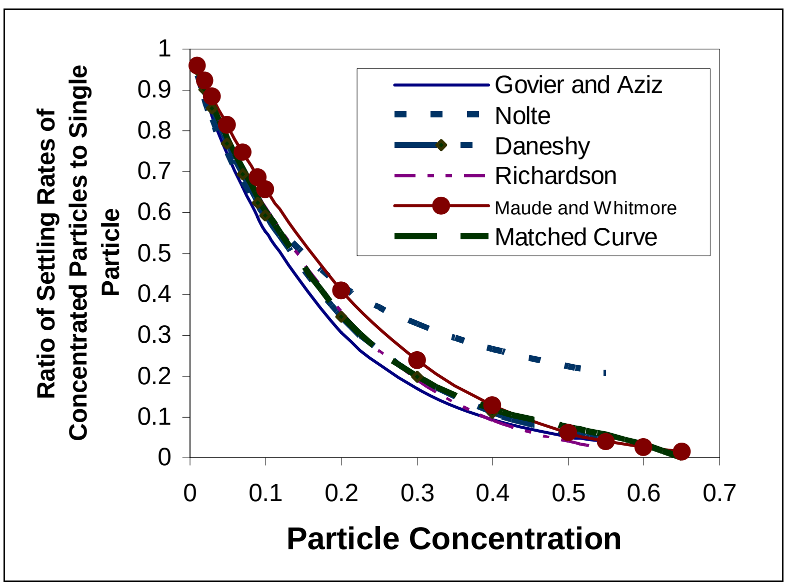

Figure 4: Past correlations and the proposed correlation (Eqn. 18) for the effects of solids concentration on settling velocity.

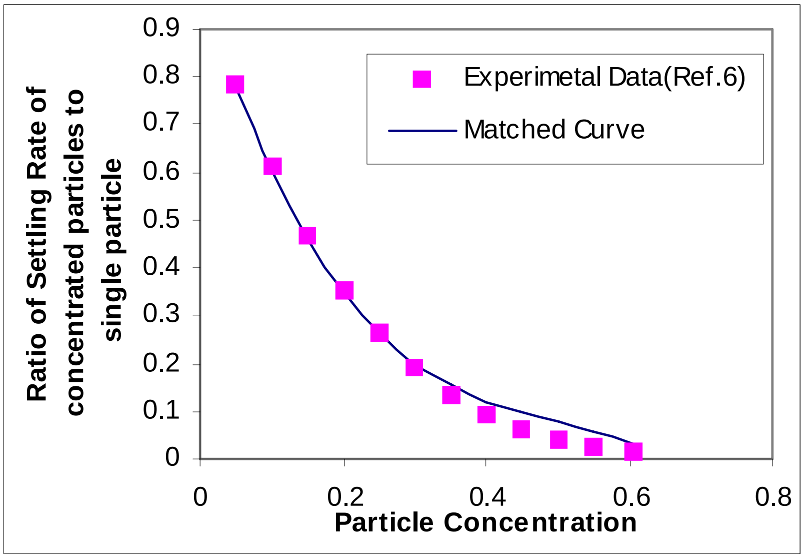

Figure 5: Comparison between matched curve and experimental data.

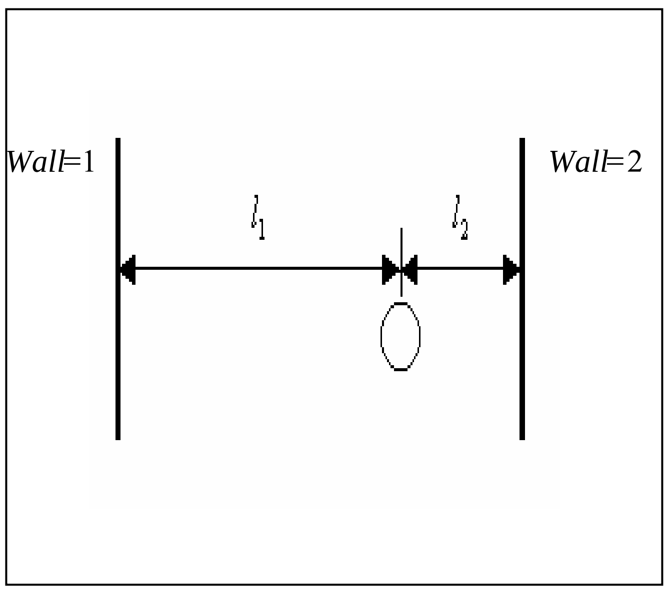

Figure 6: Particle flow in a slot (bounded by two walls).

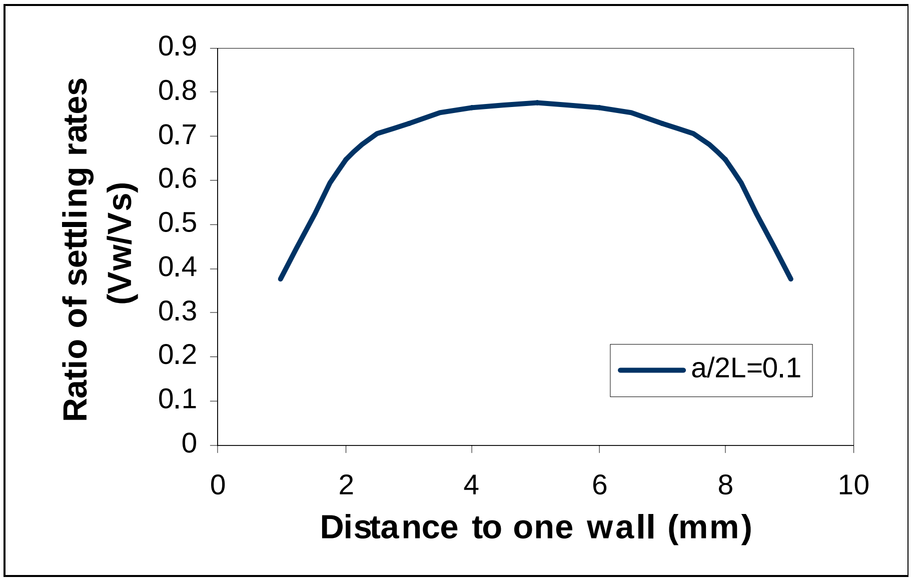

Figure 7: Wall effect for $a/2l$ =0.1.

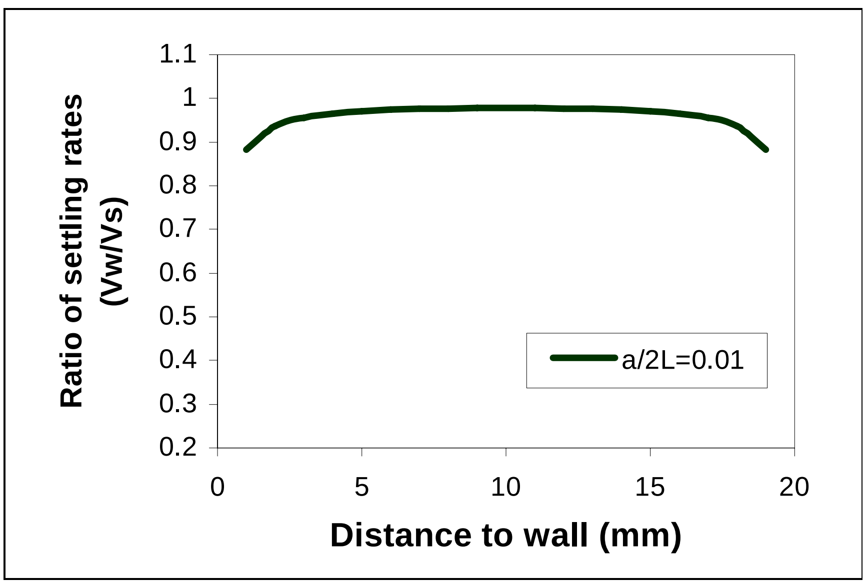

Figure 8: Wall effect for $a/2l$ =0.01.

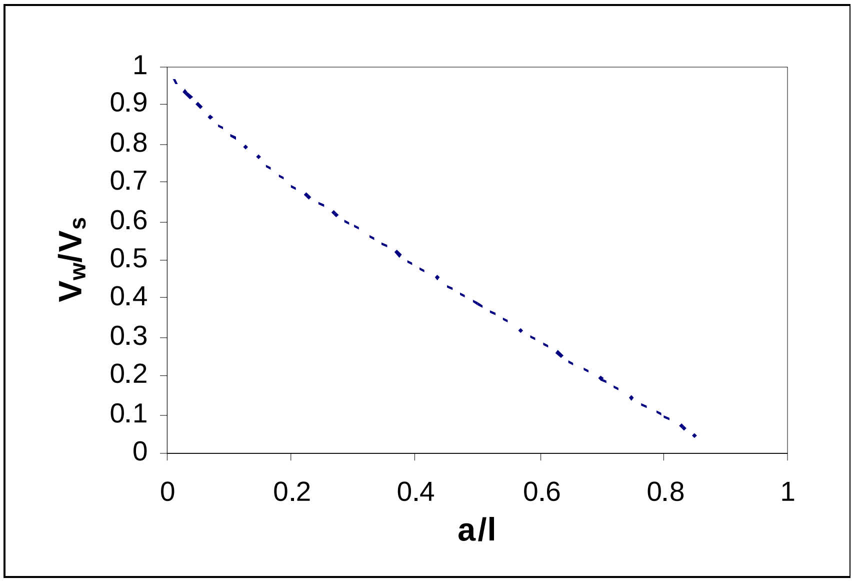

Figure 9: Wall effects using the average velocity (Eqn. 28).

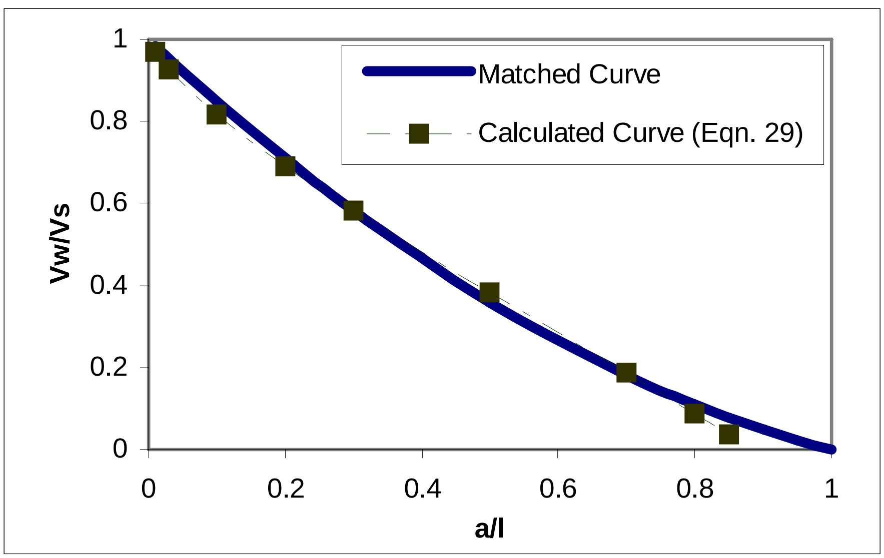

Figure 10: Proposed polynomial correlation for wall effects.

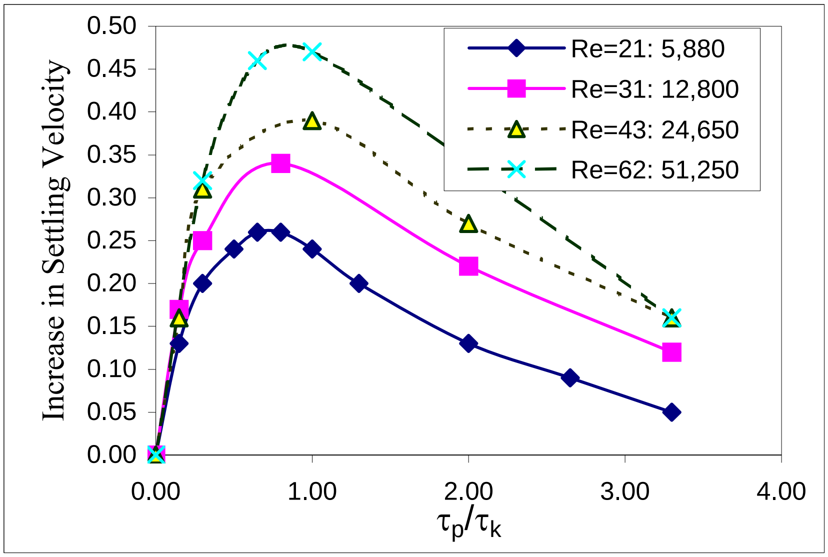

Figure 11: Extracted data from Wang and Maxey (Ref. 21).

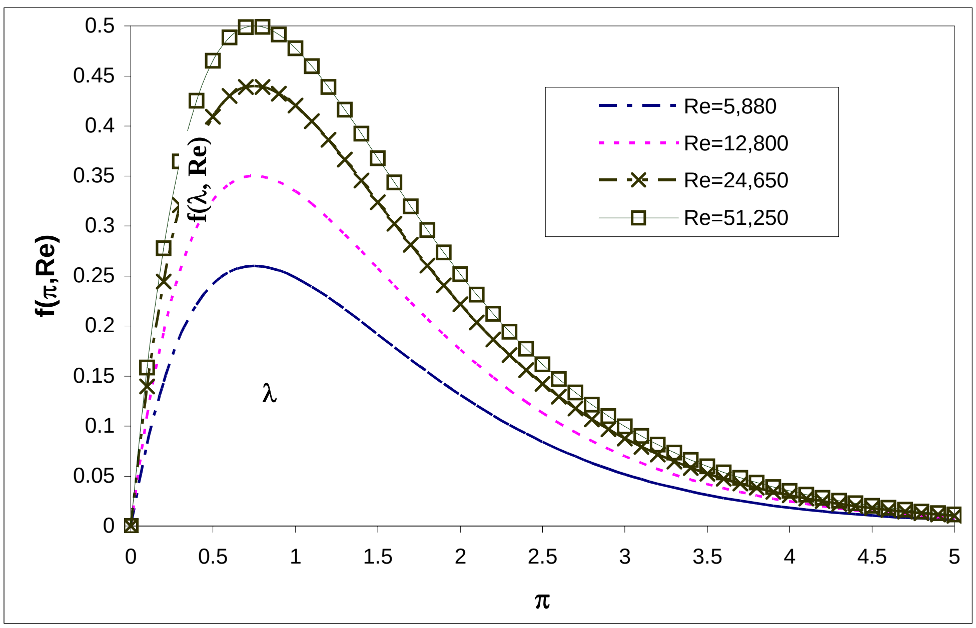

Figure 12: Proposed turbulence correlation as a Function of Re and □.

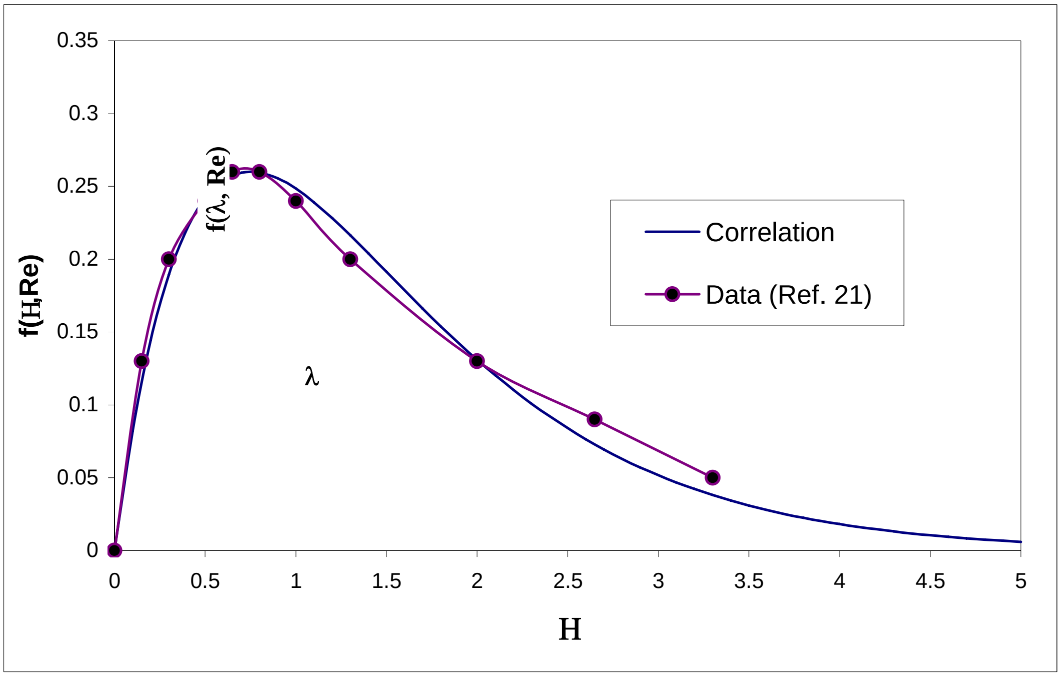

Figure 13: Correlation as a function of *Re* and , *Re*=5,880

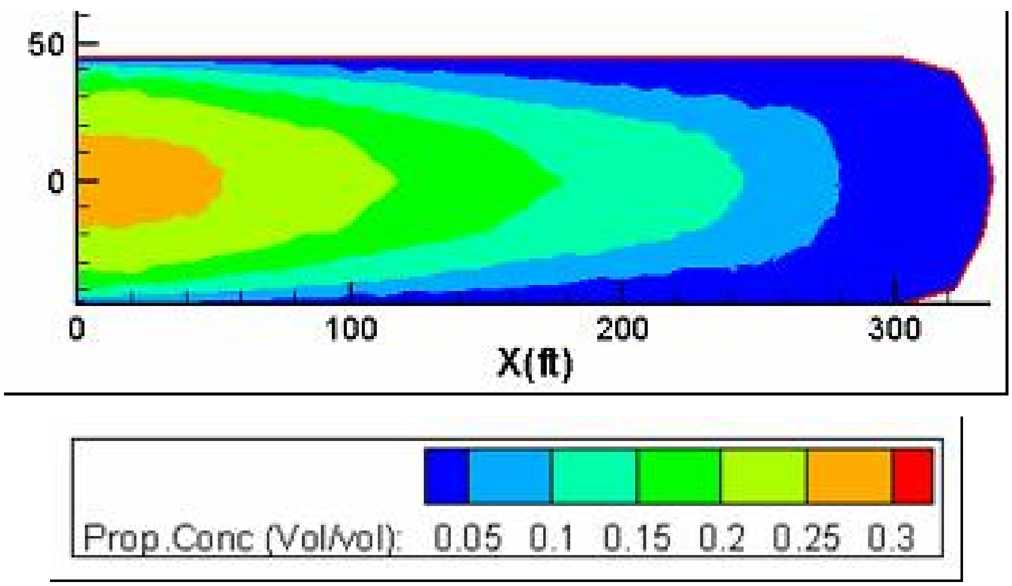

Figure 14a: Proppant concentration for 1 cp fluid without considering settling

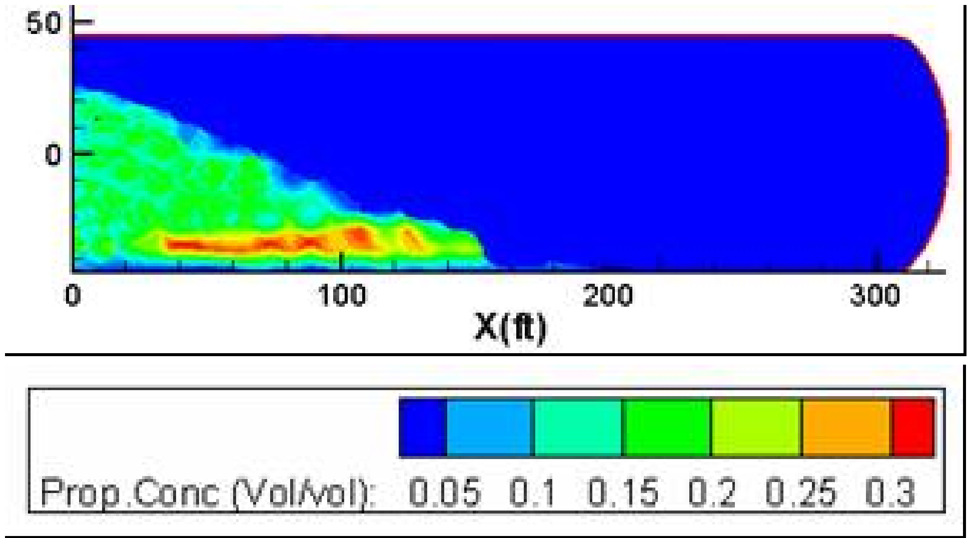

Figure 14b: Proppant concentration for 1 cp fluid considering uncorrected Stoke's settling

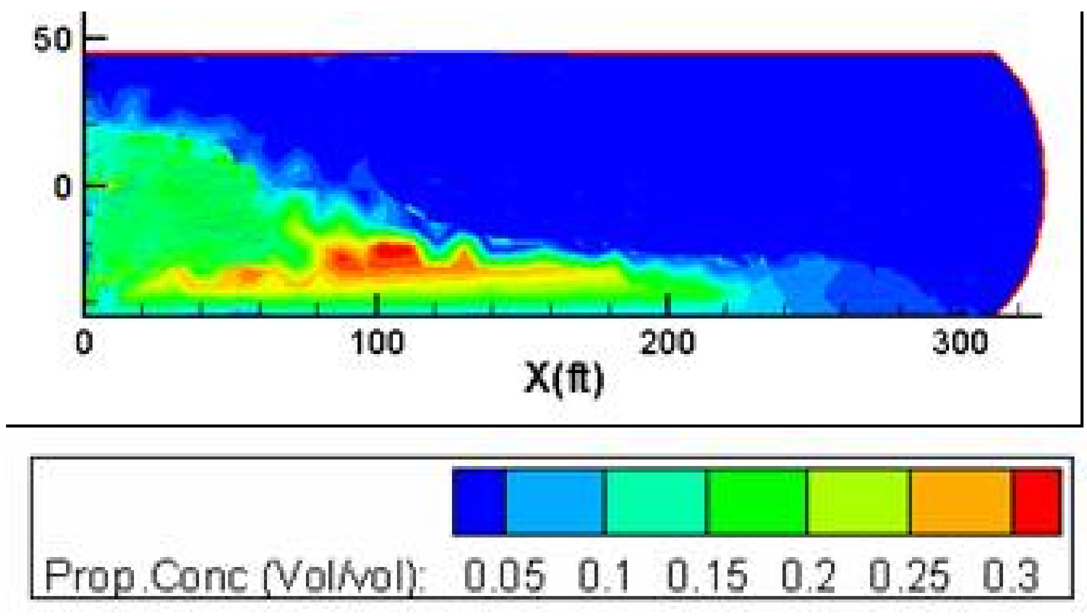

Figure 14c: Proppant concentration for 1 cp fluid considering corrected settling

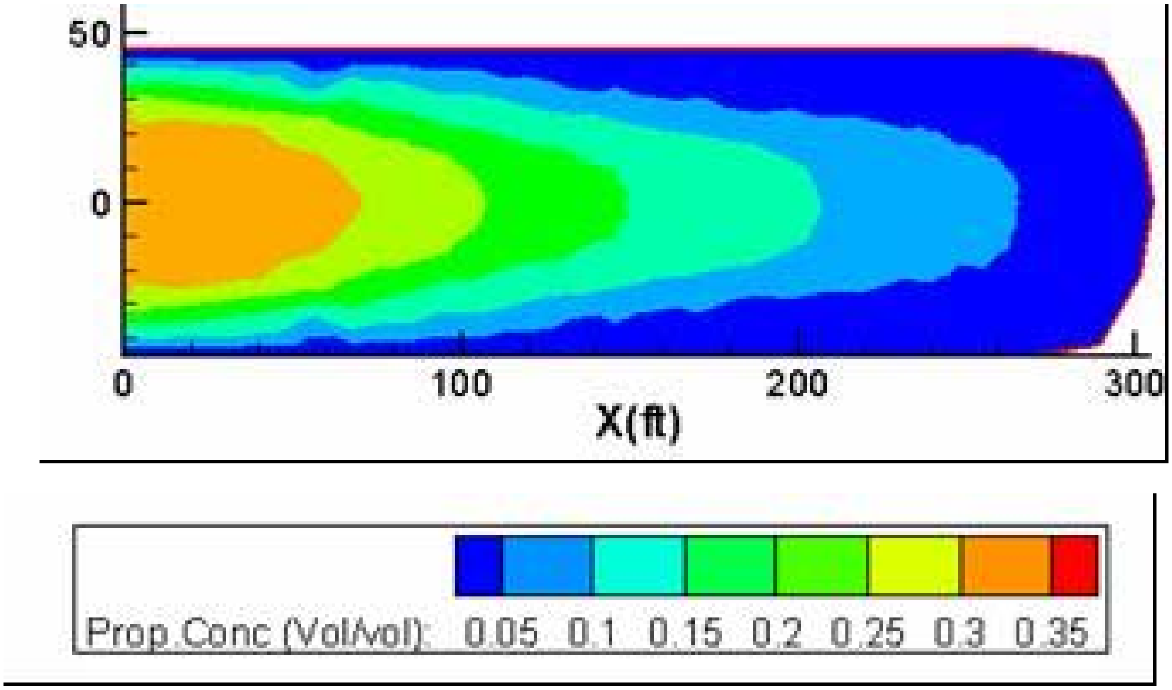

Figure 15a: Proppant concentration for 100 cp fluid without considering settling

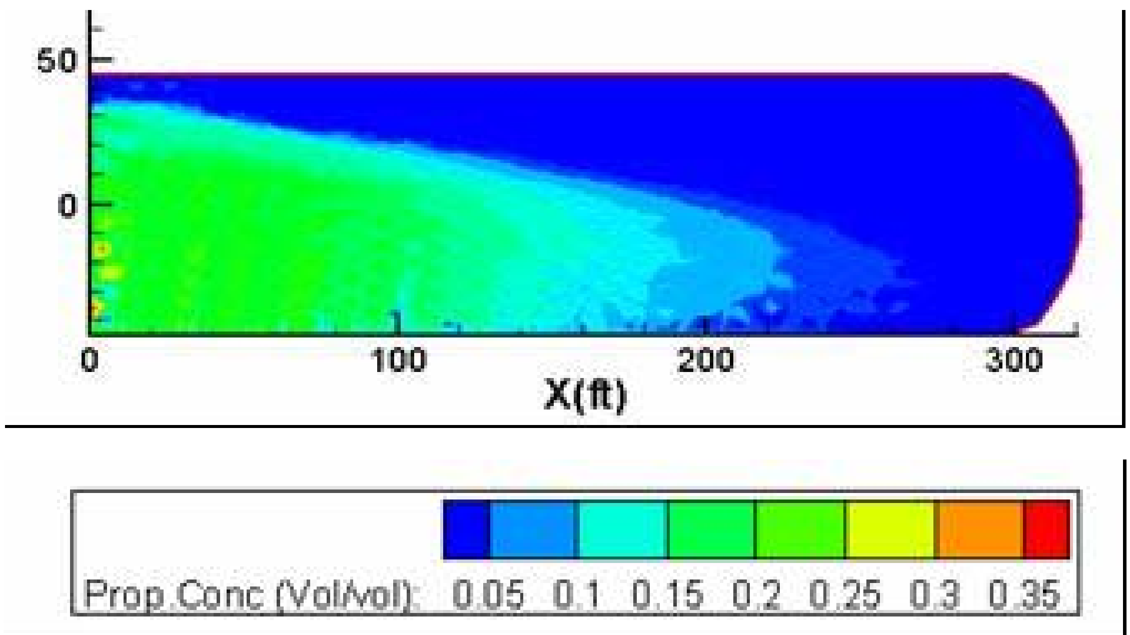

Figure 15b: Proppant concentration for 100 cp fluid considering uncorrected Stoke's settling

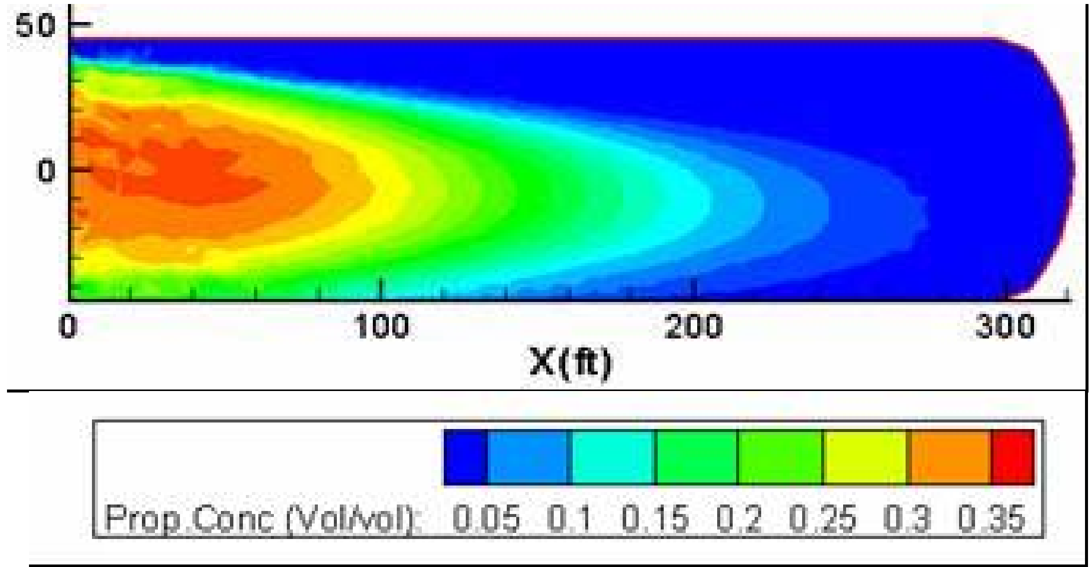

Figure 15c: Proppant concentration for 100 cp fluid considering corrected settling

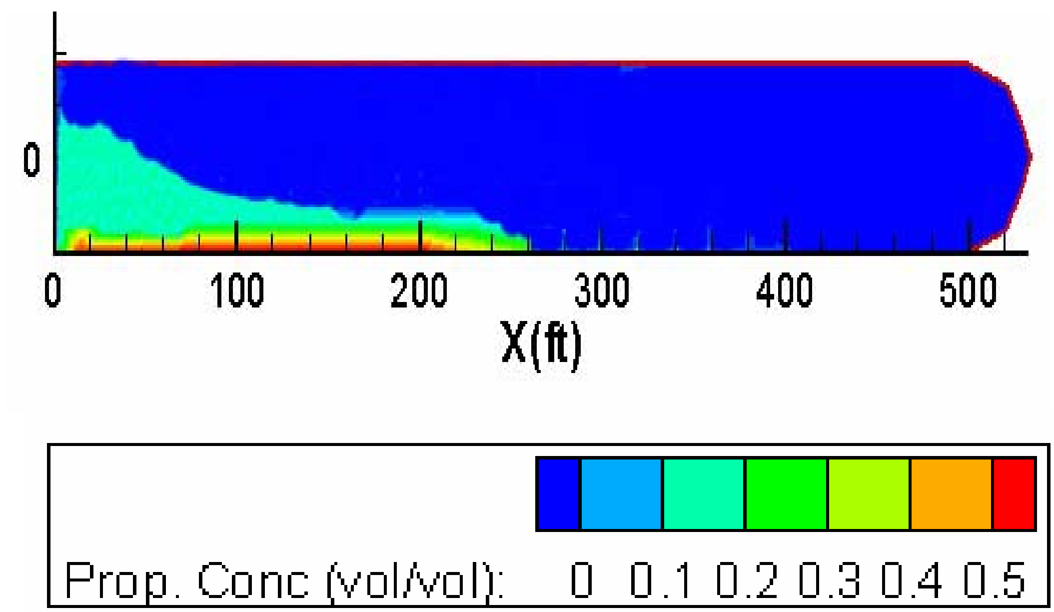

Figure 16: Proppant concentration for 1cp fluid with corrected settling

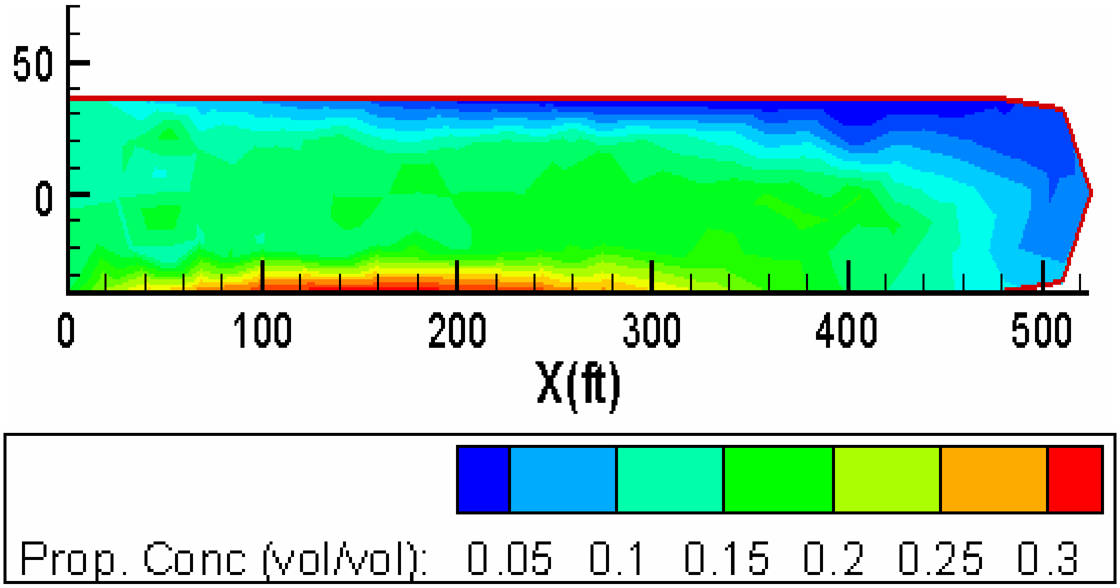

Figure 17: Proppant concentration for 100 cp fluid with corrected settling

CHAPTER 6. EXPERIMENTAL STUDY OF PROPPANT SETTLING

6.1 INTRODUCTION

McGuire and Sikora[1,2] pointed out that fracture conductivity and propped fracture length are the two main factors determining the productivity of fractured wells. In high-permeability reservoirs, fracture conductivity is more important for enhancing well productivity, while for low-permeability reservoirs, the fracture length is more critical. Both of these factors are very much dependant on effective proppant transport.

Ideally the proppant should be distributed uniformly across the production interval. This requires that the fluid have excellent sand-carrying capability to keep the sand from settling. In conventional cross-linked gel fracturing treatments, the proppant settling rate is low and proppants are well suspended in the fluid. However, in thin-fluid fracturing treatments, the viscosity of the fracturing fluid is low. As proppant particles are denser than the fluid transporting them, they will settle very quickly toward the bottom of the fractures. The use of gel-fracs is not always feasible or attractive because of unconstrained fracture height growth or incomplete fracture cleanup (gel induced damage).

Proppant settling velocity is mainly controlled by the flow behavior of the transporting fluid. The rheology of this fluid can be altered through selection of gelling agents, cross-linkers, stabilizing additives and their respective concentrations. For a given fluid, fluid rheology as well as proppant transport and suspension ability, change with time and temperature. Since fracture treatments often take hours to complete and fluid temperature can change radically from well bore to crack tip, both time and temperature are important factors in stimulation operation designs.

In conventional gel fracturing, proppant transport prediction models are generally based on Stokes' law for laminar or creeping flow of Newtonian fluids at low Reynolds numbers as well as on Newton's law for turbulent flow at high to very high Reynolds numbers (Clark and Quadir[1,2]; Shah[32]; Veatch[1]). While some fracturing fluids exhibit Newtonian flow behavior, others are power-law fluids. Proppant settling velocities in Newtonian fluids are a function of gravitational acceleration, fluid density, particle density, particle diameter, fluid viscosity and surface roughness. In slurries, settling takes place in a somewhat different manner because of particle interference or clumping (Clark and Guler[1]) and clustered proppant transport i.e. hindering gravity segregation (Sievert and Wahl[24]; Clark and Harkin[10]).

Some field operations indicate that fracture treatments using slick water and very low proppant concentrations (water-fracs) are very successful (Mayerhoer and Richardson[5], Mayerlofer and Meehan[4]; Walker and Jeffery[3]). In these fracturing treatments, fracture conductivity and propped fracture length are very sensitive to pump rates and proppant size. This is primarily because these factors control proppant distribution in the fracture, which in turn is controlled by particle transport in the fractures. The problem of proppant transport is, therefore, a very important issue in fracturing treatments, especially in water-fracs.

6.2 PAST EXPERIMENTAL WORK ON PROPPANT TRANSPORT IN FRACTURES

6.2.1 Physical Simulation of Proppant Transport in the Lab

In early investigations of proppant settling in fractures, researchers focused their attention on the determination of equilibrium velocities and equilibrium bed heights for "bank building" fluids (Kern[8], Babcock and Prokop[1], Schols and Visser[9], Clark and Sievert[10]). After 1980, researchers turned their attention to investigating single particle settling. Most of the fracturing fluids used in fracturing treatments at that time were gels with enough proppant-carrying ability.

In 1958, Kern and Perkins[8] studied the mechanics of sand movement in fracturing. They used water and gelled fluid to conduct experiments in their laboratory where they set up a 0.25-inch wide 22-inch long transparent cell to observe the movement of sands, and calculated the equilibrium height of the sand bed. They found that a bed of settled sand builds up in the bottom of a vertical fracture unless the injection rate is very high. Sand injected later in the treatment is washed over this settled sand bed. Since this settled bed is nearest the well bore, it is the most important factor affecting fracturing results. Their results indicated that the equilibrium velocity is not very sensitive to sand size or transport fluid viscosity or to sand injection rate (except at very low rates), but is apparently fairly sensitive to the difference in density between particles and fluid. Large sand grains, should not be tailed-in, but should be injected during the first part of the treatment or injected during all of the treatment. An over-flush should usually be conducted at low injection rates. They didn't attempt to measure the settling rate of particles.

In 1974, Schols and Visser[9] set up a cell which was similar to the cell Kern[8] used to study the build-up of a proppant bank. They used this plane-parallel transparent cell to simulate a rectilinear vertical fracture of uniform width and height in which no fluid loss occurred. The model was 2.5 meters long, 25 cm high and 0.63 cm wide. The proppants were 0.6mm in diameter. The viscosity of the fluid used was 25 cp. They found that a proppant bed formed very quickly, the height of the proppant bed increased as more proppant was injected until it reached an equilibrium height. The later proppant injected was pushed forward above the equilibrium height by the flowing slurry and slid down the slope of the proppant-bed front and increased the length of the proppant-bed without increasing its height. Their study resulted in a set of equations that could be used to predict bed height and length.
Sievert and Clark[24] used a large-vertical-slot model to evaluate the roles of fluid type, fluid viscosity, proppant concentration and flow rate on proppant transport and pack growth. They measured individual particle trajectories as well as the overall pack growth. They found that, with non-Newtonian fluids, changes in either proppant concentration or gel concentration (viscosity) produced significant changes in pack growth. By contrast, a 30-cp Newtonian fluid system allowed the proppant to settle so rapidly that no influence due to the variables of interest could be detected.

The above test results show that: if the particle settling rate in a fracture is high, a proppant bank forms very quickly and the build up of the proppant bank can be considered to take place in three consecutive phases. During the first phase, the bank builds up gradually as a function of time until an equilibrium height is reached near the wellbore and the bank stops growing at this point as a result of the erosion caused by the increased fluid drag forces on the proppant particles. During the second phase, the bank grows only in height until it reaches the equilibrium height over its full length. Finally, in the third phase the bank grows only in length and the injected proppant saltates over the full length of the bank towards the bank's front where it settles, increasing the length of the bank in the direction of flow.
During the formation and growth of the proppant bank, the proppants suspended in the fluid are settling at a rate that's affected by a variety of factors as discussed below.

6.2.2 Convection Dominated Proppant Transport in Fractures

During the proppant transport process, the proppant laden slurry has a density greater than the pad fluid resulting in a convective downward motion i.e. slumping of the proppant slurry.

In 1991, Cleary[17] studied the effect of convection by analyzing data from many hydraulic fracturing treatments monitored over the preceding years and concluded that: (a) actual fractures are shorter and wider than models predicted, (b) fracture width is relatively insensitive to fracturing fluid rheology and (c) dangerously fast convention settlement of proppant in imperfectly-contained fractures could occur. Natural fractures play an important role in explaining many phenomena formerly regarded as evidence for long contained fractures. In his opinion, the easiest way to avoid convection is to keep a constant density in the fracture, e.g. by staging in foam along with proppant. On the other hand, convection may enhance the fracture treatment by causing the proppant to rapidly reach the bottom of the fracture and impede further downward flow, perhaps even screening out at the top of high leak-off zones. This could cause propped heights to be much less than hydraulically created heights and may often salvage jobs designed with models that do not take this into account.

Cleary[17] also stated that: for the settling of proppant in fractures, convective downward motion, even in simple fluid treatments, dominates over particle settling; Encapsulation of viscous fluids by low-viscosity fluids available (e.g. gas/water) greatly accelerates the process. He provided a simple equation for the calculation of the ratio of convection velocity to fluid flow velocity.

In 1994, Barree[19] conducted experiments on slurry-transport and particle settling to improve the description of proppant transport and used these results to formulate a new slurry-transport model. The model was tested and verified vs experimental observations of slurry transport in a 4ft by 16ft slot model. The 4ft by 16ft slot model has a 0.313 inch gap width to observe large-scale proppant transport in lateral and vertical directions. Fluids and slurries were batch-mixed in 50-gal polypropylene tanks and pumped with progressing-cavity pumps. Barree[19] found that: convective, or density-driven, flow occurs whenever fluid bulk density gradients exist and exceed the viscous forces; vertical proppant velocities caused by convective motion can be hundreds of times faster than single particle settling velocities in viscous fluids.

Kirkby[15] conducted research on particle settling in static fluids and investigated the influence of particle interaction on hindered settling rate. He indicated in his study that: sedimentation behavior in fracturing fluids was dominated by a particle clustering phenomenon. At typical proppant concentrations, static sedimentation was dominated by particle clusters giving rise to average settling velocities many times faster than that of a single particle.

Dunand[13] experimentally studied concentration effects on proppant settling velocities in slurries. He first measured the terminal settling velocities of single spheres in hydroxypropyl guar solutions. Then he measured the settling behavior of concentrated proppant suspensions (5~41% by volume of solids). Finally settling velocities of suspensions were compared with single sphere data. Through a comparison between his measured data and calculated data with several existing models for hindered settling, he concluded that: because of wall effects, a new formula of calculating the sedimentation of particles was needed. In fluids with identical single sphere settling velocities, the average settling rate of a concentrated suspension in a static non-Newtonian fluid was two to three times higher than that in a corresponding Newtonian fluid. A size-distribution of clusters should be taken into account in order to predict the transient solid concentration profiles in non-Newtonian fluids. And a more direct quantitative evaluation of the clustering is necessary.

6.2.3 Gravity Dominated Proppant Transport in Fractures

There are two competing effects that are important as the proppant concentration is increased. One effect hinders particle settling while the other accelerates particle settling. Particles can tend to aggregate and form clusters when the concentration is high. This will cause settling rates to increase.

If there is no inter-particle aggregation during particle settling, high particle concentrations hinder particle settling (Richardson and Zaki[40]; Clark[11]; Daneshy[1]; Happel and Brenner[7]). The settling velocity of proppants was shown to decrease monotonically with increasing proppant concentration.

In 1986, Acharya[10] experimentally studied proppant settling characteristics of viscous and elastic fluids. He described theoretical and experimental analyses that accounted for viscous and elastic properties of the fluid to predict proppant settling and reviewed existing theoretical models used to correlate proppant settling. A closed form expression for the terminal settling velocity of a single particle was derived from an approximate analysis and compared with experimental data. The theoretical results were combined with the experimental data to obtain a correlation that was useful in the prediction of the settling velocity of a single particle in a viscous fluid at an intermediate Reynolds number (2<Re<500). Their experimental results showed that the hindered settling velocity of a concentrated slurry of suspended particles was smaller than that of a single particle.

Most fracturing fluids are non-Newtonian fluids. Proppant settling in non-Newtonian fluids is affected by fluid rheology and shear rate. In 1985, Roodhart[14] measured the settling of spherical particles in different fluids and showed that Stokes' settling based on a "power law" description of the viscosity is insufficient to predict particle settling rates in both flowing and quiescent fluids. In his experiments with a stagnant fluid, the settling velocities were more than those calculated using Stokes' law and an effective viscosity, while in a flowing fluid, settling was lower than that calculated. He explained this difference by extending the "power law" model with a zero shear viscosity and by assuming an anisotropic viscosity in a flowing fluid.

6.2.4 Convection and Gravity Dominated Flow

A number of investigators (Cleary[17]; Barree[19]; Kirkby[15]) claim that: convection dominates particle settling. Clark[22] conducted a series of experiments to show that there was a broad range of conditions under which convection did not occur. In 1995, Clark and Zhu[22] developed dimensionless groups for both Newtonian and non-Newtonian fluids that were useful in predicting when convection would be important. The ratios of pressure drop along the slot to the vertical force on the fluids (Newtonian and non-Newtonian) give the relevant dimensionless groups. Experiments were performed by injecting fluids into a slot to affirm the effectiveness of the dimensionless groups in predicting the dominance of convection in the transport processes. As the value of the dimensionless group increases, the tendency of the fluid to flow downwards toward the bottom decreases. If the value of the dimensionless group is close to one, the flow into the slot is very uniform, which means the effect of convection is so small that it can be neglected.

Abdulrahman[23] studied the effect of convection on slurry transport and indicated that convection was very significant even with very small density differences. He also developed dimensionless groups for interpreting proppant transport in hydraulic fractures. In his study, a small glass model was constructed to simulate a fracture. Newtonian and non-Newtonian fluids with controlled density differences were used and variables such as density difference, viscosity, fracture width, proppant concentration, and flow rate were considered. Proppant placement efficiency in the experiments was interpreted with two dimensionless groups. One group compared viscous and gravity effects and the other compared convective and dispersive effects. The experiments showed that the pattern formed by the boundary between the displaced and the displacing fluids was very similar to that observed in much larger models. He found convection was very significant even with very small density differences. As the ratio of viscous to gravity forces increased by reducing gap width or increasing the displacing fluid viscosity, the effect of convection became less pronounced and proppant placement efficiency tended to increase. The experiments conducted were simulated using a computer model (GOHFER) and the results indicated that proppant slurry transport could be accurately modeled.

In order to investigate proppant settling in inclined fractures and in fractures with some restrictions, Clark[22] used a non-vertical slot to perform experiments on slurry flow in fractures and extended the work to fractures with some restrictions. Additionally, he presented a derivation of the equations that govern the development of convection in slots. Since fractures are seldom perfectly vertical just as they are seldom perfectly uniform, deviations from vertical can impact slurry transport and result in a different distribution of proppant in a fracture. Variations in fracture width also modify slurry transport and have the effect of reducing or negating any contribution from convection that might otherwise influence the final distribution of proppant.

6.3 PAST EXPERIMENTAL WORK ON PROPPANT SETTLING

If the proppant settling rate is very slow, most of the proppant is still suspended in the fluid when pumping stops i.e. very little of the proppant settles to the fracture bottom. The suspended proppant distribution is dependent on particle settling. A lot of effort has been spent to investigate particle settling in fluids to look at the effects of a variety of factors (wall, particle concentration, fluid rheology etc).

The earliest experimental studies on particle settling focused on the effects of density difference and inertia, correlations corresponding to particle settling with different ranges of particle Reynolds number were developed (Stokes'[6]; Brenner[7]).

Besides the particle-liquid density difference and inertia, proppant concentration, fracture wall effects, turbulence, particle clustering all affect the proppant settling rate (Clark and Quadir[11]; Dunand[13]; Roodhart[14]). Even when convection is believed to dominate proppant transport (Cleary and Wright[17]; Clark and Zhu[20]), settling will continue to occur. Abdulrahman[23] proposed the issue of mixing or dispersion between the slurry injected and the resident fracturing fluids. It's extremely hard, or impossible, to investigate the effect of all the above factors on proppant settling fully and accurately. However, some effects are not important and can neglected.

6.3.1 Unbounded Particle Settling

For a single sphere settling in creeping flow, Stokes' first derived the hydrodynamics of particle settling and obtained what we now refer to as Stokes' equation. Stokes' settling equation is accurate when the particle's Reynolds number is less than 0.1. Errors can be quite large when the particle's Reynolds number is higher. Subsequent researchers investigated particle settling for higher Reynolds numbers. Schiller and Nauman[7], Gaudin[7], Orr and Dallavalle[7], Lapple and Langmuir[7], Almendra[7] summarized correlations for particle settling with different particle Reynolds numbers.

6.3.2 Effect of Fracture Walls / Slot Width

Particle motion in fluids is different in the presence of a boundary. Lorentz[38] was the earliest investigator to derive a solution for the motion of a sphere in the presence of a plane wall at a low Reynolds number. Faxen[38] considered the problem of a sphere translating between two parallel walls in the special case where the sphere is either moving along the center-line or in a plane at one quarter the distance between the two walls. Faxen obtained expressions for the force and torque acting on the sphere by the method of reflections.

Wakiya[7] used a similar approach to treat the problem of a rigidly held sphere in Couette flow or two dimensional Poiseuille flow. Wakiya's solution is only for cases where the sphere is at one quarter the distance between the walls.

Ganatos and Pfeffer[7] presented exact solutions for the three-dimensional creeping motion of a sphere of arbitrary size and position between two plane parallel walls. To the best of our knowledge, no experimental data are available to systematically study the effect of two parallel walls on single particle settling. Such a study is presented in this Chapter.

6.3.3 Effect of Particle Concentration

Under normal fracturing conditions, particle concentration effects as well as wall effects could be significant and could affect proppant settling and final distribution. Clark and Harkin[10] designed a 4-ft by 12-ft transparent cell and used it to study the proppant carrying abilities of both non-Newtonian and Newtonian fluids. They measured the suspended proppant flow rate in vertical fractures. The fluid tested was uncross-linked hydroxypropyl guar gel at 20, 30 and 40 pounds per thousand gallons. Glycerol was used as a Newtonian fluid. The viscosity range for the glycerol was 30~100 cps. At higher proppant concentration, they used small amounts of colored sand in order to follow a single particle with some degree of certainty. They found that horizontal sand transport velocities ranged from 70 to 90 percent of the bulk fluid velocity (in laminar flow). Measured proppant settling velocities during flow were up to three times the single particle settling rate. An important factor in proppant transport was the agglomeration or clustering effects observed during these tests; when flow was stopped the existing clusters began to settle and coalesced with other particles. As the clusters grew, they fell faster, resulting in settling velocities many times greater than that for a single particle.

Clark and Quadir[11] summarized the correlations between the calculation of particle settling rate and the hindered velocity of clustered particles and concluded that the choice of an equation to compute hindered settling velocities can make a difference in the results because different correlations focus on the effect of different factors on particle settling.

Through a comparison with their test results, they found that some of the equations give very different results.

The major problem in studying proppant settling in cross-linked fracturing fluids is the extremely slow settling velocity. This limits the type of experimental apparatus that can be used to measure long particle residence times. Clark[11] investigated how to determine the settling velocity of proppants in cross-linked gels. In this study, two different experimental models were used to obtain particle settling data. One model consisted of a parallel plate apparatus in which the shear on the fluid was provided by a moving belt and the other consisted of a concentric cylinder device. Both of these models were capable of providing adjustable shear rates and long particle residence time necessary for data collection. Data was presented for both non-cross-linked fluids and cross-linked fluids. The moving belt parallel plate model and the concentric cylinder model gave comparable results for the settling velocities of particles in the fluids that they studied.

6.3.4 Effect of Fluid Rheology

The Stokes' settling equation can be utilized to calculate spherical particle settling in high-viscosity Newtonian fluids. However, most fracturing fluids are non-Newtonian. In the past, an equivalent Newtonian viscosity has been usually used in Stokes' law to calculate the particle settling rate in these fracturing fluids for low particle Reynolds number (Novotny[1]; Harrington and Hannah[21]; Acharya[16]; Daneshy[1]; Shah[32]). For high particle Reynolds number, the equivalent viscosity (or apparent viscosity) is also substituted for the Newtonian viscosity to calculate particle settling. Novotny was the first to correlate particle settling rate with the non-Newtonian characteristics of the fracturing fluids. He and Daneshy both derived the fluid equivalent viscosity based the particle shear rate.

Harrington and Hannah[21] investigated the sand settling characteristics in cross-linked water-based fracturing fluid using a concentric cylinder transparent tester with the inner cylinder rotating and outer cylinder stationary. Fracturing fluids containing proppants screened to a 20-25 mesh tolerance were cross-linked in the fluid and both were introduced into the annular gap between the rotor and stator. Variable shear rates were then imposed upon the fluid/proppant combination and settling velocity observed. It had long been observed that most cross-linked gels, when at rest, would support proppants perfectly without separation. When pumped through transparent fracture models at low velocities no measurable proppant separation occurred. The fluid they used was a high-viscosity cross-linked fluid. The particle settling rate was so low that it could be neglected. The experimental design appears to be flawed since Taylor vortices are expected to be formed in the concentric cylinder geometry they used.

McMechan and Shah[32] designed a test apparatus to investigate the settling behavior of proppants in various fracturing fluids. They found that clustering occurs in linear gels at sand concentrations below 10 lb/gal and results in a higher settling velocity than the single particle settling rate. At sand concentrations above 10 lb/gal, hindered settling effects are dominant. For cross-linked fluids, the sand suspension time is much shorter than the fluid break time (less than 25% of the fluid break time).

6.3.5 Effect of Wall Roughness

Hydraulic fracture surfaces in general are not smooth but show roughness. Fracture roughness is usually neglected in hydraulic fracturing (proppant transport) models due to the difficulty in describing fracture roughness.

Rough fracture surfaces influence the mechanical behavior and conductivity of fractures. If a small displacement of the opposing fracture surfaces relative to each other occurs during fracture propagation, the opposing fracture surfaces will not close perfectly owing to the non-matching surfaces. This can lead to a residual width after closure (Hossain and Rahman[29]), which leads to a fracture conductivity that can be great after closure. But the fracture conductivity provided by the residual width is hard to predict and the injection of proppant can improve fracture conductivity (Fredd[27]).

Fredd and McConnel[27] used the conductivity cell to measure stressed fracture conductivity under the following conditions: aligned fracture faces with no proppant, displaced fracture faces with no proppant, aligned fracture faces with proppant, and displaced fracture faced with proppant. They pointed out that in the presence of proppants, the conductivity can be proppant or asperity dominated depending on the proppant concentration, proppant strength and formation properties. Under asperity-dominated conditions, the conductivity varies significantly and is difficult to predict. Low concentrations of high-strength proppant reduce the effects of formation properties and provide proppant-dominated conductivity. The use of high strength proppants or proppants at conventional field concentrations provides better fracture conductivity than the non-proppant asperity dominated fracture conductivity.

Fracture roughness can also cause problems with proppant transport. Significant fracture roughness can hinder proppant horizontal transport as well as slow down proppant settling. To the best of our knowledge, no experimental or modeling studies have been reported on the effect of fracture roughness on proppant transport and settling. This study investigates the effect of fracture wall roughness on proppant transport by setting up a cell with rough walls to measure particle transport rates in the cell.

6.4 EXPERIMENTAL APPARATUS

The objective of this chapter is to investigate the effect of the above mentioned factors on proppant settling through experiments and then summarize how these effects can be described in real fractures. These experiments start with the simplest case: measuring single particle settling rates in unbounded fluids using different particles. These calibration tests were compared to theoretical calculation results. Then a series of tests were conducted to measure the effects of inertia, particle size, fluid rheology, fracture width, fracture roughness and viscous fingers on particle settling.

6.4.1 Design of Large Fracture Cell

In order to use the flow cell to simulate proppant transport in real fractures, the flow cell was designed to make four dimensionless numbers close to those for the real fracture: channel Reynolds number (R_e), particle Reynolds number (R_{ep}), Shields number (S), and the ratio of the advective and settling times (t_{adv} / t_{set}).

In the fracture and the flow cell:

$$R_e = Uw / \nu$$

$$R_{ep} = R_e (d / w)$$

$$t_{adv} / t_{set} = L v_s / UH$$

$$S = \Delta \rho g a / \rho U^2 \quad S = \Delta\rho g a/\rho U^2$$

Here, U is the fluid horizontal flow velocity, w is the fracture (cell) width, v is the fluid kinematic viscosity, d is particle diameter, v_s is particle settling velocity, L is the fracture (cell) length, H is the fracture (cell) height, ρ is the fluid density and Δρ is the density difference between the fluid and particle.

The channel Reynolds number (R_e) is the ratio of the fluid inertial forces to viscous forces. The particle Reynolds number (R_{ep}) is the ratio of the inertial force acting on the particle to the viscous force acting on the particle. Through a comparison between the ratios of advective to settling times in the cell and in the fracture, we can compare the proppant locations in the flow cell and in the real fracture. The Shields parameter (S) indicates whether resuspension of settled particles is important.

The dimensions and the dimensionless groups for a typical fracture in a water-frac treatment and for the cells are shown in Figure 6.1 and Table 6.1. The pictures of the fracture flow cell are shown in Figures 6.2, 6.3 and 6.4.

6.4.2 Design of Small Fracture Flow Cells

In order to minimize the cell entrance effects on proppant transport, three small cells (50cm x 4.7cm x 4mm, 50cm x 4.7cm x 1.5mm and 50cm x 4.7cm x 1mm) were designed to measure proppant settling rates. The dimensionless numbers for one small cell are shown in Table 6.1.

As shown in figure 6.9, these three small cells are made of transparent Lucite plates. The particle transport in the transparent cells is recorded with a video camera. The entrance of the cell is a fluid column, which helps to maintain fluid flow uniformly into the cell.

6.4.3 Preparation of Rough Walls

A fracture is usually modeled as a set of smooth parallel plates separated by a slot of constant width. However, the surface of real fractures is not smooth and can be very rough. Proppant transport between two parallel rough walls can be very different from proppant transport between two parallel smooth walls. There are no studies in the literature of the effect of fracture wall roughness on proppant transport in hydraulic fracturing.

This section describes how transparent rough walls are made and how proppant transport experiments are conducted in the cell with rough walls.

In order to simulate the fracture with rough surfaces that can close completely and leave no residual width after closure, a rock sample was fractured into two pieces with rough surfaces (Figure 6.11). Figure 6.12 and 6.13 show how the rough surface of this rock sample was used as a stencil to make a transparent rough surface on the transparent lucite plate. First, a piece of transparent tape was fixed to one transparent lucite plate and silicone was pasted on the tape to form a thin layer of silicone on the lucite plate. After about one hour, the core sample was used as a stamp to cover the silicone layer, and to imprint the rough surface of the core sample in the silicone layer. This ensures that the surface of this plate is as rough as the core sample. The tape can be removed from the plate and a transparent rough wall can be seen in Figure 6.14 (a, b).

In the same way, the rough surface of another core sample can be imprinted in the silicone layer on the second lucite plate. The rough surfaces on these two lucite plates match. These two plates can be used as two side walls to build a cell (shown in Figure 6.14 c). The roughness of the walls is shown in Figure 6.15.

6.5 EXPERIMENTAL PROCEDURE

The big transparent cell built for our lab is shown in Figure 6.5. Here (1) is the inlet valve which provides water from the faucet, (2) is a container where the polymer can be put in and mixed with water to make the fracturing fluid, proppants are also input from this container, (3) is a hose which feeds the mixture of proppants and fluid into the pump (5); (4) is the valve which controls the injection, (5) is a pump which can provide enough power to maintain the flow rate in the cell, (6) is a hose at the outlet to recycle the fluid from the cell back to the container (3), (7) is the transparent cell, (8) is the valve controlling the injection into the cell, (9) is the hose transporting fluid and proppants into the cell, (10) is a safety valve which opens to recycle the fluid back to the container (3) when the fluid pressure is too high, and closes when the fluid pressure becomes low, (11) is the hose which recycles the fluid back to the container (3).

The cell is transparent, so the proppant transport in the cell can be recorded with a video camera, and the proppant bed buildup process can be observed.

The small cells are shown in Figures 6.8 and 6.10. In Figure 6.8: (1) is the faucet which provides water if water is used, (2) is a hose connected to a fluid container (3), (4) is a hose connected with a hole on the side of the fluid container (3) which drains the fluid back to the fluid tank (8) and maintains a constant fluid level in the container (3), (5) is a hose connecting the container (3) to the cell (7), (6) is a hose from which the proppants can be injected into the cell, (7) is the transparent cell, (8) is the drainage tank, (9) is a video camera which records the positions of particles at different times, and can be used to calculate the particle flow rate as well as the fluid flow rate, (10) is a TV screen where the images recorded in (9) can be enlarged.

Since the widths of the small cells are comparable to the proppant particle diameters, the wall effect on proppant transport is significant and can be measured in these cells. The cell entrance effect is very small, and only occurs within 2cm from the cell entrance. In addition, rough walls can be made for small cells to measure the effect of wall roughness on proppant transport, but it is very difficult to make rough walls for the big cell.

Due to height limitations, a proppant bed can not be seen in the small cells when the proppants are injected. The height of the small cells is less than the equilibrium gap that can appear in the big cell.

Therefore, the big cell was utilized to establish the relationship between the proppant bed equilibrium height and the injection rate. The small cells were used to measure particle settling rates under the effect of a variety of factors.

6.5.1 Fluid Preparation

Three kinds of fluids were prepared for the tests: water, solutions of water-glycerin and guar gels. Solutions of water-glycerin are Newtonian fluids and the viscosity can be changed to observe particle transport at different viscosities. The glycerin was obtained from Fisher Chemical (G33-500). Glycerin can have a viscosity as high as 780 cp (Figure 6.17). Guar gels (mixtures of guar gum and water) are power-law fluids.

A rotational viscometer was used to measure the rheology of the fluids. Water, pure glycerin, and solutions of glycerin-water are Newtonian fluids as seen in Figure 6.20(a). Table 6.3 also shows the properties of water-glycerin solutions. The viscosities of the fluids are in Table 6.2: 10.2 cp, 104 cp and 780 cp. The guar gum solutions are power-law fluids, as shown in Figure 6.20(b) and Table 6.4.

6.5.2 Proppant Preparation

Two kinds of proppants provided by BJ Services Company and one kind of ceramic proppant provided by the Carbo Ceramic Corporation are used in the tests:

(1) Black high-strength ceramic particles (16/30, 30/60 and 40/70 mesh)

(2) Yellow light-weight ceramic particles (16/25 and 20/30 mesh)

(3) Walnut hull based light-weight particles (14/30 and 20/30 mesh)

The density of the walnut hull based light-weight particle is very low (1.25 g/cc), its settling rate is very low. But these particles are not spherical or uniform and cannot be used to evaluate particle settling or horizontal transport. The yellow light-weight ceramic particles (1.75 g/cc) are approximately spherical, but these particles are coated with resin and tend to stick to each other and stick to the walls of the cell. Therefore, the high-strength black ceramic particles, which are spherical and do not stick to each other in fluid, were mainly used in the tests. The density of this kind of particle is 6.3 g/cc. The yellow light-weight ceramic particles and the black high-strength particles are shown in Figure 6.17.

6.5.3 Particle Static Settling in Water

As shown in Figure 6.16, the pipe and the cell are first filled with water. Next, a spherical particle is immersed in the water and allowed to settle. A video camera is used to record the settling process. The particle settling distances are read from the meter stick pasted beside the cell and the pipe. The settling time can be read in the camera. The particle settling rates at different positions can be calculated from the recorded video.

6.5.4 Particle Static Settling in Glycerin (or Guar Gels)

The cell and pipe (shown in Figure 6.16) are filled with glycerin (or guar gel). A single spherical particle is immersed in the glycerin (or guar gel) and allowed to settle. A stop watch is used to record the time of particle settling. No video camera is needed here since the settling velocities are low. The particle settling distance can be read from the meter stick.

Table 6.2 shows some measured particle settling rates in water and glycerin.

6.5.5 Particle Dynamic Settling in Water

As shown in Figure 6.9, the fluid in the container is driven by gravity and flows to the cell at a constant rate. The average fluid flow rate can be calculated by measuring the volume of water at the outlet of the cell within a fixed period of time. The particle is dropped into the fluid and the particle trajectory in the cell can be recorded by a video camera. Then the particle settling rate in the flowing fluid is calculated. This particle settling rate can be compared to the particle static settling rate to evaluate the effect of fluid horizontal flow on particle settling. The highest average fluid velocity in the cell that is driven by gravity is 70 cm/sec for water, which makes the channel Reynolds number in the cell as high as 2800.

6.5.6 Particle Dynamic Settling in Glycerin (or Guar Gels)

If the fluid used in the tests is not water, the fluid in container (3) in Figure 6.9 can be maintained at a constant level by continuously injecting fluid into the container. This maintains a constant fluid flow rate in the cell. The position of the container (3) can be adjusted to change the fluid level and to change the flow rate in the cell.

In order to measure particle dynamic settling in glycerin (or guar gel), a particle is dropped into the pipe (6) in Figure 6.9, and then flows into the cell. The particle settles while flowing with the glycerin. The video camera is used to record the particle trajectory. The distance read from the meter stick shows the particle settling distance. The time is shown in the video camera. This allows us to calculate the particle settling rate.

For high-viscosity fluids, such as glycerin and guar gels with high guar concentration, a dye is injected into the fluid container to see how the fluid flow velocity profile changes with time and distance; because the dispersion effect of dye in high-viscosity fluid is small, the advancing rate of the dye front will be approximately equal to the maximum velocity of fluid in the cell. For low-viscosity fluids, we measure the volume of fluid within a period of time at the outlet end of the cell and calculate the average flow rate in the cell.

6.5.7 Errors in the Calculation of Particle Settling Rate

The minimum unit of the meter stick pasted on the side of the cell measuring distance is 1mm, so the maximum error in measuring distance is 1mm. The maximum relative error is 1% when measuring a distance of 10 cm. This meter is suitable for measuring the particle transport distance in the tests because the minimum distance measured in the tests is more than 2 cm (a maximum error of 5%).

The tools utilized to record time are a stop watch and an automatic watch in the video camera. The resolution of the automatic watch is 1/30 second, the error in measuring the time is 0.5*1/30 second, and the maximum relative error is 1.65% when measuring a period time of 1 second. So the error is small when measuring time intervals of more than 1 second.

The minimum unit of the stop watch is 0.1 second. So the stop watch is used to record longer period of time. Since the particle settling rate in water is very high (the settling rate of the black ceramic particles in water is between 5 cm/s and 20 cm/s), the particle settling time in the cell is very short. The video camera is used to record the particle positions at different times and then calculate the particle settling rate in water.

For example, if a particle settling process in a cell was recorded in a video camera, two positions of the particle are chosen to calculate the particle settling rate: one position is 6.54 cm from the cell top, the recorded time is 0’1’’20, the other position is 20.32 cm from the cell top, the recorded time is 0’2’’20, so the settling rate is (20.32-6.54)cm/1 sec=13.78 cm/sec.

The maximum error in the distance measurement is 0.2 cm, and the maximum relative error in the distance measurement is 1.2/13.78=1.4%. The maximum error in the time measurement is 1/30 sec, the maximum relative error in the time measurement is 3.3%. The maximum relative error in the calculation of particle settling rate is $|\Delta V/V|=|\Delta L/L|+|\Delta T/T|=1.4\%+3.3\%=4.7\%$. The real settling rate should be between 14.42 cm/sec and 13.13 cm/sec.

The particle settling rate in glycerin and guar gels is very low. The stop-watch can be used to measure particle settling in the glycerin and guar gels because the stop watch is convenient to operate and the error in the measurement of a long period of time is low.

For example, if a particle settles in the glycerin, when the particle is 10 cm from the cell top, the stop watch starts to record the time, the particle reaches a position 25.44 cm from the cell top after 2 minutes, the calculated settling rate is 15.44/120=0.13 cm/sec. The maximum error in the measurement of time is 0.2 sec. The maximum relative error in the measurement of time is 0.2/120=0.1%. So the maximum relative error in the calculation of settling rate is: 1.3%+0.1%=1.4%. This error is small.

Every reported measurement of particle velocity was conducted at least 3 times. Average settling rates and error bars are provided for each set of measurements.

6.6 TEST RESULTS AND DISCUSSION

6.6.1 Particle Settling Velocity Distribution in Unbounded Water

The purpose of this test is to investigate how long a particle takes to reach steady state when it is settling. A black ceramic particle (density=3.3 g/cc, diameter=0.86mm) was dropped into a container full of water and its motion was recorded with a video camera. The particle settling rates were calculated based on the recorded particle positions at different times. As shown in Figure 6.19, it is clear that the particle reached a steady state velocity very quickly (within a few centimeters).

6.6.2 Comparison between Measured and Calculated Particle Settling Rate

The above apparatus can be utilized to measure particle settling rates. Theoretical correlations are available to calculate the particle settling rate in water and high-viscosity Newtonian fluids. The measured settling rates of spherical particles with different diameters were compared with the calculated particle settling rates. The comparisons are shown in Figure 6.21. The measured and calculated settling rates are very close. This means that the above apparatus can measure particle settling rates to an acceptable level of accuracy.

6.6.3 Particle Settling in Different Fluids

In water, particle settling rates are high. A wake can be seen behind the particle. A particle smeared with blue dye was seen to settle with a blue wake (shown in Figure 6.22 (a) and (b)). When this dyed particle settles in glycerin, only a line of blue dye appears behind this particle (shown in Figure 6.22(c)). This shows that there are no inertial effects when the particle settles in glycerin. The particle Reynolds number (R_{ep}) (defined earlier) for settling in water is about 180, while that for glycerin is less than 0.1. Inertial effects are expected for particle Reynolds number (R_{ep}) > 2.

6.6.4 Wall Effects on Particle Settling in Quiescent Water

Comparisons are made between tests of particle settling conducted in a big transparent Lucite pipe (internal diameter is 150 times bigger than the particle diameter) and a slot flow cell (width comparable to the particle diameter). Particle settling in the big diameter pipe can be considered to represent particle settling in an unbounded fluid while settling in the cell is clearly influenced by wall effects.

The particle is dropped into the cell, and its settling is recorded with a video camera. The particle settling rate between two parallel walls (V_w) can be calculated based on recorded particle positions at different time. The particle settling rate in the unbounded fluid (V_s) was measured following the same procedure. The effect of the slot walls on particle settling rate can be obtained by comparing V_w to V_s.

Flow cells with different slot width were conducted (slot width=1 mm, 1.5 mm, 4 mm). The effect of fluid rheology on particle settling can be evaluated by comparing particle settling rates in different fluids (shown in Figure 6.23 (b)). The effect of the ratio of particle size to cell width on particle settling can be evaluated by comparing particle settling rates in different cells or comparing the settling rates of different particle diameters in a given cell.

As shown in Figure 6.23(a) and (b), in water, wall effects are not significant until the slot width is 10-20% larger than the particle diameter. Inertia plays a more important role in particle settling than wall effects (R_{ep} =180). Table 6.5 also shows the wall effect on particle settling in water.

6.6.5 Effect of Fracture Walls on Proppant Settling in Newtonian Fluids

The results of the previous section were generalized to high-viscosity Newtonian fluids by using mixtures of glycerin and water. As shown in Figure 6.29, increasing the viscosity of fluids significantly increases the impact of walls on the settling rate. Clearly, the hydrodynamic interaction between the particle and the walls becomes more significant when the viscosity of the fluid is increased. These results bring in a significant reduction of the settling velocity even when the slot width is 5 times larger than the particle diameter.

It should be noted that, in Figure 6.29, the settling velocity of the proppant is normalized with respect to the settling velocity in a quiescent fluid with the same velocity. Figure 6.30 shows the change in the settling velocities of a particle (diameter: 0.1 cm, density: 3.3 g/cc) in unbounded quiescent Newtonian fluids with different viscosity. This figure shows that fluid viscosity affects particle settling rate and the measured settling rates agree well with the calculated data.

6.6.6 Effect of Fluid Rheology on Particle Settling in Non-Newtonian Fluids

Experiments were conducted with a guar gel (40 lb/Mgal) at low shear rates, the viscosity of this guar gel is close to that of the glycerin (780 cp). As seen in Figure 6.23, the impact of the cell walls on the settling rate for the guar gum is very similar to that observed for the glycerin solutions. This suggests that, for such shear thinning fluids, the impact of fracture walls is similar to that observed with high-viscosity fluids, such as glycerin.

The experimental data can be represented by empirical correlations that allow us to account for the impact of fracture walls on particle settling rates. The data appear to lie on two lines; one when the ratio of particle diameter to cell width is less than 0.9 and the other when the ratio exceeds 0.9. These empirical correlations are as follows:

$$\frac{V_w}{V_s} = 1 - f(\mu) * \frac{D_p}{W_c} \qquad \left(\frac{D_p}{W_c} < 0.9\right) \tag{6.1}$$

$$\frac{V_w}{V_s} = g(u) * \left(1 - \frac{D_p}{W_c}\right) \qquad \left(\frac{D_p}{W_c} >= 0.9\right) \tag{6.2}$$

$$f(\mu) = 0.16\mu^{0.28} \tag{6.3}$$

$$g(\mu) = 8.26e^{-0.0061\mu} \tag{6.4}$$

μ -fluid viscosity (or apparent viscosity of non-Newtonian fluids)

Clearly, the impact of the fracture wall is more significant as the fluid viscosity increases. In addition, when the particle diameter is much smaller than the slot width, the impact of the slot walls increases linearly. However, when the particle diameter becomes almost equal to the slot width, only a very thin layer of fluid exists between the sphere and the slot walls resulting in additional lubrication forces coming into play. This causes the settling velocity to decrease very sharply beyond this point. Ultimately, the settling velocity approaches zero when the particle diameter becomes equal to the slot width.

6.6.7 Impact of Particle Concentration on Settling

Several studies have been conducted on the effect of particle concentration on settling (Novotny[1]; Harrington and Hannah[21]; Acharya[16]; Daneshy[1]). All these studies indicate that the settling rate of particles decreases with increasing particle concentration. The experimental data is summarized in Figure 6.31. Equations 6.5 and 6.6, given below, are matched polynomials for the effect of particle concentration on settling rate.

$$V_{\phi} = V_s \left(2.3703\phi^2 - 3.0792\phi + 1\right) \tag{6.5}$$

$$V_{\phi} = V_s \left(-5.918\phi^3 + 8.8477\phi^2 - 4.7892\phi + 1\right) \tag{6.6}$$

Here ϕ is volumetric concentration of particles; V_{ϕ} is settling rate of concentrated particles and V_s is the settling rate of a single particle. It is evident from the experimental data and correlations above that the settling rate of particles goes to zero as the particle concentration approaches a close pack (about 0.65).

6.6.8 Effect of Wall Roughness on Particle Settling Velocity

Experiments have been conducted on cells made of Lucite plates which have rough surfaces as described in the previous section. It is thought that these experiments are representative of flow in a realistic fracture geometry. The width of the cell is defined as the average width. Experiments were conducted with water and with high-viscosity Newtonian fluids (solutions of glycerin and water).

Figure 6.32 clearly indicates that the settling velocity decreases faster as the ratio of particle diameter to cell width increases between the rough fracture walls. Indeed, the settling velocity drops to zero as the ratio of particle diameter to the average cell width is about 0.7 to 0.8. This occurs because even though the average cell width is larger than the particle diameter, there is a point along the settling path of the particle where the cell width is smaller than the particle diameter, causing the settling velocity to drop to zero. This effect is quite pronounced and is obvious for both the low and the high-viscosity fluids investigated.

Although experiments were conducted only for one set of cell wall roughness, it is expected that similar results will be obtained for different types of wall roughness. It is expected that differences in the settling velocity will be obtained depending on the magnitude of the surface roughness (Figure 15). Large amplitude of surface roughness will result in a large reduction in the average settling velocity.

6.6.9 Effect of Horizontal Flow on Particle Settling Velocity

All the previous experimental data are measured settling velocities in quiescent fluids. In the actual fracturing process, the proppant will settle while the fluid is moving at a high velocity in the horizontal direction. In order to replicate this process, some experiments were conducted while the fluid was flowing at up to 70 cm/sec. Figure 6.25 shows a schematic of how these tests were conducted. The trajectory of the particle in the cell was recorded on a video camera. The sample of the particle trajectory in the cell is shown in Figure 6.26. The settling velocity was measured by measuring the vertical component of the particle velocity in the cell. Figure 6.27 shows the settling rate in the cell as a function of the particle diameter to cell width.

The settling velocities with and without the horizontal flow of water are shown in the same figure (Figure 6.27). It is evident that the settling velocities do not change whether the water is stagnant or flowing in the horizontal direction. This is expected for Newtonian fluids. However, for non-Newtonian fluids, other more complex shear thinning effects will give rise to larger settling rates because of the dependence of viscosity on shear rate.

6.7 CONCLUSIONS

Based on the experiments conducted, the following conclusions can be obtained:

1. Proppant settling is impacted by several factors, including wall effects, particle concentration effects, effects of fluid rheology and the horizontal flow of fluid. These effects have been experimentally quantified in the results presented in this chapter.
2. Proppant settling in low-viscosity fluids is significantly impacted by the effect of inertia. When the particle Reynolds number exceeds 2, inertial effects need to be taken into account when calculating the settling velocity. Settling velocities are reduced by a factor of 2 to 6 due to inertial effects.
3. In high-viscosity Newtonian fluids, particle Reynolds numbers for settling generally are less than 2, therefore, Stokes' settling equation appears to adequately calculate the settling velocity.
4. The effect of cell walls on particle settling is quite significant and has been quantified. In general, the settling velocity decreases as the ratio of particle diameter to cell width approaches 1. The effect of fracture walls is more pronounced as the viscosity of fluid is increased.
5. The effect of fracture walls for high-viscosity Newtonian fluids and for power-law shear thinning fluids is similar. Both types of fluids show significant reduction in the settling rate as the ratio of particle diameter to cell width increases.
6. Wall roughness seems to have a significant effect on the particle settling rate. Comparison made between rough walls and smooth walls indicates that the settling rate for rough walls is significantly lower than the settling rate for smooth walls for the same particle diameter to cell width ratio. This occurs primarily because the particles have to settle through regions where the particle diameter becomes comparable to the cell width resulting in a significant reduction in the settling rate.
7. Comparisons made between the settling velocity in the stagnant fluids verse fluids flowing at different velocities in the horizontal direction indicate that the settling velocity is not impacted by the horizontal flow of Newtonian fluids. However, for non-Newtonian fluids, the increased shear rate will result in a smaller effective viscosity, which will then increase the settling rate.

8. Increased particle concentration, in general, hinders particle settling. As the particle volumetric fraction increases to about 0.6, the settling velocity approaches zero. Past experimental data showing this effect was curve fitted with polynomial expressions that provide a reasonable correlation with these experimental data.

6.8 REFERENCES

1. D. Mader: “Hydraulic proppant fracturing and gravel pack”, Elsevire Schience Publishing Company Inc. 1989.
2. Michael J. Economides, A.Daniel Hill, Christine Ehlig-Economides, “Petroleum Production Systems”, Prentice Hall Petroleum Engineering Series, 1994.
3. Ray N. Walker, Jr., Jeffery L. Hunter, Al C. Brake, Paul A. Fagin, Nick Steinsberger, “Proppants, We Still Don’t Need No Proppant-A Perspective of Several Operators”, SPE 49106.
4. Michael J. Mayerhofer, D.Nathan Meehan, “Waterfracs-Results from 50 Cotton Valley Wells”, SPE 4910.
5. M.J.Mayerhoer, M.F.Richardson, R.N. Walker, D.N.Meehan, M.W.Oehler, R.R.Browning Jr., “Proppants? We don’t need No Proppants”, SPE38611.
6. G.G.Stokes, Trans. Cambridge Phil. Soc., 9,8-106(1851). For creeping flow around an object of arbitrary shape, see H. Brenner, Chem. Engr. Schi., 19,703-727 (1964).
7. J. Happel, H. Brenner, “Low Reynolds Number Hydrodynamics” by Prentice- Hall, Inc., 1965.
8. L.R. Kern, T.K.Perkins, R. E.Wyant, “The Mechanics of Sand Movement in Fracturing”, SPE 2037, prepared for presentation at the 33rd Annual Fall Meeting of SPE held in Houston, Tex, Oct. 5-8, 1958.
9. Schols, R.S., Visser,W. “Proppant Bank Buildup in a Vertical Fracture Without Fluid Loss”, SPE 4834, SPE-European Spring Meeting 1974 of the Society of Petroleum Engineers of AIME, held in Amsterdam, the Netherlands, May 29-30, 1974.
10. P.E. Clark, M. W. Harkin, H.A. Wahl, J.A. Sievert, “Design of A Large Vertical Prop Transport Model”, SPE 6814, prepared for presentation at the 52nd annual fall

technical conference and exhibition of the SPE held in Denver, Colorado. Oct.9-12, 1977.

11. P.E. Clark, Jamal A. Quadir, "Prop Transport in Vertical Fractures", SPE 10261, prepared for presentation at the 56th annual fall technical conference and exhibition of SPE held in San Antonia, Tex, Oct 5-7, 1981.
12. P.E. Clark, Jamal A. Quadir, "Prop Transport in Hydraulic Fractures: A Critical Review of Particle Settling Velocity equations", SPE 9866, prepared for presentation at the 1981 SPE/DOE Low Permeability Symposium, held in Denver, Colorado, May 27-29, 1981.
13. Dunand A., Soucemarianadin A., "Concentration Effects on the Settling Velocities of Proppant Slurries", SPE 14259, 60th Annual Technical Conference and Exhibition of the Society of Petroleum Engineers held in Las Vegas, NV September 22-25,1985.
14. Roodhart, L.P., "Proppant Settling in Non-Newtonian Fracturing Fluids", SPE 13905, presented at the SPE/DOE 1985 Low Permeability Gas Reservoirs held in Denver, Colorado, May 19-22, 1985.
15. Kirkby, L.L., Rockefeller, H.A.,"Proppant Settling Velocities in Nonflowing Slurries", SPE 13906, presented at the SPE/DOE 1985 Low Permeability Gas Reservoirs held in Denver, Colorado, May 19-22, 1985.
16. Acharya, A.Ruma, "Particle Transport in Viscous and Viscoelastic Fracturing Fluids", SPE 13179, 1986 SPEPE.
17. Cleary M.P., Wright, C.A., Wright, T.B., "Experimental and Modeling Evidence for Major Changes in Hydraulic Fracturing Design and Field Procedures", SPE 21494, prepared for presentation at the SPE Gas Technology Symposium held in Houston, Texas, January 23-25, 1991.
18. Cleary M.P., Fonseca Jr., Amaury, "Proppant Convection and Encapsulation in Hydraulic Fracturing: Practical Implications of Computer and Laboratory Simulations", SPE 24825,onseca Jr., Amaury, prepared for presentation at the 67th Annual Technical Conference and Exhibition of the Society of Petroleum Engineers held in Washington, DC, October 4-7, 1992.
19. In 1994, R. D. Barree, "Evaluation of Frac and Pack Completions and Future Outlook", SPE 38184 , prepared for presentation at the 1997 SPE European

Formation Damage Conference held in The Hague, The Netherlands, 2-3 June 1997.

20. Clark P.E., Zhu Qinsheng, “Convective Transport of Propping Agents During Hydraulic Fracturing”, SPE 37358, presentation at the 1996 SPE Eastern Regional Meeting held in Columbus, Ohio, 23-25, 1996.

21. Harrington Larry, J.Hannah, Robert R., Williams Dennis, “Dynamic Experiments on Proppant Settling in Cross-linked Fracturing Fluids”, SPE 8342, presented at the 54th Annual Fall Technical Conference and Exhibition of the Society of Petroleum Engineers of AIME, held in Las Vegas, Nevada, September 23-26, 1979.

22. Clark P.E., Zhu Quishen, “Flow Visualization of Flow Into 8 Point-Source Fractures II: The Effect of Fracture Non-Uniformity and Fluid Crosslinking”,SPE 29503, prepared for presentation at the Production Operations Symposium held in Oklahoma City, OK, U.S.A., 2-4 April 1995.

23. Abdulrahman A. Al-quraishi, King Abdulaziz, Richard L. Christiansen, “”Dimensionless Groups for Interpreting Proppant Transport in Hydraulic Fractures”, SPE 53262, prepared for presentation at the 1999 SPE Middle East Oil Show held in Bahrain, 20-23 February 1999.

24, Sievert John A., Wahl Harry A., Clark P.E., Harkin Michael W., “Transport in a Large Vertical Model”, SPE 9865, presented at the SPE/DOE 1985 Low Permeability Symposium held in Denver, Colorado, May 27-29, 1981.

25. James M. Peden, Yuejin Luo, “Settling Velocity of Variously Shaped Particles in Drilling and Fracturing Fluids”, SPE 16243, SPEDE, December 1987.

26. D. B. Van Dam, C.J.de Pater, “Roughness of Hydraulic Fractures: Importance of In-Situ Stress and Tip Processes”, SPE 68775, presented at the 1999 SPE Annual Technical Conference and Exhibition held in Houston, 3-6 Oct. 1999.

27. C.N. Fredd, S.B. McConnell,C.L. Boney, and K.W. England, “Experimental Study of Hydraulic Fracture Conductivity Demonstrates Benefits of Using Proppant”, prepared for presentation at the 2000 SPE Rocky mountain Regional/low-permeability reservoir symposium held in Denver, CO, 12-25 March,2000.

28. C.N, Fredd, S.B. McConnell, C.L. Boney, K.W. England, SPE 74138, “Experimental Study of Fracture Conductivity for Water-Fracturing and Conventional Fracturing Applications”.

29. M.M. Hossain, M.K. Rahman, S.S. Rahman, “Volumetric Growth and Hydraulic Conductivity of Naturally Fractured Reservoirs During Hydraulic Fracturing: A Case Study Using Australian Conditions”, , SPE 63173, prepared for presentation at the 2000 SPE Annual Technical Conference and Exhibition held in Dallas, Texas, 1-4 October 2000.
30. M.M. Hossain, M.K. Rahman, S.S. Rahman, SPE 78355,”A Shear Dilation Stimulation Model for Production Enhancement From Naturally Fractured Reservoirs”, a revised version of SPE 63173.
31. M.M.Hossain ,M.K. Rahman and S.S. Rahman, “Application of HDR Stimulation Technology to Develop Tight Gas Reservoirs”, SPE 64484, prepared for presentation at the 2000 SPE Asia Pacific Oil and Gas Conference and Exhibition held in Brisbane, Australia, 16-18 October 2000.
32. D.E. McMechan, S.N. Shah, ”Static proppant-settling characteristics of non-Newtonian fracturing fluids in a large scale test model”, SPE 19735.
33. K.W. England, B.D. Poe, J.G.Conger, “Comprehensive Evaluation of Fractured Gas Wells Utilizing Production Data”, SPE 60285, presentation at the 2000 SPE Rocky Mountain Regional/Low Permeability Reservoirs Symposium held in Denver, CO, 12-15 March 2000.
34. Batchelor G.K., “Sedimentation in a Dilute Dispersion of Spheres”, J. Fluid Mech. 52,245-268, 1972.
35. Dallavalle, J.M. Micromeritics, “The Technology of Fine Particles”, 2nd edition, Pitman, London, 1948.
36. Di Felice, R., Foscolo, P.U.& Gibilaro, L.G., “On the Hindered Settling Velocity of Spheres in the Inertial Flow Regime”, Chem. Engng Sci. 50, 3005-3006. 1995
37. Di Felice, R., “Hydrodynamics of Liquid Fluidisation”, Chem. Engng Sci. 50, 1213-1245, 1995.
38. Fidleris, V. & Whitmore, R.L., “Experimental Determination of the Wall Effect for Spheres Falling Axially in Cylindrical Vessels”, Brit. J. Appl. Phys. 12, 490-494. 1961.
39. Happel, J., “Viscous Flow in Multiparticle Systems: Slow Motion of Fluids Relative to Beds of Spherical Particles”, AIChE J. 4,197-201, 1958.

40. Richardson, J.F. & Zaki, W.N. "Sedimentaion and Fluidisation. Part I". Trans. Inst. Chem. Engrs 32, 35-53, 1954.

Table 6.1 Dimensions of the fracture and the cells

	Fracture	Big flow cell	Small flow cell
Length: (m)	92	3	0.4
Height: (cm)	1219	40	4.7
Width: (cm)	0.5	2	0.4
Flow rate: (cm/sec)	200	40	70
Particle diameter: (cm)	0.1	0.1	0.1
Particle settling rate: (cm/sec)	19.8	19.8	19.8
Density difference between fluid & particle	2.3	2.3	2.3
Channel Reynolds number (R_e):	10000	8000	2800
Particle Reynolds number (R_{ep}):	2000	400	700
Ratio of advection to settling (t_{adv}/t_{set}):	0.75	3.75	2.5
Shields number (S):	2.45	61	20

Table 6.2 Measured particle settling rates in water and glycerin

Particle Diameter: cm	Settling rate in water: cm/sec (μ=1 cp)	Settling rate in glycerin: cm/sec (μ=10.2 cp)
0.055	10.02	3.41
0.083	16.02	5.44
0.092	18.01	6.12
0.096	18.91	6.43
0.1	19.81	6.73
0.116	23.46	7.97
0.122	24.85	8.45

Table 6.3 Properties of solutions of water-glycerin

Water-glycerin Ratio	Viscosity: cp	Density : g/cc
0	780	1.3
1:1	10.2	1.15
1:5	104	1.25

Table 6.4 Properties of guar gels

Guar concentration: lb/Mgal	Power-law Exponent (n)	Consistency Index (K): eq cp
20	0.59	156
30	0.53	307
40	0.42	892

Table 6.5 Particle settling rates in unbounded water and in a cell

Particle Diameter: cm	Particle Settling Rate in Water: cm/sec	Particle Settling Rate in water in a cell (width=0.15cm): cm/sec
0.061	11.8	10.6
0.088	18.5	15.3
0.095	19.8	16.2
0.115	23.4	18.3

Table 6.6 Particle settling in unbounded glycerin (780cp) and in a cell

Particle Diameter: cm	Particle Diameter / Cell width	Particle Free Settling Rate: cm/sec	Particle Settling Rate in Cell: cm/sec
0.85	0.567	0.1078	0.08
1.17	0.78	0.2093	0.123

Table 6.7 Particle settling in unbounded glycerin solution (112 cp) and in a cell

Particle Diameter: cm	Particle Diameter / Cell width:	Particle Free Settling Rate: cm/sec	Particle Settling Rate in Cell: cm/sec
0.52	0.347	0.43	0.335
0.85	0.567	0.94	0.57
1.21	0.807	1.87	0.94

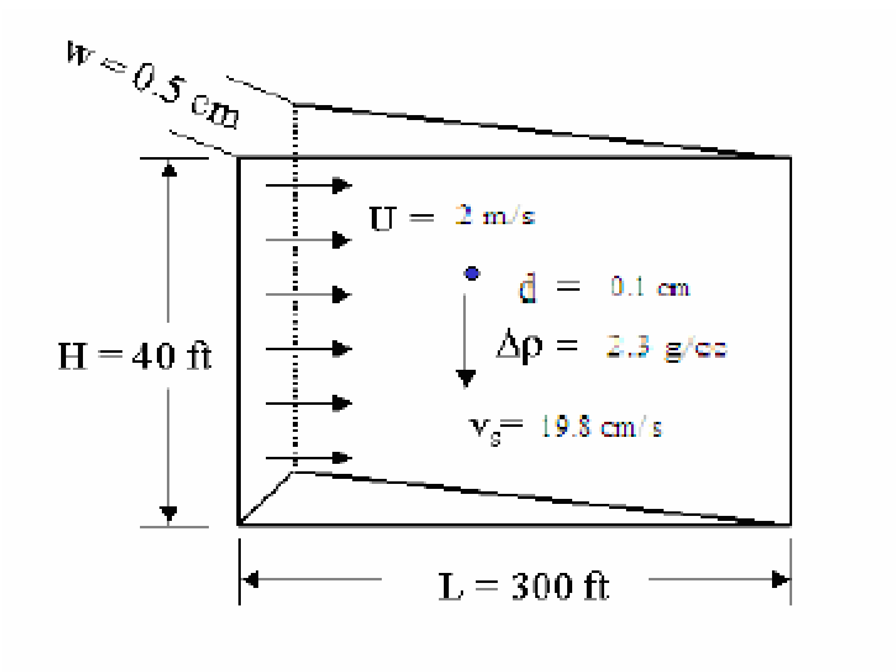

Figure 6.1 Dimensions of the fracture.

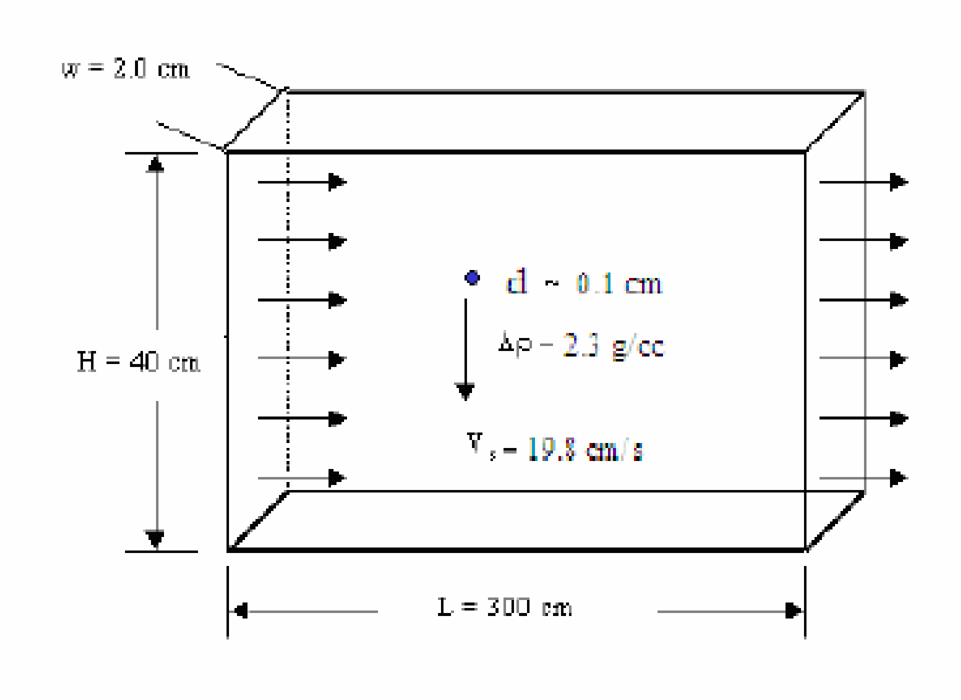

Figure 6.2 Dimensions of the cell.

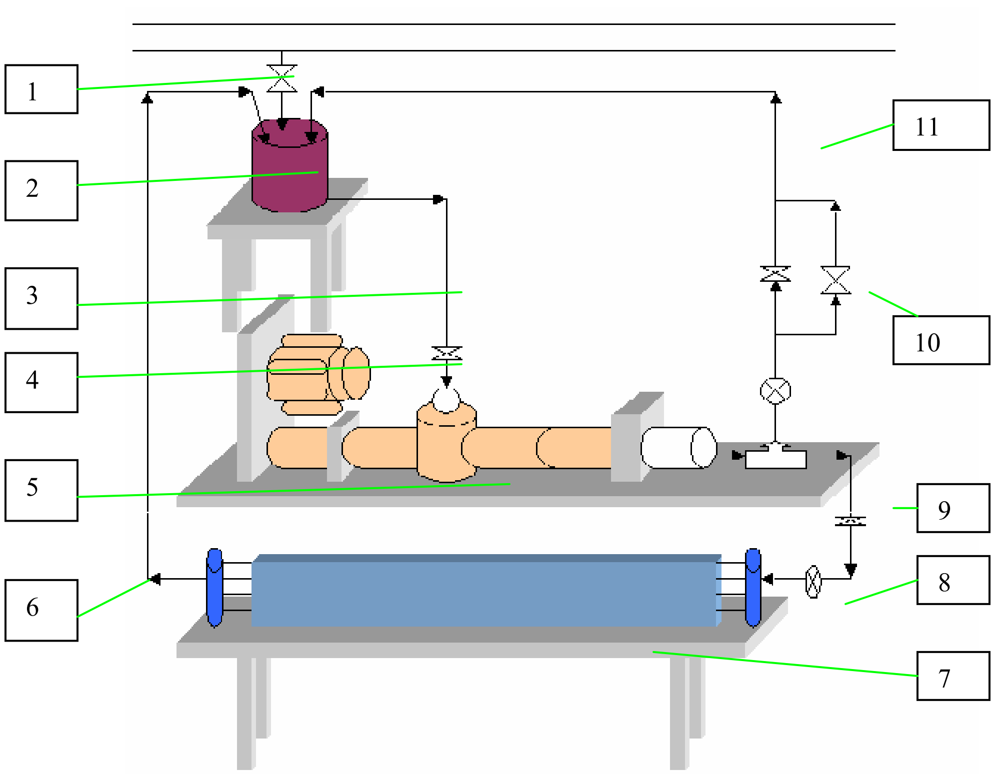

Figure 6.3 Schematic of apparatus to measure particle transport (Introduction of this apparatus is in Section 6.5).

Figure 6.4 Apparatus of measuring proppant transport in a cell.

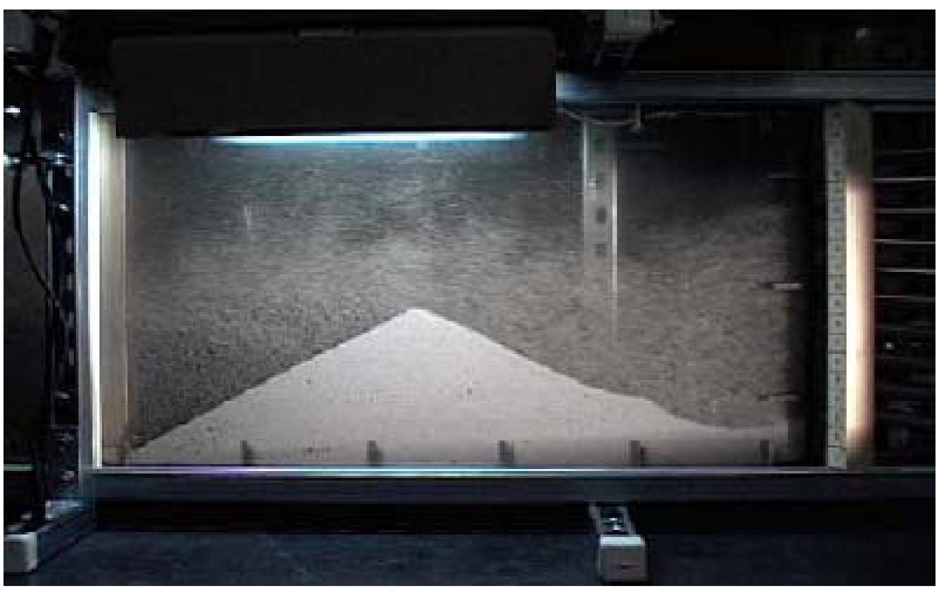

Figure 6.5 Early stage of proppant bed buildup.

Figure 6.6 Flow pattern in the cell due to entrance effects.

Figure 6.7 Formation of a proppant bed.

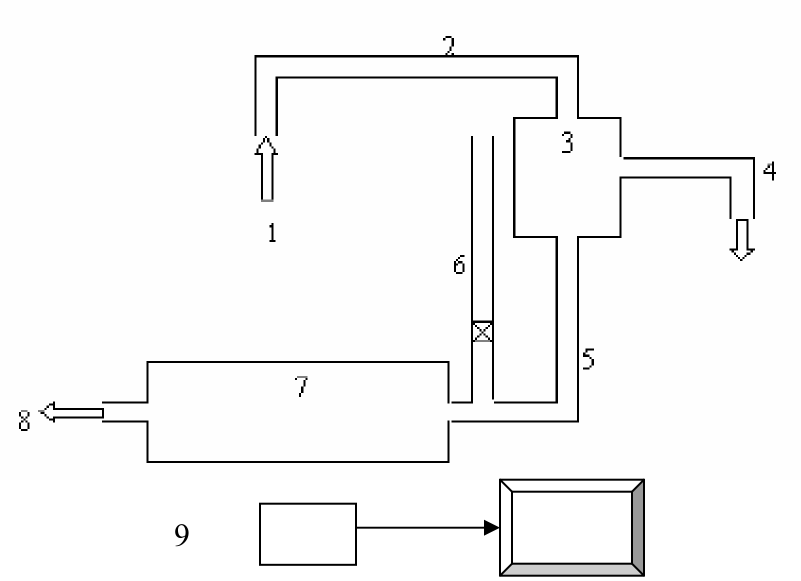

Figure 6.8 Schematic of apparatus measuring particle transport in small cells (A description of this apparatus is provided in Section 6.5).

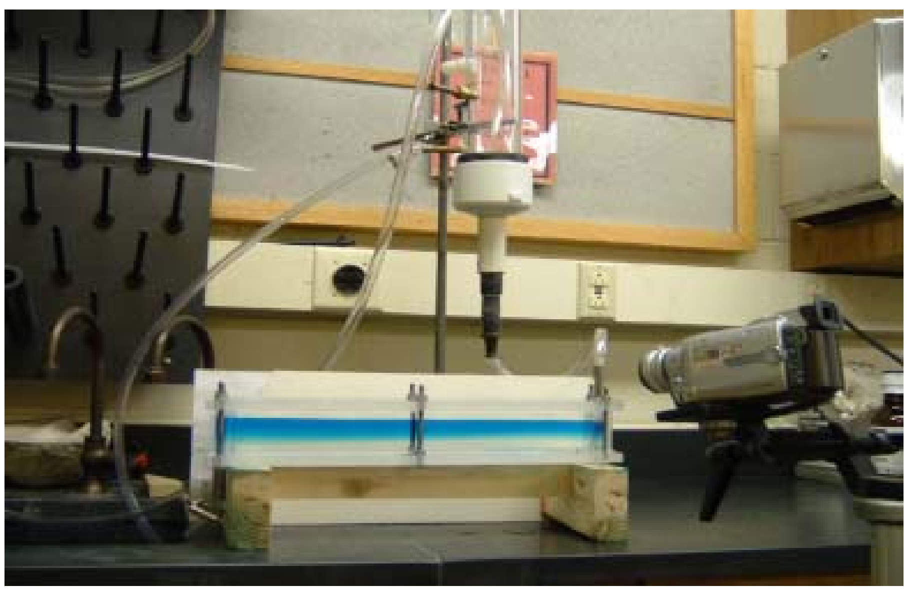

Figure 6.9 Apparatus for measuring particle transport in small cells.

Figure 6.10 Small cells to measure particle settling.

Figure 6.11 Core samples and transparent Lucite plates.

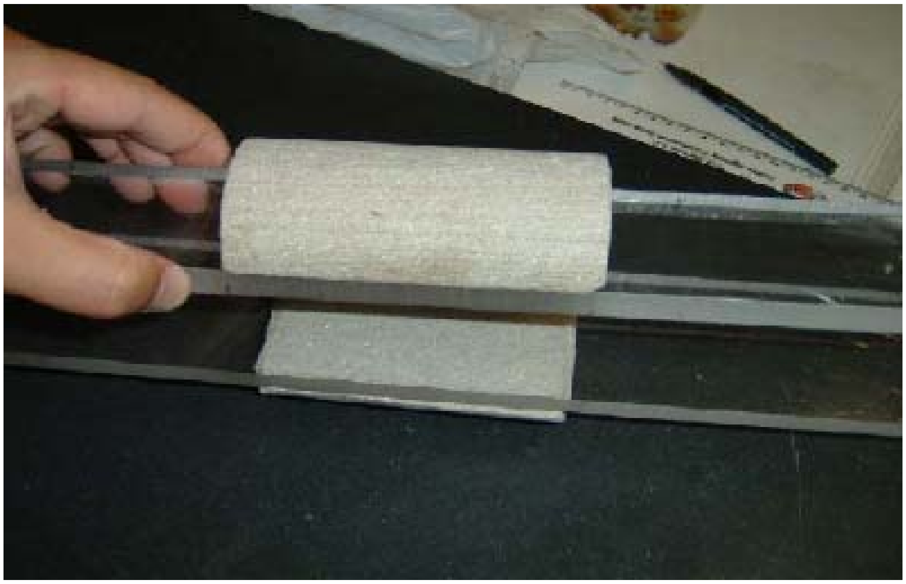

Figure 6.12 Two rough surfaces of core samples used to make rough fracture surfaces.

Figure 6.13 Rock samples act as stamps.

Figure 6.14(a) A transparent rough fracture wall from core sample 1.

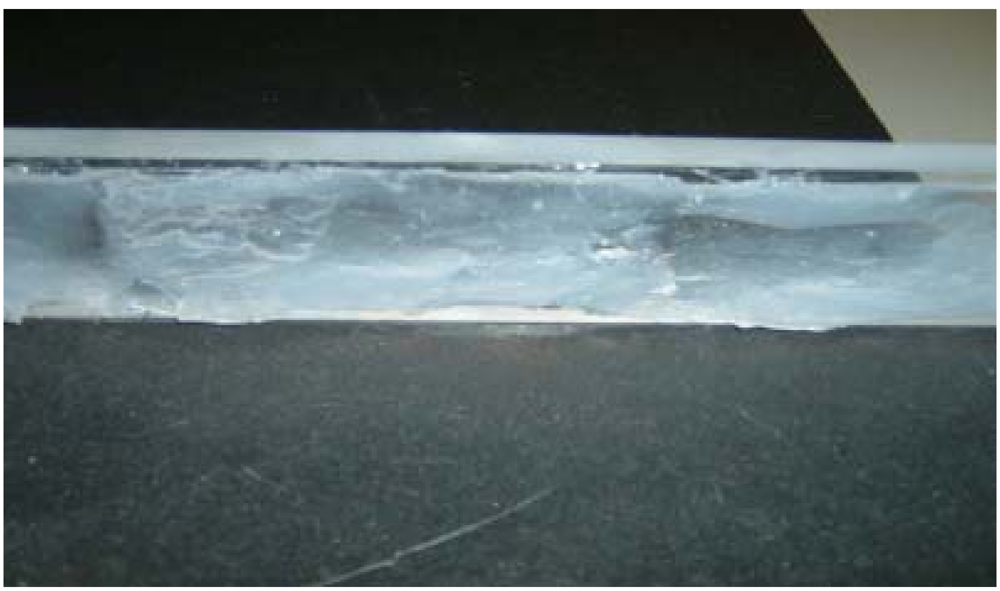

Figure 6.14(b) A transparent rough wall from core sample 2.

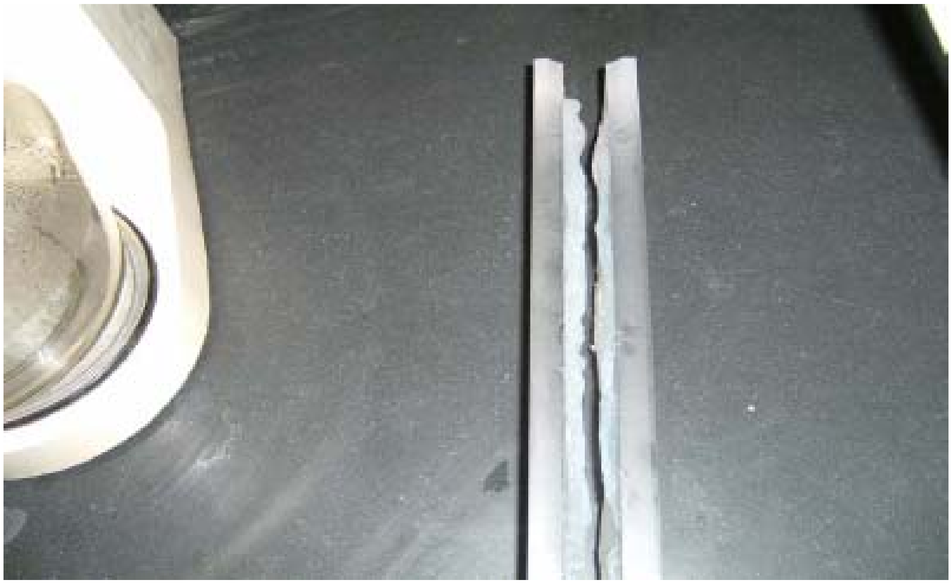

Figure 6.14(c) Two transparent rough walls approximately match the fractures from the rock fracture surfaces.

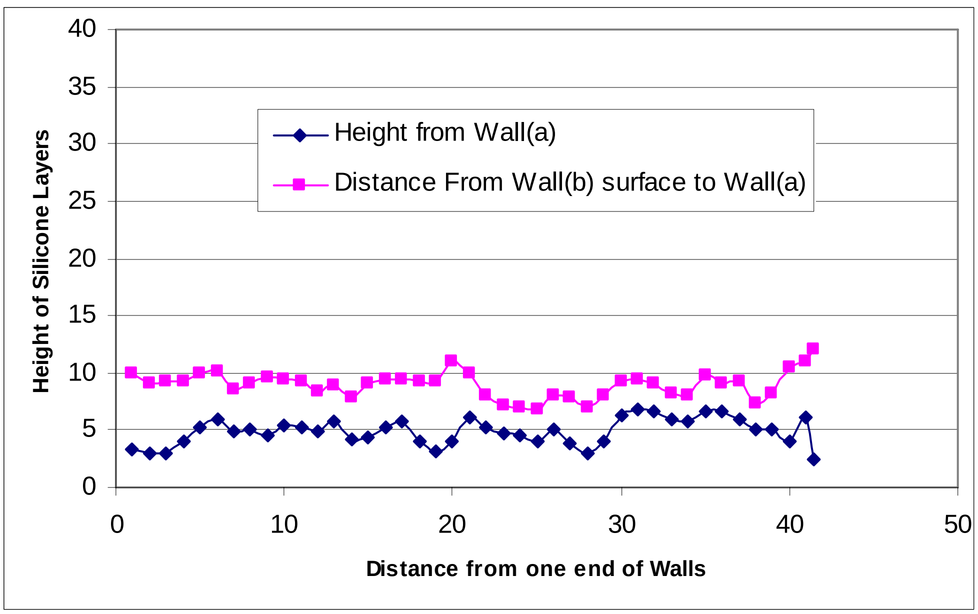

Figure 15 Roughness of walls of core sample 2

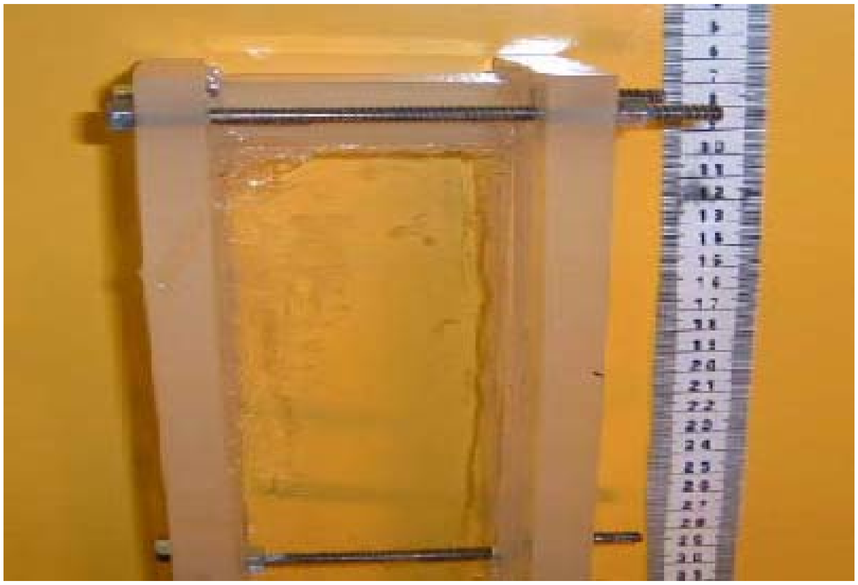

Figure 6.16 Apparatus to measure particle static settling in water.

Figure 6.17 Glycerin and proppants used in the tests.

Figure 18. Guar gum and a guar gel.

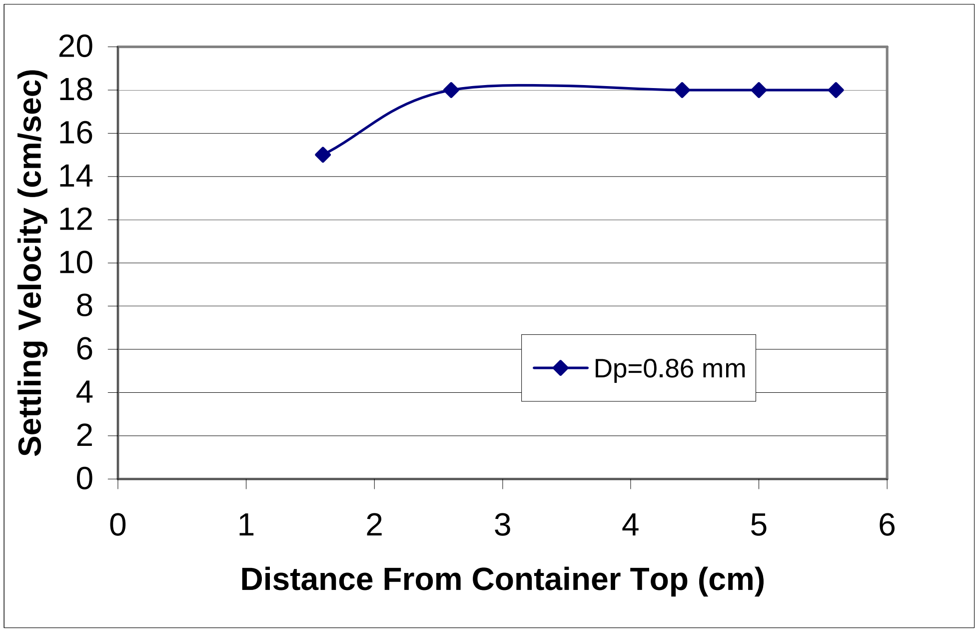

Figure 6.19 Particle settling velocity distribution.

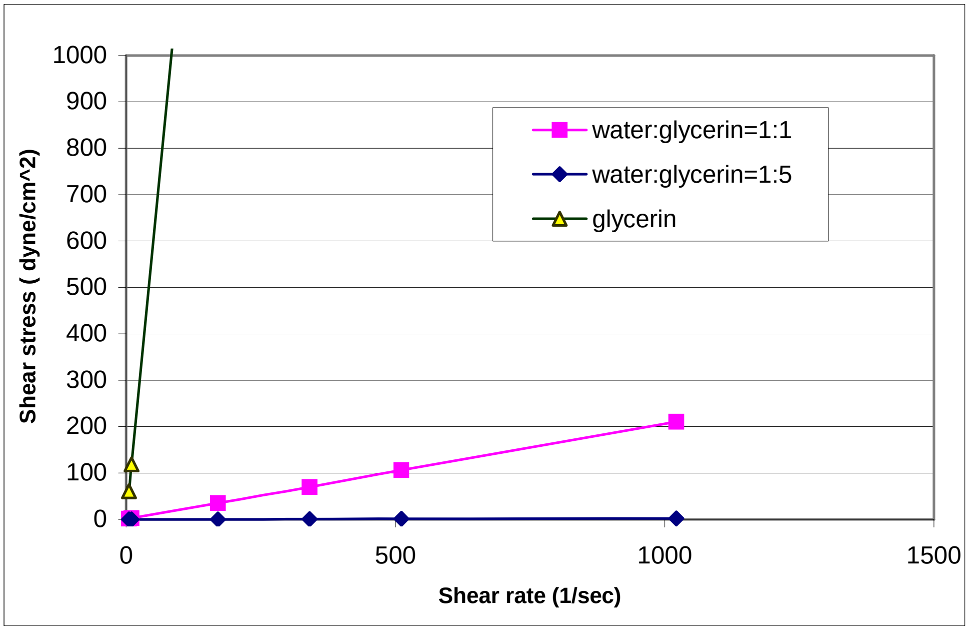

Figure 6.20(a) Rheology of glycerin and solutions of water-glycerin.

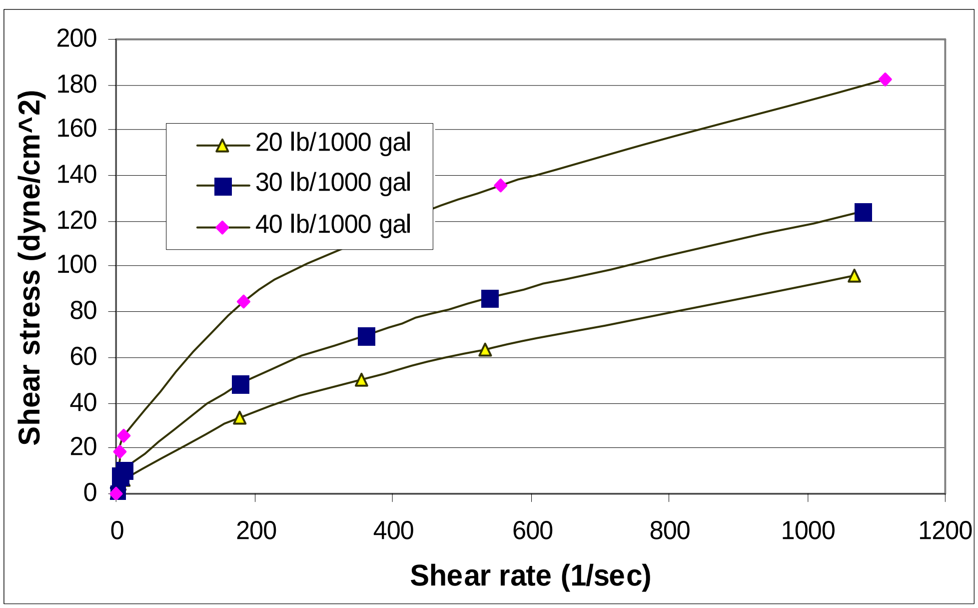

Figure 6.20(b) Rheology of Guar gels.

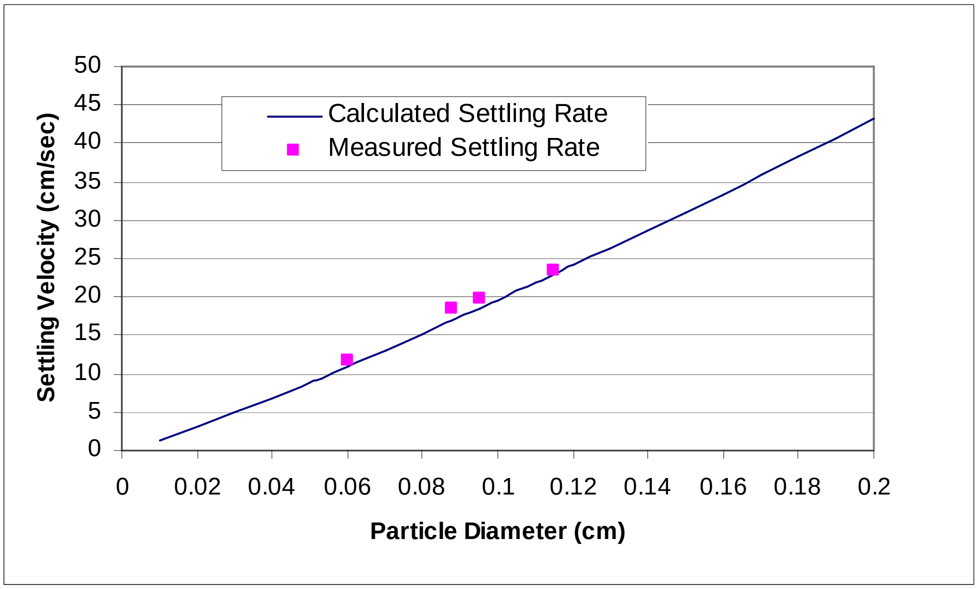

Figure 6.21 Comparison between calculated and measured spherical particle settling rate in unbounded water.

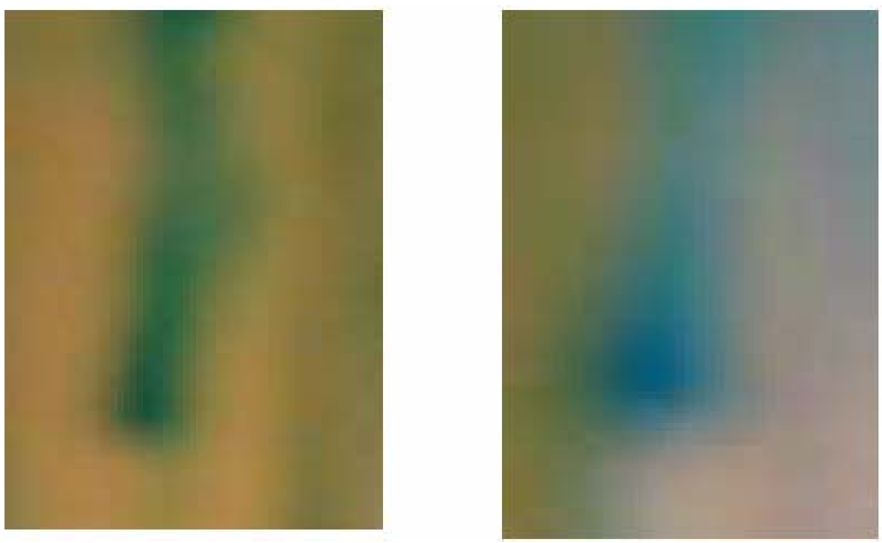

Figure 22 (a) and (b) Dyed particle settling in water.

Figure 22(c) Dyed particle settling in glycerin.

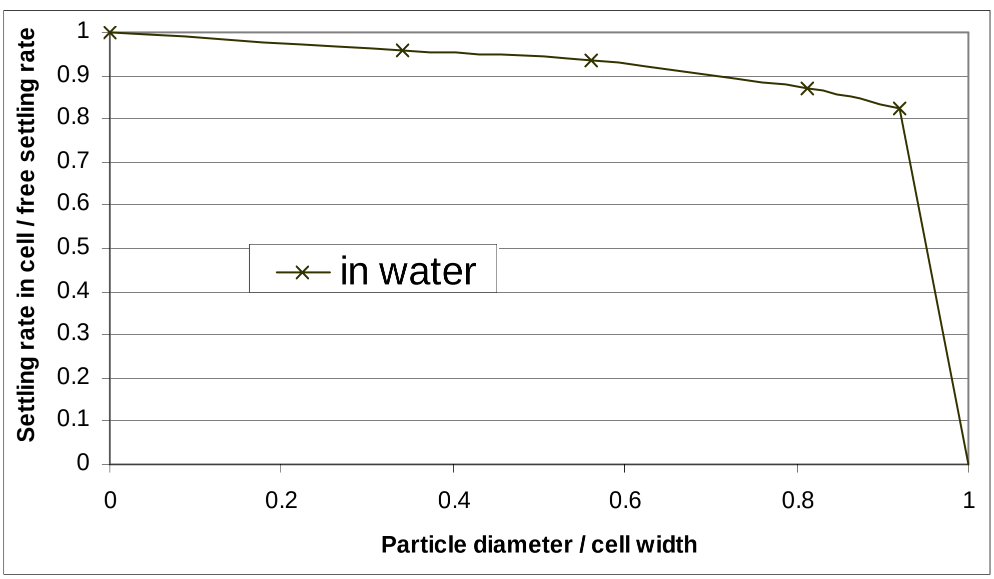

Figure 6.23(a) Wall effect on single particle settling.

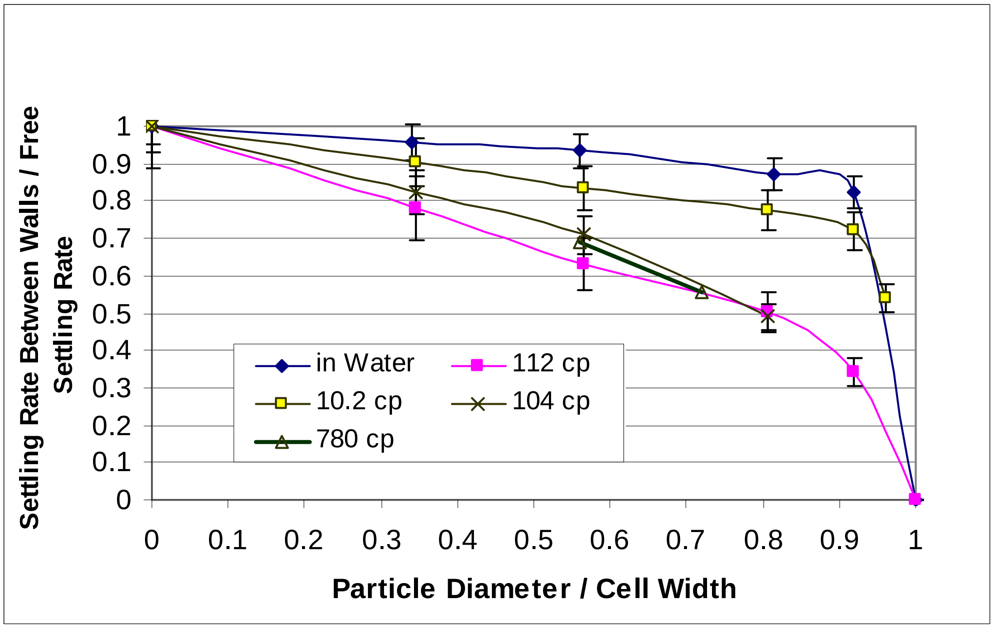

Figure 6.23(b) Rheology effect on particle settling.

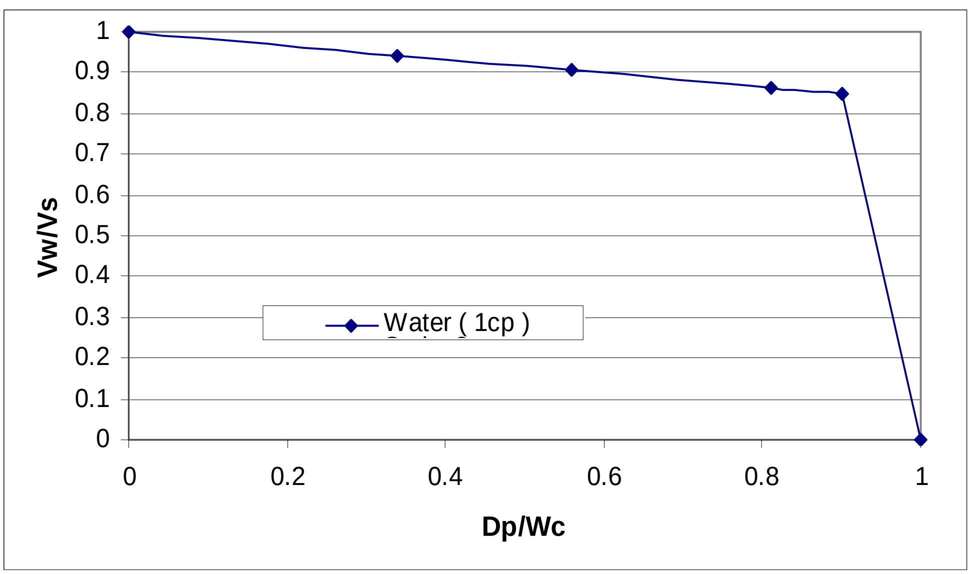

Figure 6.24 Matched curve of wall effect on particle settling in water.

Figure 6.25 Schematic of tests measuring flowing water effect on particle settling.

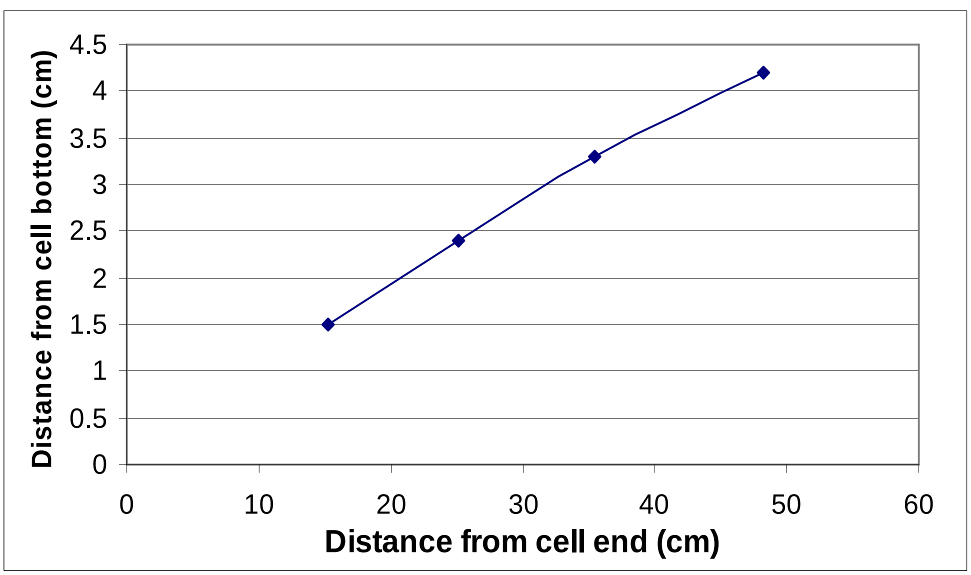

Figure 6.26 Particle trajectory in a cell.

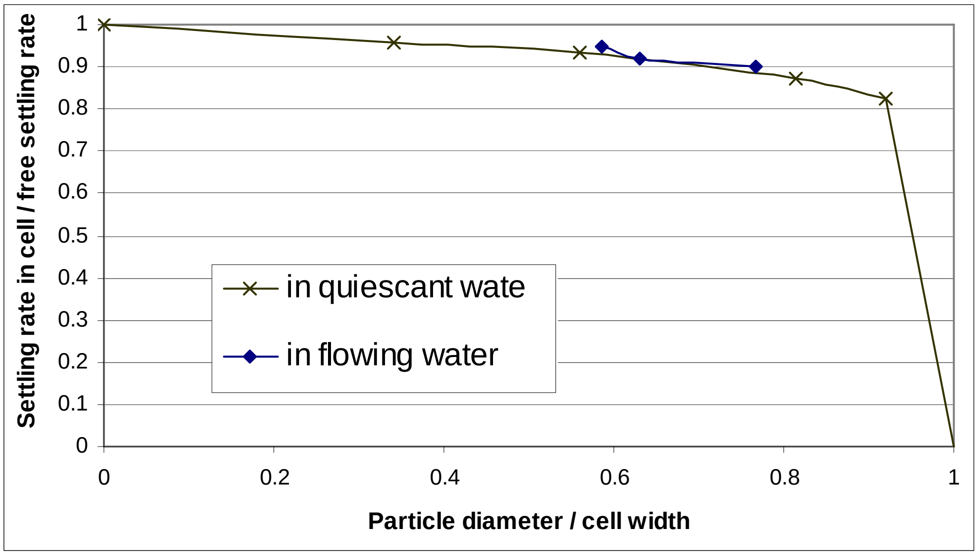

Figure 6.27 Effect on flowing water on single particle settling.

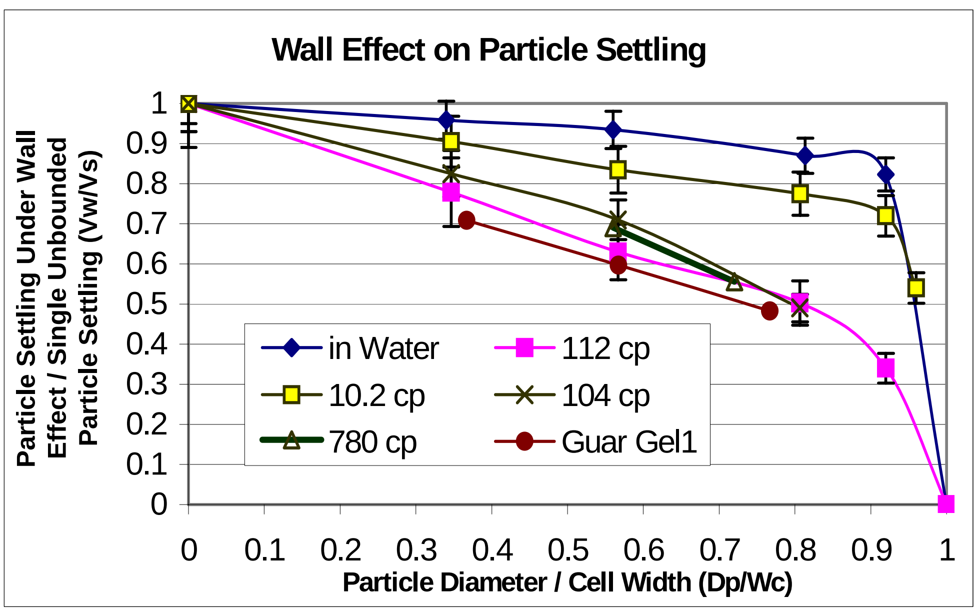

Figure 6.28 Particle settling in Newtonian and power-law fluids.

(Guar gel 1: 40 lb/Mgal)

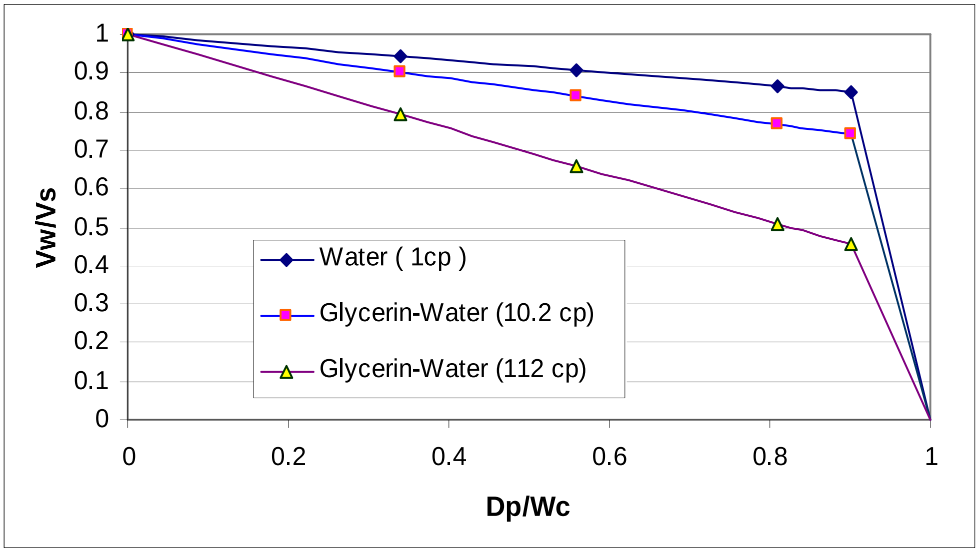

Figure 6.29 Matched curve of wall effect on particle settling in fluids.

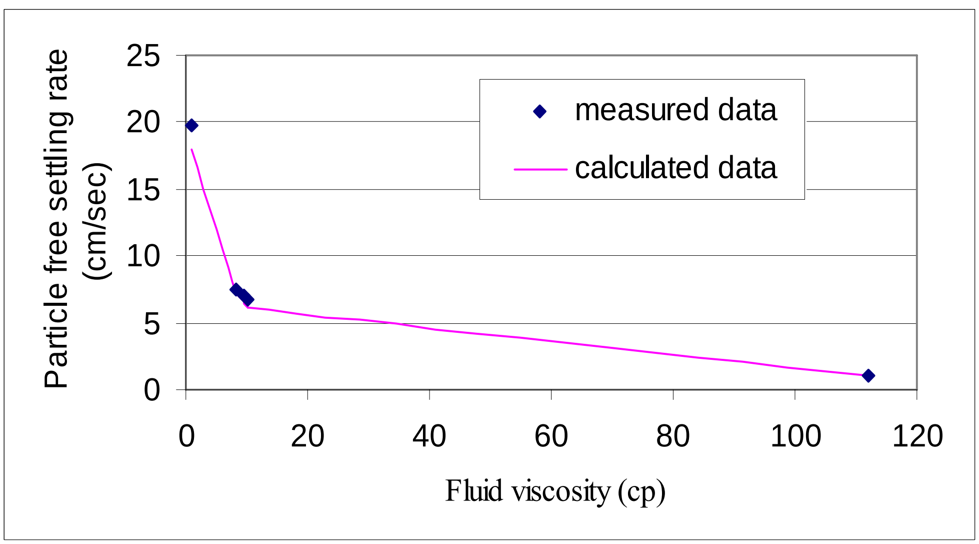

Figure 6.30 Comparison between measured particle free settling rates and calculated particle free settling rates in fluids of different viscosities.

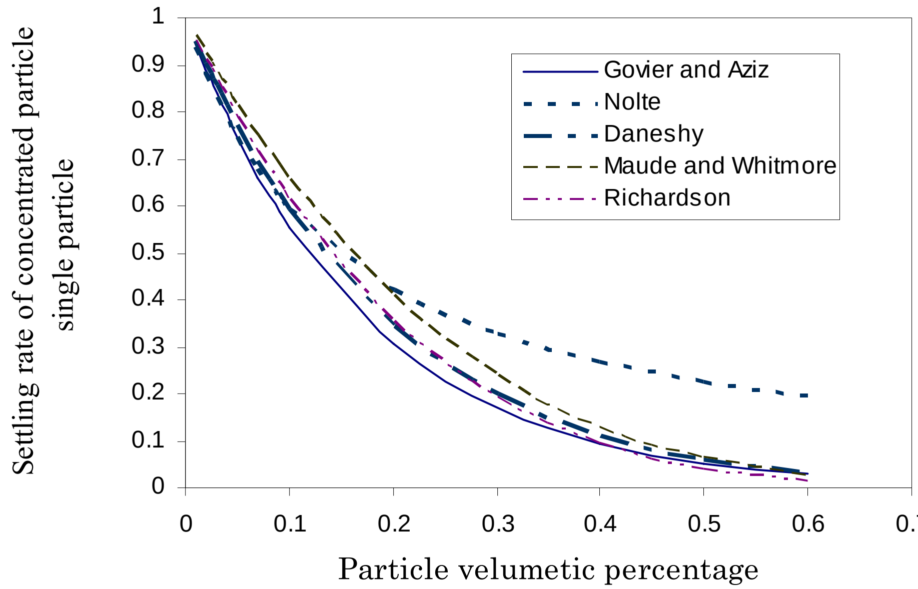

Figure 6.31 Concentration effect on particle settling.

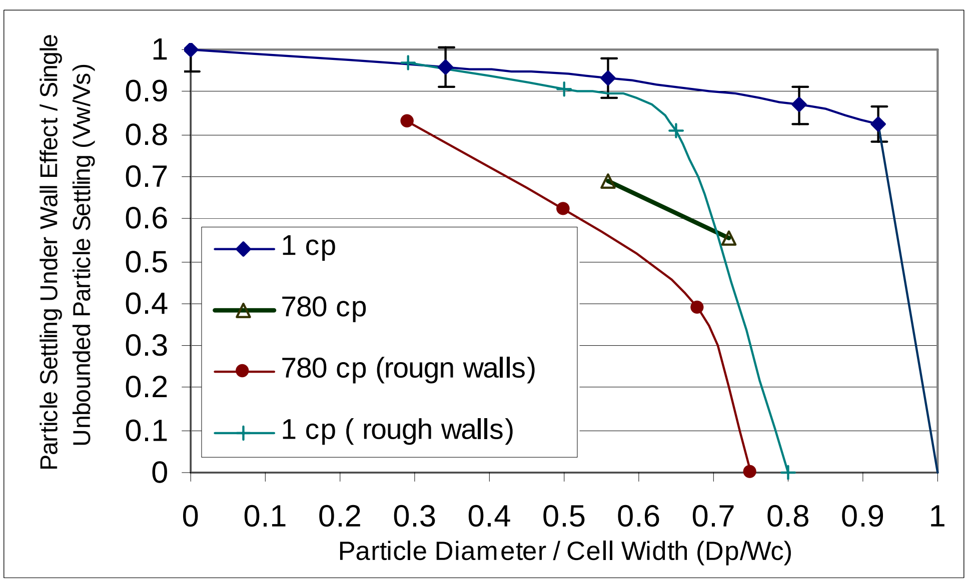

Figure 6.32 Wall roughness effect on particle settling.

CHAPTER 7. EXPERIMENTAL STUDY OF PROPPANT RETARDATION

7.1 INTRODUCTION

Proppant placement in a vertical fracture is mainly dependant on proppant settling and horizontal transport. While a lot of effort has been spent to investigate proppant settling in hydraulic fractures, relatively little attention has been paid to the horizontal transport of proppants. Proppant transport models usually simplify proppant transport as a two-dimensional flow in a slot. The proppant flows at the same velocity as the average local fluid velocity (Nolte[15]; Tehrani[16]; Barree[11]). The proppant concentration, like other variables such as fluid pressure and fracture width, is assumed to be a two dimensional function in the vertical fracture plane. Proppant concentration is usually assumed constant across the fracture width. (Novotny[2]; Nolte[15]; Tehrani[16]; Barree[11]; Weng[1])

For hydraulic fractures, the slot width varies from zero near the tip to the maximum value towards the middle of the fracture. This implies that the ratio of the proppant diameter to the slot width changes at different locations in the fracture. In regions where the fracture width is comparable to the proppant diameter, significant differences between the fluid velocity and proppant horizontal velocity may be expected. This effect, which is referred to as proppant retardation, can cause the transport of proppants to be hindered significantly. In some instances, it is possible that the proppant may travel at a velocity higher than the average fluid velocity, due to the reasons discussed in the following section.

All fracture simulators assume that the proppants travel at the same velocity as the fluid. As shown in this chapter, considerable evidence exists to suggest that this is not the case. The proppant can speed up in the wide portion of the fracture, and slow down (or is retarded) in the narrower portion of the fracture. Both experiments and models are presented to account for this change in proppant velocity due to the finite width of the fracture.

The extent to which the proppant is speeded up or slowed down, relative to fluid in the fracture, is a strong function of the distribution of proppant concentration within the fracture. For example, if the proppant concentration is high near the centerline of the fracture slot, the proppant will travel at a significantly higher velocity than the average fluid velocity.

However, if wall effects for a narrow part of the fracture become dominant, then the proppant velocity can decrease to zero, relative to the fluid. The distribution of proppants between the two walls is discussed in some detail in the following section.

For two-dimensional horizontal flow between parallel walls, a sphere near the wall tends to rotate due to the parabolic velocity profile, and tends to leave the wall and move towards regions of low shear. Thus, under no leak-off conditions, the proppant distribution across the fracture width is not uniform (Novotny[2]; Weng[1]). As stated above this can have a large influence on the average velocity of the proppant relative to the average fluid velocity.

In this chapter, we first review some past work done on modeling of the horizontal transport of neutrally buoyant solids in slot flow. A great deal of theoretical work has been done to calculate the velocity of the solids relative to the fluid. A simple model is presented to estimate the average particle velocity in the fracture without taking into account the hydrodynamic interaction between the particle and fracture walls. Experimental results are then presented for different ratios of particle diameter to cell width and for different fluid viscosities. These experiment results form the basis for the empirical correlations that we propose for the horizontal velocity of proppant particles in slot flow.

7.2 PAST WORK ON PARTICLE HORIZONTAL TRANSPORT IN SLOT FLOW

7.2.1 Particle Flow in a Slot

Many researchers have investigated particle motion between two parallel walls (Lorentz[5, 9]; Faxen[3]; Wakiya[4]; O'Neal[8]; Brenner[7]; Cox[6]; Ho and Leal[10]; Novotny[2]; Weng[1], Michelle[9]). For Newtonian fluids, a parabolic velocity profile is obtained with the fluid at the centerline having a maximum velocity 1.5 times higher than the average velocity.

Lorentz[5, 9] was the earliest investigator to derive a solution for the motion of a sphere in the presence of a plane wall at a low Reynolds number. Faxen[3] considered the problem of a sphere translating between two parallel walls in the special case where the sphere is either moving along the centerline or in a plane at one quarter the distance between the two walls. Faxen obtained expressions for the force and torque acting on the sphere by the method of reflections.

Wakiya[4] used a similar approach to treat the problem of a rigidly held sphere in couette flow or two-dimensional Poiseuille flow. Wakiya's solution only applies in the case where the sphere is at one quarter the distance between the walls.

Cox and Brenner[6] provided expressions for the drag and torque on a sphere translating parallel to a single plane wall, rotating adjacent to the wall or in the presence of a shear field. Ho and Leal[10] provided similar expressions with reasonable agreement with Cox and Brenner's results.

In 1974, Ganatos, Pfeffer and Weinbaum[5] presented exact solutions for the three-dimensional creeping motion of a sphere of arbitrary size and position between two plane parallel walls.

In two-dimensional Poiseuille flow, a particle maintains a preferred position in the slot/tube. Ho and Leal[10] showed that spheres reach a stable lateral equilibrium position independent of the initial condition of release. For simple shear flow in a slot, this position is midway between the centerline and the wall, whereas for Poiseuille flow, it is 0.6 of the channel half-width from the centerline.

In a tube, a sphere also tends to maintain a stable position. Segré & Silberberg[5] provided the first conclusive demonstration that neutrally buoyant rigid spheres in Poiseuille flow could, under appropriate circumstances, migrate across streamlines. They observed that the spheres eventually attained an equilibrium position at approximately 0.6 of the tube radius from the tube centerline. Subsequent studies by Goldsmith & Mason[9], Brenner[7], Tachibana[9], Halow and Wills[9] showed that the general behavior for rigid spheres depends strongly on the specific bulk flow geometry and on whether or not the particle is neutrally buoyant. For Couette flow, neutrally buoyant rigid spheres migrate to the centerline, while for both two- and three- dimensional Poiseuille flows, the sphere ultimately attains an equilibrium position which is approximately 60% of the way from the center-line to the vessel walls. On the other hand, a non-neutrally buoyant sphere in Poiseuille flow through a vertical flow channel is found to migrate towards the walls if the velocity is greater than the undisturbed fluid velocity evaluated at the same point, but towards the centerline if the particle velocity lags behind the undisturbed fluid velocity.

Nolte[15] discussed the occurrence of proppants migrating across fluid streamlines in non-Newtonian and viscoelastic fluids in a pipe or channel. The consequence of such migration is a higher proppant concentration in the centerline of the vessel.

In 2003, Michelle, Alexander. Zinchenko and Davis[9] developed a new boundary-intergal algorithm for the motion of a particle between two parallel plane walls. They computed the translational and rotational velocities for a broad range of particle sizes and depths in a channel in Poiseuille flow at a low Reynolds number. Their calculation results indicate that the average particle velocity for a uniform distribution of particles was generally found to exceed the average fluid velocity, due in large part to exclusion of the particle centers from the region of slowest fluid near the walls (Figure 7.1). The maximum average particle velocity is 18% greater than the average fluid velocity and occurs for particle diameters that are 42% of the channel height. Particles with diameters greater than 82% of the channel height have smaller average velocities than does the fluid, due to the retarding effect of the nearby walls.

In two-dimensional flow, a single particle tends to rotate and flow to the low-shear regions of flow. However, for a concentrated suspension, the particle concentration affects the particle distribution across the slot width. Barree and Conway[11] set up a series of annular-flow experiments to construct the velocity distribution from the observed frequency distribution of velocities of the beads in suspension. Visual observation of the flowing particle stream indicated that at low concentration (0~10%), the particles flow only near the centerline of the flow cell. They also investigated the concentration effect on particle horizontal transport. The particle velocity profile, represented by the cumulative distribution curve, approaches the expected parabolic shape at about 10 volume% solids concentration. Particle distribution appeared to be nearly uniform across the flow channel. As solids concentration increases to greater than 10% (by volume), the observed maximum velocity begins to decrease, resulting in a blunted flow profile.

Tehrani[16] generated shear-rate gradients in pipe flows similar to those within a fracture. Visual observation showed that migration of particles to the pipe axis is strongest in highly elastic fracturing fluids and occurs even within a 3-foot length of pipe, (which is shorter than a conventional fracture length of several hundred feet). The particle concentration in the pipe central core is higher (30%) than the original injected concentration

(15%). Tehrani also showed that particle concentration in the central core may not reach the maximum packing.

In 2001, Li[17] presented a three-dimensional model to study the deposition of sands in turbulent flowing water. Several assumptions were used in his formulation: the first assumption is that the discrete particles can be represented by a continuous density field, similar to the continuum assumption applied to molecules; secondly the Boussinesq assumption is valid; and third that the drift velocity between the particles and the fluid is constant. By using these assumptions, he solved four governing equations (one continuity and three momentum equations) for the fluid phase and one mass balance equation of the particle phase. His computed results were in satisfactory agreement with available experimental data.

In 2001, Joseph[17] described numerical simulations and experiments that he did to determine the settling velocity of sands in fluids (including water). The experiments were conducted in a cell (0.68cm, 20.3cm, 70.22cm) and he noticed that particles could settle down to the cell bottom when the flow velocity was low and would be suspended when the flow rate was high. The experiments included concentrated particles as well as single particle lift off and levitation to equilibrium. The simulation results agreed well with the data from experiments.

7.2.2. Effect of Horizontal Fluid Flow Rate on Particle Settling

In slot flow, the force acting on an immersed body in the direction that is orthogonal to the flow is usually upward (Wakiya[4]; Brenner[7]; Cox[6]). This lift force is the combined effect of particle rotation, shear and inertia in the fluid. The effect of the horizontal flow is usually to decrease the particle settling rate.

Early theoretical work studying the lift force acting on a sphere considered a sphere suspended in an unbounded fluid, in which case the lift force arises due to translation or rotation of the particle, relative to the undisturbed fluid flow.

Stokes studied the force acting on an immersed sphere early in middle 1900’s and derived the well known relation for the drag force acting on the sphere. Subsequent researchers continued to study the drag force and found many higher order corrections to Stoke’s drag force formula (Feuillebois[13]; Nolte[15]).

The effect of lift force was also reported by Poiseuille[12, 14]. Segré and Silberberg[5] demonstrated the existence of the lift force through rigorous experiments. In 1965, Saffman[12, 14] provided an expression for the lift on a sphere in an unbounded linear shear flow. He concluded that the lift force due to particle rotation is less by an order of magnitude than that due to shear when the Reynolds number is low. Feuillebois[9] gave a comprehensive review of experimental and theoretical work describing the lift force acting on a sphere (particle) immersed in fluids.

Dwyer[4], Mclaughlin and Dandy[14] reported computational studies of the inertial lift on a sphere in linear shear flow. Mei[14] obtained an expression for the lift force by fitting an equation to Dandy and Dwyer's data for high Reynolds numbers and Saffman's expression for low Reynolds number. The problem of inertial lift on a moving sphere in contact with a plane wall in shear flow was analyzed as a perturbation of Stokes' flow with inertia by Leighton and Acrivos[20], Cherukat and Mclaughlin[14], Krishnan and Leighton[14].

In hydraulic fracturing treatments, especially in water-fracs, the horizontal flow rate is high (>1m/s) and this results in turbulent flow in the fractures. The effect of turbulence tends to increase the settling (Mobbs[21]). But our test results showed that these effects (including turbulence effects and lift) on proppant settling are small under normal hydraulic fracturing conditions (Refer to Section 7.3.2).

7.2.3. Re-Suspension of Settled Particles by Horizontal Fluid Flow

The phenomena of re-suspension is usually associated with large Reynolds number flows and turbulence. Thomas[19] discussed this phenomena in 1961. Gadala[18] appears to be the first to observe that such re-suspension could also occur at low values of Reynolds number, 0 (10^{-4}). Gadala used a parallel plate device to measure the rheological properties of suspensions of coal particles in viscous Newtonian fluids. His test results indicated that particles, whose density is greater than the liquid, settle down when the flow rate is low. However, when the flow rate increases, the settled layer of particles are re-suspended due to the increased rate of shear.

Leighton and Acrivos[20] explained this phenomena in terms of a shear-induced diffusion process, in which the diffusivity results from inter-particle interactions within a suspension as it is sheared. This diffusion mechanism is quite different from conventional Brownian diffusion, arising from molecular motion, which is negligible for large particles.

The phenomena of viscous re-suspension is of practical importance in many industrial operations. In hydraulic fracturing treatments, it is suspected that viscous re-suspension can have a positive influence on proppant transport. When a fracture is created, a fluid containing proppant particles is pumped into it. Ideally, the proppant particles should settle evenly along the entire length of the fracture, so that when pumping ceases, the fracture is wedged open by the settled particles. By taking advantage of the viscous re-suspension effect, it is suspected that particles are entrained from a settled bed and saltate. This enables them to be convected deep into the fracture channel and thus avoid the possibility of a premature screenout. In order to investigate whether re-suspension can help transport proppant further into the fracture, many researchers did experiments to investigate the mechanisms of re-suspension of proppant beds (Kern[22]; Novotny[2], Nolte[15], Tehrani[16]).

Kern[23] built a cell to study the problem of the flow of particles in a hydraulic fracture and reported data on proppant bank formation and growth for Newtonian fluids. He summarized the relationship between the proppant bed equilibrium height and the injection rate. He found that proppant particles could be re-suspended if the slurry injection rate was increased.

Babcock[22] studied the characteristics of prop pack growth and developed equations to predict the rate of pack buildup for both Newtonian and non-Newtonian fluids. Schols and Visser[24] developed a set of equations to predict the height and length of a proppant pack due to proppant settling. They also presented equations to predict the equilibrium height of a proppant bed (bed height that does not increase as more proppants are injected due to the viscous re-suspension of the proppants).

Mobbs and Hammond[21] performed a computer simulation to investigate proppant transport based on the assumption that particles are uniformly distributed across the fracture width (homogeneous flow), and compared their results with that in a slurry in which some unspecified process causes all proppants to migrate across the fracture width into a close-packed sheet at the fracture center (sheet flow). They concluded that: convection rates are slightly greater in sheet flow than in homogeneous flow, and settling is greatly enhanced in sheet flow. Overall, settling in sheet flow gives the worst vertical motion of proppants.

In all these above studies, the walls of the slot are assumed to be impermeable. However, in hydraulic fracturing, the flow of proppants occurs in a slot, in which fluid leak-off occurs from both walls. This causes an additional hydrodynamic force to add on the proppant particles, pushing them against the fracture wall. This effect has been recognized and discussed qualitatively by past authors (Weng and Klein[1]). While it is clear that the fluid leak-off will cause the proppant concentration at the fracture wall to increase and proppant concentration near the centerline to decrease, it is not clear how significant this will be. Some initial calculations are presented in this chapter that indicate that this effect can be quite significant, resulting in a substantial slow down of proppant relative to the average fluid velocity.

7.3 COMPARISON BETWEEN SINGLE PARTICLE HORIZONTAL FLOW VELOCITY AND AVERAGE FLUID FLOW VELOCITY

7.3.1 Theoretical Basis for Calculating Particle Flow Velocity:

As shown in Figure 7.1, the fluid flow velocity profile in 2D laminar slot flow is parabolic. The fluid flow rate at the centerline is 1.5 times higher than the average fluid flow rate.

For a cell width of 2B, and a fluid viscosity μ, the fluid flow velocity $V_x(y)$ is:

$$V_x(y) = \frac{dP}{dx} * \frac{1}{2\mu} * (B^2 - y^2) \qquad (7.1)$$

The maximum flow velocity (V_m) is:

$$V_m = \frac{1}{2}\frac{B^2}{\mu}\frac{dP}{dx} \qquad (7.2)$$

The average fluid flow velocity V_{avf} is:

$$V_{avf} = \frac{1}{3}\frac{B^2}{\mu}\frac{dP}{dx} \qquad (7.3)$$

7.3.1.1 The Particle Average Velocity without Wall Retardation

Assume the particle concentration is uniform in the cross-section of the cell, the average velocity of the particle (V_{avp}) is:

$$V_{avp} = \frac{2 * \int_{0}^{B-a} Vx(y) * H * dy}{2 * H(B-a)} \qquad (7.4)$$

The ratio of the average particle velocity V_{avp} to average fluid velocity V_{avf} is:

$$\frac{V_{avp}}{V_{avf}} = 1 + \frac{a}{B} - 0.5 * \left(\frac{a}{B}\right)^2 \qquad (7.5)$$

Note that: the particle flow rate is greater than the average fluid flow rate (Figure 7.3). This is primarily because the particle is excluded from the regions near the wall where the fluid velocity is low. The bigger the particle size, the higher its velocity since it is excluded from a larger region of low fluid velocity. This does not account for the hydrodynamic interaction between the particle and the wall.

The above calculations are based on the assumption that the particles are distributed uniformly across the slot cross-section. As discussed earlier, particles tend to migrate towards regions of low shear (towards the center of the slot). However, if the slot walls are porous and fluid leaks off from the wall, particles will be pushed towards the fracture walls, negating the effect of shear-induced migration towards the centerline.

7.3.1.2 Particle Horizontal Flow Velocity with Wall Retardation

Michelle et. al.[9] conducted a numerical simulation of the horizontal flow of particles in a slot, taking into account the hydrodynamic interaction between the particles and the slot walls. Figure 7.4 shows the numerical simulation results of different ratios of particle diameter to slot width. It is evident from this figure that the average particle velocity is greater than the average fluid velocity for most ratios of particle diameter to slot width.

However, as the particle diameter approaches the slot width, the ratio approaches one, the average particle velocity decreases rapidly and approaches zero when the particle diameter becomes equal to the slot width. These results are important in allowing us to calculate the retardation or speed up of the proppant relative to the flowing fluid.

7.3.2 Particle Horizontal Transport Velocities: Experimental Results

7.3.2.1 The Experiments Conducted to Directly Measure the Particle Horizontal Flow Velocity between Two Parallel Walls

A schematic of the experimental setup is shown in Figure 7.5. A video camera was used to record the particle motion as a function of time. These images were analyzed to calculate the horizontal component of the velocity at different locations in the cell. The average fluid velocity, which is different than the particle velocity, was obtained by collecting the fluid effluent from the cell and dividing the flow rate by the cross sectional area of the cell. A description of this procedure is provided in the previous chapter.

Several parameters were varied in the different experiments conducted. The average fluid velocity, particle size as well as fluid viscosity were changed to study the impact of these parameters on the retardation or enhanced transport of the proppant. Based on the experiments, trends were observed for the impact of cell walls, particle size and fluid rheology on the average velocity of the proppant particles.

7.3.2.2 Entrance Effects on Particle Horizontal Flow

There is a sudden contraction of the fluid flow streamlines at the cell entrance causing the flow velocity to be higher than in other regions. The particle flow rate at the entrance is also higher than in other regions. The particle horizontal flow rates were measured along the cell length. The entrance effect which causes the particle to flow faster only occurs within 2.5 cm from the entrance (Figure 7.6). In order to remove the entrance effect, particle velocities were measured more than 2.5 cm away from the entrance. These velocities were compared with the average fluid flow velocity.

7.3.2.3 Measured Particle Horizontal Flow Rates

In dilute particle flow, the particles tend to flow in the centerline of the slot, as shown in Figure 7.7 (a) and (b). The particles tend to flow to the low-shear region causing them to flow to the centerline of the slot.

Table 7.1 shows the measured velocities of two different particles and compares them with the average fluid flow velocity. For the smaller particle, the particle horizontal flow rate is greater than the average fluid flow rate. For the bigger particle, the particle horizontal flow rate is less than the average fluid flow rate. As shown in Figure 7.8 and 7.9, the particle velocity is, in general, higher than the average fluid velocity as the particle diameter is less than 70% of the cell width. However, as the particle diameter increases to more than 70% of the cell width, hydrodynamic retardation becomes dominant, the particle velocity decreases quickly, and ultimately goes to zero as the particle diameter becomes equal to the cell width. These test results obtained with water are consistent with the theoretical calculation results presented by Michelle et. al.[9].

7.3.2.4 Measured Particle Flow Rates in Different Fluids

Besides water, solutions of glycerin and water were used to measure particle flow rates. Comparisons between particle horizontal flow rates and average fluid flow rates of different Newtonian fluids are shown in Figure 7.9. The trends observed with water are consistently observed with the more viscous fluids.

The experimental data can be curve fit into the following empirical relations:

$$\frac{V_p}{V_{af}} = -0.862\left(\frac{a}{B}\right)^2 + 0.0475\left(\frac{a}{B}\right) + 1.2713 \qquad \left(\frac{a}{B} < 0.93\right) \qquad (7.6)$$

$$\frac{V_p}{V_{af}} = -7.71\left(\frac{a}{B}\right) + 7.71 \qquad \left(\frac{a}{B} >= 0.93\right) \qquad (7.7)$$

V_p is particle flow rate, V_{af} is average fluid flow rate, a is particle radius and B is the cell half-width. From this comparison, the following conclusions can be drawn: for Newtonian fluids in laminar flow, the wall retardation effect on particle horizontal transport seems to be the same regardless of fluid viscosity. Only the ratio of particle size to cell width affects the wall retardation effect.

7.3.2.5 Particle Horizontal Transport in Different Guar Gels

Most fracturing fluids are non-Newtonian fluids. Guar gum was used to make guar gels to measure particle horizontal transport in power-law fluids. The guar concentrations used are: 20 lb/1000gal, 30 lb/1000gal, and 40 lb/1000gal. The rheology of these fluids is shown in Figure 3.20(b) in Chapter 3.

Particle horizontal flow velocities in these different fluids were measured and compared to the average fluid velocity, the comparison results are shown in Figure 7.10. The wall retardation effect is identical for different Newtonian fluids, but is different for power-law fluids. The higher the fluid apparent viscosity is, the smaller the wall retardation effect is for a single particle. To the best of our knowledge, this is the first time this effect has been reported for shear thinning fluids in slot flow.

7.4 CONCENTRATION EFFECT ON PARTICLE HORIZONTAL TRANSPORT

In Section 7.3, the horizontal transport rates of single particles or dilute suspensions of particles were compared with the average fluid flow rate. The results show that the particle size and slot width affect the particle horizontal flow rate.

This section investigates the effect of concentration on particle horizontal flow rate in concentrated particle suspensions. In particle settling, high concentrations tend to decrease particle settling velocity if there is no particle clustering. In horizontal flow, particle clustering is insignificant because the fluid flow causes particles to be separated from each other due to shear. Figure 7.11 shows that the particles form clusters in static fluid (40 lb/1000gal guar gel). But in flowing guar gel, particle clustering is not observed (shown in figure 7.12(a) and (b)).

The effect of particle concentration on horizontal transport of proppant in Newtonian fluids was observed using a video camera in a transparent flow cell. Particles were allowed to settle to the bottom of the flow channel. The flow channel was then inverted, so particles began to settle in the inverted channel causing the particle concentration to vary from a dense packing of the solids on the top to individual particles towards the middle of the channel. A horizontal flow of fluid was then initiated, and the velocities of the particles were recorded by the video camera. A blue dye was used as the tracer to measure the average fluid velocity in the channel.

The results clearly indicate that, in the region of higher particle concentration, the particles move at a significantly slower velocity than particles at lower particle concentration. This effect is shown in Figure 7.13, where the particle concentrations vary from zero to 0.6 as recorded. It is evident that, for a close pack, the flow velocity of particles decreases to zero. The single particle velocity was recorded for very dilute suspensions.

These measurements were consistent with the single particle experiments in previous sections. As seen in Figure 7.13, as the ratio of particle diameter to cell width increases from 0.4 to 0.7, the particle velocity decreases substantially due to the hydrodynamic retardation of the wall. These results are also consistent with the results of several other authors in the past (Novotny[2]; Barree[11]).

Particle concentration effects were also measured with high-viscosity fluids (glycerin and guar-gel), as shown in Figure 7.14. The effects observed are consistent with the effects observed with water. This indicates that the particle concentration effect on particle horizontal velocity depends primarily on the volumetric fraction of particles in the suspension and less on the fluid rheology.

It appears that the guar gel is less sensitive to the particle concentration than the glycerin since the particle velocity was reduced more significantly in the glycerin as compared to the guar gel suspensions. However, the effect of fluid rheology appears to be a second order effect and not as significant as the particle concentration.

7.5 EFFECT OF WALL ROUGHNESS ON PARTICLE HORIZONTAL VELOCITY.

7.5.1 Effect of Wall Roughness on Single Particle Horizontal Transport

Two pairs of transparent rough walls were made to measure the effect of wall roughness on particle horizontal transport (described in an earlier chapter). The surfaces of the first pair of rough walls (small roughness) are not as rough as the second pair of walls (large roughness). The particle horizontal flow rates measured in the cell made up of the first pair of rough walls are very close to the particle flow rates measured between smooth parallel walls (shown in Figure 7.15).

The second pair of transparent walls are very rough (shown in Figure 7.16). The cell made up of this pair of rough walls was used to measure the particle horizontal flow rate. Severe fluid fingering is observed due to the wall roughness (shown in Figure 7.17). The particle horizontal flow rate is hindered by the wall roughness and is much lower than the particle flow rate measured between two smooth walls (shown in Figure 7.18).

7.5.2 Effect of Viscous Fingering on Horizontal Transport of Proppants

In the previous Chapter, the effect of wall roughness was discussed (Section 6.6.8). Results showed that fingering induced by the wall roughness can cause the proppants to be diverted into a few channels. This effect can be magnified if significant viscosity contrast exists between the resident fluid and the injected fluid. For the tests shown in Figure 7.19, the water displaced a high-viscosity guar gel. The cell was first filled with water. Then about 0.5 CV (cell volume) of guar gel (40 lb/Mgal) was injected into the cell. Some fingers appeared due to the wall roughness. Finally, about 1 CV (cell volume) of water that carries proppants was injected to displace the guar gel. It is observed that the wall roughness and viscous fingering cause proppants to be placed along several channels in the cell. This might be a very desirable way of placing proppants in fractures since the presence of these channels will act to keep the fracture open while allowing the proppant to be transported far away from the wellbore.

7.6 CONCLUSIONS

Experiments have been performed in a two-dimensional transparent flow cells to study the effect of fracture walls and fluid rheology on the horizontal transport of proppant particles. The following conclusions can be summarized based on the experimental observations:

1. In two-dimensional slot flow with no leak-off, particles tend to flow to regions of low shear causing accumulation of particles near the centerline. This causes the average velocity of particles to be significantly greater than the average fluid velocity.

2. When the particle diameter becomes comparable to the slot width, the hydrodynamic retardation due to the fracture walls causes a significant reduction in the proppant velocity. This effect is clearly observed in our experiments.

3. The effect of proppant retardation can be very significant when the particle diameter is approximately equal to the slot width. However, when the particle diameter is small compared to the slot width, the particle travels faster than the average fluid velocity.

4. Reasonable agreement between the model presented by Michelle et. al. (2003) and our experimental data is observed for water.

5. Both high-viscosity Newtonian fluids and shear-thinning fluids (guar gels) behave similarly with regard to proppant retardation or speed up. The primary variable affecting the proppant retardation appears to be the ratio of particle diameter to cell width. In shear-thinning fluids, larger particle velocities are observed in higher apparent-viscosity fluids.

6. The roughness of the slot walls causes a significant retardation (reduction) in the proppant velocity. When the fracture wall roughness becomes large, fingering of the

injected fluid was observed into the fracture, resulting in severe channeling of flow. This can cause proppants to be diverted to channels with very little flow.

7. When a low-viscosity fluid carrying the proppants displaces a high-viscosity fluid (guar gel), the effects of wall roughness and channeling are magnified. In such situations, severe channeling is observed, resulting in the placement of proppants in a small portion of the fracture area. This might be a desirable thing to accomplish since it may be possible to place the proppants much deeper into the fracture.

7.7 REFERENCES

1. Weng X., Klein, H.H., "Numerical Simulation of Proppant Accumulation at Fracture Wall Due to Fluid Leak-off", SPE 40061, SPE Rocky Mountain Regional/Low Permeability Reservoirs Symposium and Exhibition held in Denver, Colorado, 5-8 April, 1998.
2. Novotny E.J., "Proppant Transport", SPE 6813, 52nd Annual Fall Technical Conference and Exhibition of the Society of Petroleum Engineers of AIME, held in Denver, Colorado, Oct. 9-12, 1977.
3. Faxen H., Arkiv. Mat Astron. Fys. Vol. 17 No. 27, 1923.
4. Wakiya, S., "Effect of A Submerged Object on A Slow Viscous Flow (Report V)-pheroid at An Arbitrary Angle of Attack", Res. Fac. Engng Niigata Univ (Japan) 8, 17, 1959.
5. Peter Ganatos, Robert Pfeffer and Sheldon Weinbaum, "A Strong Interaction Theory for the Creeping Motion of A Sphere Between Plane Parallel Boundaries", Part 2 Parallel motion.1990.
6. Cox, R.G. & Brenner, H., Chem Engng Sci. 23, 147, 1968.
7. Brenner, H., "Advances in Chemical Engineering", Vol.4. Academic, 1966.
8. M.E. O'Neal, "A Slow Motion of Viscous Liquid Caused By A Slowly Moving Solid Sphere", Mathematika 11, 67, 1964.

9. Michelle E.Staben, Alexander Z. Zinchenko, and Robert H. Davis, “Motion of Particle between Two Parallel Plane Walls in Low Reynolds Number Poiseuille Flow”, physics of fluids, Vol 15, No.6, June 2003.
10. B.P. Ho, L.G. Leal, “Inertial Migration of Rigid Spheres in Two Dimensional Unidirectional Flow”, Journal of fluid mechanics, Vol 65, Part 2 Page365-400,1974.
11. Barree,R.D.,Conway, M.W., “Experimental and Numerical Modeling of Convective Proppant Transport”, SPE 28564, prepared for presentation at the SPE 69th Annual Technical Conference and Exhibition held in New Orleans, LA, U.S.A., 25-28 September 1994.
12. A. Jäsberg, A. Koponen, M. Kataja, J. Timonen, “Hydrodynamic Forces Acting on Particles in A Two-Dimensional Flow Near A Solid Wall”, computer physics communication 129, P196-206, 2000.
13. F. Feuillebois, “Multiphase Science Technology 4 (1989) 583”, 1989.
14. I.Miskin, L. Elliott, D.B. Ingham and P. S. Hammond, “Viscous Re-suspension of Particles in An Inclined Rectangular Fracture”, Int. J. Multiphase Flow, Vol22, No.2, P403-415, 1996.
15. Nolte, K.G., “Fluid Flow Consideration in Hydraulic Fracturing,” SPE 18537 presented at the SPE Eastern Regional Meeting, Charleston, West Virginia, 1-4 November, 1988.
16. Tehrani, M.A., Hammond, P.S., and Unwin A.T., “Experimental Study of Particle Migration in Suspensions Undergoing Poiseuille Flow,” Proceedings 66th Annual Meeting Society of Rheology, Philadelphia, Pennsylvania, Oct. 1994.
17. C. W. Li, “3D Numerical Simulation of Deposition Patterns Due To Sand Disposal In Flowing Water”. Journal of Hydraulic Engineering, 2001.
18. Gadala-Maria, F.A., “Rheology of Concentrated Suspensions”, Ph.D thesis, Stanford University, CA, 1979.
19. Leighton, D., “Shear-Induced Migration of Particulates in Concentrated Suspension”, Ph.D thesis, Stanford University, CA, 1985.
20. Leighton, D., Acrivos, A., “Viscous Re-suspension”, Chem. Engng Sci. 41, 1377-1388, 1986.

21. Mobbs A.T. and Hommond P.S., "Computer Simulations of Proppant Transport in a Hydraulic Fracture", SPE 69212, prepared for presentation at the 1995 SPE Western Regional Meeting held in Bakersfield, California, 8-10 March, 2000.
22. Babcock R.E., Perry R.H., "Non-Linear Dynamic Programming of Hydraulic Fracturing Models", SPE 2159, 43rd Annual Fall Meeting of the Society of Petroleum Engineers of AIME, held in Houston, Tex., Sept. 29-Oct. 2, 1968.
23. L.R. Kern, T.K.Perkins, R. E.Wyant, "The Mechanics of Sand Movement in Fracturing", SPE 2037, prepared for presentation at the 33rd Annual Fall Meeting of SPE held in Houston, Tex, Oct. 5-8, 1958.
24. Schols, R.S., Visser,W. "Proppant Bank Buildup in a Vertical Fracture Without Fluid Loss", SPE 4834, SPE-European Spring Meeting 1974 of the Society of Petroleum Engineers of AIME, held in Amsterdam, the Netherlands, May 29-30, 1974.

Cell Width (Wc)=1.5 mm

Particle Diameter (mm)	Average Fluid Velocity (cm/s)	Particle Velocity (cm/s)
0.96	24.8	26.1
1.19	24.8	21.6

Table 7.1 Measured particle and fluid flow rates

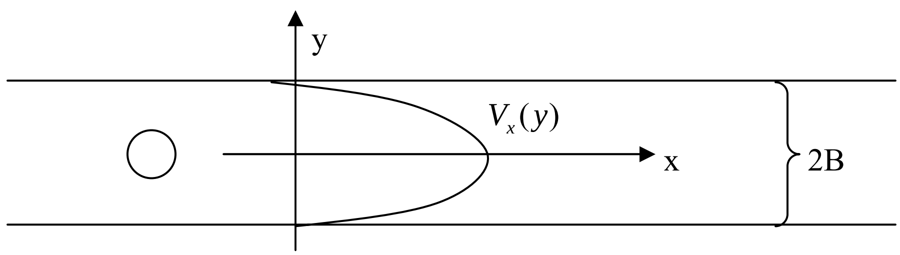

Figure 7.1 Fluid flow velocity profile in a 2-D flow

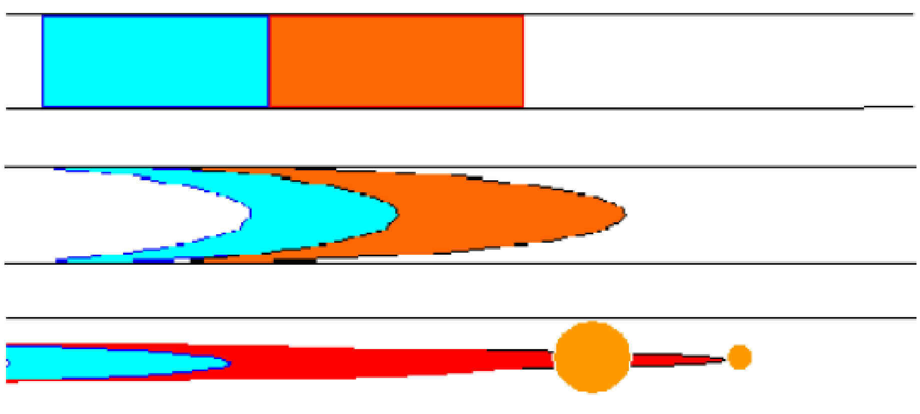

Figure 7.2 Flow pattern in a 2-D slot flow

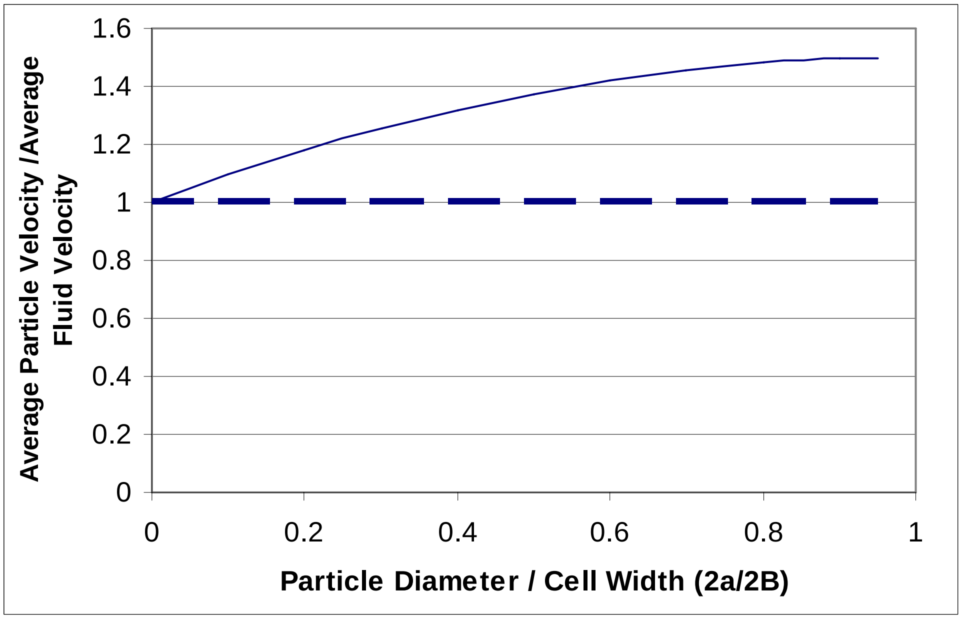

Figure 7.3 Comparison between particle and fluid flow rate

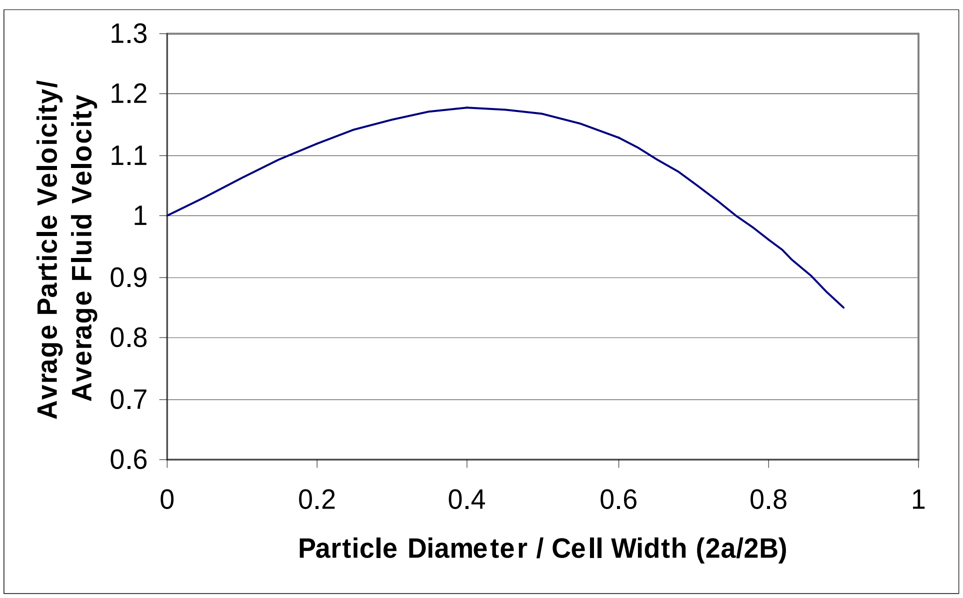

Figure 7.4 Comparison between particle and fluid velocity simulation result (Michelle et. Al. in 2003)

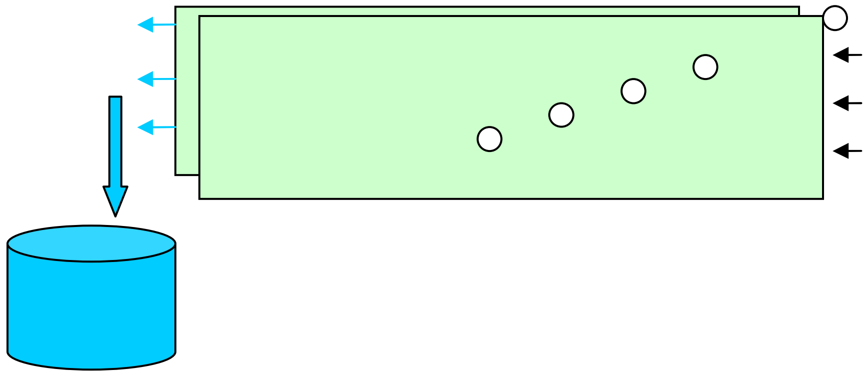

Figure 7.5 Schematic of measuring particle and fluid horizontal flow rate

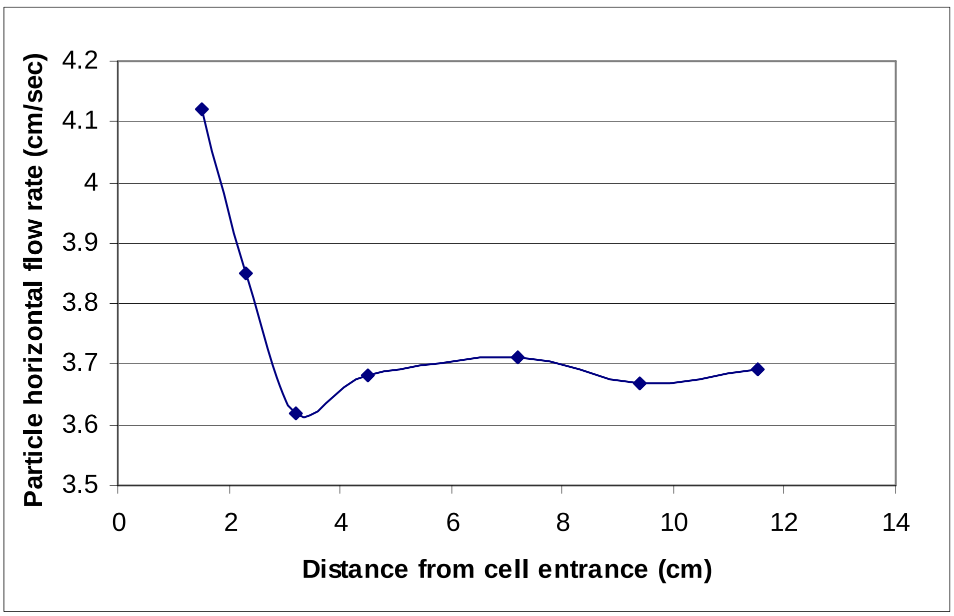

Figure 7.6 Measured particle flow rates near the cell entrance

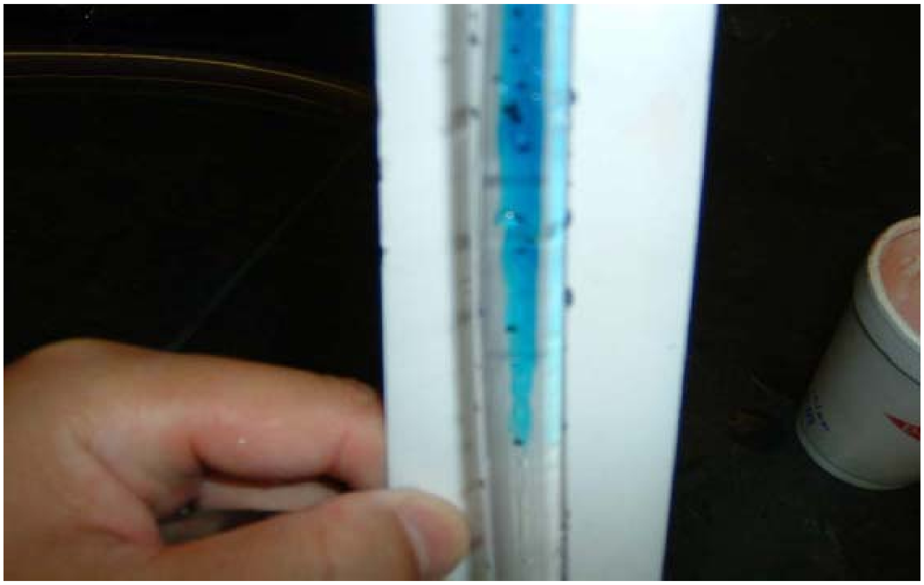

Figure 7.7(a) Flow pattern of glycerin with particles

Figure 7.7(b) Particles flow to the centerline of the tube

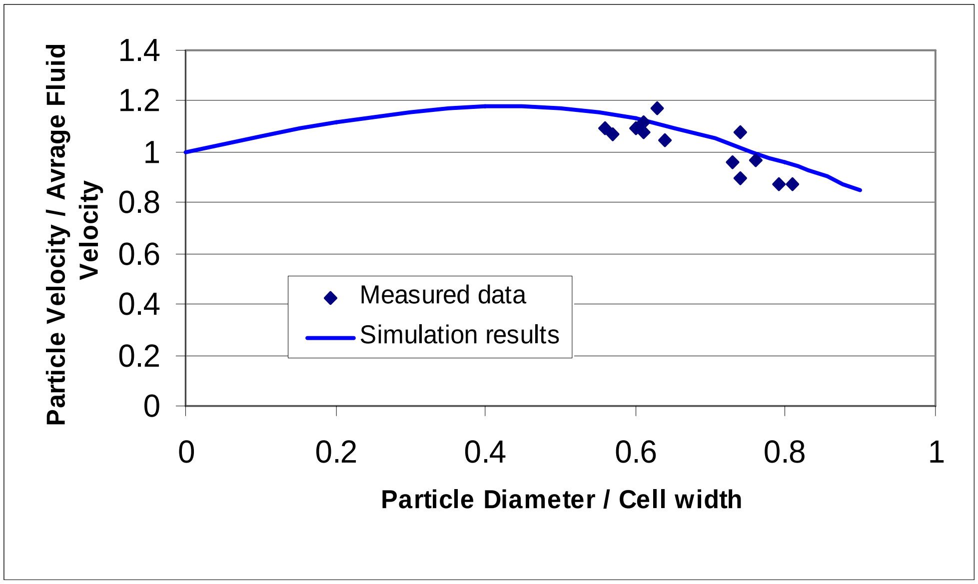

Figure 7.8 Effect of particle size on particle horizontal transport in water (Average water velocity is 25 cm/sec)

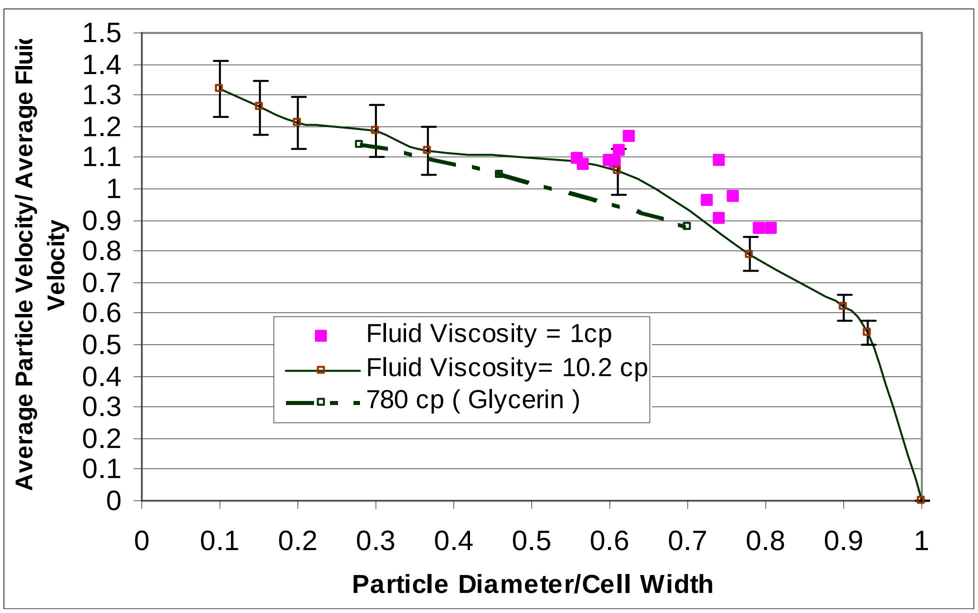

Figure 7.9 Comparison between particle flow rate and average fluid flow rate in different fluids

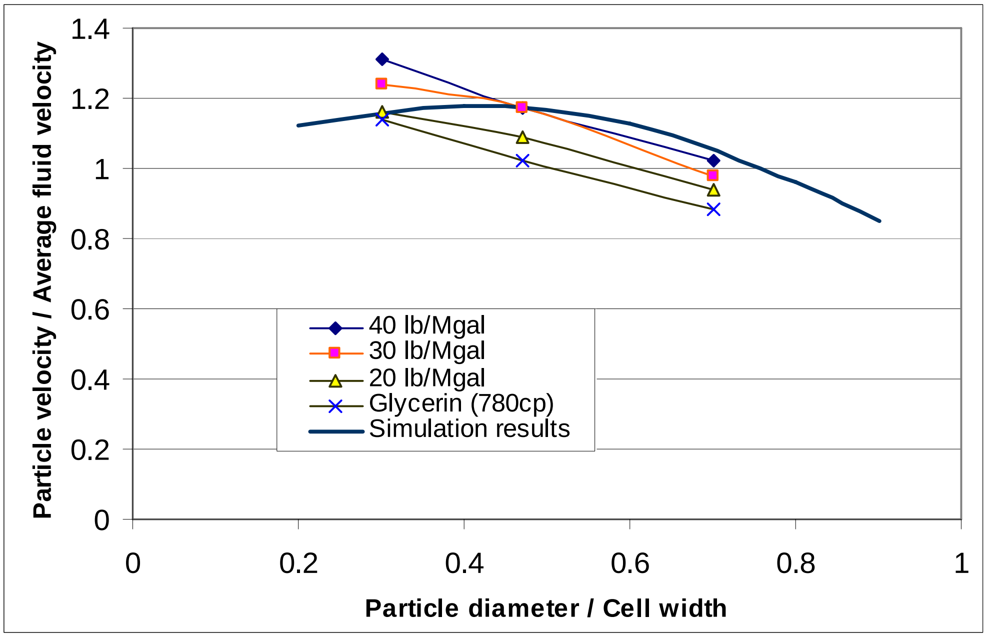

Figure 7.10 Wall effect on particle horizontal transport in guar gels and in glycerin (Simulation was conducted by Michelle in 2003)

Figure 7.11 Settling of concentrated particles in static gel (40 lb/Mgal guar gel)

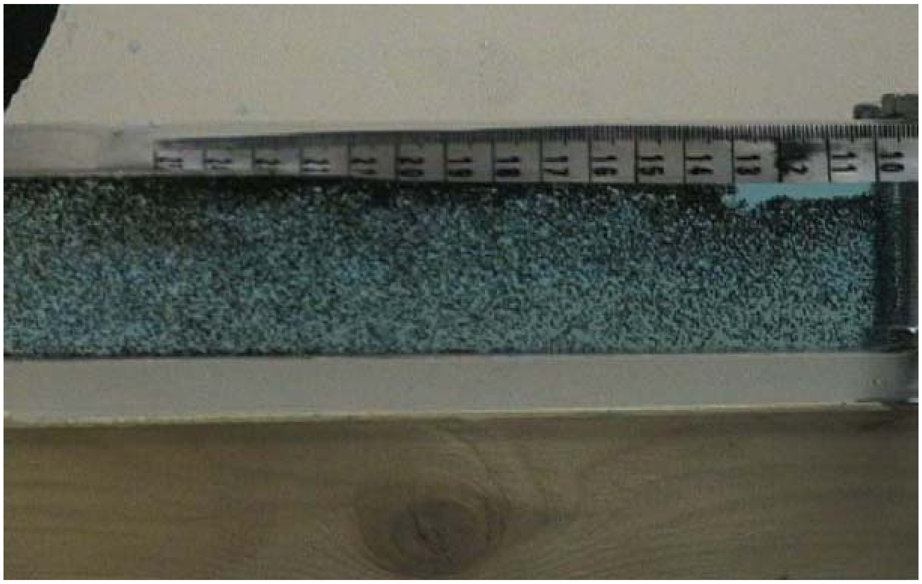

Figure 7.12(a) Particle horizontal transport in a concentrated suspension

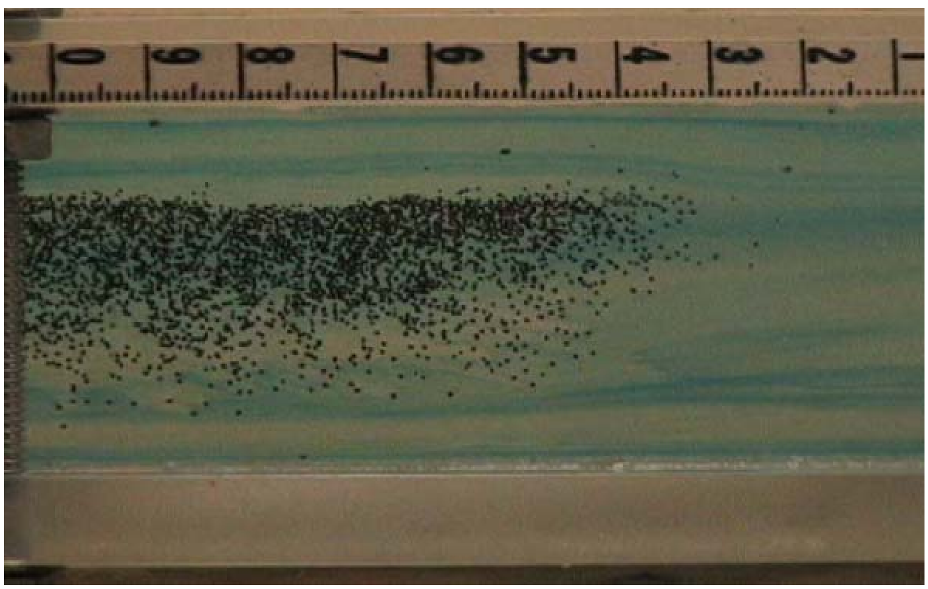

Figure 7.12(b) Concentrated particles transport in a cell

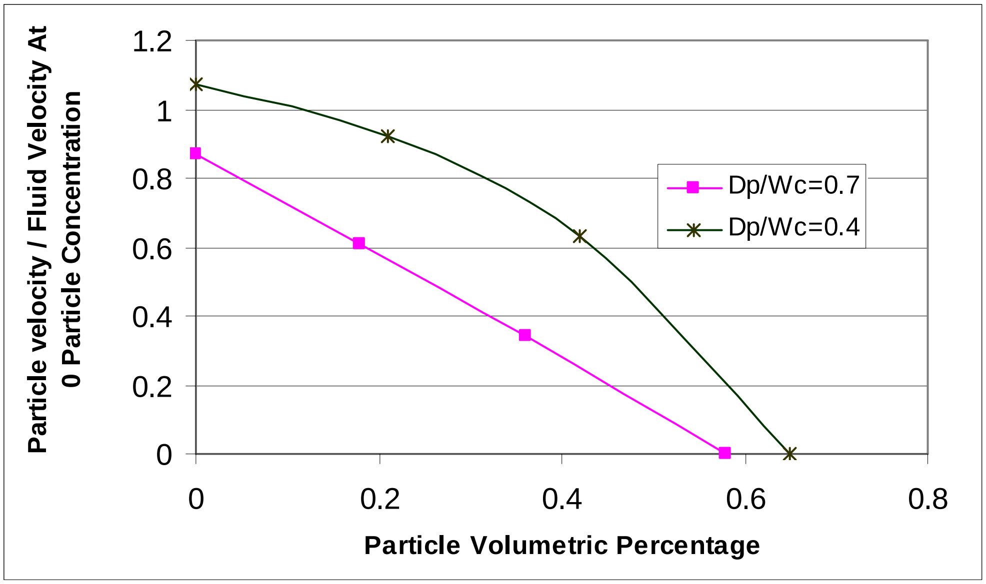

Figure 7.13 Concentration effect on particle horizontal flow rate

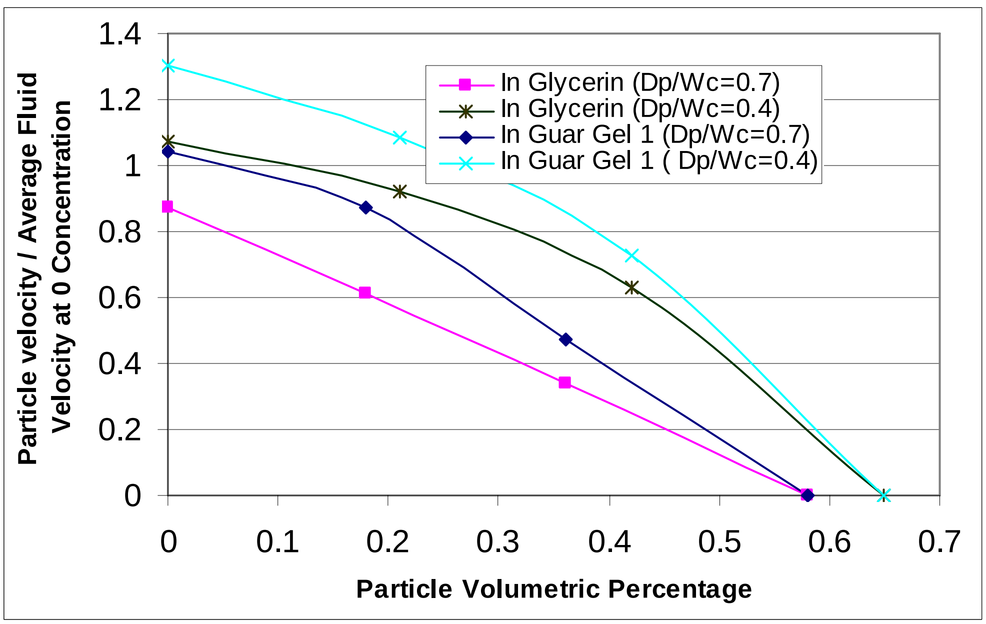

Figure 7.14 Concentration effect on particle horizontal transport in glycerin and guar gel1(40 lb/Mgal)

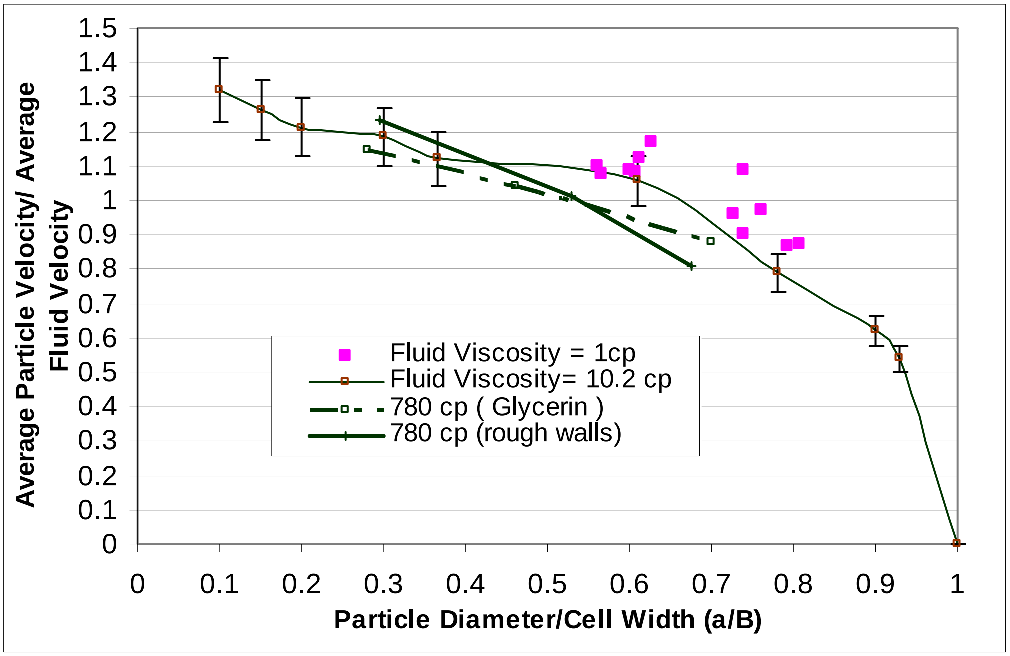

Figure 7.15 Wall effect on particle horizontal flow in different cells

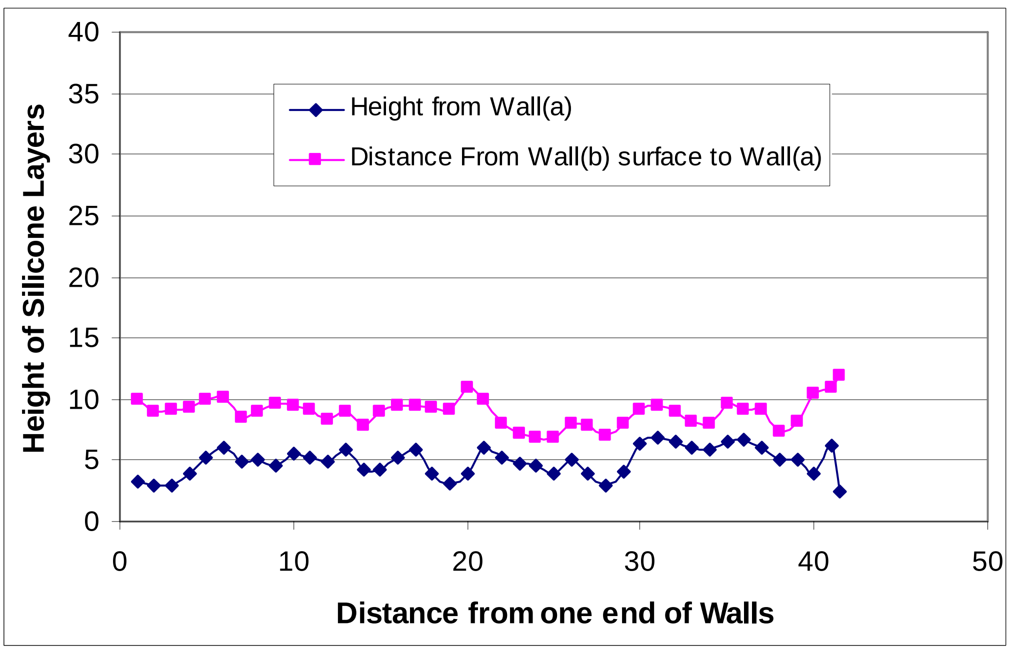

Figure 7.16 Roughness of the wall (2) surfaces

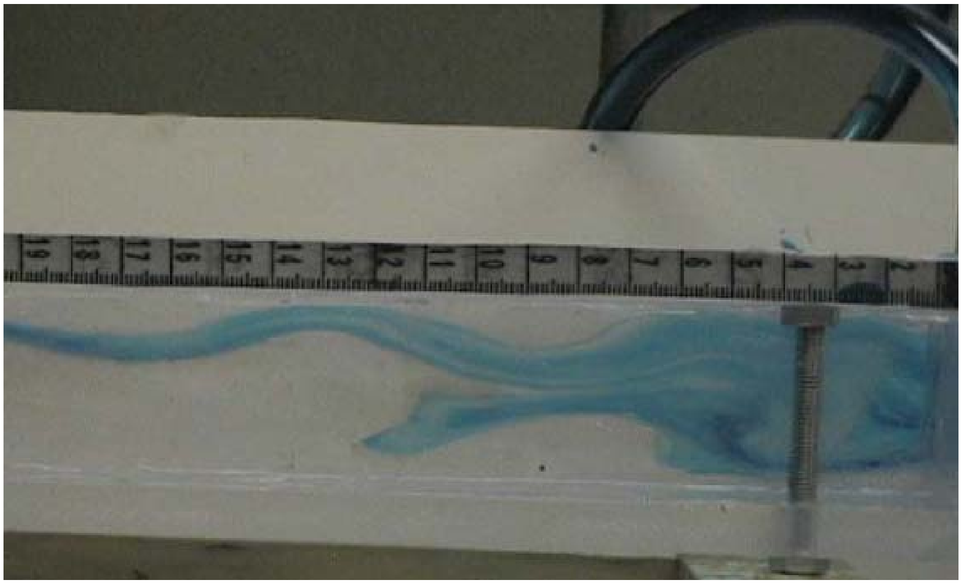

Figure 7.17 Effect of roughness on glycerin flow pattern in a cell

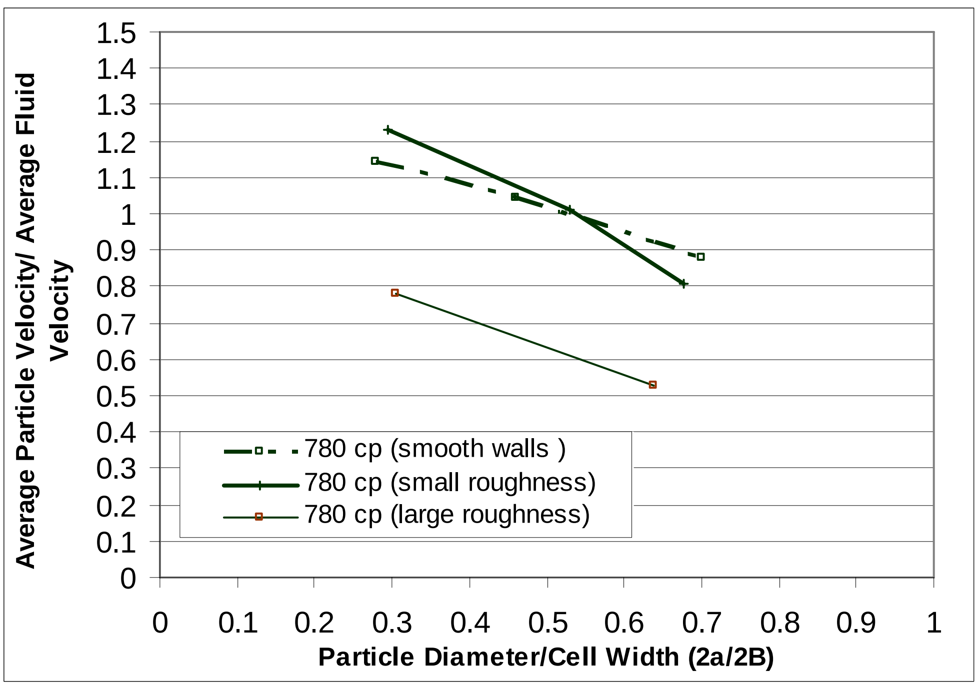

Figure 7.18 Effect of wall roughness on proppant horizontal transport in glycerin (780 cp)

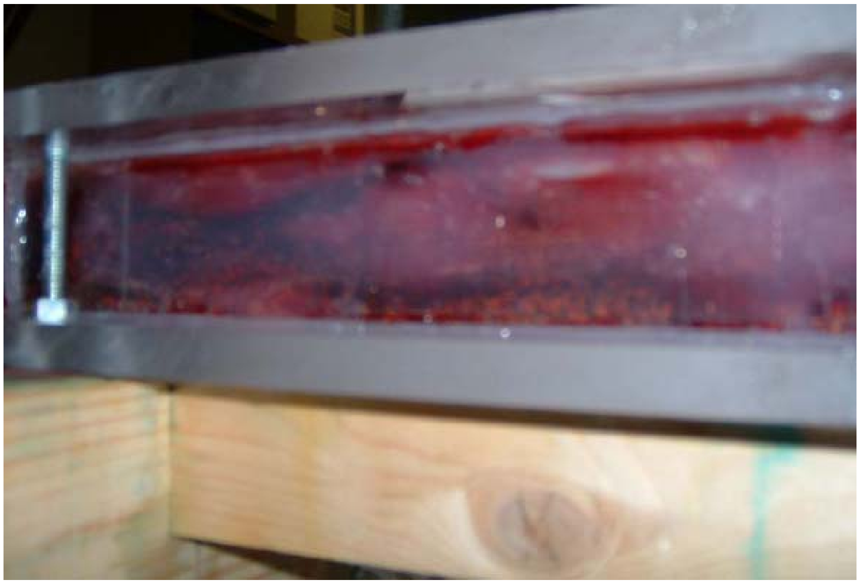

Figure 7.19 Roughness effect on the transport of concentrated particles

CHAPTER 8.
A LABORATORY STUDY OF THE CLEAN-UP OF WATER BLOCKS IN LOW PERMEABILITY FORMATIONS

8.1 ABSTRACT

Water-blocked low permeability gas formations with drawdown pressures comparable to capillary entry pressures can take a very long time to clean up. The clean up of water blocks in gas wells occurs in two regimes: displacement of the fluids from the formation followed by vaporization by the flowing gas, which becomes under-saturated as the pressure decreases.

This work aims to study the effect of rock permeability, wettability, temperature, drawdown and surfactants on the clean up of cores containing brine. The effectiveness of using solvents for cleanup under different conditions has been evaluated by comparing gas relative permeabilities with and without methanol.

Gas displacement experiments were conducted on cores fully saturated with brine. The gas relative permeability increases with pore volumes of gas injected for long periods of time (up to 100,000 PV) at ambient temperature. The addition of methanol, increasing temperature and increasing core permeability resulted in faster cleanup after about 50 to 100 PV of gas flow. The change of wettability of the rock from water-wet to oil-wet also resulted in faster recoveries in gas relative permeability.

Our observations show that the clean up of water-blocks can be improved by: 1. Influencing the displacement of brine, i.e. by changing the wettability and, 2. By increasing the rate of vaporization by introducing volatile solvents such as methanol. It is found that changing wettability also has an impact on the rate of vaporization of the brine and methanol. The study quantifies the effects of factors such as rock permeability, wettability, surface tension, and temperature on gas relative permeability. The results of this study will help in selecting strategies for clean-up of water blocks created due to various operations such as drilling and fracturing, and making recommendations for the use of surfactants or solvents for well treatments for removing water blocks.

8.2 INTRODUCTION:

Invasion of aqueous drilling, completion or fracturing fluids during well completion, workover or stimulation operations can reduce the relative permeability to gas and thereby cause a water-block. Cimolai *et al.*[1] report that gas reservoirs, which were under-saturated, readily accommodated the invaded aqueous fluids creating a water block. The gas phase relative permeability depends on the water saturation in the porous medium and the fractional flow characteristic of gas in the presence of water. The water-block can be removed by reducing the saturation of the invaded fluid in the well bore region and/or by affecting the fractional flow characteristics of the gas.

Studies show that the clean up of water-blocks in gas wells is faster if the absolute permeability of the formation is high (Tannich[2]). In the case of low permeability formations the capillary pressure tends to be high because of the smaller pore sizes. However, Holditch[3] showed that when the drawdown pressures are very high the capillary pressure end effects do not affect the gas flow rates even in low permeability formations. Studies by Parekh[4] show the effect of relative permeability curve exponents on the clean up of water block is significant with faster clean up for high values of Corey exponents. Abrams and Vinegar[5] show that the effect of additives such as alcohol and/or surfactants does not create a significant improvement in the final gas flow when the drawdown pressures are significantly greater than the capillary entry pressures.

Earlier studies by McLeod *et al.*[6] conclude that alcohols increase the water recovery and clean up rate in gas wells when used as part of the stimulation fluid. The authors attributed the increase to better displacement of the fluids from the formation due to a decrease in interfacial tension and also the volatility of alcohols.

A recent study by Kamath *et al*.[7] shows that the clean up of water blocks in gas wells occurs in two regimes: displacement of the fluids from the formation followed by vaporization by the flowing gas which becomes under-saturated as the pressure decreases. The first phase of liquid removal is an immiscible displacement of water by gas, which solely depends on the fractional flow characteristics. The second phase is a continual evaporation of the invaded water by the expanding gas flow. The equation for gas saturation change given in the paper by Kamath *et al*[7] shows that even if the entering gas has a relative humidity of 100 percent the water saturation in the core decreases as more gas is injected. This is because of evaporation from the core due to the pressure drop across the core.

The improvement in gas return permeabilities with the addition of alcohol can occur due to two possible reasons: 1. Reduction in the interfacial tension between gas and the liquid phase, 2. Higher volatility of the alcohol. The data presented in this paper clearly indicates that the volatility of methanol is primarily responsible for its effectiveness. The use of alcohols, however, has found little favor in many offshore and to some extent onshore operations because of environmental considerations. There has been limited work done on the application of alcohols in the field for clean up of near well bore region[6].

Based on results presented by Kamath *et al*[7] and on results presented in this paper, the evaporative regime lasts for thousands of pore volumes of gas flow resulting in a slow clean up and improvement in gas relative permeability. Since this evaporative regime is poorly understood one of our objectives in this study was to study the factors that influence the vaporization of solvents and water during gas flow back. Factors such rock permeability, rock wettability, temperature and drawdown have been investigated.

8.3 EXPERIMENTAL METHODS:

Gas displacement experiments were conducted to displace brine from a fully brine saturated rock sample. A schematic of the experimental set-up is shown in Figure 1. The displacement was conducted at a constant pressure drop across the core and at constant temperature. For experiments that were conducted at elevated temperatures, the gas was flowed at a constant backpressure of 4.4 atm at the outlet end to prevent any evaporation before the start of the experiment. The brine permeability of the core was measured before the start of every experiment. The effectiveness of clean up of the core sample was determined by the rate of increase of gas relative permeability with time (pore volumes injected). Gas flow rates at the outlet end of the core sample were monitored with time and the relative permeability of the gas at the outlet end was calculated by simply dividing the measured flow rate with the dry core gas flow rate at the same pressure drop. The cumulative fluid expelled from the core (with time) was measured to determine the end of the displacement phase. Two methods were used to estimate the water content of the effluent gas: 1. the outlet gas humidity was measured to estimate the amount of water vaporized, 2.

the outlet vapors were condensed to measure the amount of vapor (both water and solvent) evaporated from the core. Appendix A provides details of how these measurements were made.

Experiments were conducted to study the effect of various factors such as rock permeability, wettability, temperature, drawdown and solvents on the evaporative phase of clean up. The high temperature experiments were conducted at 70 ^{o}C.

8.4 FLUIDS USED:

A 3 % by weight solution of sodium chloride solution was first evacuated to eliminate any dissolved gases. The evacuated brine was stored in an airtight container and later used to saturate the evacuated cores.

Industrial grade dry nitrogen, which is humidified by bubbling it through a column of distilled water, is used to displace the brine in the core. Methanol of purity 99.8% is used as the solvent in experiments performed for evaluating the effect of additives.

8.5 CORE PREPARATION:

Cylindrical cores 2.5 cm in diameter and 7.6 cm long are cut from homogeneous slabs of Berea sandstone and Texas Cream limestone using water as cutting fluid. Special care is taken to ensure that the limestone core is free from any visible fractures and vugs. The core is dried in an air-oven at 100 ^{o}C for at least 24 hours and is weighed before being placed inside the Hassler apparatus.

Berea sandstone and Texas Cream limestone in their original state are water-wet. To artificially render the core oil-wet the core was treated with a wettability-altering agent, a 1% v/v solution of OTS (octadecyltrichlorosilane) in chloroform. A detailed procedure for wettability alteration is described in Appendix B.

8.6 EXPERIMENTAL PROCEDURE:

The core is placed into the sleeve, which separates the core from the confining fluid of the core holder. A confining pressure of 55 atm is applied for the sandstone cores. In the case of limestone cores the confining pressure is maintained at 85 atm using high-pressure oil because of the greater pressure drops expected across the cores during the gas displacement.

The gas flow rate at a predetermined pressure drop is measured. The core is then evacuated for about 2 hours and checked for vacuum stability by shutting the vacuum pump and observing for any vacuum leaks. The core is then saturated with the prepared brine through a burette. The burette scale reading before and after the saturation is recorded to determine the pore volume and hence the porosity. The brine permeability of the core is estimated by measuring the pressure drop for a constant flow rate of brine and substituting in Darcy's Law.

When a solvent was used, the brine in the core was displaced with several pore volumes (about 50) of the desired solution (with additive) before the gas displacement was started. A schematic of the experimental setup is shown in Figure 1.

8.7 RESULTS AND DISCUSSION:

The relative permeability of gas, liquid expelled and liquid condensed are primary data collected from experiments and are represented here as varying with the pore volumes of gas injected. Figure 2 shows the relative permeability of gas (nitrogen) changing with the number of pore volumes injected for displacement of different liquids: brine, methanol-brine mixture (50 % each by volume) and only methanol. The plot shows that the relative permeability continues to increase even after 10,000 PV of humid gas was injected into the core. The clean up is faster with the methanol-brine mixture and pure methanol. An interesting thing to note is that the relative permeability to gas for either brine or methanol is almost identical for the first fifty pore volumes. This indicates that in the displacement regime (<50 PV) the methanol and brine behave in an almost identical manner. However, in the evaporative regime (>100PV) the increased volatility of methanol results in significantly better clean up with methanol when compared to brine.

Figure 3 shows the gas relative permeability plotted versus gas saturation in the core. It is apparent that methanol and water show the same gas relative permeability curves over a wide range of saturations. This is an additional indicator that the fractional flow curve for brine and methanol are almost identical. Any differences observed in the gas relative permeability recovery could, therefore, be primarily attributed to the increased volatility of methanol. In all cases the gas relative permeability approaches one when a large number of pore volumes of gas are injected.

Figure 4 shows the effect of methanol on gas relative permeability curves in a Texas Cream limestone. This low permeability limestone shows the same trend as shown in Figure 2 with Berea sandstone. The improvement in gas relative permeability is faster with methanol compared to brine. However, the relative permeabilities achieved after several thousand pore volumes are still relatively low. The difference between the two clearly increases over the course of evaporative regime. It is evident that low permeability rocks do not clean up as readily as higher permeability rocks. This difference is highlighted in Figures 5 and 6. The clean up achieved with limestone is significantly less than that achieved with Berea sandstone. This is consistent with the fact that it is more difficult to remove the wetting phase from low permeability formations due to capillary pressure effects. A capillary number can be defined for gas flooding experiments as the ratio of viscous to capillary forces. The expression for capillary number is given by[8],

$$N_{vc} = \frac{k\nabla P}{\sigma}$$

where σ is the interfacial tension between gas and water.

The capillary number computed using the above relation for brine displacement in Berea sandstone is 2.48E-06 whereas the capillary number computed similarly for Texas Cream limestone is 8.56E-08. These capillary numbers are too small to have an impact on mobilizing the residual liquid in the core.

Figures 7 and 8 show the effect of increasing temperature on the clean up of Berea sandstone and Texas Cream limestone cores. The higher temperature (T = 70 ^{o}C) experiments were done at a backpressure of 4.4 atm to prevent premature evaporation of the saturating liquid. The plots show the change in the gas relative permeability with the number of pore volumes injected. The clean up is marginally faster at 70 ^{o}C for both Berea and Texas Cream at large pore volumes injected. The difference between the 70 ^{o}C case and the ambient case is not large because the 70 ^{o}C case was done at a 4.4 atm backpressure, which reduces the evaporation rates.

Figure 9 shows the effect of increasing the temperature on gas relative permeability with solvent (methanol) as the displaced fluid in a Texas Cream Limestone core. The clean up in the higher temperature case is much faster at large pore volumes injected. The higher temperature increases the rate of evaporation of methanol and hence clean up is faster.

Figures 10 and 11 show the effect of wettability on the clean up of Berea sandstone and Texas Cream limestone. The plots show change in gas relative permeability with number of pore volumes of nitrogen injected for oil-wet and water-wet Berea sandstone and Texas Cream limestone. The clean up is about the same for oil-wet and water-wet Berea cores whereas the clean up is faster for the oil-wet Texas Cream limestone.

The reasons for the difference between water wet and oil wet samples of Berea and Texas Cream are not immediately evident. These differences must arise as a consequence of differences in the distribution of residual brine phase in the pore space. Our conjecture is that, in the low permeability of the limestone sample, our changing the wettability has a more significant impact on the ability of the gas to displace the brine from the smaller pores. In the limestone sample that has been rendered oil-wet the flowing gas phase clearly has better access to the residual brine than in the water-wet case where the brine is placed in the small pores.

Figures 12 and 13 show the effect of changing wettability from water-wet to oil-wet when methanol is the liquid being displaced from the cores. For the oil-wet case Texas Cream limestone shows significantly better clean up during the evaporative regime. Very little influence is seen in the case of the Berea sandstone. Clearly the flowing gas phase has better access to the residual methanol phase in the oil-wet limestone sample than the water-wet case. Such differences do not appear to be present for the Berea sandstone.

Our experiments indicate that the low permeability limestone sample is much more susceptible to changes in wettability both with brine and with methanol than the higher permeability sandstone sample. We do not have a good explanation for these observations at this time and this has to be investigated. Additional experiments needs to be done on different core types to resolve this issue.

Figure 14 shows the volume of liquid (brine) removed from Texas Cream limestone core by displacement and evaporation (measurement technique for volume of displaced and evaporated liquid is discussed in Appendix A). Figure 15 shows the rate of liquid removal (brine) from the limestone core by displacement and evaporation. At about 100 PV the rate of displacement becomes smaller than the rate of evaporation. This marks the onset of evaporation regime.

Figure 16 shows the volume of liquid removed from Berea sandstone core by displacement and evaporation. Figure 17 shows the rate of liquid removal (methanol) from the sandstone core by displacement and evaporation. At about 60 PV the rate of displacement becomes smaller than the rate of evaporation. This crossover position occurs earlier in the case of Berea than in the case of the Texas Cream limestone. This is because in the low permeability rocks the displacement is much slower and the evaporation takes much longer time.

Increasing the drawdown or the pressure drop in the core also has significant effect on the clean up. Figures 18 and 19 show the effect of increasing the pressure drop on the clean up of Berea sandstone core and Texas Cream limestone. The clean up of the Berea sandstone does not show any change with doubled pressure drop but the limestone shows a significantly better clean-up with respect to increased pressure drop. We suspect that this could be an artifact of capillary end effect in the limestone (Berea cores are less subject to capillary end effect because of their large pore size).

8.8 CONCLUSIONS:

This experimental study quantifies the effects of factors such as rock permeability, wettability, and temperature on clean up of water blocks i.e. gas relative permeability. The following conclusions can be reached based on our observations.

1) The gas relative permeability increases with pore volumes of gas injected for long periods of time (up to 50,000 PV).
2) The addition of solvent (methanol) resulted in faster clean up of water blocks in Berea sandstone cores. A similar effect was also observed for Texas cream limestone.
3) When methanol is used, the clean up is improved primarily due to its volatility and not changes in capillary number (reduction in interfacial tension).
4) The volume of liquid removed by displacement becomes less significant than the amount of liquid removed by evaporation after about 100PV of gas injected.
5) An increase in core permeability from 0.7 mD to 327 mD (from limestone to Berea) resulted in faster cleanup whether brine or methanol was used.
6) An increase in temperature (with all other parameters held constant) resulted in faster clean up for Berea sandstone as well as Texas cream limestone. The

increase in temperature when methanol is used produced significantly faster clean up in the case of Texas Cream limestone.

7) The change of wettability of the rock from water-wet to oil-wet also resulted in slightly faster clean up of Texas Cream limestone but not for the Berea sandstone. Changing wettability of Texas Cream limestone from water-wet to oil-wet gave significantly better clean up when methanol is used as the displaced liquid.

8) An increase in drawdown (doubling the pressure drop) resulted in slightly faster clean up in the case of Berea. A similar change in the case of limestone produced a significantly faster clean up, perhaps due to capillary end effects.

Nomenclature

ρ_w	*density of water;* g/cm^3.
y_A	*mole fraction of water in gas.*
$y_{A1,}, y_{A,2}$	*mole fractions of water in gas at positions 1 and 2 respectively.*
$Q_{g,1,}, Q_{g,2}$	*volumetric flow rate of gas at positions 1 and 2 respectively;* cm^3/s.
M_w	*molecular weight of water;* g.
k	*permeability of core;* mD(9.87E-10 cm^2).
P_1	*constant inlet pressure of gas;* atm (X 14.7 psi).
P_2	*constant outlet pressure of gas;* atm(X 14.7 psi).
T	*temperature;* ^{o}C.
T_{std}	*standard temperature;* 25 ^{o}C.
P_{std}	*standard pressure;* 1.0 atm (14.7 psi).

8.9 REFERENCES:

1. Cimolai et al.: “Mitigating Horizontal Well Formation Damage in a Low-Permeability Conglomerate Gas Reservoir,” paper SPE 26166 presented at the SPE Gas Technology Symposium held in Calgary, Alberta Canada (June 1993).
2. Tannich, J. D.: “Liquid Removal From Hydraulically Fractured Gas Wells,” JPT (November 1975) 1309.

3. Holditch, S. A.: "Factors Affecting Water Blocking and Gas Flow From Hydraulically Fractured Gas Wells," JPT (December 1979) 1515.
4. Parekh, Bimal: " Studies on Clean up of Water Blocks-A Numerical Simulation Approach", MS Thesis, The University of Texas, Austin, 2003.
5. Abrams, A. and Vinegar, H. J.: "Impairment Mechanisms in Vicksburg Tight Gas Sands", paper SPE/DOE 13883 presented at the SPE/DOE 1985 Low Permeability Gas Reservoirs held in Denver, Colorado (May 1985).
6. McLeod, H. O. and Coulter, A. W.: "The Use of Alcohol in Gas Well Stimulation," paper SPE-AIME 1663 presented at the Eastern Regional Meeting of the Society of Petroleum Engineers of AIME, held in Columbus Ohio (November 1966).
7. Kamath, J. and Laroche, C.: "Laboratory-Based Evaluation of Gas Well Deliverability Loss Caused by Water Blocking," Society of Petroleum Engineers Journal, (March 2003) 71-80.
8. Lake, L. W.: "Enhanced Oil Recovery", Prentice Hall, Englewood Cliffs, New Jersey, 1989.

8.1 APPENDIX A

Evaporation from limestone core

Method 1

The volume of water evaporated from a water wet limestone core of length 15.3 cm, porosity 0.21 and a permeability of 7.2 mD was estimated from experimental data. The following procedure was used in the calculations to obtain the volume of water evaporated from the core.

For a gas containing both water and nitrogen (inert) in the core,

$$N_T = N_A + N_{N_2} . \qquad \text{(A-1)}$$

N_T, N_A, N_{N2} are the total moles, moles of water, and moles of nitrogen respectively in the gas mixture.

We know that

$$N_A = y_A N_T = H y_{As} N_T .$$

The volume of water in 1 ml of the gas is therefore,

$$V_w = \frac{H y_s N_T M_w}{\rho_w} \text{ where } y_s = \frac{P_s \gamma_A x_A}{\phi_A P} . \qquad \text{(A-2)}$$

For an ideal gas and an ideal solution (liquid phase) $\phi_A = 1$ and $\gamma_A = 1$.

Hence equation A-2 becomes,

$$V_w = \frac{H P_s x_A N_T M_w}{P \rho_w} \qquad \text{(A-3)}$$

Also, we know that for an ideal gas one mole occupies 22400ml. Therefore, $N_{T,std}$=4.5E-05 moles of gas/ml.

Saturation pressure, Ps, of water at standard conditions is 0.3 atm and does not vary much with pressure. x_A the mol fraction of water in brine is 0.98.

For conditions other than standard,

$$N_T = \frac{P}{P_{std}} \frac{T_{std}}{T} \frac{N_{T,std}}{z} \qquad \text{(A-4)}$$

We apply the above to our experiment.

Knowing the gas flow rate at the inlet end one can calculate the volume (or mass) of water entering the core from saturator.

$$q_{w,inlet} = V_{w,1} Q_{g,1} = \frac{H_1 P_s x_A N_{T,1} M_w Q_{g,1}}{P_1 \rho_w} \qquad \text{(A-5)}$$

where,

$$Q_{g,1} = \frac{P_2}{P_1} \frac{T_1}{T_2} z_1 Q_{g,2}.$$

We know P_1=4.5 atm, T_1=25 °C and H_1=1.

Knowing the gas flow rate at the outlet end we can calculate the volume of water leaving the core.

$$q_{w,outlet} = V_{w,2} Q_{g,2} = \frac{H_2 P_s x_A N_{T,2} M_w Q_{g,2}}{P_2 \rho_w} \qquad \text{(A-6)}$$

$P=P_{std}$=1 atm, $T=T_{std}$=25 °C. The humidity (H_2) values, which change with time, are recorded in the experiment using a digital hygrometer.

Subtracting the equations A-6 and A-5, we get,

$$PV_{evaporated} = \frac{q_{w,evaporated}}{PV_{core}} = \frac{q_{w,outlet} - q_{w,inlet}}{PV_{core}} \qquad \text{(A-7)}$$

Thus one can plot the pore volumes of evaporated water versus the pore volumes of gas flowed through the core at standard conditions.

Method 2

The second method of determining the amount of evaporation is to directly measure the mass of water that leaves the core by condensing it in a chiller that is placed at the outlet of the core holder (see Figure 1). The condensed water will then contain water that came in from the saturator and also due to evaporation from the core. In order to find the volume of water due to evaporation from the core we calculate the volume of condensate from the saturator using a procedure similar to Method 1. The amount of water from the saturator is given by equation A-5. The amount of water leaving the core is directly measured. This method is less accurate and is assumes complete condensation of fluids, which is difficult to achieve, given the wide range of flow rates encountered in the experiments. However for experiments containing fluids like methanol this method may be most suitable as hygrometers measure only humidity.

APPENDIX B

Preparation of Cores

The method to change the cores from water-wet to oil-wet is described below.

Preparation of Oil-wet samples:

The cores required to be made oil wet are cleaned, dried in an oven for 24 hours and placed in the Hassler apparatus (with a Viton sleeve to prevent damage from chloroform to be used later). The cores are evacuated for 2 hours and saturated with decane by directly flowing it into the evacuated cores. The decane imbibed is displaced with 50 pore volumes of a 1% by wt solution of OTS (octadecyltrichlorosilane) in chloroform. The cores are allowed to sit in with the solution for about 15 minutes and then flushed with 50 pore volumes of chloroform. The cores are removed from the core holders and placed in an oven to heat-dry at 100 ^{o}C.

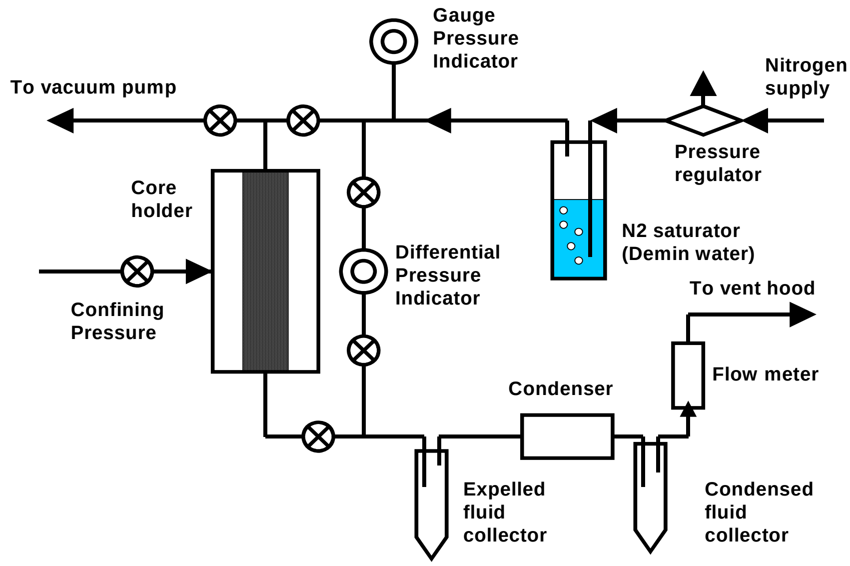

Figure 1: Schematic of experimental setup.

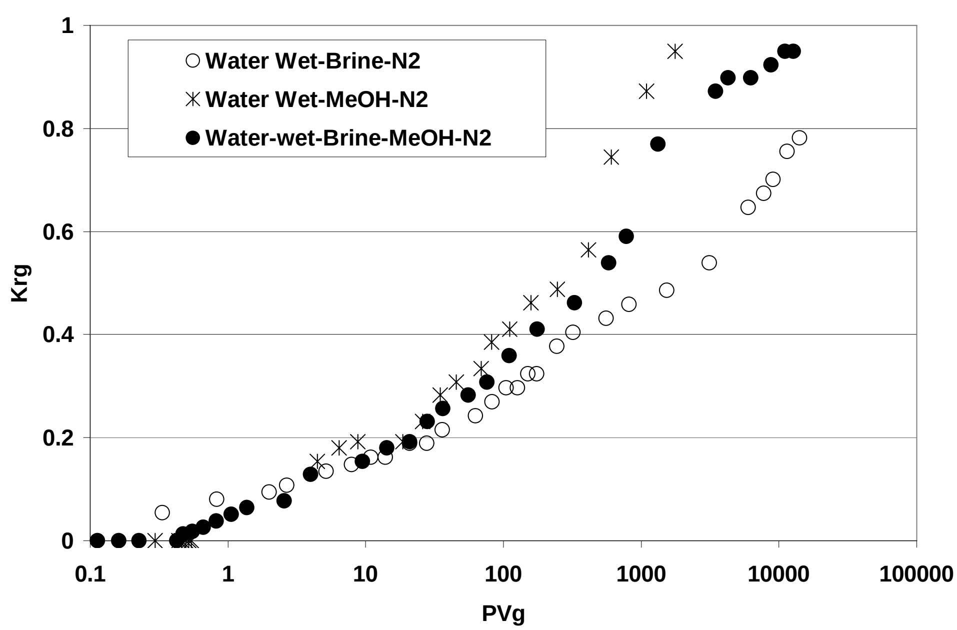

Figure 2: Relative permeability of gas versus pore volumes of gas injected for water wet Berea sandstone for displacement of different liquids. The mean pressure is 1.1 atm and the length of core is 7.6 cm. Absolute permeability of the core is 327 mD.

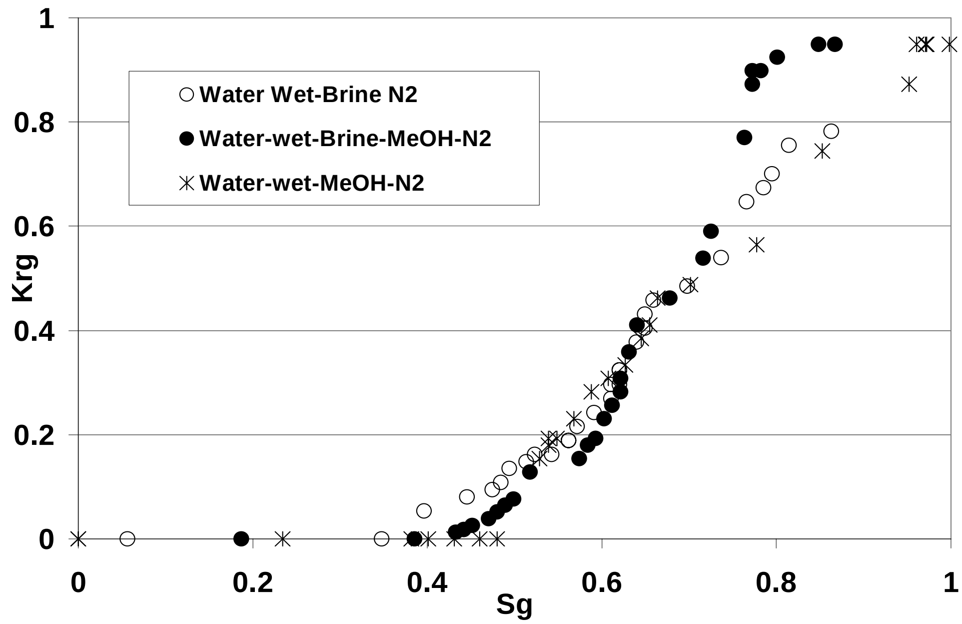

Figure 3: Relative permeability of gas versus pore gas saturation in the water-wet Berea sandstone core for displacement of different liquids at a mean pressure of about 1.1 atm. Absolute permeability of the core is 327 mD and length of core is 7.6 cm.

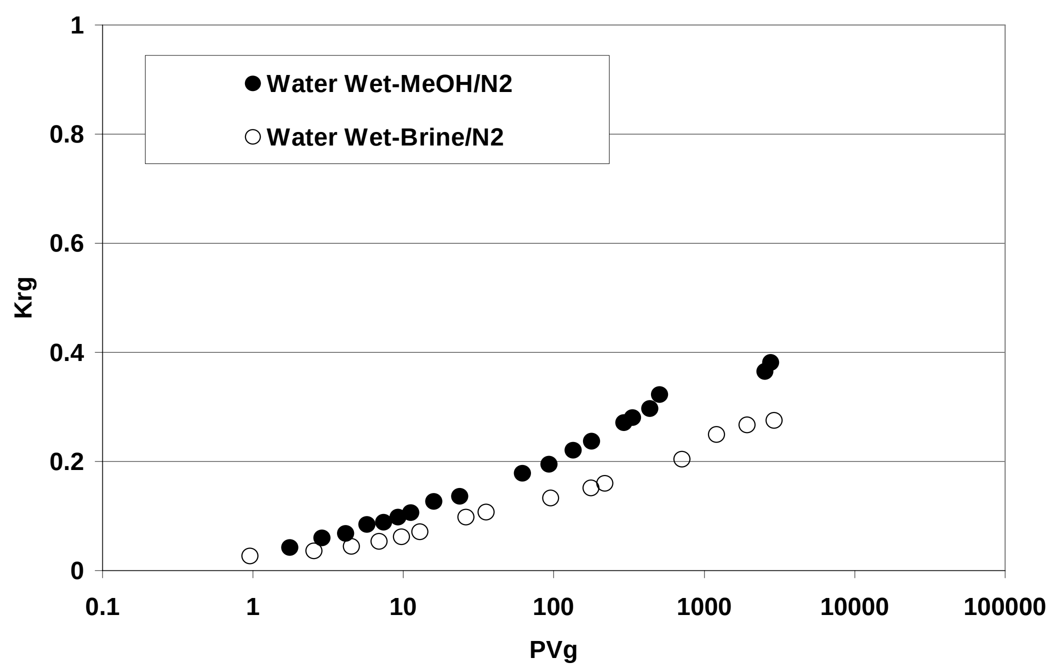

Figure 4: Effect of solvent on the gas relative permeability in a water-wet Texas-Cream limestone core at a mean pressure of 9.0 atm. Absolute permeability of the core is 0.7 mD and core length is 7.6 cm.

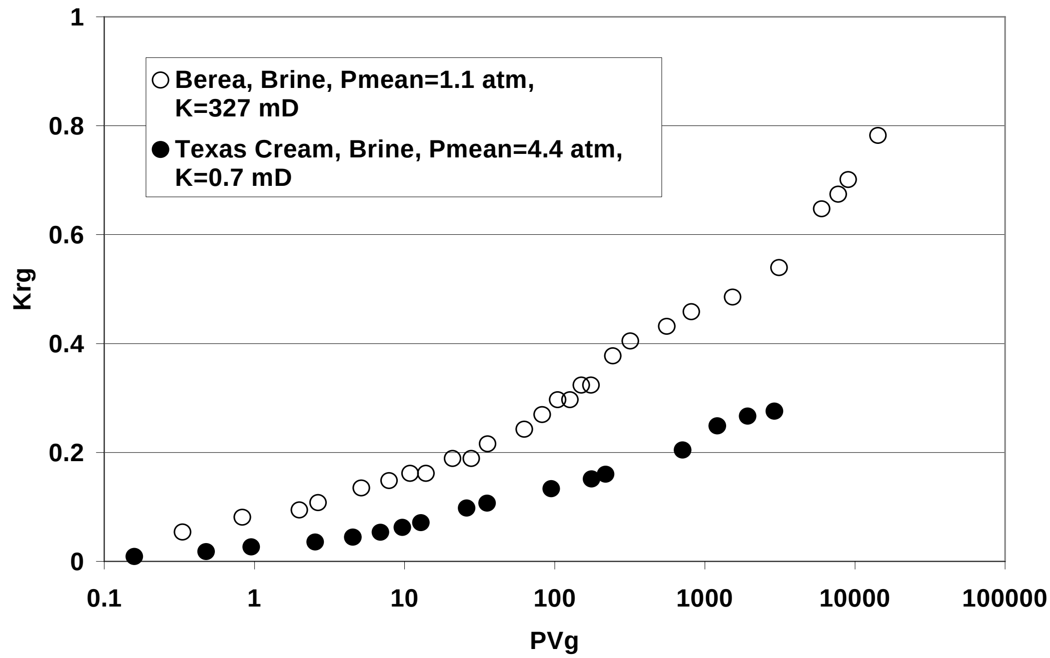

Figure 5: Effect of permeability of rock on the gas relative permeability for water-wet rock with brine as the liquid displaced. The lengths of the cores are 7.6 cm.

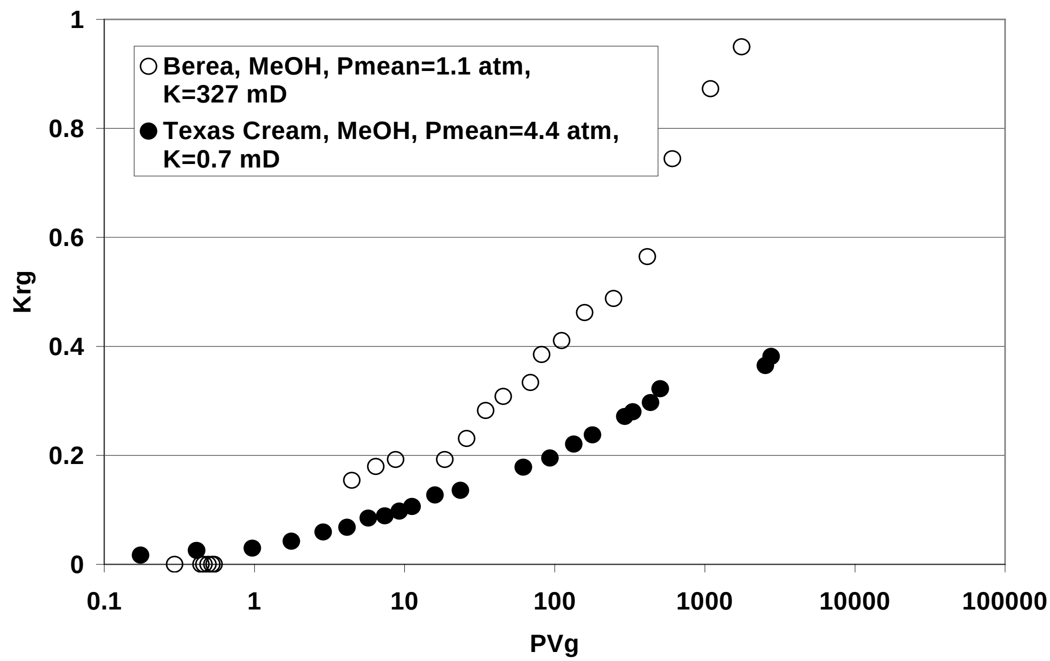

Figure 6: Effect of permeability of rock on the gas relative permeability for water-wet rock with MeOH as the liquid displaced. The lengths of the cores are 7.6 cm.

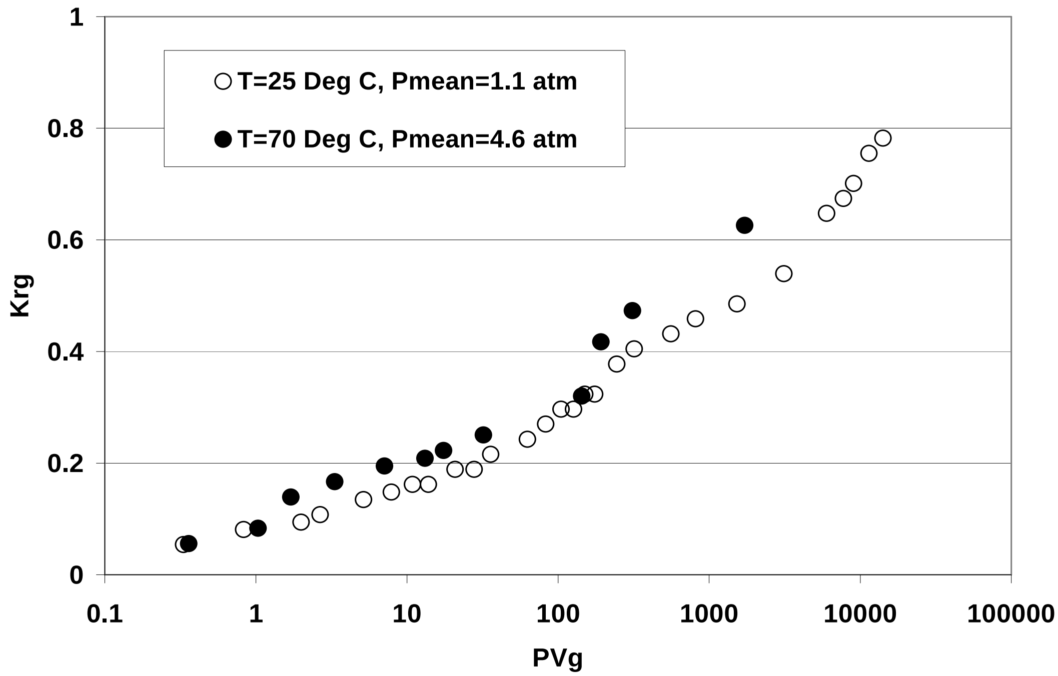

Figure 7: Effect of increasing temperature on gas relative permeability in a water-wet Berea sandstone core. The liquid displaced is brine. Absolute permeability of the core is 327 mD and core length is 7.6 cm.

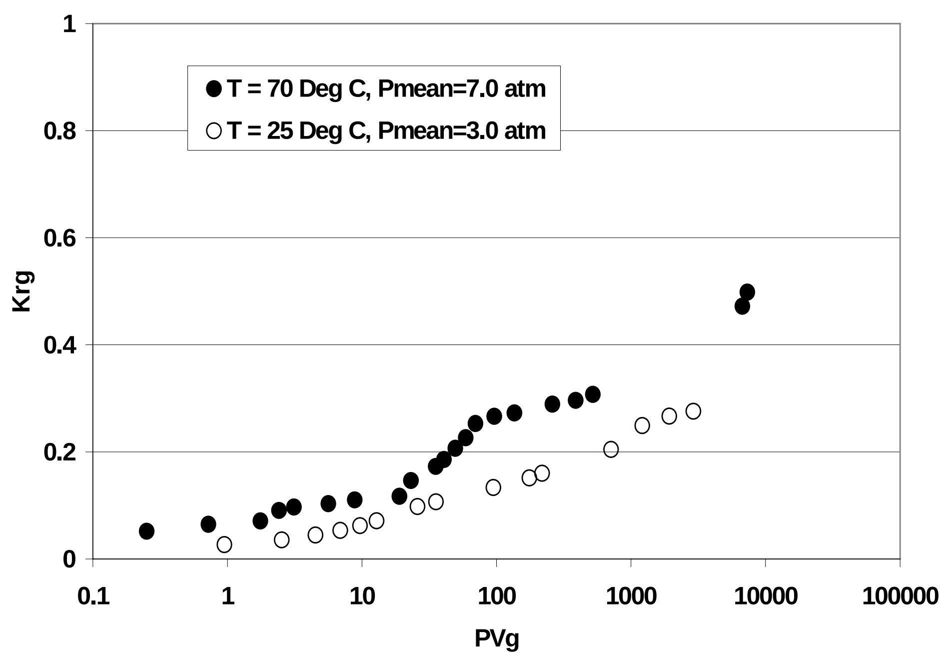

Figure 8: Effect of increasing temperature on gas relative permeability of water-wet Texas Cream limestone core with brine as displaced liquid. Absolute permeability of the core is 0.7 mD and core length is 7.6 cm.

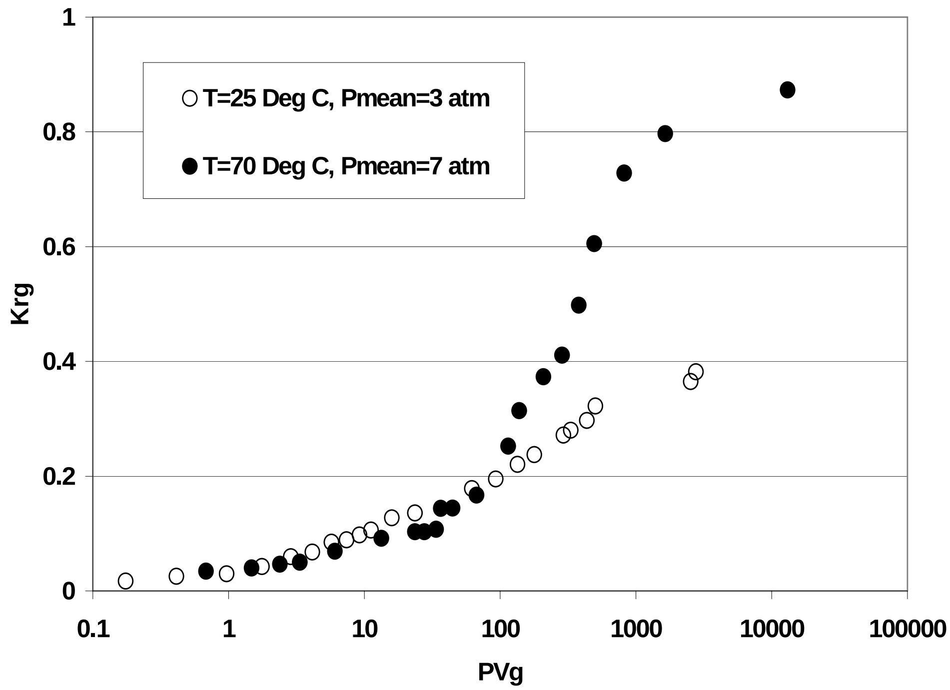

Figure 9: Effect of increasing the temperature on gas relative permeability with a methanol as displaced fluid in a Texas Cream Limestone core at a mean pressure of about 6.0 atm. Absolute permeability of the core is 0.7 md and core length is 7.6 cm.

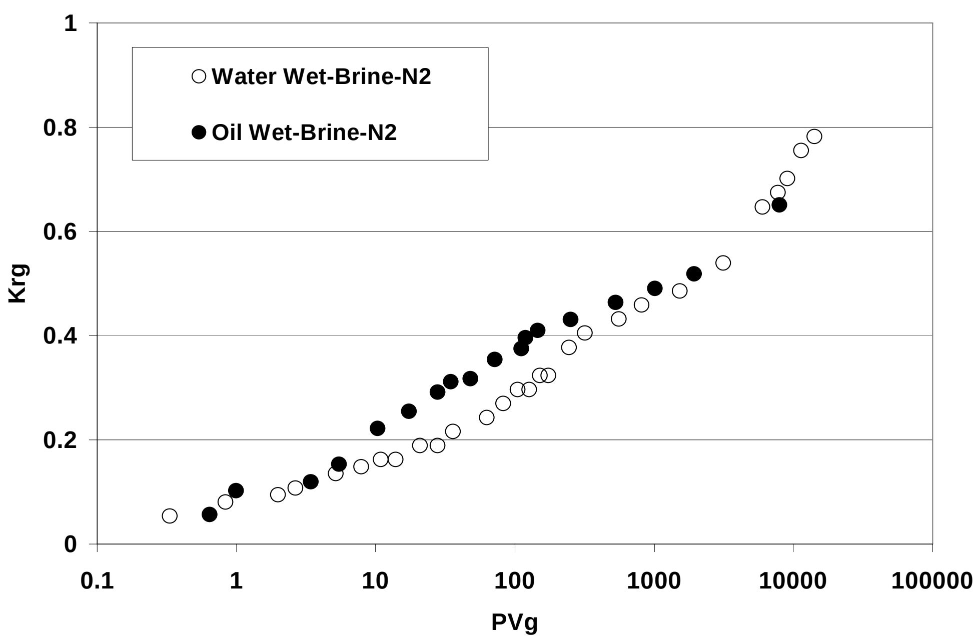

Figure 10: Effect of changing wettability on gas relative permeability in Berea sandstone core at a mean pressure of about 1.1 atm. Absolute permeability of the core is 327 mD and core length is 7.6 cm.

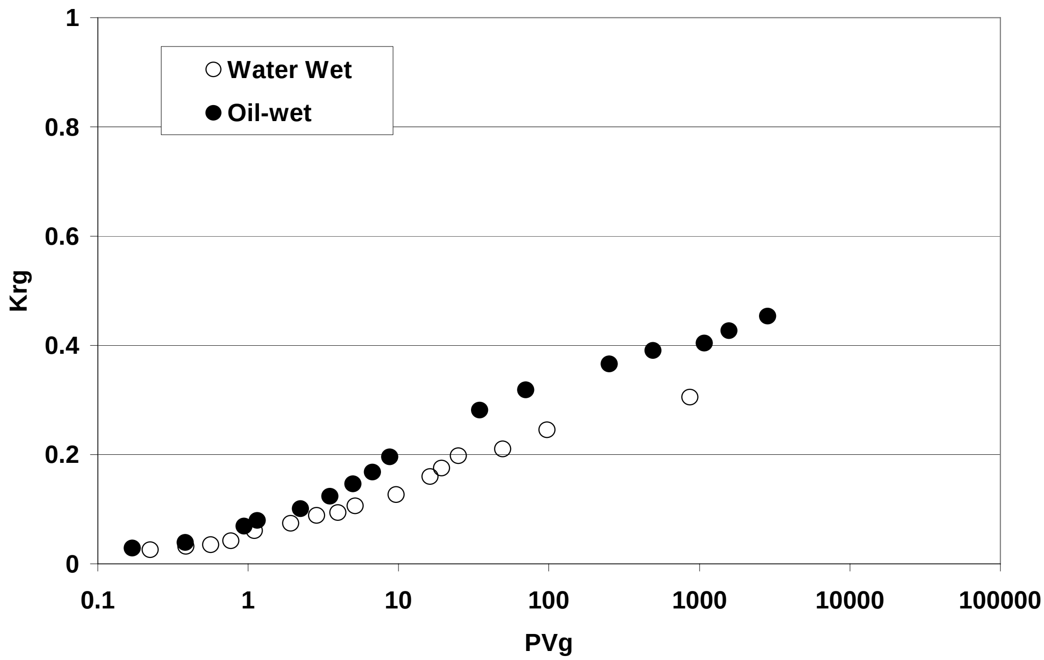

Figure 11: Effect of changing wettability on gas relative permeability in Texas Cream Limestone core at a mean pressure of about 3.0 atm and brine as displaced liquid. Absolute permeability of the core is 7.6 mD and core length is 7.6 cm.

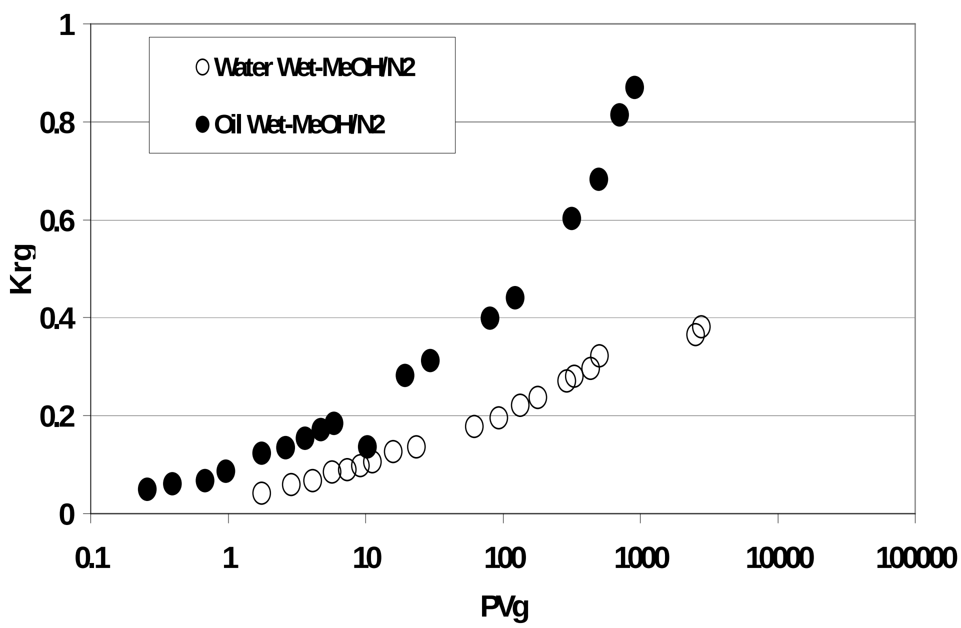

Figure 12: Effect of wettability change on the gas relative permeability in Texas cream limestone with methanol as displaced liquid at a mean pressure of 3.0 atm. Absolute permeability of the core is 0.7 md and core length is 7.6 cm.

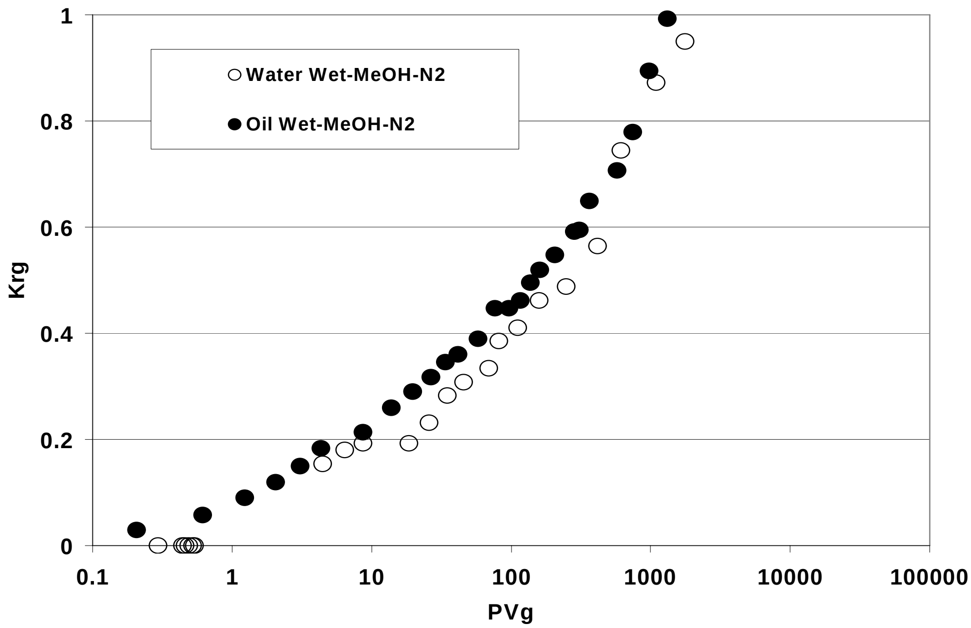

Figure 13: Effect of wettability change on the gas relative permeability in Berea sandstone core with methanol as displaced liquid at a mean pressure of about 1.1 atm. Absolute permeability of the core is 327 md and core length is 7.6 cm.

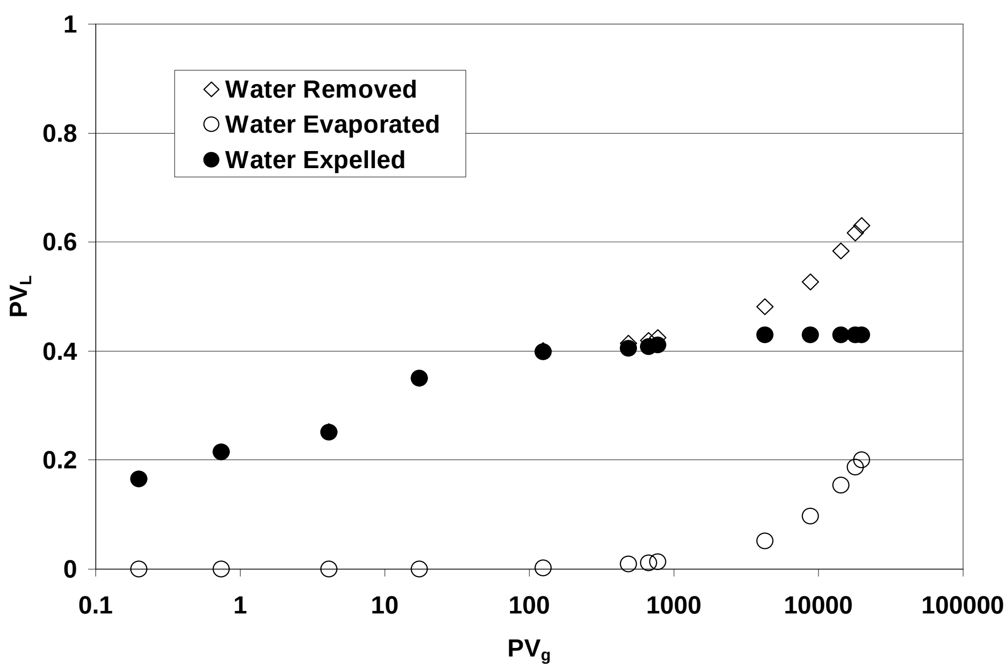

Figure 14: Liquid (brine) removed from Texas Cream Limestone core by displacement and evaporation. The mean pressure of experiment is about 3.0 atm. Absolute permeability of the core is 7.2 mD and core length is 15.3 cm.

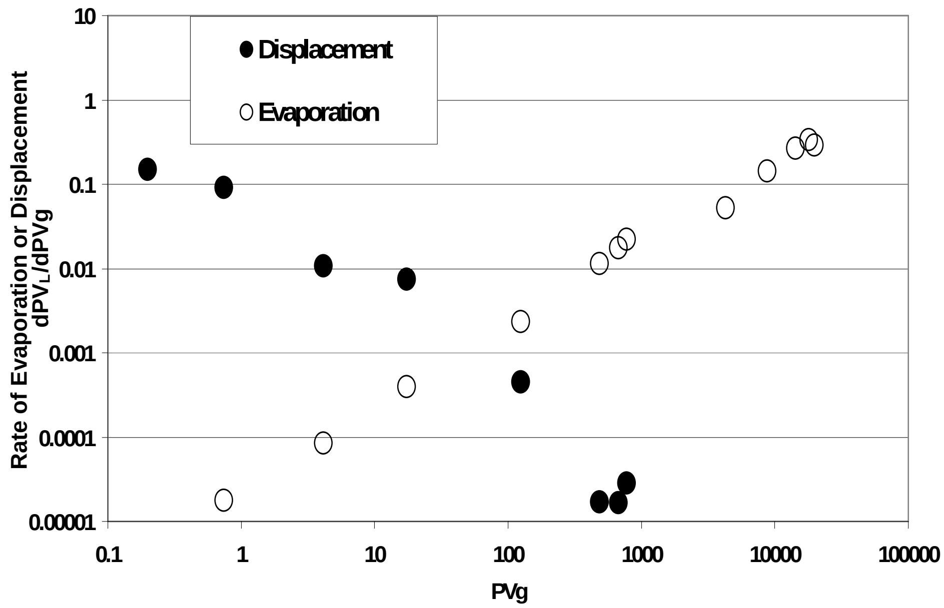

Figure 15: Rate of Liquid removal (brine) from Texas Cream Limestone core by displacement and evaporation. The mean pressure of experiment is about 2.7 atm. Absolute permeability of the core is 7.2 mD and core length is 15.3 cm.

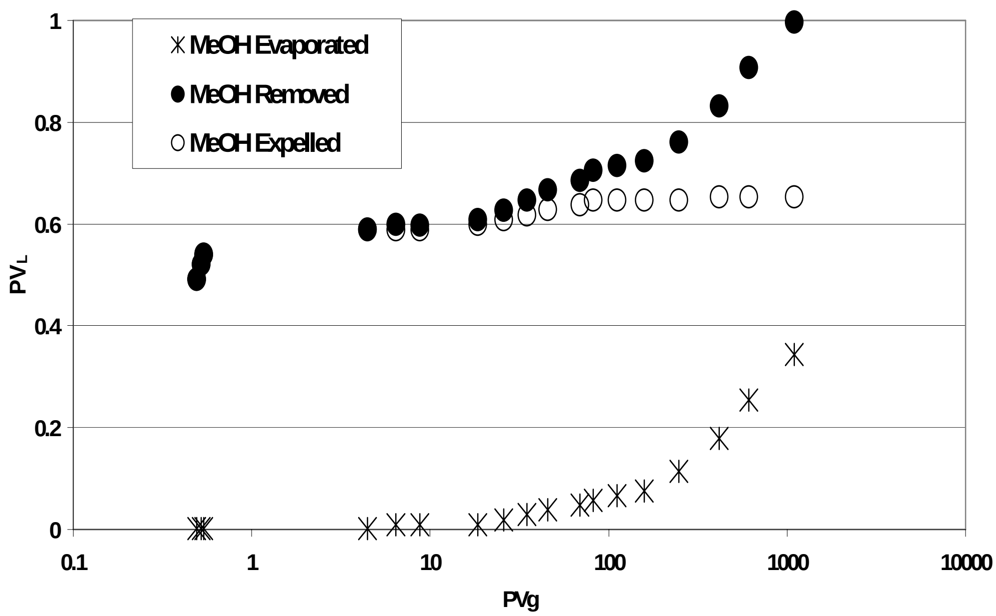

Figure 16: Liquid removed from Berea sandstone core by displacement and evaporation. The mean pressure of experiment is about 1.1 atm. Absolute permeability of the core is 327 mD and core length is 7.6 cm.

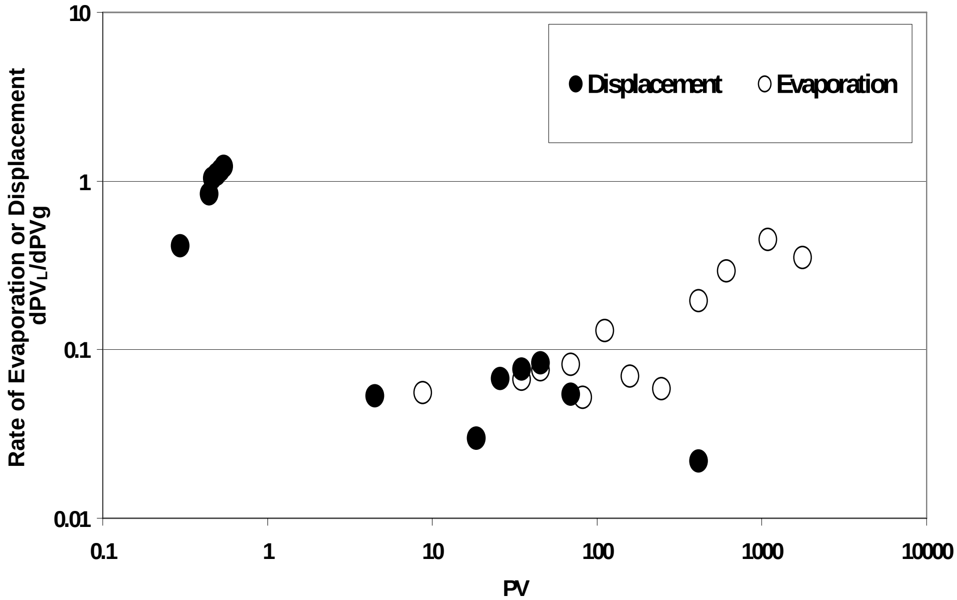

Figure 17: Rate of Liquid removal (MeOH) from Berea sandstone core by displacement and evaporation. The mean pressure of experiment is about 1.1 atm. Absolute permeability of the core is 327 mD and core length is 7.6 cm.

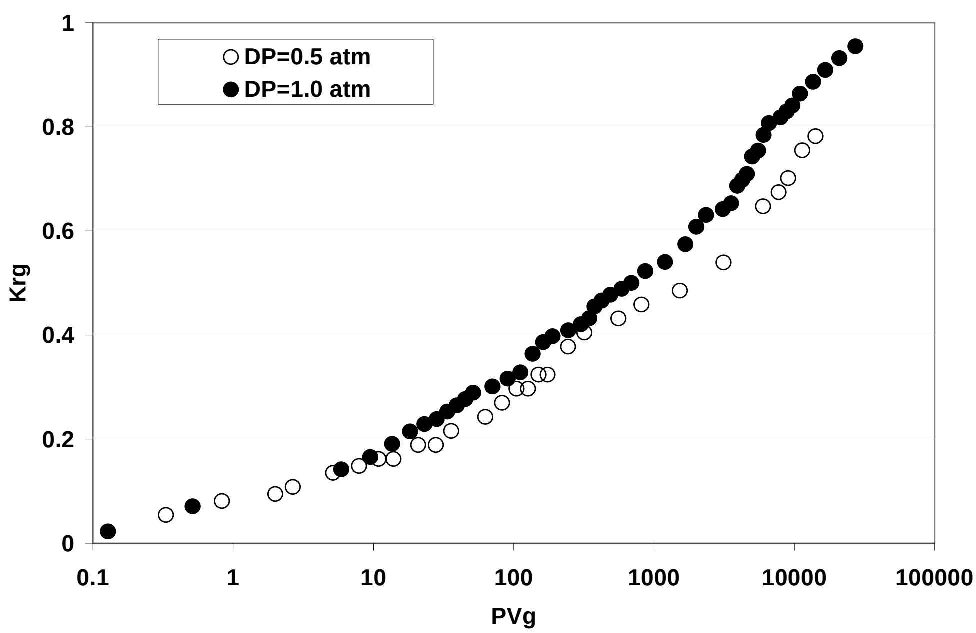

Figure 18: Effect of increasing drawdown (pressure drop across core) on gas relative permeability in Berea sandstone core. Absolute permeability of the core is 327 mD and core length is 7.6 cm.

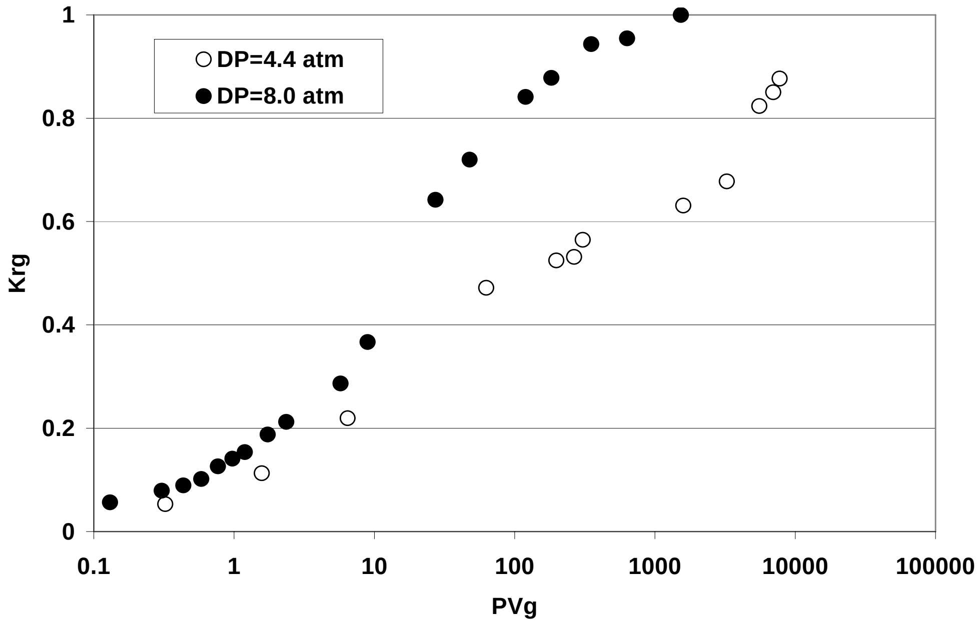

Figure 19: Effect of increasing drawdown (pressure drop across core) on gas relative permeability in Texas Cream limestone. Absolute permeability of the core is 7.6 mD and core length is 15.3 cm.

CHAPTER 9. AN IMAGING STUDY OF LIQUID REMOVAL BY GAS FLOW: APPLICATION TO WATERBLOCK CLEANUP

9.1 ABSTRACT

The flow of a saturated gas through a porous medium, partially occupied by a liquid phase, causes evaporation due to gas expansion. This process, referred to as flow-through drying, is important in a wide variety of natural and industrial applications, such as, natural gas production, convective drying of paper, catalysts and membranes.

X-ray imaging experiments were performed to study the flow-through drying of water-saturated porous media during gas injection. Our results show that the liquid saturation profile and the rate of drying are dependent on the viscous pressure drop across the porous medium, the state of saturation of the gas and the capillary characteristics of the porous medium. During the injection of a completely saturated gas, drying occurs only due to gas expansion. Capillary-driven flow from regions of high saturation to regions of low saturation lead to more uniform saturation profiles. During the injection of a dry gas, a drying front develops at the inlet and propagates through the porous medium.

9.2 INTRODUCTION

Water entrapped in porous media can be removed by the continuous flow of gas, at constant pressure, which displaces and eventually evaporates the water. A recent study by Mahadevan et al.[4] shows that in low permeability samples such as micro-Darcy sands, which have a median pore size of the order of 0.01 μm, gas flow rates recover much slower than high permeability samples such as Berea sandstone samples with median pore size of about 2.5 μm.

Recent research (Mahadevan et al.[4], Kamath et al.[3]) in this area has shown that the liquid removal takes place in two steps[4, 3]. The first step is a displacement of the water from the pores by the viscous pressure drop, followed by an evaporation regime that lasts for large volumes of gas flowed. Additionally the relative permeability of gas, reduced due to the partial occupation of the pore space, also increases as more trapped liquid is removed. Higher pressure drops, hydrophobicity and solvent addition were also shown (Mahadevan et al., 2003) to improve the relative permeability of the injected gas in both the displacement and the evaporative regime. The study reported that in addition to the capillary trapping, the capillary end effect, which causes the water saturation to build up near the producing end is important.

Evaporation effects due to flow of a dry gas, termed as flow-through drying, was studied early on by Allerton et al.[1]. The paper reports results from through-drying experiments in which dry gas, at elevated temperature, is flowed through porous beds of different materials such as glass beads and crushed quartz and also mentions the effect of pressure drop on evaporation rates. No experiments were reported with injection of gas saturated with water vapor such as presented in this paper.

Investigation by Yiotis et al.[7] shows that transport by liquid films is an important mechanism in the process of drying in porous media. Pore network simulations were conducted to show the effect of diffusive mass transfer on the drying rates and the role of liquid films through capillary channels. They show that the effect of film flows become dominant when capillarity controls the process of drying. The removal of water is complicated by the effects of gas compressibility and concentration, in addition to the capillarity of the sample. In order to quantify the effects of displacement, evaporation and the capillarity it is important to understand the physical processes on a local scale instead of an average scale.

Imaging studies (Peters and Hardham[6], Abrams and Vinegar[2]) have been used in flow through porous media to identify the physical processes which are not easily recognizable by studying only the outflow variables. Using X-Ray imaging studies it is feasible to visualize the two regimes of flow, displacement and the evaporation, in the porous media during the injection of gas. Wettability change and solvent addition for clean-up produce local variations on the two phase flow which is difficult to quantify by any other means than imaging.

This study presents information on the local variations of liquid saturation during both displacement and evaporative regimes. It is shown that the capillary end effect is present in the case of both high-permeability larger pore size sandstones (~2.5 μm) and low-permeability smaller pore size (~0.3 μm) limestones. This effect is minimized when wettability is changed to non-wetting. A mathematical model is developed (Appendix B) to predict the capillary end effect based on the flow relationships of the medium such as primary drainage capillary pressure curve and gas-water relative permeability curves. This model can also be used as an inversion procedure to obtain the flow parameters such as the capillary pressure curve and relative permeability exponents from the displacement data.

When a wet gas is injected the drying is predominantly due to the compressibility of the gas. In this regime it is seen that, for the low permeability limestones, the drying rates produce larger saturation changes near the outlet end whereas, for high-permeability sandstones the changes are more uniform. This uniformity is attributed to redistribution of liquid within the sample due to capillary driven film flows or the "wicking" effect. The effect of capillary redistribution, seen in the results of this study, is to increase the drying rates by conveying liquid from low drying-rate areas near the inlet end to the high drying-rate areas. When a dry-gas is injected a propagating evaporation front is observed, in addition to drying due to compressibility. The effect of wettability and and solvent addition on local saturation evolution are also shown in the results of this study.

9.3 EXPERIMENTAL PROCEDURE

In this study we use a high-energy X-ray scanning technique to obtain images of saturated porous samples encapsulated in epoxy resin while gas injection experiment is taking place. The experimental set-up is similar to that shown in the work by Mahadevan et al.[4].

9.4 FLUIDS USED

A 1 % by weight sodium chloride solution in de-ionized water was used as the saturating fluid. The solution is de-aerated and stored in an air-tight container and used later for saturation. The building's instrument air supply was used as the injected gas after passing it through a filter. In order to humidify the air, it was bubbled through a column of water with glass beads. The presence of glass beads increases the residence time of the air bubbles thus providing a 100% relative humidity air. This was verified experimentally by using a hygrometer. In the case of dry gas injection, the instrument air was passed through a Matheson brand inline oil/water purifier to completely dry the air and to remove any particulates.

9.5 SAMPLE PREPARATION

Cylindrical samples 2.5 cm in diameter and 7.6 cm long are cut from homogeneous slabs of Berea sandstone and Texas Cream limestone using water as the cutting fluid. Special care is taken to ensure that the limestone sample is free from any visible fractures and vugs. The sample is dried in an air-oven at 100 ^oC for at least 24 hours and is weighed before being placed inside the Hassler apparatus. More details of the procedure for obtaining chemically treated and hydrophobic samples are presented in Appendix A.

9.6 SCANNING PROCEDURE

The capsules are vertically supported on a stand with a cylindrical boss, which holds the stand in place on the scanning table. Once the stand is placed on the table, the angle of view is marked on the scanning table and this alignment is retained through-out the series of experiments. A dry calibration scan is taken to create a base image. The sample is then fully vacuum-saturated with 1% sodium chloride in deionized water and the porosity is determined. The weight of the capsule after saturation is noted. The humidity, flow rate and expelled water are measured during the gas injection experiments. The dry gas injection experiments were scanned at frequent intervals initially and the wet gas scans were taken at larger intervals and less frequently.

X-ray Source

The high-resolution/high-energy system at the UT CT Facility utilizes a dual-spot 420-kV X-ray source (Pantak HF420), with spot sizes of 0.8 and 1.8 mm. For this study X-rays were set at 420kV and 1.8 mA, utilizing the 0.8 mm spot size and generating a continuous spectrum of X-Ray energies from ~30 keV to 420 keV; the mean energy is ~200keV.

Scanning Configuration

The cylindrical rock sample in epoxy capsule is placed vertically while the gas is injected from the top. X-rays pass through the sample and the exiting beams are detected by a series of detectors that measure the extent to which the X-ray signal has been attenuated by the object. The sample is fixed to the table of the scanner conforming to the original alignment. The sample is not rotated and remains fixed while the collimated fan-beam takes a scan from the top to the bottom of the cylindrical capsule with a constant angular orientation. The time of travel can be adjusted to suit the level of vertical resolution needed. In our case we used a 9 second travel time to cover a length of approximately 10 cm.

X-ray Attenuation

As the X-rays pass through the object being scanned, the signal is attenuated by scattering and absorption. The basic equation for attenuation of a mono-energetic beam through a homogeneous material is Beer's Law:

$$I = I_o \exp[-\mu x], \qquad (1)$$

where Io is the initial X-ray intensity, μ is the linear attenuation coefficient for the material being scanned (units: 1/length), and x is the length of the X-ray path through the material. If the scan object is composed of a number of different materials, the equation becomes:

$$I = I_o \exp[\sum_i (-\mu_i x_i)], \qquad (2)$$

where each increment i reflects a single material with attenuation coefficient μ_i over a linear extent x_i. To take into account the fact that the attenuation coefficient is a strong function of X-ray energy, the complete solution would require solving the equation over the range of the effective X-ray spectrum:

$$I = \int I_o(E) \exp[\sum_i (-\mu_i(E) x_i)] dE. \qquad (4)$$

However, the solution is difficult to obtain, as the precise form of the X-ray spectrum, and is usually only estimated theoretically rather than measured. Most interpretation strategies solve equation (2), insofar as they assign a single value to each pixel rather than some energy-dependent range.

X-ray Detectors

The high-resolution/high energy system at UT has two separate detectors. The P250D detector consists of a linear array of 512 discrete cadmium tungstate scintillators with dimensions 0.25 mm x 5.0 mm x 5.0 mm, packed in a comb to prevent crosstalk between channels, and each connected to a Si photodiode. Its channel-to-channel pitch is 318 µm, and its total horizontal extent is 195 mm. The fan-beam was collimated to 1.5 mm thickness.

9.7 ACQUISITION OF DATA

Calibration Scans

In this experimental study, the calibration material is the oven-dry rock sample in the epoxy capsule. Therefore a calibration scan is first taken before the rock sample is flooded with 1 % sodium chloride solution. However, to remove any attenuation or variations due the air present in the scanning chamber a separate calibration scan is taken before every experiment series.

Background and Noise Processing

The background readings are taken from the epoxy encasing the sample, immediately to the left of the sample proper. It is assumed that large-scale fluctuations in the background are caused by fluctuations in X-ray intensity, and that the effect is thus multiplicative. The basic correction factor applied to intensity readings is thus:

$$corr = bkg_{calib} / bkg_{u} ,$$

which effectively makes the unknown match the background.

To reduce noise effects associated with local heterogeneity while retaining boundary sharpness (particularly important because the sample holder goes through a transition near the top and bottom of the sample), we use a median filter (filter width currently 15). Edge effects are incorporated by using the median of all valid values within the filter half-width.

9.8 IMAGE PROCESSING: SATURATION FROM X-RAY INTENSITY NUMBERS

The porous sample is an aggregation of a number of minerals and has a complex geometrical shape at pore scales. Hence accounting for the linear attenuation in each material and the geometry is nearly impossible. We have assumed a single linear attenuation coefficient to represent the attenuation in the dry porous medium and that it remains constant during the experiment. In the presence of 1 % sodium chloride solution, the X-Ray intensity is attenuated based on the attenuation coefficient of the solution and the percentage of the solution occupying the pore spaces.

Basic equation:

$$I_w = I_d e^{-\mu x}, \tag{5}$$

where I_w and I_d are intensity (in this case, grayscale) of a pixel in radiographs of wet and dry calibration scans, respectively, μ is the attenuation coefficient of water, and x is the linear distance of water traversed. Isolating with exponential term, we get:

$$\mu x = \ln\left(I_d / I_w\right). \tag{6}$$

So, in other words, the linear distance of water traversed is proportional to the log of the ratio of the intensities. For a particular region of interest (ROI), in the saturated case the total "water distance" traversed is equal to the sum of the distances along each ray:

$$\mu x_{sat} = \mu \sum x_i = \sum \ln\left(I_{d,i} / I_{w,i}\right). \tag{7}$$

Percent saturation in an unknown case (S_u) is then proportional to the linear distance of water traversed, normalized to the wet calibration scan:

$$s_u = \frac{\mu x_u}{\mu x_{sat}} = \frac{\sum \ln\left(I_{d,i} / I_{u,i}\right)}{\sum \ln\left(I_{d,i} / I_{w,i}\right)}. \tag{8}$$

For this study, each region of interest corresponds to a row of pixels in a radiograph image.

9.9 EXPERIMENTAL RESULTS AND DISCUSSION

The experimental data includes saturation profiles at different times and the cumulative volume of gas injected. The cumulative volume of gas injected is normalized with the volume of the pore space in the sample and reported as a number of pore volumes.

9.9.1 Wet Gas Injection

Figure 1 shows the imaging results for an untreated Berea sandstone sample during the injection of a wet gas. The first scan approximately corresponds to the end of displacement phase as it was taken 30 minutes after the gas injection was started and about 432 pore volumes (PV) had been flowed. The plot shows the trapped water saturation which gradually rises to greater values near the outlet end where the capillary pressure is zero.

This is due to the existence of the capillary end effect in addition to the trapping, where the water saturation increases to one towards the outlet. The saturation however does not reach the value of one as expected in a purely primary drainage process (shown by model developed in the following section). This could be due to a combination of marginal evaporative effects and the capillary pressure curve hysteresis (due to minor pressure variations) which can cause the experiment to deviate from the assumed primary drainage conditions.

The evaporative regime occurs over long times and spans over thousands of pore volumes of gas injected. The evaporation occurs purely due to the compressibility of the injected gas as it is completely saturated with water prior to injection. At long periods of gas injection the saturation profiles in the Berea sandstone decrease rather uniformly while still retaining some of the end effects. The gravity effects are normally quantified using the dimensionless Bond number which is the ratio of the gravity to capillary forces as given below.

$$N_B = \frac{k \Delta \rho g}{\gamma} \qquad (9)$$

where k is the gas permeability (representing a characteristic pore size), $\Delta \rho$ is the water-gas density difference, g is the gravitational constant, and γ is the interfacial tension. Bond numbers in this study ranged on the order of 1E-10 to 2E-8 which is not significant to cause any end effect due to gravity forces.

In the case of limestone (figure 2), which has a lower permeability (0.0044 D, ~0.42 μm median pore diameter), the pressure drops are greater (6.8 atm) compared to the Berea sandstone (0.87 atm, ~2.0 μm median pore diameter). Here too the capillary trapping and end effect is seen at the approximate conclusion of the displacement period. While the saturations are approximately uniform with time in Berea, the saturations in limestone are uniform up to 24,747 pore volumes, and thereafter the saturations decrease faster near the outlet. The lower saturation near the inlet end is probably because of marginal undersaturation of the injected gas.

The uniform saturations in Berea are due to a redistribution of the water within the sample that is caused by capillary driven film flow effects. It has been shown in several studies (Dullien et al.[7], Yiotis et al.[7]) that liquid saturated pores are drained due to transport through films which form on the capillary channels in the porous medium. However, in limestone, this redistribution of liquids within the sample occurs only until a certain time after which the saturation profiles show greater drying rates near the ends. This suggests that the liquid film flow rate competes with or is on the same scale as the drying rates, which depend on the pressure drop across the sample (Mahadevan *et al.*[4]), near the outlet end. That is, when the drying rates are higher than the rate of transport due to films, the saturations fall more rapidly.

9.10 DRY GAS INJECTION

The displacement regime in both dry- and wet-gas injection remains the same as very little evaporation takes place in this phase. In the case of evaporation regime, the dry gas injection produces drying due to both concentration difference and pressure drop, whereas, in the case of wet gas injection the drying takes place only due to pressure drop.

Figure 3 shows the effect of dry gas injection in a hydrophilic Berea sample saturated with brine. The displacement regime happens approximately in the first 1 hour of the displacement while the evaporation regime takes place over a much longer time scale (several hours in this experiment). The reduction in saturation is relatively smooth and fast until about 1.45 hours after which the saturations decrease slowly indicating that the displacement is almost complete. The saturations near the inlet continue to decrease until about 7 hours when the saturations become zero and a propagating drying front begins. The spread of this drying front continues to increase as the saturations decrease. This spreading is due to the dispersive nature of the capillarity which conducts water in small channels in the porous media (Yiotis *et al.*[7]).

In the case of limestone, shown in figure 4, the saturations decrease both at the inlet and the outlet. This is so because of the higher drying rates near the outlet due to higher pressure drop (4.8 atm) in the limestone experiment compared to the Berea (0.87 atm). Thus in limestone we see a forward moving drying front and a receding front. The spread of the drying front in limestone also appears to be larger than in the Berea experiment.

When a wet gas is injected into a sample saturated with methanol, the displacement phase shows trapping of methanol in addition to marginal end effects. In the evaporation phase the forward and receding fronts in limestone (figure 5) are more apparent due to the higher drying rates of the more volatile methanol. The fact that the results still show a forward moving evaporation front is due to the relative independence of the vapor pressure of methanol in the presence of water and the system behaves as if a dry gas has been injected.

Figure 6 compares the saturation profiles at the end of displacement phase for a hydrophobic Berea sandstone sample to that of a hydrophilic sample. The samples were obtained from adjacent locations in a single slab of Berea and can be considered similar. The gas permeabilities of the samples were also compared and found to be similar (k=0.250 D, ~2.5 μm median pore diameter). Both the samples show similar saturation profiles near the inlet end suggesting that the trapping due to capillarity is not changed significantly by treatment to hydrophobic (Appendix A). However, the saturations near the outlet end, in the case of hydrophobic sample, are minimized by the chemical treatment. Therefore changing the wettability to hydrophilic minimizes the capillary end effects.

The effect of wettability on evolution of evaporation phase saturation profiles for a dry gas injection in a hydrophobic Berea is shown in figure 7. This is the same sample as that of figure 6. Results for wet- and dry-gas injection for chemically treated sandstone (Appendix A) are shown in figures 8 and 9 respectively. The figures 7-9 show film flow effects, such as spreading front and uniform saturations, similar to that of the untreated samples. Evidently, the chemical treatment of the sample has not impacted the surface of the pore spaces completely which has resulted in wetting micro-channels that can still conduct water due to capillary pressure gradients. However, the capillary end effect seems to have been minimized with the chemical treatment.

9.11 CONCLUSIONS

X-Ray scanning was used to obtain the evolution of saturation profiles of trapped liquid in samples due to gas injection. The results from the scanning experiments agreed with the gravimetric measurements made at the end of the experiments. The injection condition is shown to have a significant difference in the saturation profiles during the evaporation period. While the dry-gas injection produces spreading drying fronts, wet-gas injection shows relatively uniform drying in samples with larger median pore size and low pressure drops. The spreading of these fronts is due to capillary film flows. When methanol is displaced, both a forward moving drying front and a receding evaporation front is seen at higher pressure drops.

The results clearly show the existence of capillary trapping and end effect at the conclusion of displacement period for both low and high permeability samples. These effects are more significant at lower drawdown pressures. Changing the wettability to hydrophobic or fluoro-chemical treatment minimized these effects. However, in the evaporation regime the effect of wettability change by chemical treatment is not readily apparent.

When wet-gas is injected, the competition between drying rates and the film flow rates determines the nature of saturation profile. In low permeability, smaller pore size samples, the compressibility driven drying is higher due to greater pressure drops compared to the larger pore size samples.

9.12 APPENDIX A

9.12.1 SAMPLE PREPARATION

Preparation of hydrophobic samples

1. The porous samples required to be made hydrophobic are cleaned, dried in an oven for 24 hours and placed in the Hassler apparatus (with a Viton sleeve to prevent damage from chloroform to be used later).
2. The samples are evacuated for 2 hours and saturated with decane by directly flowing it into the evacuated samples.

3. The decane imbibed is displaced with 50 pore volumes of a 1% by wt solution of OTS (octadecyltrichlorosilane) in chloroform.
4. The samples are allowed to sit in with the solution for about 15 minutes and then flushed with 50 pore volumes of chloroform.
5. The samples are removed from the sample holders and placed in an oven to heat-dry at 100 ^{o}C.

Preparation of chemically treated samples

1. The samples required to be treated are cleaned, dried in an oven for 24 hours and placed in the Hassler apparatus situated inside a Blue-M oven.
2. The samples are evacuated for 2 hours until the vacuum attains 30mmHg and saturated with a de-aerated 3% solution of sodium chloride in water by directly flowing it into the evacuated samples.
3. The temperature of the oven is set to 70 deg C. The imbibed brine is displaced by at least 60 pore volumes of a solution of methanol plus water mixture (80:20 by volume) under a 4 atm backpressure.
4. The displacement is then continued with a solution of a 1% by weight Fluoro-chemical in a methanol-water mixture (80:20) for about 60 pore volumes. The flow rate is adjusted to give a residence time of more than 40 minutes in the sample (According to vendor recommendations of Flourosyl).
5. Finally the temperature in the oven is brought back to 25 deg C while the flow is switched to a pure methanol injection for about 60 PV.
6. The sample is removed from the sample holder and placed in an oven to heat-dry at 100 ^{o}C.

Preparation of Samples for X-Ray Scanning

Three-inch long cylindrical samples of Berea sandstone and limestone are cut from the same source to obtain similar specimens. The samples are then dried in a convection oven at 100^{o}C to remove the imbibed water used during cutting. The gas permeability is measured for the sample by using Nitrogen. They are then placed in a poly-carbonate holder which holds the sample in place with an annular space between the sample and the poly-carbonate tube. The face of the sample is inserted into a groove on the end piece, which has flow channels on the face. The annular space in the holder is then filled with epoxy resin by pouring through a hole made in the wall of the tube. The epoxy is allowed to cure overnight and the gas permeability of the sample is determined again after the encapsulation to make sure that there is no damage or channeling. The weight of the capsule is also noted.

Nomenclature

D *Darcy, unit of permeability, 9.8E-13*m^2

k *gas permeability at mean pressure, D.*

L *length of the sample, cm.*

9.13 REFERENCES:

1. Allerton, J., Brownell, L. E. and Katz, D. L., "Through-Drying of Porous Media," Chemical Engineering Progress, (October 1949), Vol. 45, No. 10, 619-635.
2. Abrams, A. and Vinegar, H. J., "Impairment Mechanisms in Vicksburg Tight Gas Sands", paper SPE/DOE 13883 presented at the SPE/DOE 1985 Low Permeability Gas Reservoirs held in Denver, Colorado (May 1985).
3. Kamath, J. and Laroche, C., "Laboratory-Based Evaluation of Gas Well Deliverability Loss Caused by Water Blocking," Society of Petroleum Engineers Journal, (March 2003) 71-80.
4. Mahadevan, J., and Sharma, M. M., "Clean up of Water Blocks in Low Permeability Formations", paper 84216 presented at the Society of Petroleum Engineers Annual Technical Conference in Denver, Colorado, U. S. A., 5-8 October 2003, accepted to 2nd review for publication in Society of Petroleum Engineers Journal.
5. Peters, E. J. and Hardham, W. D., "Visualization of Fluid Displacements in Porous Media Using Computed Tomography Imaging," Journal of Petroleum Science and Engineering (1990), Vol. 4, 155-168.
6. Peters, E. J. and Hardham, W. D., "A Comparison of Unstable Miscible and Immiscible Displacements," paper 19640 presented at the 64th Annual Technical Conference and Exhibiion of the Society of Petroleum Engineers held in San Antonio, Texas, October 8-11, 1989.
7. Yiotis, A. G., Boudouvis, A. G., Stubos, A. K., Tsimpanogiannis, I. N. and Yortsos, Y. C., "The effect of liquid films on the drying of porous media," American Institute of Chemical Engineers Journal, 2004.

8. Whitaker, S., "Simultaneous Heat, Mass, and Momentum Transfer in Porous Media: A Theory of Drying," Advances in Heat Transfer, Vol. 13 (1977) 119-203.

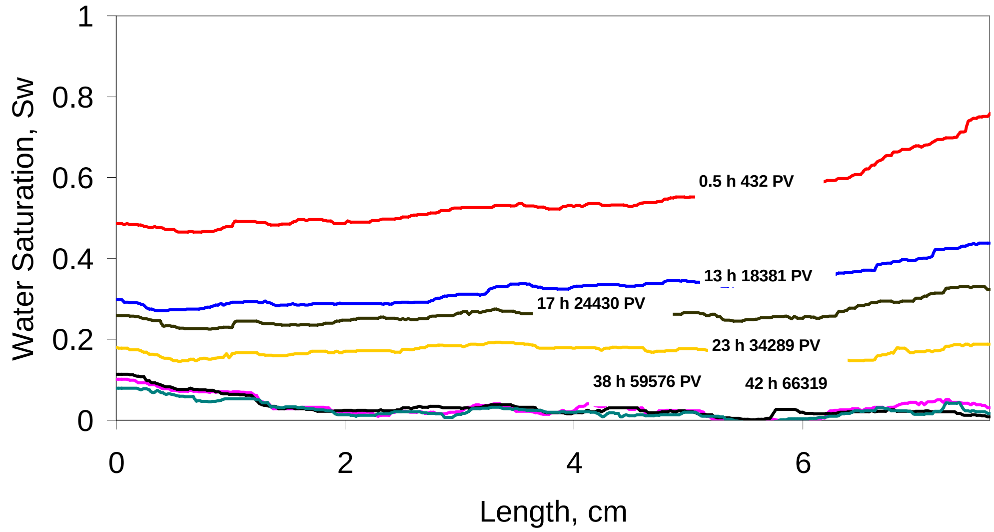

Figure 1: Brine saturation evolution in hydrophilic Berea sandstone sample (k=0.085 D, ΔP=0.87 atm) during injection of wet gas.

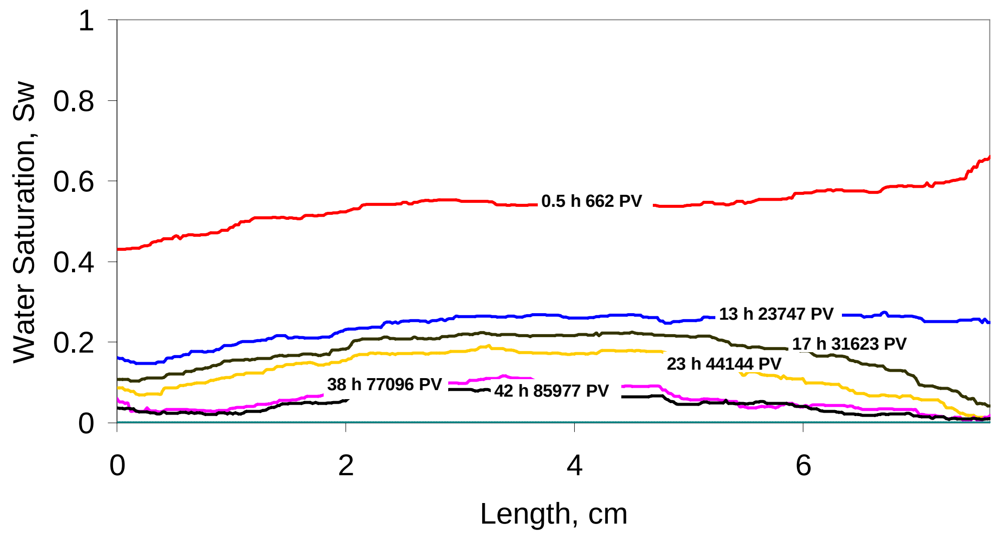

Figure 2: Brine saturation evolution in hydrophilic limestone sample (k=0.0044 D, ΔP=6.8 atm) during injection of wet gas.

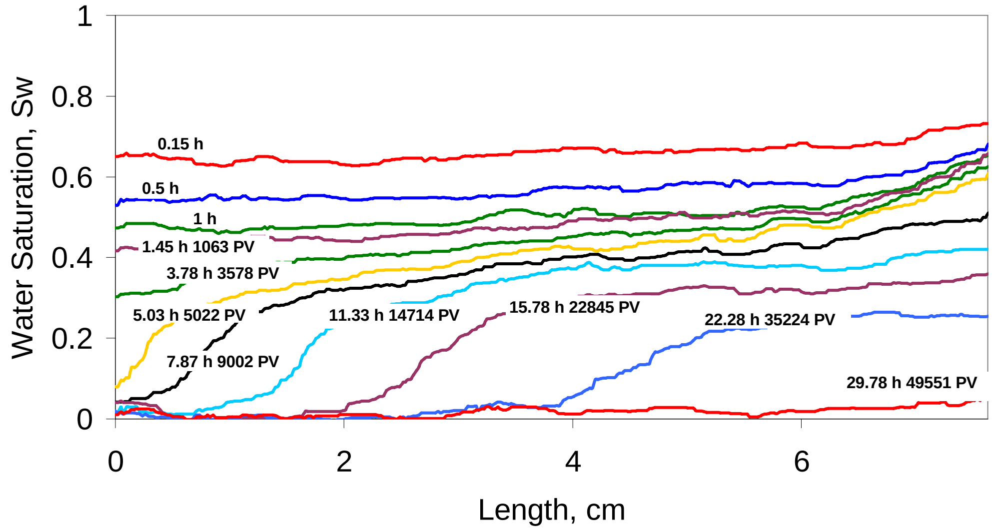

Figure 3: Brine saturation evolution in hydrophilic Berea sandstone sample (k=0.085 D, ΔP=0.87 atm) during injection of dry gas.

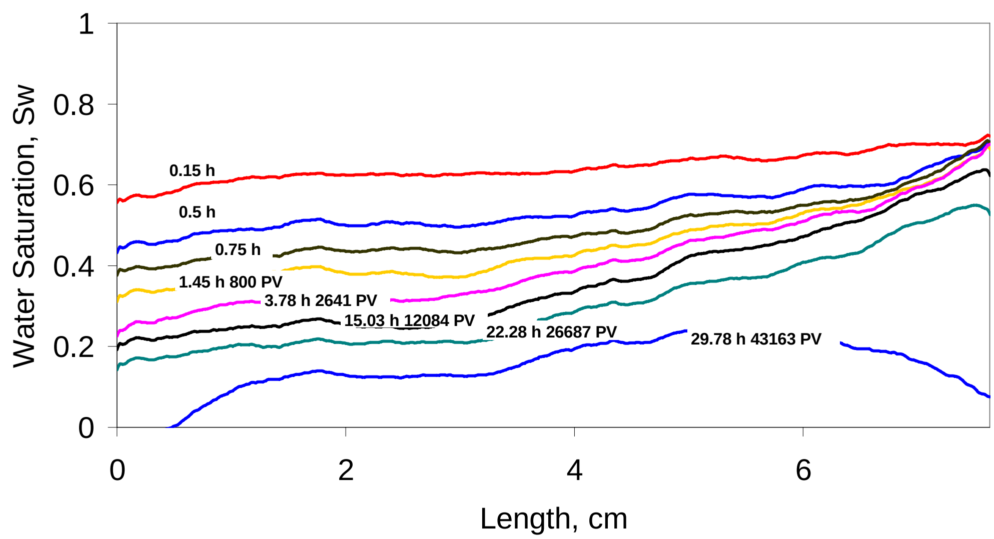

Figure 4: Brine saturation evolution in hydrophilic limestone sample (k=0.0044 D, ΔP=4.8 atm) during injection of dry gas.

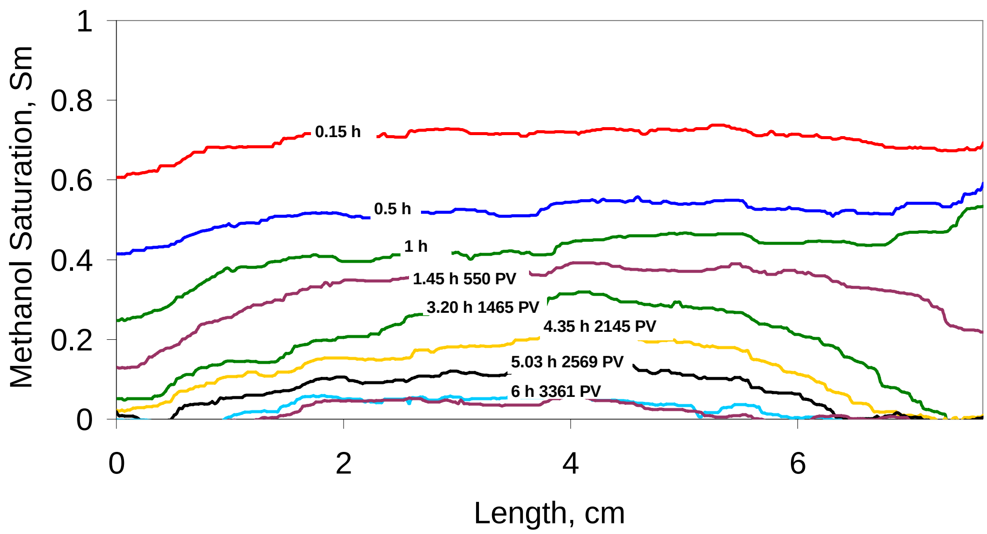

Figure 5: Methanol saturation evolution in hydrophilic limestone sample (k=0.005 D, ΔP=4.8 atm) during injection of dry gas.

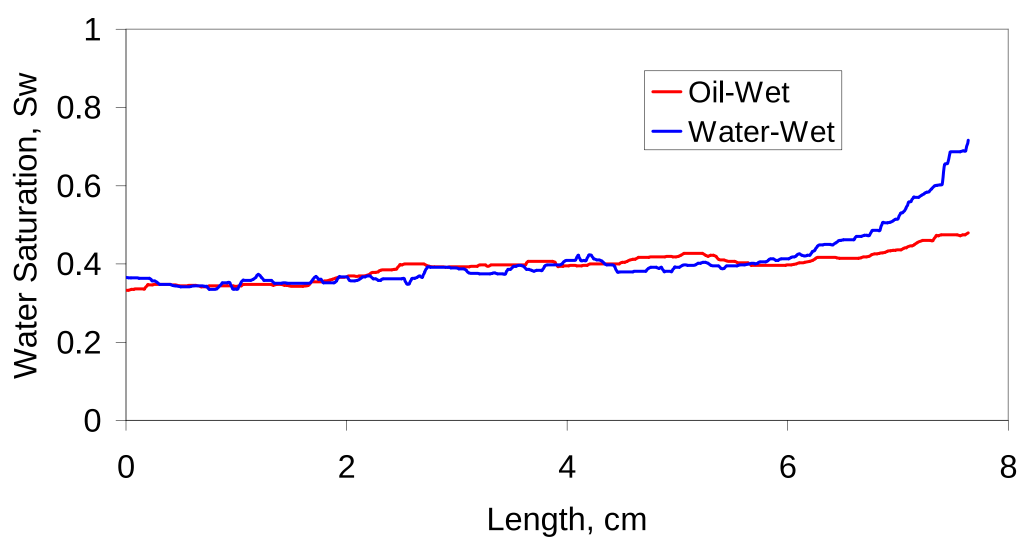

Figure 6: Effect of wettability change of Berea sandstone (hydrophilic-k=0.249 D, ΔP=0.4 atm, hydrophobic-k=0.264 D, ΔP=0.4 atm) on capillary end effect.

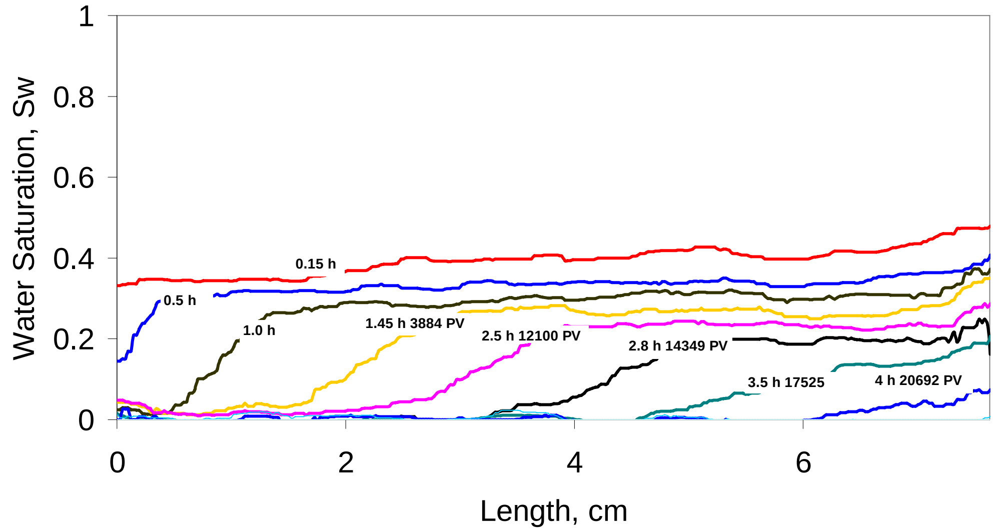

Figure 7: Brine saturation profiles in a hydrophobic Berea sandstone (k=0.264 D, ΔP=0.87 atm) during dry gas injection.

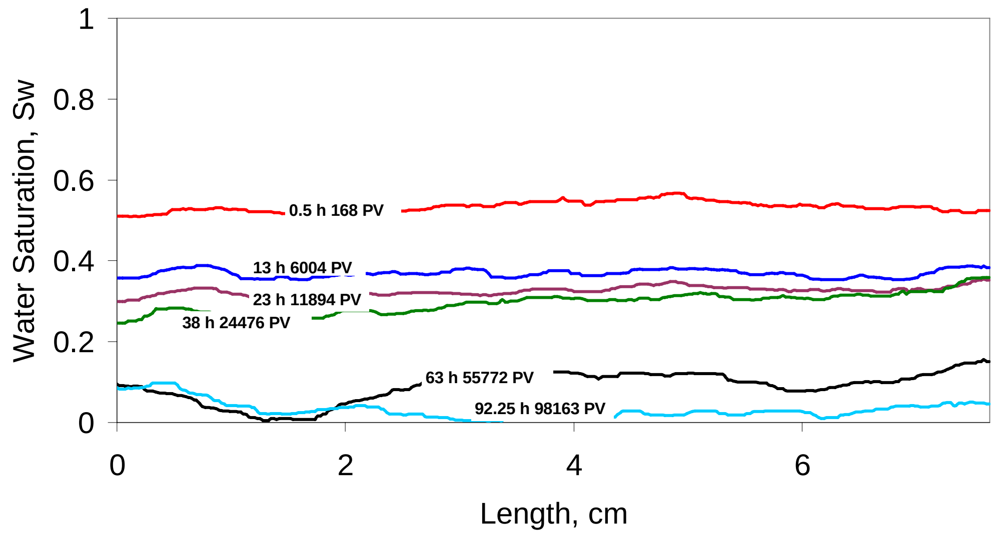

Figure 8: Brine saturation evolution in chemically treated Berea sandstone sample (k=0.076 D, ΔP=0.87 atm) during injection of wet gas.

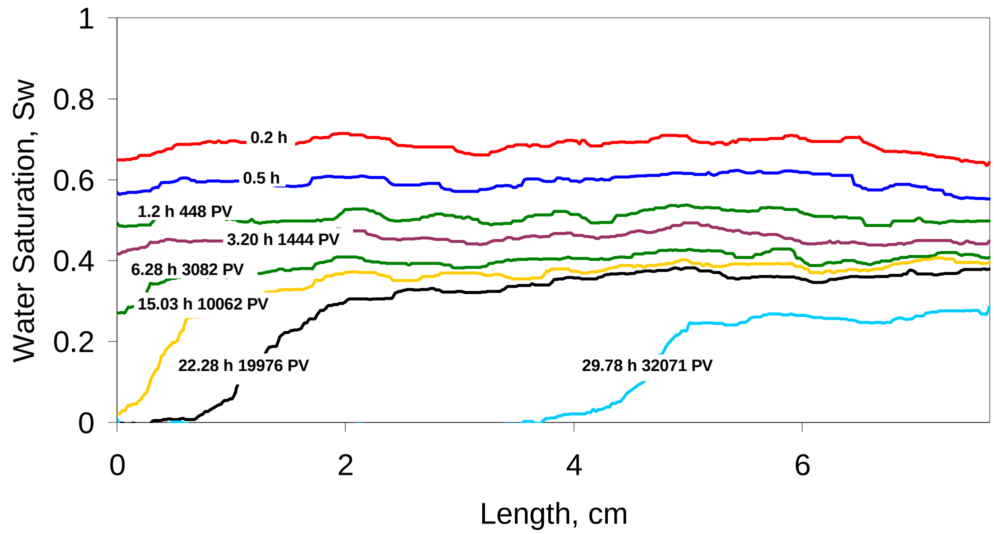

Figure 9: Brine saturation evolution in chemically treated Berea sandstone sample (k=0.076 D, ΔP=0.87 atm) during injection of dry gas.

CHAPTER 10. A SIMULATION STUDY OF CLEANUP OF WATER BLOCKS IN DEPLETED LOW-PERMEABILITY RESERVOIRS

10.1 ABSTRACT

Poor gas inflow performance is observed in some depleted, low permeability, reservoirs after completion and workover operations. The use of aqueous treatment fluids often results in a 'water block' due to poor recovery of the fluids that have leaked-off. This curtails well deliverability due to reduced relative permeability to gas/oil in the invaded region.

This study analyzes the effect of various factors governing the cleanup of water blocks in fractured and un-fractured wells for both gas and oil reservoirs. The effects of drawdown, capillary pressure, relative permeability, and heterogeneity as well as the influence of fracture geometry on well deliverability following some well operations, such as fracturing, have been examined by detailed simulations.

Drawdown, fracture length and shapes of relative permeability curves strongly affect the recovery in productivity. On the other hand, end point relative permeabilities and horizontal well length have an insignificant impact on cleanup. Higher vertical permeabilities favor early recovery of well productivity in 'high perm' layers and delay cleanup of water blocks in 'low perm' layers.

The results suggest the need to lower capillary pressure by reducing interfacial tension and/or altering wettability of the rock surface from strongly water-wet to intermediate-wet. With the correct selection of treatment fluids, proper design of fracture geometry and optimum drawdown applied it is possible to cleanup water blocks more rapidly in depleted low-permeability reservoirs.

10.2 INTRODUCTION

Loss of water-based fluids commonly occurs in drilling, completion and fracturing operations. These fluids are quickly recovered during flowback when the drawdown is much larger than the capillary forces holding the water in the pore space. However, in heterogeneous formations or depleted low-permeability reservoirs, drawdowns are often of the same order of magnitude as the capillary forces. In such cases well inflow performance is found to be poor following some well operations such as fracturing. This is due to an extended period of cleanup or incomplete cleaning of injected fluids. Leak off of aqueous fluids creates a zone of high water saturation around the wellbore and along the fractures. This reduces the relative permeability to hydrocarbons in the invaded region. This phenomenon is referred to as a "water block".

Experiments and numerical studies have been carried out in the past to study the problem of "water blocks". Holditch[1] accounted for capillary pressure and relative permeability in his numerical study of formation damage around a hydraulic fracture in a tight gas reservoir. Results presented in the study show that reservoir properties such as capillary pressure and relative permeability in low-permeability reservoirs are important in determining the behavior of a fractured well during cleanup. He also observed that the damaged zone permeability must be reduced by several orders of magnitude before a serious water block to gas flow will occur. Even if the reservoir rock permeability is not reduced, gas production can be severely curtailed if the pressure drawdown does not exceed the formation capillary pressure.

Penny et al[2] found in laboratory as well as in field studies that the judicious alteration of wettability to control capillary pressure and/or relative permeability can promote a rapid and thorough cleanup of injected water. Increasing fracture conductivity can further enhance gas well cleanup. They claim that "oil-wetting" (reducing water wetting in a gas-water system) the rock surface would lower the capillary pressure sufficiently to reduce water blocks.

Abrams and Vinegar[3] used CAT Scans to measure brine saturations and image the fluid flow in microdarcy gas sand cores under stress conditions that simulate a hydraulic fracture. The lab results suggest that water blocks are not important when drawdown pressures at the fracture face exceed the capillary entry pressure by several hundred psi. The addition of alcohol or an alcohol/surfactant package did not significantly improve the gas flow in these cores. On the other hand, McLeod[4,5] noted that alcohol causes a quick recovery of stimulation fluids and a rapid return of gas production in sandstone formations by lowering surface tension and thus reducing capillary forces. Methanol also facilitates faster vaporization, which lowers the liquid saturation in the invaded zone, thereby, increasing the gas productivity.

Kamath and Laroche[6] and Jagannathan and Sharma[7] reported results of laboratory studies to measure the waterblocking effect in core samples. The data showed that gas well deliverability recovers in two phases. The first phase corresponds to fluid displacement while the second phase is dominated by evaporation and mass transfer, which lasts for a long time. It is during the mass transfer regime that volatile fluids, such as methanol, show an improvement in the gas deliverability.

The main objective of this study is to systematically analyze the effect of various factors on the cleanup of water blocks in a depleted low-permeability gas reservoir as well as to assess the impact of water blocking on well deliverability. Parameters dealt with in the study are drawdown, shape and end point of capillary pressure and relative permeability curves, depth of invasion, fracture length and conductivity as well as horizontal well length. The study also covers oil-water systems to understand the differences in cleanup behavior as compared to gas-water systems.

10.3 SIMULATION METHODOLOGY

This study is performed using UTCHEM[8,9,10], the University of Texas Chemical Flooding Simulator. The assumptions made for these simulations are:

- Reservoir bounded at the top, bottom and external perimeter by a no-flow boundary
- Dispersion / diffusion neglected
- No mass transfer between phases
- No interaction between the formation material and invading water
- All properties, except k, are identical in all layers

To capture near-wellbore effects, the reservoir was divided into fine grids of the order of 3 to 4 inches near the wellbore and along the fractures. Separate gridding schemes were used for fractured and unfractured wells. One-fourth of the drainage area was modeled for a fractured system (Figure 1). For the unfractured system, simulations were carried out for one-eighth of the reservoir using a variable grid size option which allowed the use of fine grids close to the wellbore.

For different cases, the model is setup differently in terms of the gridding scheme. The grid sizes for the single layer systems are provided in a study by Parekh and Sharma (2004). In the case of a three-layered system, the x-y grid pattern is kept the same as for a single-layered system and the total thickness is divided equally among each of the three layers.

Capillary Pressure and Relative Permeability. The capillary pressure is modeled using the Brooks-Corey function:

$$\left(\frac{P_b}{P_{c12}}\right)^{\lambda_d} = S_{n1} \qquad (1)$$

where λ_d is a measure of the pore size distribution of the medium, P_b is the entry pressure and P_{c12} is the capillary pressure between phase 1 and phase 2. S_{n1} is the normalized water saturation defined as:

$$S_{n1} = \frac{(S_1 - S_{1r})}{(1 - S_{1r})} \qquad (2)$$

where S_{1r} is the residual water saturation. Capillary pressures for layers with different permeability are scaled with respect to k using the J-function.

$$J = \frac{P_c}{\sigma \mathrm{Cos}\theta}\sqrt{\frac{k}{\phi}} \qquad (3)$$

The relative permeabilities for the two phases are molded as:

$$k_{r1} = k_{r1}^{0}(S_{n1})^{n_1} \qquad (4)$$

$$k_{r2} = k_{r2}^{0}(1 - S_{n1})^{n_2} \qquad (5)$$

where k_{r1}^0 and k_{r2}^0 are relative permeability end points for phase 1 and phase 2 respectively. The normalized water saturation S_{n1} is given by equation (2).

10.3.1 Reservoir Parameters. Table 1 lists the basic inputs used in the study. For a gas-water system, layers with absolute permeability of 0.001 md and 0.01 md were studied. For an oil-water system, the values of permeabilities used are 0.1 md and 1.0 md.
For the three-layered system, k = 0.1 md, 0.01md and 0.001 md were used for the top, middle and bottom layers respectively. The effect of crossflow was studied using values of k_V / k_H = 0 , 0.1 and 1.

Relative permeability curve parameters and data on physical properties of fluids are summarized in Table 2 and Table 3 respectively.

Productivity Index. In the wellbore, P_c equals zero, therefore the pressure in the gas and the water phase is the same. On the other hand, in the formation, the gas phase pressure is the sum of the water phase pressure and P_c. In low permeability reservoirs, P_c can be significant (Figure 2). The productivity index (PI) for a gas well is defined as the gas flow rate at standard conditions for unit pressure drawdown in the gas phase.

$$PI = \frac{q_{gas}}{\left(\overline{P}_{gas} - P_{wf}\right)} \qquad (6)$$

10.3.2 Interpretation of Output Data. Simulations were initialized by injecting sufficient water to achieve a desired depth of invasion and then the well was flowed back using typical capillary pressure and relative permeability relationships for tight sands. For each parameter set, a comparison was made with the uninvaded case. The results of the study indicate how the productivity of the well improves with time and what kinds of fluid returns are obtained.

A productivity half recovery time ($R_{1/2}$) is defined as the time when the productivity index for the invaded case (PI) reaches 50% of the productivity index for the uninvaded case (PI_0).

$$R_{1/2} = \text{Time}_{\left(PI / PI_0 = 0.5 \right)} \qquad (7)$$

The output from the simulations is presented in terms of:

- Productivity half recovery time, $R_{1/2}$
- Percentage of water recovered, R_{iw}

10.4 CLEANUP OF WATER BLOCKS IN GAS WELLS

10.4.1 Base Case Simulation Results. The results for base case scenarios are presented in Table 4 and Table 5. Table 4 shows results for a single-layer system. Figure 3 to Figure 6 show the saturation profile and the production history for the base cases for various single-layer scenarios. A saturation profile plot reveals the variation in S_w in the reservoir with time. The plot shows the initial water distribution generated by injecting water and how it changes with time once the well is put back on production. This plot helps to visualize the extent of cleanup taking place over time for a given set of conditions.

Figure 3 shows that for this particular base case, the PI does not recover beyond 50% of PI_0 even after 200 days of production. This is because the capillary forces (P_c = 1475 psi) are comparable to the drawdown (= 1675 psi). Significant amounts of water remains permanently trapped in the formation as S_w does not drop down to its value prior to invasion. For the fractured gas-water system the recovery in the productivity takes place over 150 days.

10.4.2 Effect of Drawdown in Gas Wells. Figure 7 and Figure 8 show the effect of drawdown on the half recovery time ($R_{1/2}$) and the invaded water recovery (R_{iw}), respectively, for a layer with k = 0.001 md (P_c at S_{wr} = 1475 psi). For the unfractured case, it can be seen that when $P_{d/c}$ (which is defined as the ratio of drawdown to capillary pressure) is close to unity, $R_{1/2}$ is more than 1000 days ($PI / PI_0 = 0.24$ on 1000th day). The curve for $R_{1/2}$ becomes asymptotic to the y-axis when $P_{d/c}$ is close to unity suggesting that when drawdown is less than the capillary pressure gas productivity may be permanently hampered. As $P_{d/c}$ increases, $R_{1/2}$ reduces rapidly and for $P_{d/c}$ greater than 3 it nearly becomes asymptotic to the x-axis indicating that further increases in drawdown do not result in much improvement. At lower drawdowns, the water in the region adjacent to the wellbore does not flow, blocking the flow of gas.

It is observed that the water saturation around the wellbore decreases as the drawdown increases. By the 100th day, the water saturation adjacent to the wellbore is reduced to 60% for $P_{d/c} = 1$, but beyond that there is not much change in S_w adjacent to the wellbore (Figure 4). It is interesting to note that the water saturation never drops to the residual value. This is due to the shape of the relative permeability curve, which effectively renders the water immobile below a certain saturation for a particular drawdown. From Figure 8 it can also be seen that there is an increase in R_{iw} with increase in drawdown and it plateaus at around 60%, confirming the previous observation that not all of the water is recovered.

For the fractured case, there is a decline in the $R_{1/2}$ as the $P_{d/c}$ increases. When compared to the unfractured system, the absolute value of $R_{1/2}$ is small. It can also be seen from Figure 8 that R_{iw} is less than 20% suggesting that not all of the water is recovered. Though the percentage of water recovery is less than the unfractured case, productivity recovers faster due to larger flow area provided to gas by the fracture and early set in of the gas production after the cleanup of water near the wellbore.

For a horizontal well, trends observed are similar to that for a vertical well. For a given drawdown, the gas flow rate for a horizontal well is more than that for an unfractured vertical well but less than the gas flowrate from a fractured vertical well. Accordingly, the $R_{1/2}$ for a horizontal well is in between the fractured and unfractured cases. Figure 9 shows the results for a vertical well, with and without a fracture, in a layer with k = 0.01 md. Again, the trends are similar to that for the layer with k = 0.001 md but the absolute value of $R_{1/2}$ is less due to higher flowrates in the more permeable layer. Thus it can be said that as the ratio of the drawdown to P_c increases, higher production rate, faster recovery in productivity index and better flowback of invaded water is achieved.

10.4.3 Effect of Capillary Pressure Curves. Figure 10 shows a decrease in $R_{1/2}$ with an increase in capillary pressure endpoint for the same wellbore pressure (P_{wf}). The pressure differential in the gas phase increases which results in higher gas flow rates. This improves the gas productivity index and thus lowers the $R_{1/2}$. On the other hand, it has no effect on the pressure differential in the water phase so the water recovery (R_{iw}) trend remains nearly flat with an increase in the end-point P_c.

Figure 11 shows the effect of the shape of the P_c – S_w curve. The capillary pressure exponent (λ_d) is a measure of the pore size distribution. Larger λ_d values suggest a narrower distribution. This means that for higher λ_d values, pore size variations are small and do not have an impact on the productivity for a given drawdown. On the other hand, R_{iw} increases slowly with an increase in λ_d (Figure 12). This is because, for higher λ_d, capillary pressures are lower at a given S_w, thus, more water is recovered. This drops S_w to a lower value around the wellbore for the same drawdown.

For a fractured well, $R_{1/2}$ increases with an increase in the capillary pressure curve exponent. This reversal in trend is likely due to the predominant impact of effective fracture length on the productivity index as compared to that of the direct benefit obtained from greater recovery of water with an increase in λ_d. This is because even though the fracture may be long, the presence of water reduces the effective fracture length available to the gas.

10.4.4 Effect of Relative Permeability Curves. The effect of the shape of the gas relative permeability curve on the gas productivity for the layer with k = 0.001 md is shown in Figure 13. As the gas exponent increases, $R_{1/2}$ increases. This is due to decreasing relative permeability to gas which results in lower gas production on the one hand and an increase in water recovery on the other. The shape of the $R_{1/2}$ curve suggests that it is highly sensitive to changes in the gas exponent.

The effect of the shape of the water relative permeability curve on productivity of gas is shown in Figure 14. $R_{1/2}$ increases with an increase in the water exponent due to a reduction in the relative permeability to water at a given saturation. This causes the rock to hold more of the invaded water at a particular drawdown resulting in a lower gas saturation, hence lower permeability to gas.

Figure 15 shows the sensitivity of $R_{1/2}$ and water recovery to the end point water relative permeability (k_{rw}^0). There is a decrease in $R_{1/2}$ with an increase in k_{rw}^0. This is because water flows at a higher rate at the same S_w for higher k_{rw}^0. Thus, the water block cleans up faster and hence lowers $R_{1/2}$. As with previous parameters, S_w in the vicinity of the wellbore does not drop to S_{wr} due to the small k_{rw} for $S_w \rightarrow S_{wr}$. While studying the sensitivity of $R_{1/2}$ and water recovery to the end point gas relative permeability (k_{rg}^0), it appeared that $R_{1/2}$ and R_{iw} are independent of the k_{rg}^0 value.

10.4.5 Effect of Depth of Water Invasion. $R_{1/2}$ increases rapidly as the depth of invasion (DOI) increases (Figure 16). This is to be expected as it takes longer for the additional water to be displaced from the pores. The invasion depth determines the pressure profile in both the phases, which control the pressure gradients close to the wellbore. It was observed that, for small DOI, the pressure gradient is steep as compared to the case with a large DOI. Larger gradient facilitates rapid cleanup so the water saturation drops quickly until relative permeability effects become more important than capillary pressure effects.

The trend of $R_{1/2}$ is similar for a fractured case, although not as steep, as observed in the unfractured system. On flowing back, for greater DOI, gas has to wait longer until sufficient relative permeability to the gas is established to restore productivity. Once the gas breaks through, the relative mobility of water in the fracture, at some distance from the wellbore, becomes small, delaying cleanup. This explains the slow increase in R_{iw}.

10.4.6 Effect of Fracture Geometry. The effect of fracture geometry is studied using two different approaches. In the first approach, the amount of water injected (W_{inj}) is kept constant for different fracture lengths, while in the second approach, a fixed depth of water invasion is considered while varying the fracture length.

Figure 17 shows the results with a constant W_{inj}. It can be seen that as the fracture length increases, the recovery in productivity is faster. This is because, for a fixed volume of water injected, the depth of invasion decreases with increasing fracture length and, as was seen earlier, $R_{1/2}$ decreases for smaller DOI. For smaller fractures, gas flow rates are small, which also contribute to longer $R_{1/2}$. It may be inferred that as fracture length approaches zero, $R_{1/2}$ will approach that for an unfractured well for same W_{inj} due to greater DOI and low flow rate.

Figure 18 shows that $R_{1/2}$ increases with an increase in the fracture length for a fixed DOI. When the well is put on production, initially some water cleans up in the vicinity of the wellbore and gas flow is established. As soon as enough gas saturation builds up in the fracture near the wellbore, the relative mobility of the water is reduced, delaying further recovery.

For the uninvaded case, the area available for the gas flow is fixed, as there is no mobile water. On the other hand, for the invaded case, there is an increase in the effective fracture length with time as water cleans up farther away from the wellbore resulting in improved productivity. For longer fractures, it takes more time for the distant water to clean up and the presence of high water saturation in and along the fracture adversely effects the recovery in gas productivity.

Figure 19 shows the sensitivity of $R_{1/2}$ and R_{iw} to fracture width. $R_{1/2}$ decreases and R_{iw} increases with increase in fracture width. In fractures, capillary pressures are low, so as width increases, more water is able to move before gas relative permeability takes over. With an increase in the width, fracture conductivity increases, hence the flow rates are higher resulting in quicker recovery.

10.4.7 Effect of Horizontal Well Length. Half recovery time is found to be insensitive to the horizontal well length as the flow area per unit length remains the same. This means that cleanup rate per unit length will remain the same for a given time even though the total flow rate is higher for a longer well.

10.4.8 Effect of Heterogeneity. To understand the effect of heterogeneity, a three-layered system is modeled with top layer having k = 0.1 md and referred to as 'high perm' layer. Middle and bottom layers have k = 0.01 md and 0.001 md respectively and are termed as 'medium perm' and 'low perm' layers. Vertical permeability is an additional variable considered. When k_v equals zero, each layer is found to behave as an independent unit. It can be seen from Figure 20 that the water saturations adjacent to the wellbore for different layers approach each other suggesting that the duration for cleanup is a strong function of cumulative gas flow in the absence of crossflow between layers. Even in the 'high perm' layer, cleanup becomes very gradual below $S_w = 0.55$ because of the dominance of relative permeability effects.

Figure 21 shows the result of simulations carried out for four different drawdowns and two sets of vertical permeabilities. On considering the entire system as a single unit, the half recovery time is fairly small due to the major contribution coming from the 'high perm' layer. The behavior of the system as a single unit does not show the extent of cleanup in various layers, therefore, each layer's behavior is evaluated separately. Due to the presence of crossflow, the cleanup in layers with different permeabilities is found to be different as compared to the case when there is no vertical permeability. Crossflow favors early recovery of productivity for the 'high perm' layer whereas it delays the cleanup in the other two layers. This is because vertical communication permits the gas to take a path along which a high gas relative permeability is established i.e. through the 'high perm' layer. For layers with lower permeability, it takes longer for the productivity to recover. For the period simulated (100 days) the 'low perm' layer does not cleanup much, as shown in Table 6. When k_v is 10% of k_H the productivity for the 'low perm' layer recovers to only 38 % even for a high drawdown of 3700 psi. For higher k_v the extent of recovery is further suppressed ($PI/PI_0 = 29\%$ for $k_v = k_H$).

On observing the trend of water recovery it appears that it is not very sensitive to variations in vertical permeability although increase in crossflow slightly reduces the amount of water recovered. This is due to reduced cleanup of 'low' and 'medium' perm layers.

In the presence of a fracture, the trends of the half recovery time and the water recovery are similar to the unfractured case.

10.5 CLEAN-UP OF WATER BLOCKS IN OIL WELLS

Some of the important observations for oil wells are discussed below.

10.5.1 Effect of Drawdown. Figure 22 show the effect of the drawdown on half recovery time ($R_{1/2}$) and invaded water recovery (R_{iw}) for a layer with k = 0.1 md (P_c at S_{wr} = 147 psi). For an unfractured well, the trends are similar to those observed for the gas-water system.

Figure 22 shows that the $R_{1/2}$ curve starts to flatten beyond $P_{d/c} = 2.5$. This is similar to the trend seen for the gas-water system (Figure 7) suggesting that a further increase in drawdown does not result in much improvement. It can be inferred that it is the ratio of the drawdown to the P_c that is an important parameter rather than the absolute value of the drawdown.

10.5.2 Effect of Capillary Pressure Curves. Figure 23 shows the effect of capillary pressure curve end point for k = 0.1 md. It indicates a decrease in $R_{1/2}$ and R_{iw} with an increase in capillary pressure endpoint for the same wellbore pressure (P_{wf}). Change in capillary pressure endpoint alters the drawdown in the oil phase but the pressure differential in water phase remains the same. At higher capillary pressure endpoint, total fluid volume produced remains the same for a given P_{wf} but oil cut increases. This explains the trends observed for $R_{1/2}$ and R_{iw}. This suggests that as capillary pressure endpoint increases, S_w also creeps up as more oil flows under higher pressure differential compared to the water.

Figure 24 shows that beyond some value of capillary pressure exponent (λ_d) there is not much change in $R_{1/2}$ for the unfractured oil-water system. On the other hand, $R_{1/2}$ increases with an increase in the λ_d. This behavior is the same as for a gas-water system.

10.5.3 Effect of Wettability. A few runs were conducted to study the effect of wettability in a fractured oil-water system with k = 0.1 md (Table 7). Two sets of drawdown (250 psi and 1000 psi) and three sets of capillary pressure curves and relative permeability curves were used.

Figure 25 shows the oil production trend for a drawdown of 1000 psi for two different sets of relative permeability curves (Set I and Set III of Table 8). It can be observed that, with the same P_c curve (as in Case 1 and Case 2 of Table 7), as the k_r curves shift toward a more oil-wet scenario it takes a longer time for the oil production to recover. For Case 1, recovery is almost immediate but for Case 2 it takes nearly two months to match the production rate for an unflushed case. This is because of a reduction in the relative permeability to oil. This explains the longer recovery time for Case 2 as compared to Case 1 as seen in Figure 26. Using Set III relative permeability curves results in an increased relative permeability to water for a given value of S_w, thus, a higher water recovery is reflected in Figure 26 for Case 2.

Using the same set of relative permeability curves but varying P_c for a drawdown of 1000 psi (Case 2 and Case 3) also affects the production rates. For lower P_c (Case 3) the half recovery time as well as the water recovery is more (Figure 26). This is because at lower P_c, water is able to move more freely. More water is produced for a given drawdown, though the total volume of fluid production remains the same in the given time period for both the cases. This is in line with earlier findings that at lower P_c, there will be a better cleanup of water blocks. Once the majority of water is produced, oil production is observed to recover quickly. This shows that cleanup of water block is dependent on total fluid flow which, in turn, depends on the drawdown. For example, with Set III relative permeability curves (Figure 27), oil production reaches a plateau value in 2 weeks for a drawdown of 1000 psi (Case 2 and Case 3). On the hand, when the drawdown is 250 psi (Case 6 and Case 8), the trends suggest that recovery is not complete even in 100 days. Recovery time is more for Case 8 as P_c is low and water flows for a longer time.

For a drawdown of 250 psi for three sets of P_c and k_r curves each, the trends were found to be the same as observed for higher drawdown but cleanup continues over a longer time as flow rates are small.

It can be concluded that cleanup is faster at higher drawdowns for a given set of conditions. More water is recovered by shifting the relative permeability curves from strongly water-wet to intermediate wetting. This shift delays recovery of oil productivity by adversely affecting the oil relative permeability. Furthermore, lowering of P_c also favors water cleanup but it is also at the cost of oil productivity during the early period. The observations with respect to the altering of the wettability from strongly water-wet towards oil-wet can be extended to a gas-water system. By making the formation less water-wet, it is possible to achieve early and better cleanup of water without affecting the gas relative permeability, which may result in early recovery in productivity.

10.6 SUMMARY

The detailed parametric study conducted here for a gas-water system and an oil-water system show the effect of various factors on the cleanup of the water blocks. Some key parameters which have a strong influence on the cleanup of water blocks and hence on gas or oil productivity are:

- Drawdown,
- Formation permeability
- Fracture length,
- Shapes of relative permeability curves,
- Volume of water leak-off and formation hetetogeneity.

1. An increase in drawdown results in higher production rates which accelerates the cleanup. This helps to achieve the goal of early recovery of the productivity. However, it was also seen that the benefit of applying larger drawdowns become less significant as the ratio of the drawdown to the capillary pressure increases. This suggests that the effect of water blocks can be greatly reduced but cannot be totally eliminated by applying very high drawdowns. In the fractured oil-water system the effect of applying high drawdowns is less significant. Nevertheless, an increase in drawdown in a fractured oil-water reservoir favors quicker recovery of the invaded water.
2. The effect of changing the capillary pressure curve end point is to alter the draw down in the non-wetting phase only. A P_c curve end point steps up the gas/oil flowrate but has no effect on the water flowrate. Thus, a reduction in the productivity recovery time is observed but it is not as rapid as seen for large drawdowns due to limited variations in the water recovery.
3. Simulation of cases with varying fracture length revealed that, for longer frac tures, the productivity recovers faster when the volume of injected water was kept constant as the amount of depth of invasion is reduced. On the other hand, with a fixed depth of water invasion for different fracture lengths, it was observed that recovery in the productivity is delayed for longer fractures and water recovery is also comparatively low.
4. An increase in the relative permeability curve exponents has an impact that is similar

to lowering the flowrate. A reduction in flowrate, either for gas/oil, water or for both, delays the cleanup of the invaded water. This results in slower recovery in productivity. The PI recovery time is observed to be very sensitive to the flowrates.

5. Greater leak-off (deeper invasion) results in longer recovery times. Furthermore with increase in depth of invasion it becomes more difficult for the water to flowback resulting in lower water recovery.
6. For multi-layered reservoirs, presence of crossflow favors early recovery of the pro ductivity from layers with higher permeability and delays the cleanup of the water block from low permeability layers.
7. Altering wettability from strongly water-wet to intermediate wetting or even oil-wet improves recovery of invaded water but hampers the oil productivity at early times.

The cleanup time increases at lower drawdowns.

On the other hand, the following parameters were found to have a smaller impact on cleanup:

- Fracture width,
- Relative permeability curve end points,
- Pore size distribution, and
- Horizontal well length

8. With an increase in the fracture width, a slight improvement is obtained in the gas/oil productivity which results in comparatively early recovery. This is because of the increase in fracture conductivity with increase in the width. The gain is perceptible up to a certain fracture width beyond which not much of a benefit is seen.
9. Recovery of productivity and invaded water are found to be insensitive to the gas/oil relative permeability curve end point. On the other hand, an increase in water relative permeability curve end point facilitates rapid cleaning of the invaded water so an early recovery is seen. Nevertheless, there is no gain in the overall amount of the water recovered.
10. Variation in pore size distribution accounted for by the shape of capillary pressure curve appears to have a limited effect on the cleanup of the water block and the time of recovery of the gas/oil productivity.

11. Cleanup of water block and recovery in productivity were found to show no depend ence on the horizontal well length. This is primarily because the pressure drop along the wellbore is small relative to the drawdown.

10.7 CONCLUSIONS

From the study, it can be concluded that rapid and thorough cleanup can be achieved by:

- Ensuring that the drawdown is at least three times the capillary pressure. In cases where this ratio is not attainable, extreme care should be exercised when using water-based fluids in the well and proper measures must be taken to minimize leak-off.
- Reducing leak-off as the time for PI recovery is directly proportional to the depth of invasion.
- The use of additives in stimulation fluids to lower the capillary pressure can be potentially beneficial. This can be achieved by reducing interfacial tension and/or altering wettability of the rock surface from strongly water-wet to intermediate-wet. This allows for better cleanup at lower drawdowns.

10.8 REFERENCES

1. Holditch, A. S.: Factors Affecting Water Blocking and Gas Flow from Hydraulically Fractured Gas Wells. JPT, Dec 1979.
2. Penny, G. S., Soliman M. Y., Conway M. W. and Briscoe J. E.: Enhanced Load Wa ter-Recovery Technique Improves Stimulation Results. Paper SPE 12149 presented at the 1983 SPE Annual Technical Conference and Exhibition held in San Francisco, CA, October 5-8.
3. Abrams, A. and Vinegar, H. J.: Impairment Mechanisms in Vicksburg Tight Gas Sands. Paper SPE/DOE 13883 presented at the 1985 SPE/DOE Joint Low Permeability Gas Reservoirs Symposium held in Denver, Colorado, May 19-22.
4. McLeod, H.O. McGinty, J. E. and Smith, C. F.: Deep Well Stimulation with Alcoholic Acid. Paper SPE 1558 presented at the 1966 SPE Annual Fall Meeting held in Dallas, Texas, October 2-5.

5. McLeod, H. O. and Coulter, A. W.: The Use of Alcohol in Gas Well Stimulation. Pa per SPE 1663 presented at the 1966 SPE Eastern Regional Meeting held in Columbus, Ohio, November 10-11.
6. Kamath, J. and Catherine, L.: Laboratory Based Evaluation of Gas Well Deliver ability Loss Due to Waterblocking. Paper SPE 63161 presented at the 2000 SPE Annual Technical Conference and Exhibition held in Dallas, Texas, October 1-4.
7. Mahadevan, J. and Sharma, M.M.: Clean-up of Water Blocks in Low Permeability Formations. Paper SPE 84216 presented at the SPE Annual Technical Conference and Exhibition held in Denver, Colorado, October 5 – 8, 2003.
8. Naji S.: Field Scale Simulation of Chemical Flooding. Ph.D. Dissertation, The Uni versity of Texas, Austin, 1989.
9. Delshad M., Pope G.A., Sepehrnoori K.: A Compositional Simulator for Modeling Surfactant Enhanced Aquifer Remediation,1: Formulation. JCH 23 (1996) 303-327.
10. Technical Documentation for UTCHEM: A Three-Dimensional Chemical Flood Simulator.
11. Parekh, B.: Cleanup of Water Blocks in Depleted Low-Permeability Reservoirs. Mas ters Thesis, The University of Texas at Austin, 2003

Table 1: Input parameters for the model (base case)

Length (feet)	6000
Breadth (feet)	6000
Thickness (feet)	50
Porosity %	20
Initial water saturation (gas-water system)	0.2
Initial water saturation (oil-water system)	0.3
Compressibility of rock (psi^{-1})	2×10^{-6}
Capillary curve endpoint	3.3
Capillary curve exponent	1.2
Initial reservoir pressure (psi)	6000
Well radius (feet)	0.175
Fracture length (feet)	500
Fracture width (inches)	0.2
Horizontal well length (feet)	1500
Depth of water invasion (feet)	1.8

Table 2: Relative permeability curve parameters used for base case

	Gas-Water System		Oil-Water System	
	Water	Gas	Water	Oil
Residual saturation (S_{ir})	0.2	0.2	0.3	0.2
Endpoint (k_{ri}^0)	0.2	0.9	0.2	0.6
Exponent (n_i)	3	2	3	2

Table 3: Physical parameters of fluids

	Viscosity (cp)	Compress-ibility 10^{-6} (psi^{-1})	Specific Gravity (psi/ft)	Interfacial Tension (dyne/cm)
Gas	0.0254	110	0.0085	40
Oil	2	12	0.35	25
Water	0.7	3	0.433	

Table 4: Results for the base cases for single-layered system

Scenario	Half Recovery Time (Days)	Water Recovery (%)
Gas-Water System		
Vertical unfractured well (k = 0.001 md)	240	34%
Vertical unfractured well (k = 0.01 md)	10	60%
Vertical fractured well (k = 0.001 md)	35	13%
Vertical fractured well (k = 0.01 md)	8	13%
Horizontal unfractured well (k = 0.001 md)	104	25%
Oil-Water System		
Vertical unfractured well (k = 0.1 md)	17	52%
Vertical unfractured well (k = 1.0 md)	1.6	80%
Vertical fractured well (k = 0.1 md)	4.7	58%

Table 5: Results for the base cases for three layered system

Three-layered Gas Reservoir	Half Recovery Time Unfractured $k_V = k_H$	Unfractured $k_V = 0.1\ k_H$	Fractured $k_V = k_H$
layer 1	7	10	3.5
layer 2	#	#	32
layer 3	#	#	#

The runs were conducted for 100 days during which PI for the layer did not recover to 50 %. For these layers, the table below lists the PI/ PI_O on the 100 th day.

Three-layered Gas Reservoir	Ratio of Productivity Indicies Unfractured $k_V = k_H$	Unfractured $k_V = 0.1\ k_H$	Fractured $k_V = k_H$
layer 1	**	**	**
layer 2	39%	42%	**
layer 3	12%	18%	28%

** - not required as half recovery time is available

Table 6: Effect of drawdown and k_v in 'low perm' layer for three-layered gas-water system with one vertical well.

	For low k layer, PI/PIo (in 100 days)		
Drawdown	Unfractured		Fractured
PSI	Kv = 0.1 Kh	Kv = Kh	Kv = Kh
900	0.18	0.12	0.28
1335	0.22	0.15	0.32
2700	0.32	0.23	0.40
3700	0.38	0.29	0.50

Table 7: List of runs for fractured oil-water system to study the effect of wettability (k = 0.1 md)

Cases	k_r curves	P_c end point	P_c exponent	Drawdown
1	Set I	3.3	1.2	1000 psi
2	Set III	3.3	1.2	1000 psi
3	Set III	0.033	1.2	1000 psi
4	Set I	3.3	1.2	250 psi
5	Set II	3.3	1.2	250 psi
6	Set III	3.3	1.2	250 psi
7	Set II	0.33	1.2	250 psi
8	Set III	0.033	1.2	250 psi

Table 8: Parameters used to generate various relative permeability curves to study the effect of wettability in fractured oil-water system (k = 0.1 md)

Set	k^o_{ro}	k_{rw}	n_o	n_w
I	0.6	0.2	2	3
II	0.5	0.5	2	2
III	0.2	0.6	3	2

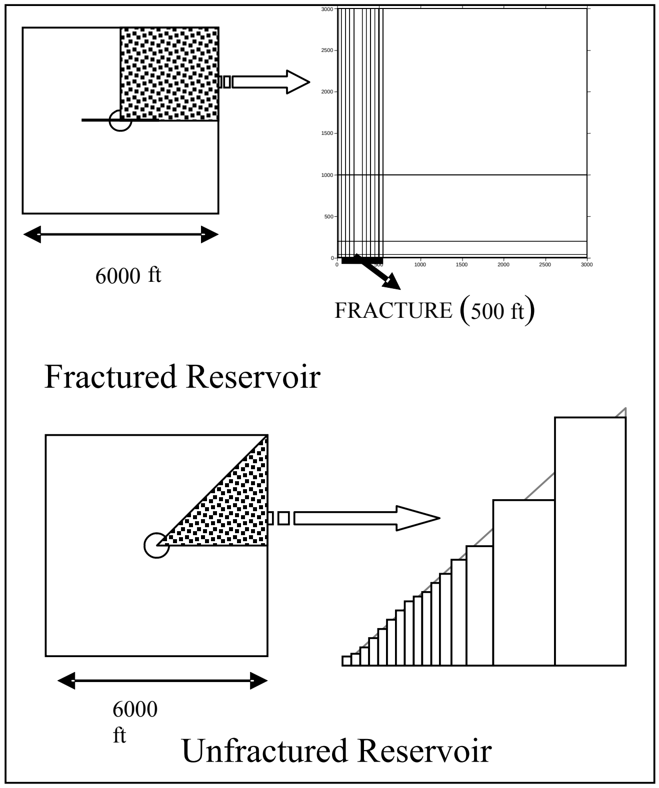

Figure 1: Different gridding schemes

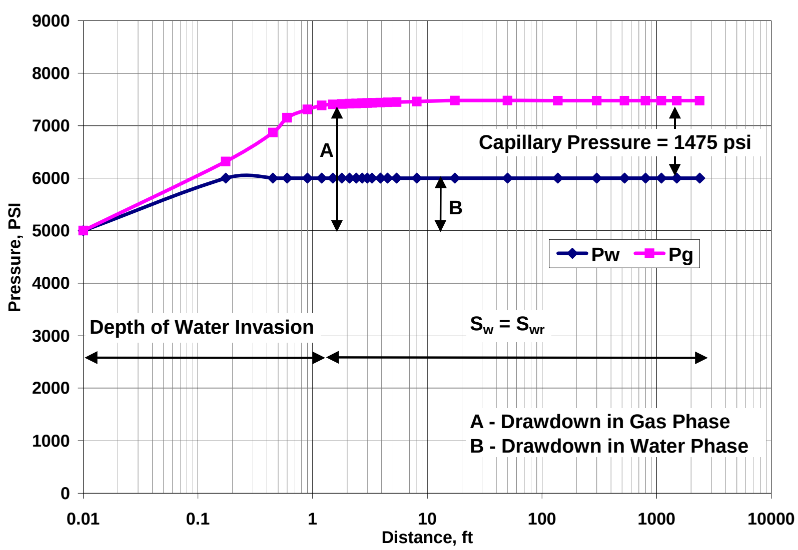

Figure 2: An illustration of the pressure profile in gas and water phases in presence of significant capillary pressures.

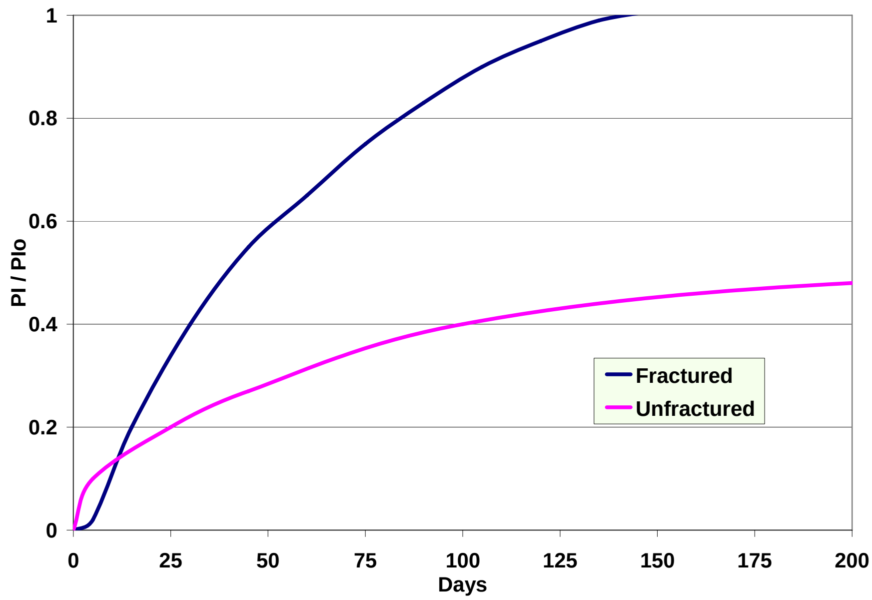

Figure 3: Half recovery time for drawdown of 1675 psi in gas-water system with one vertical well (k = 0.001 md).

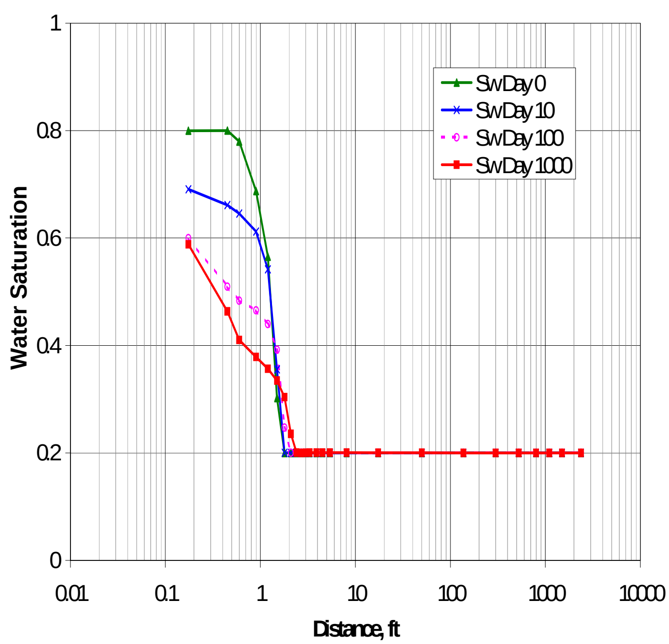

Figure 4: Saturation profile for drawdown of 1675 psi in unfractured gas-water system with one vertical well (k = 0.001 md).

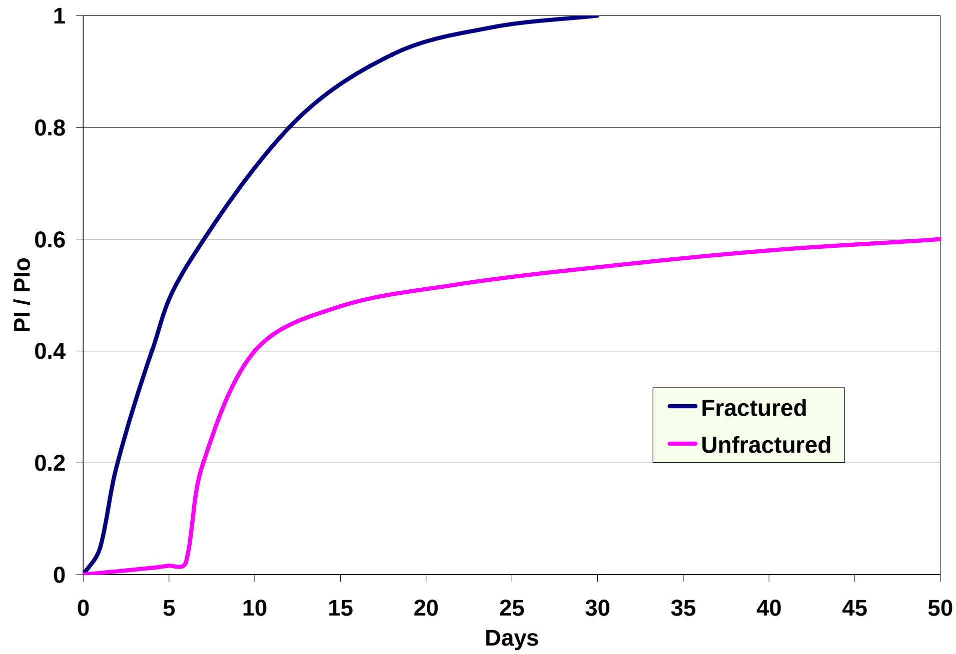

Figure 5: Production history for drawdown of 250 psi in oil- water system with one vertical well (k = 0.1 md).

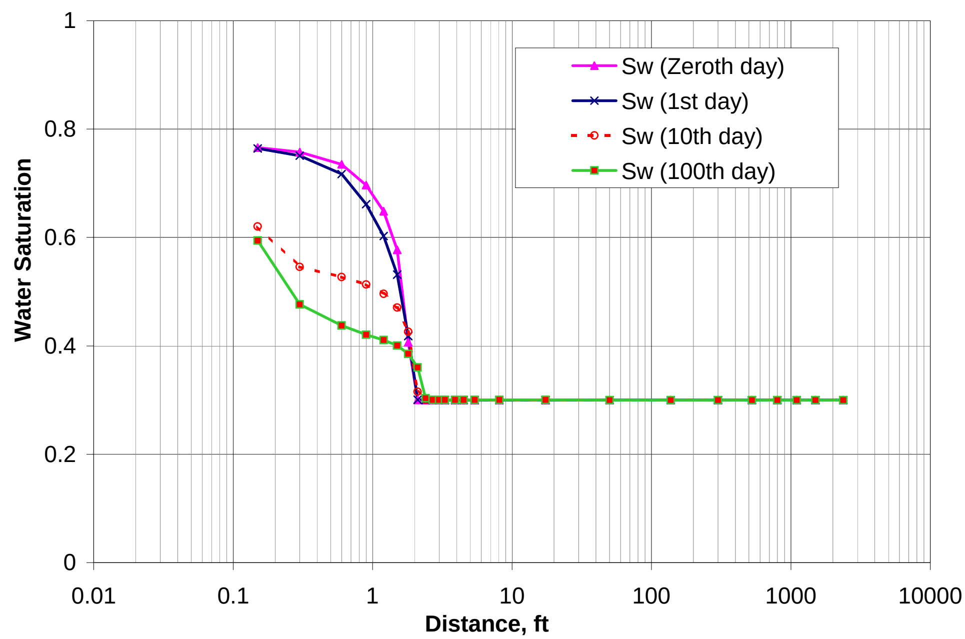

Figure 6: Saturation profile for drawdown of 250 psi in unfractured oil-water system with one vertical well (k = 0.1 md).

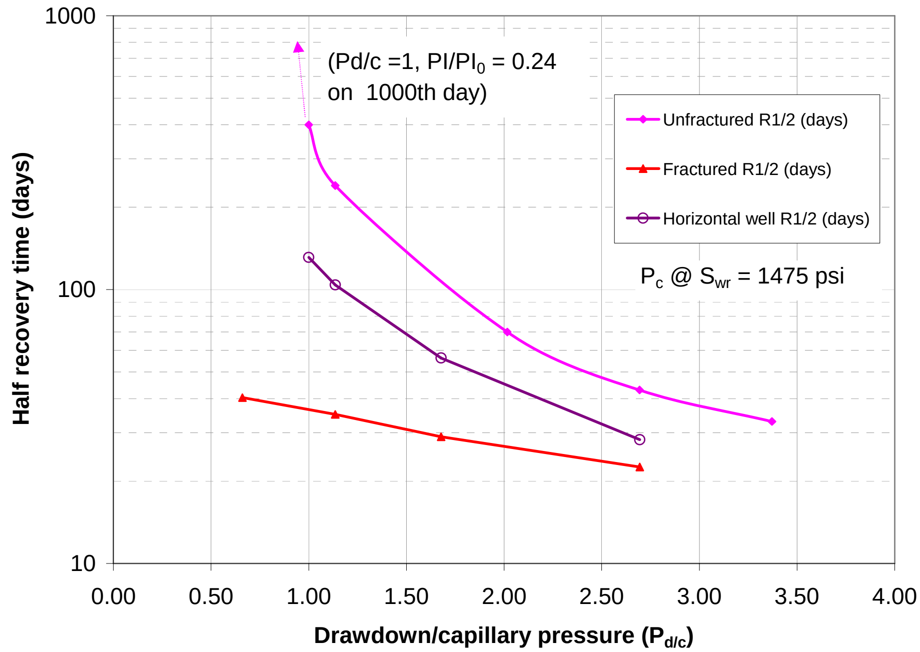

Figure 7: Effect of $P_{d/c}$ on half recovery time in gas-water ($k = 0.001$ md).

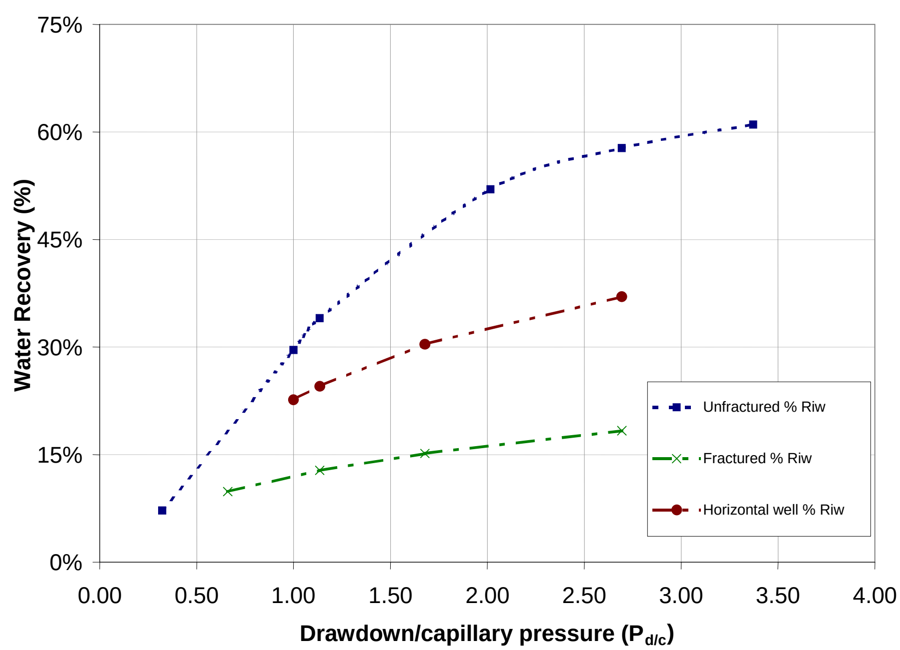

Figure 8: Effect of $P_{d/c}$ on water recovery in gas-water system ($k = 0.001$ md).

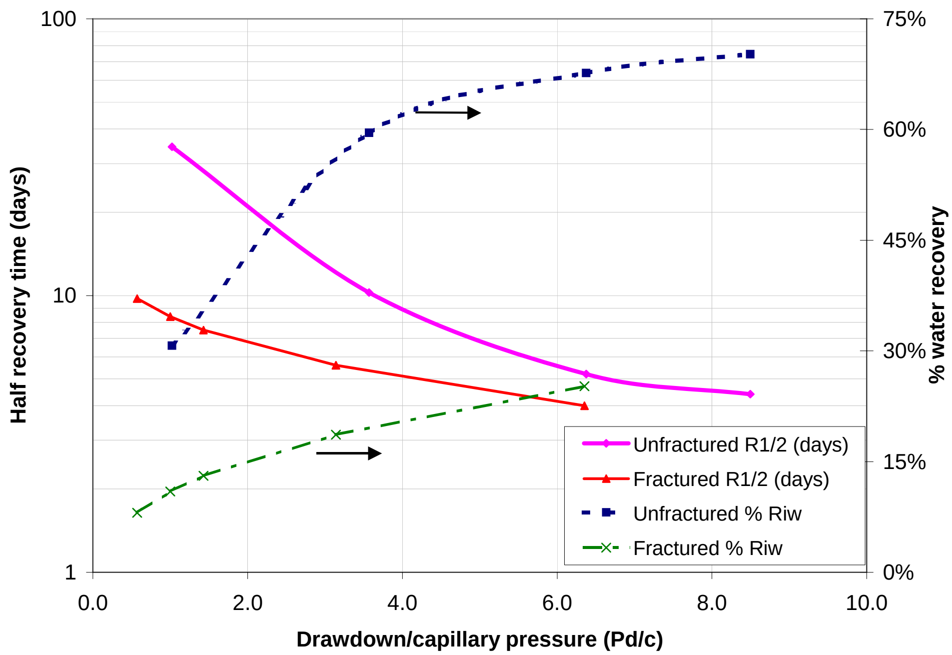

Figure 9: Effect of $P_{d/c}$ in gas-water with one vertical well (k = 0.01 md).

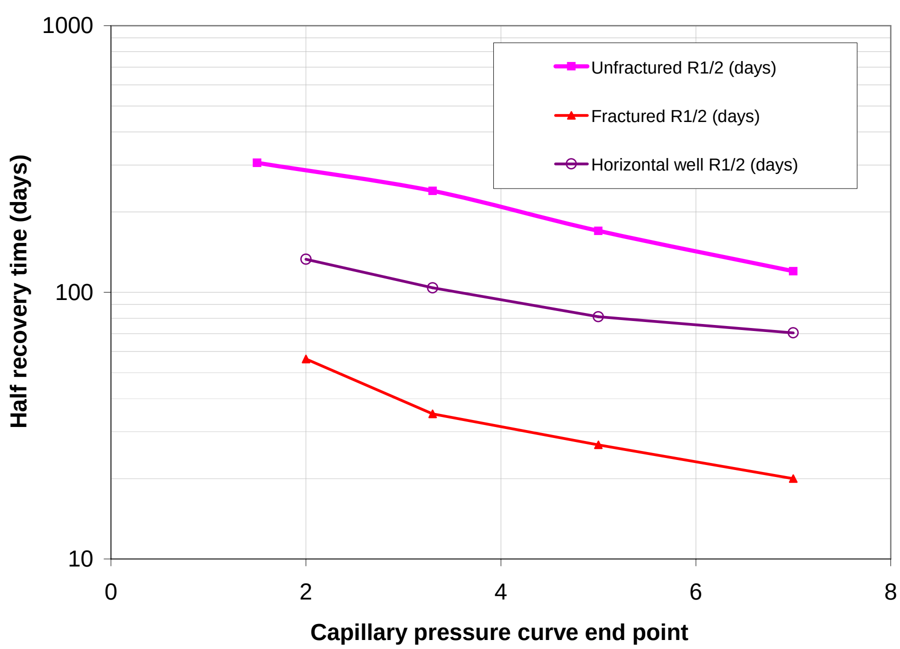

Figure 10: Effect of capillary pressure curve endpoint on half recovery time in gas-water system (k = 0.001 md).

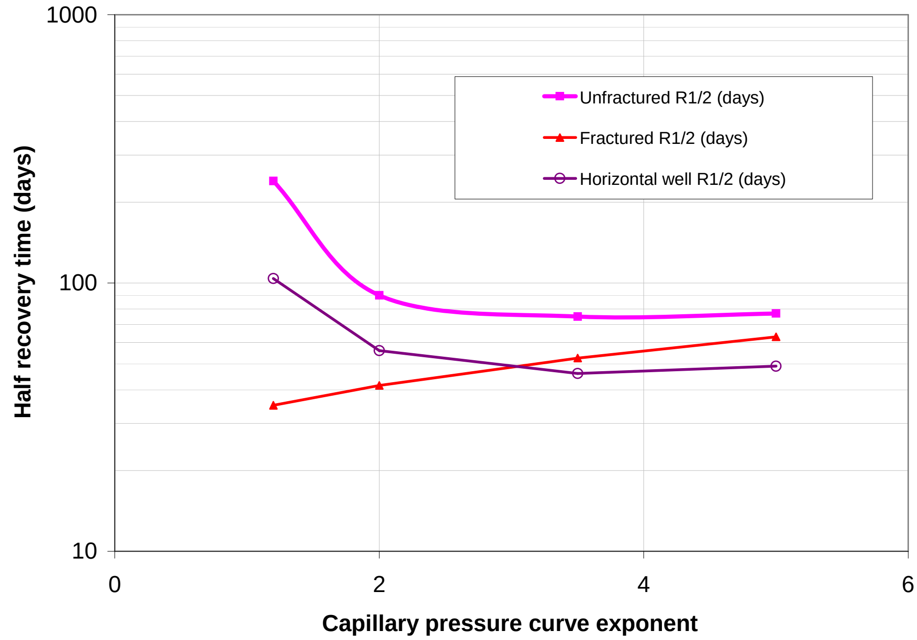

Figure 11: Effect of capillary pressure curve exponent on half recovery time in gas-water system .

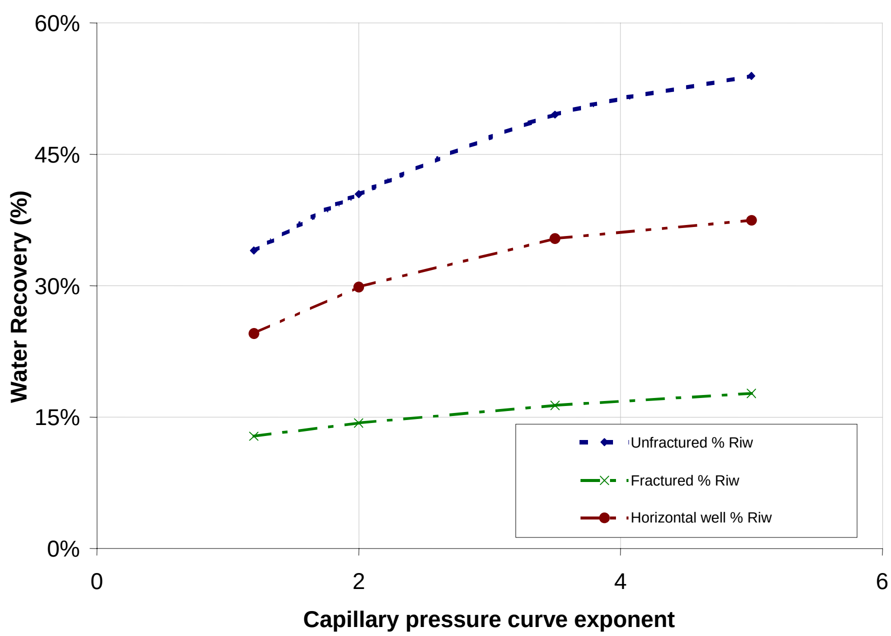

Figure 12: Effect of capillary pressure curve exponent on water recovery in gas-water system.

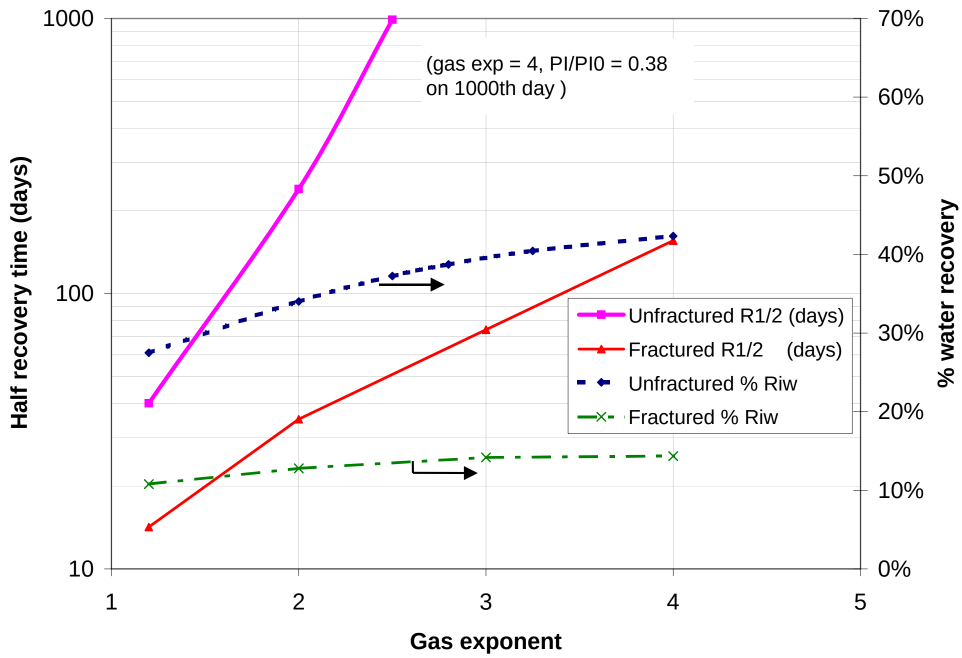

Figure 13: Effect of gas exponent in gas-water system with one vertical well .

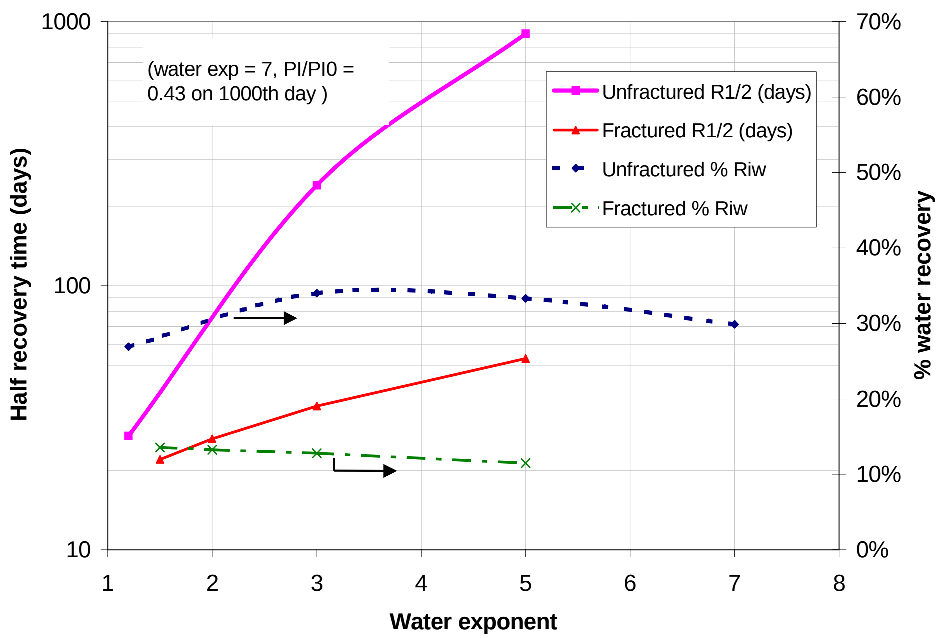

Figure 14: Effect of water exponent in gas-water system with one vertical well.

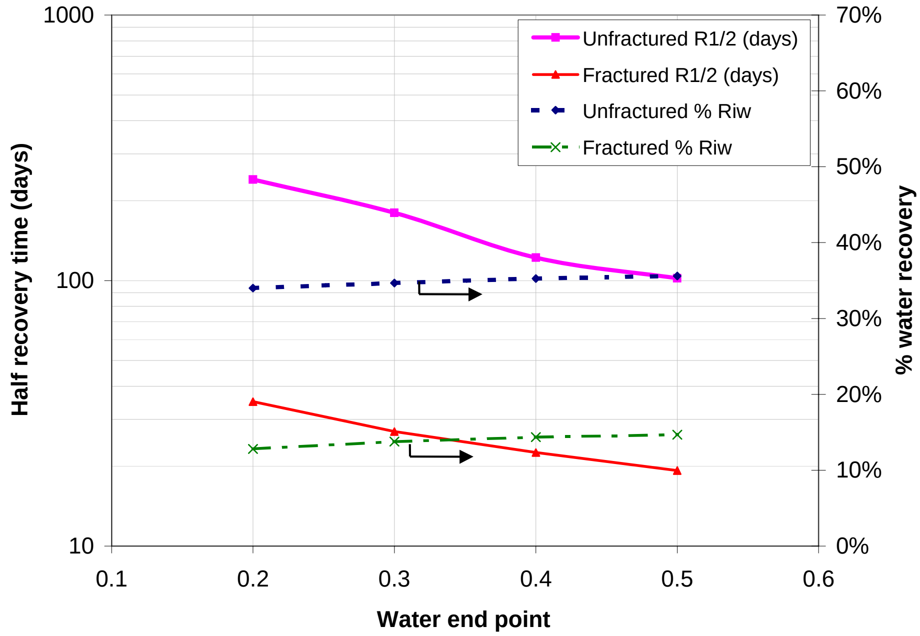

Figure 15: Effect of water end point in gas-water system with one vertical well.

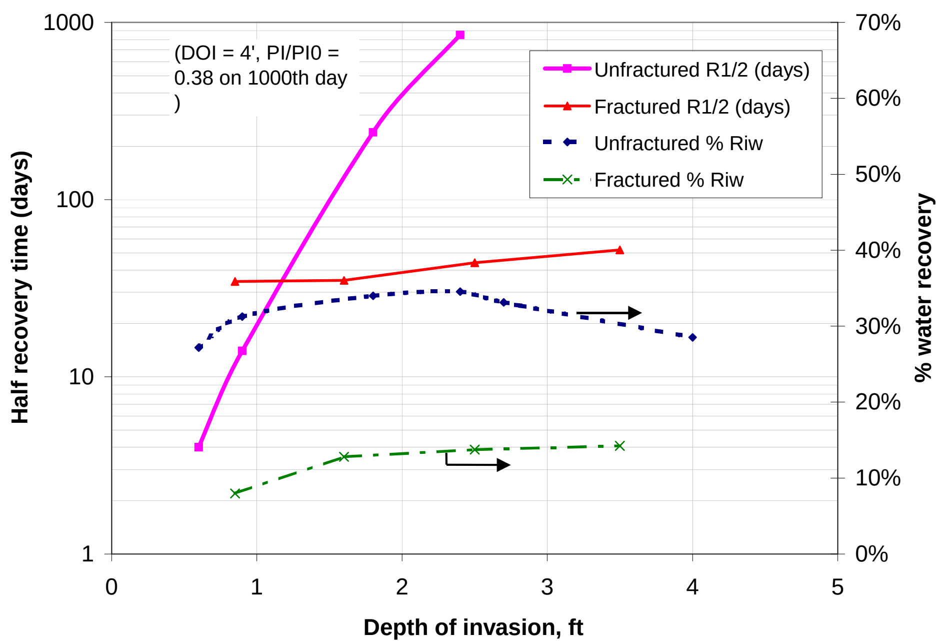

Figure 16: Effect of depth of invasion in gas-water system with one vertical well.

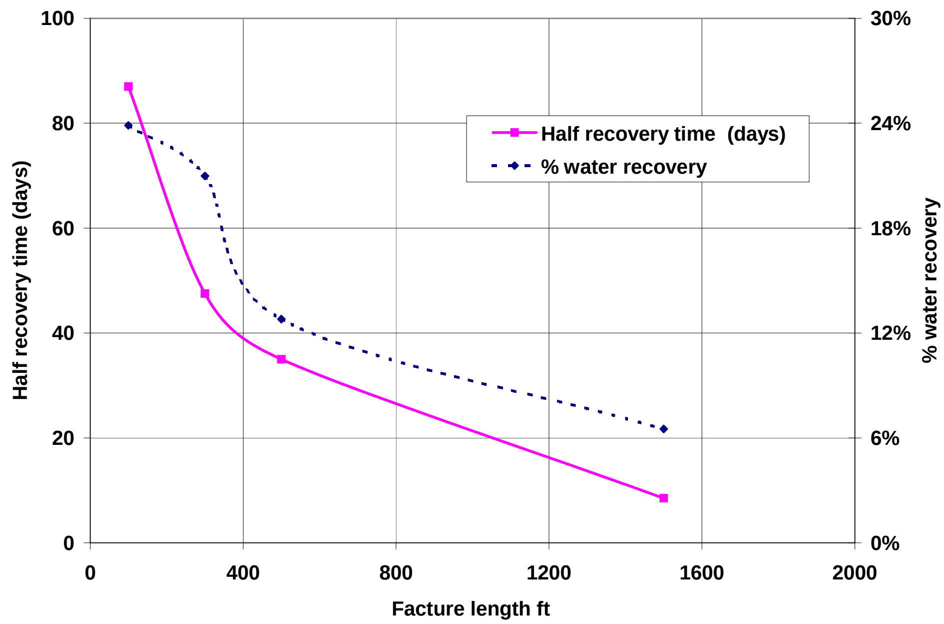

Figure 17: Effect of fracture length in fractured gas-water system with one vertical well (constant volume of water injected).

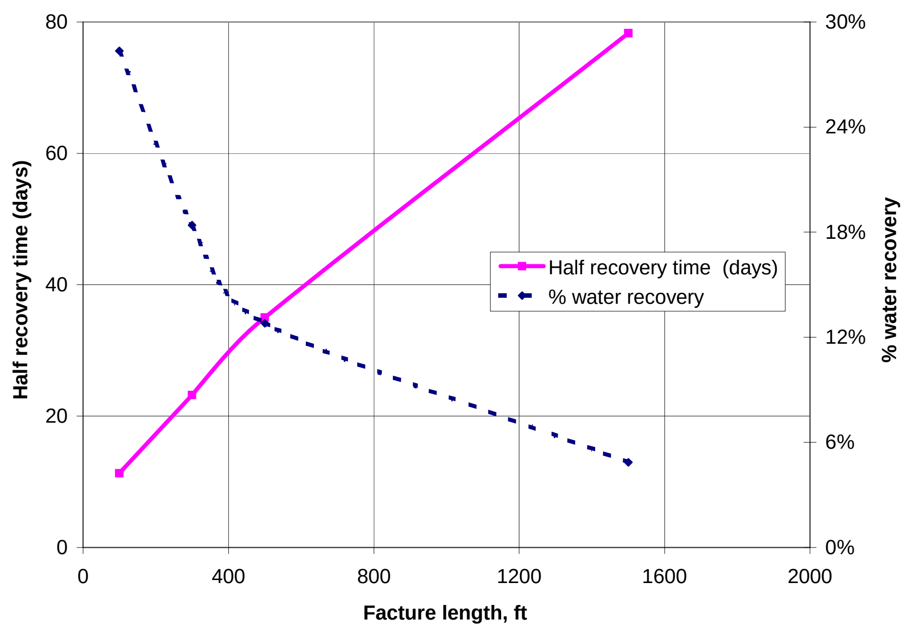

Figure 18: Effect of fracture length in fractured gas-water system with one vertical well and fixed depth of water invasion.

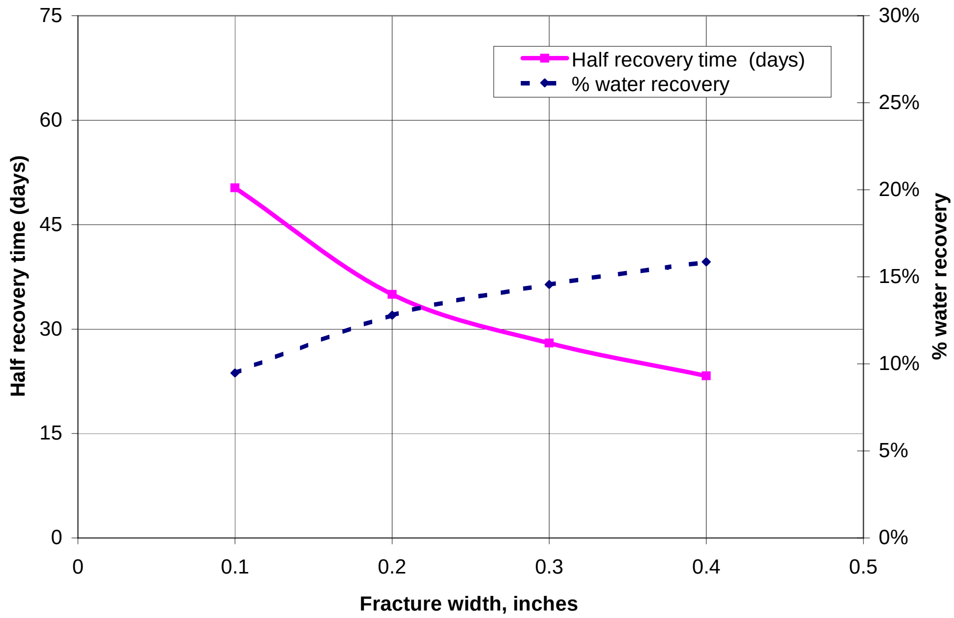

Figure 19: Effect of fracture width in fractured gas-water system with one vertical well.

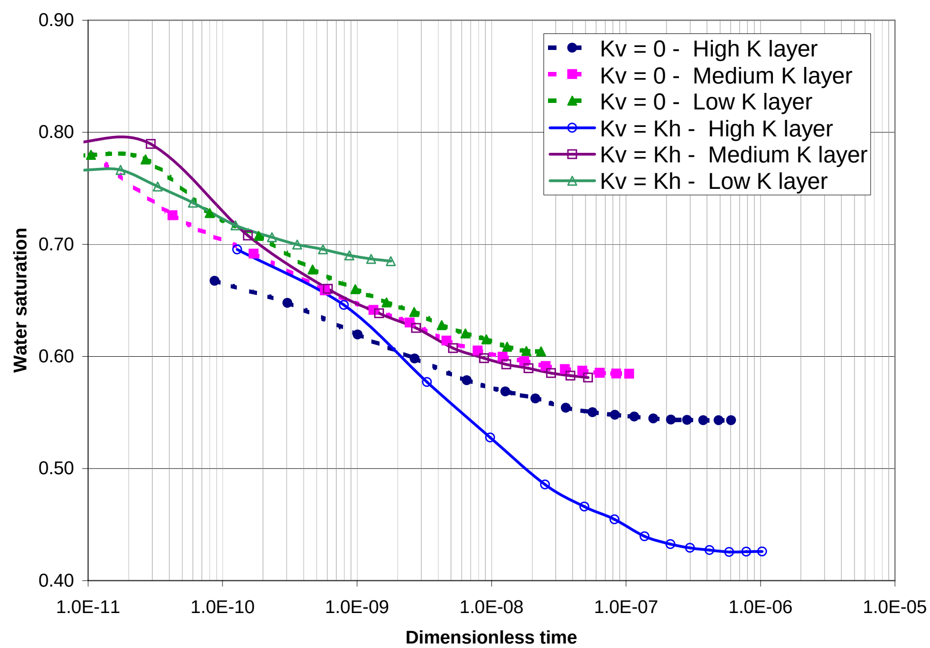

Figure 20: Trend of water saturation adjacent to the wellbore with respect to dimensionless time for Pwf = 5800 psi in unfractured three-layered gas-water system.

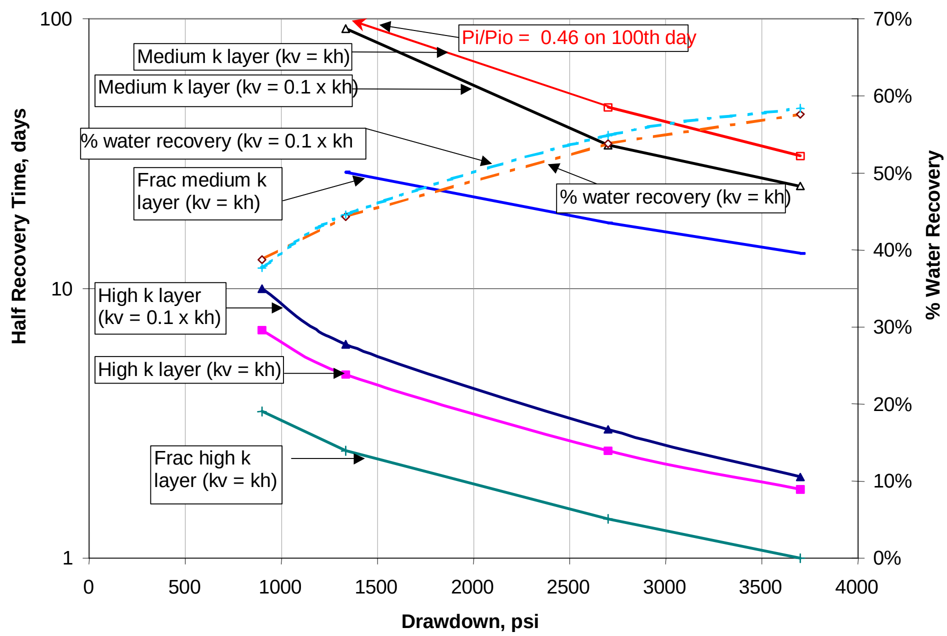

Figure 21: Effect of drawdown and k_v in three-layered gas-water system with one vertical well.

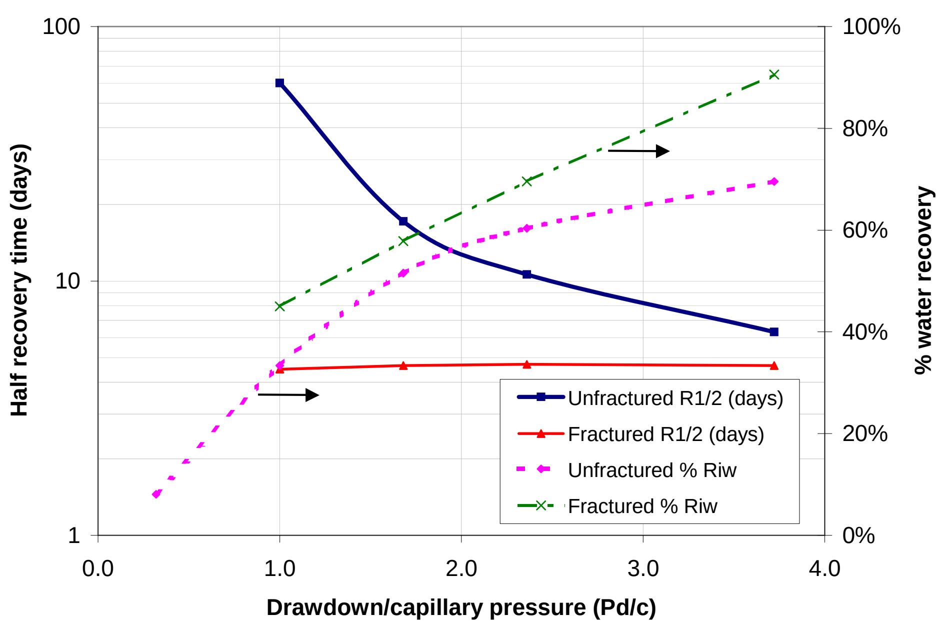

Figure 22: Effect of $P_{d/c}$ in oil-water system with one vertical well (k = 0.1 md).

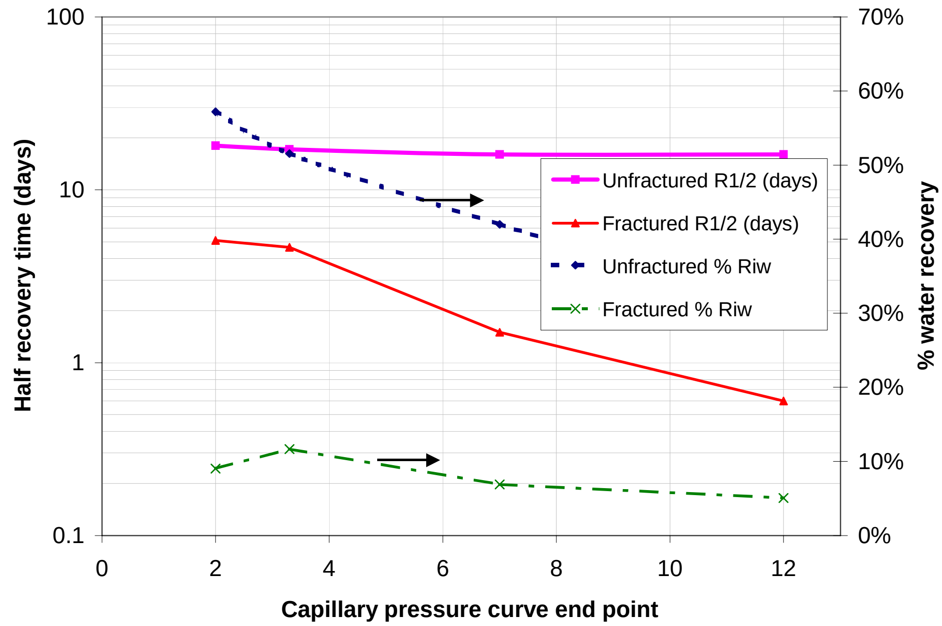

Figure 23: Effect of capillary pressure curve end point in oil-water system with one vertical well (k = 0.1 md).

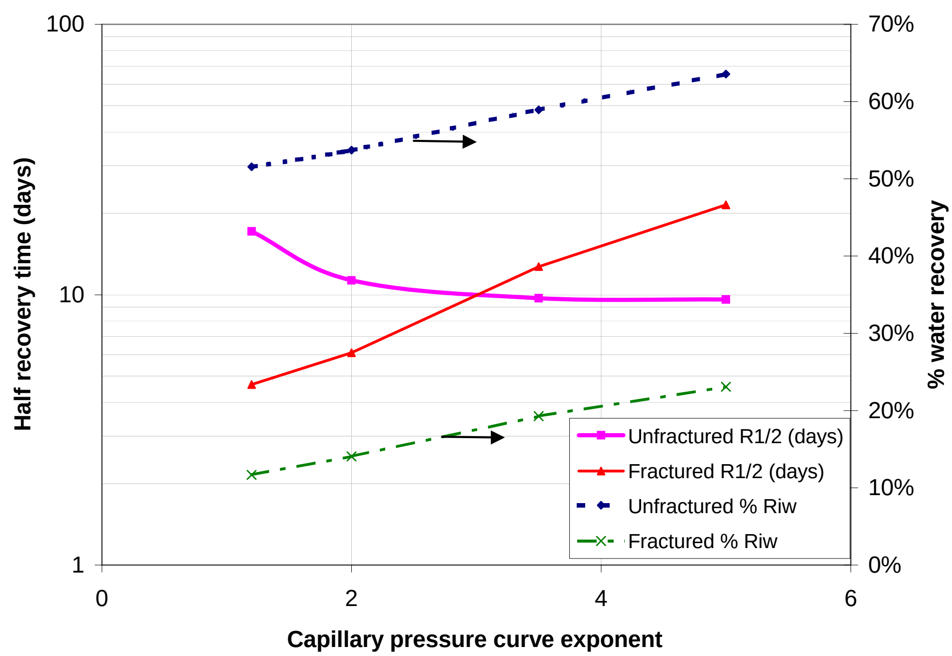

Figure 24: Effect of capillary pressure curve exponent in oil-water system with one vertical well (k = 0.1 md).

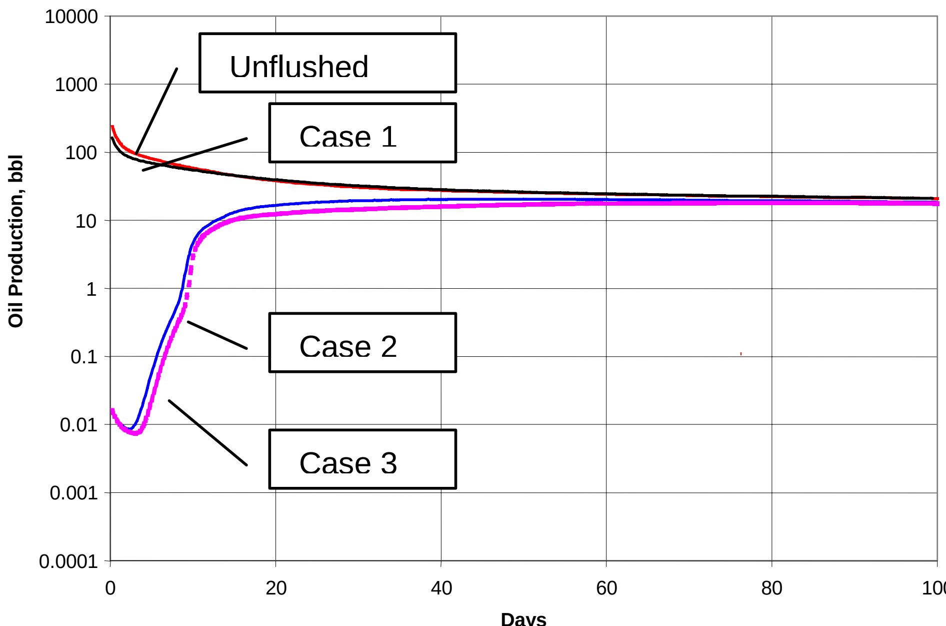

Figure 25: Oil production history for drawdown of 1000 psi in fractured oil-water system with one vertical well. (k = 0.1 md).

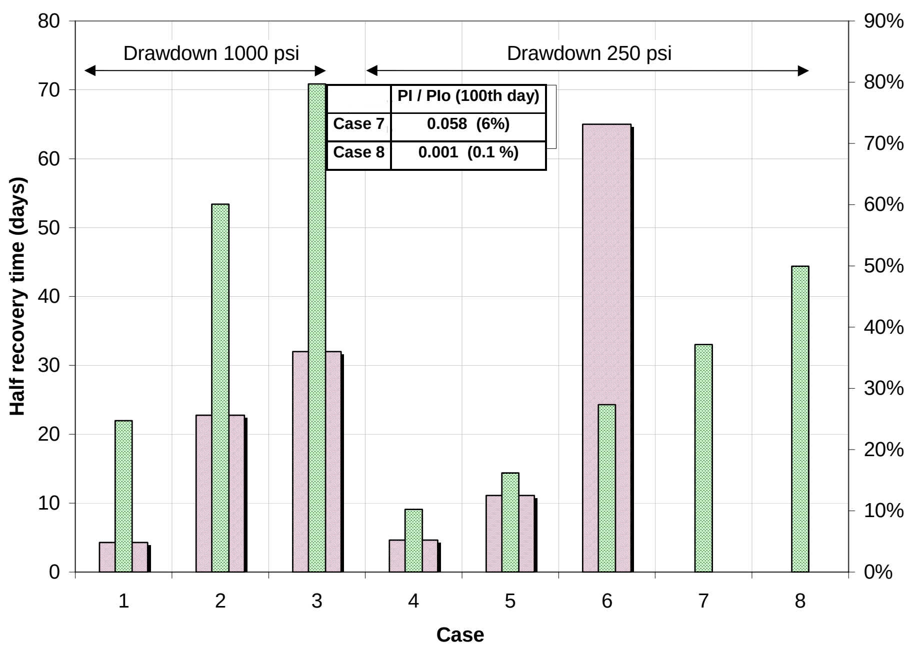

Figure 26: Effect of wettability in fractured oil-water system with one vertical well for two sets of drawdown (k = 0.1 md).

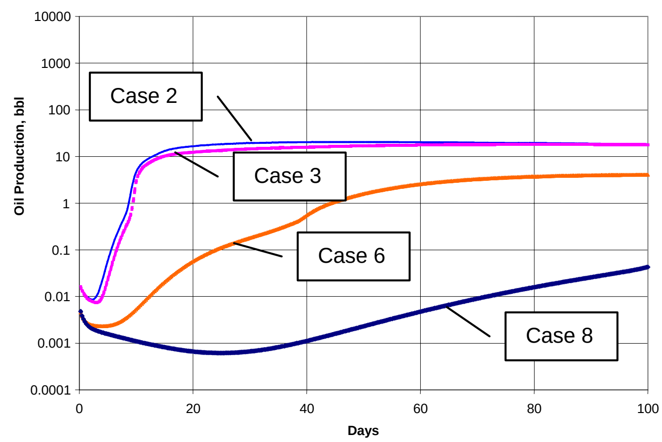

Figure 27: Oil production history with "Set III" relative permeability curves in fractured oil-water system with one vertical well. (k = 0.1 md).

CHAPTER 11. EVAPORATIVE CLEAN-UP OF WATER-BLOCKS IN GAS WELLS

11.1 ABSTRACT

The flow of a gas in to a wellbore in a production well can result in the evaporative cleanup of water blocks. This occurs primarily due to the expansion of gas resulting in additional water being evaporated in the near wellbore region. This study presents for the first time, equations and a model to calculate the rate at which the water block is removed in both fractured and unfractured gas wells.

It is shown that the removal of water by the expanding gas leaves behind a saturation profile that is qualitatively different for low and high permeability rocks. As a consequence the increase in gas relative permeability or the well productivity with time can vary substantially depending on the rock permeability and the well drawdown. The model allows us to compute the impact of evaporative cleaning on well productivity.

It is seen that high permeability rocks clean up significantly faster. It is also observed that unfractured wells may require a very long time to cleanup. Large pressure drawdowns as well as the use of more volatile fluids such as alcohols result in significantly faster cleanup. A distinctive feature of the study is that the model equations are formulated and solved completely without the assumption of skin factors for the damage zone. Thus the prediction of cleanup rates can be made more accurately.

11.2 INTRODUCTION

Water blocks in low permeability rocks clean up much slower than those with higher permeability (Mahadevan *et al.*[5]), due to the smaller pore sizes and the consequent higher capillary entry pressures. For example, water blocks in tight gas sands are not easily cleaned up, especially in cases where the reservoir pressures are too low to initiate flow.

Past simulation and experimental studies (Tannich[9], Holditch[3], Parekh *et al.*[8]) have reported the effect of gas displacement of water in the clean up of waterblocks in gas wells. These studies have shown that when the drawdown in the gas well is significantly larger than the capillary pressure, the clean up is faster. However, in cases where the drawdown becomes comparable to the capillary pressure, which is the case in depleted tight gas reservoirs, the displacement of water by the incoming gas may not be sufficient to remove the water from the near wellbore region.

The flow of a fully saturated compressible gas through a water saturated porous rock can induce evaporation. This is because the water content of the gas and the volume of the gas increases as pressure declines. In all these past studies the impact of this evaporation due to flow of gas has been neglected. In this paper we focus on the evaporative cleanup of waterblocks in gas wells where the drawdown is comparable in magnitude to the capillary pressure in the rock.

Recent research (Mahadevan *et al.*[6], Kamath *et al.*[4]) has shown that water block removal takes place by two mechanisms. The first is a displacement of the water from the pores by the produced gas, followed by an evaporation regime that lasts for a long time, sometimes in the order of months. Higher drawdowns and solvent addition were shown to impact the relative permeability of the injected gas in both the displacement and the evaporative regime and, therefore, the clean-up.

This study presents simulation data on the local variations of liquid saturation during clean-up during both displacement and evaporative regimes. Experimental results are used to verify the saturation profiles computed from the model equations. Good agreement with experiments is observed indicating that the essential physics of the problem has been adequately captured in the model. It is shown that the capillary end effect is present in the case of both high-permeability sandstones and low-permeability limestones. A mathematical model is used to predict the rate of cleanup, water removal, and the well productivity improvement. Such calculations are presented for both unfractured and fractured wells.

In order to closely simulate the conditions that exist in a water-blocked gas well, water saturated gas (wet-gas) flow is considered for modeling purposes. When a wet-gas is flowed, drying is predominantly due to the compressibility of the gas. The cleanup in this drying regime is dependant on the permeability of the formation as shown in Figure 1. It is seen that for fractured low permeability tight gas sandstone, the drying rates produce larger saturation changes near the fracture face. The saturations also decrease faster with increased pressure drop and the receding fronts appear to be sharper. In the case of unfractured gas wells the effect of pressure drawdown on saturation profiles is similar to that of a fractured case, except that the rate of cleanup is lower than that for the fractured case for a given reservoir pressure.

11.3 MATHEMATICAL MODEL

Figure 2 shows the rate of liquid removal (brine) from limestone and tight gas sandstone cores by displacement and evaporation. At about 100 PV, for limestone, the rate of displacement becomes smaller than the rate of evaporation. This marks the onset of the evaporation regime. However, this demarcation between the displacement and the evaporation regimes may not occur at 100 PV for other temperatures or when the displaced liquid is volatile, such as methanol. In this study we assume that brine is the displaced fluid and the mathematical models for the two regimes are developed separately.

11.3.1 Unfractured Gas Wells: Radial Model

In the case of an unfractured well, the cleanup happens in a radial geometry and this leads to a different behavior of the saturation profiles in the damaged zone near the wellbore. For the displacement regime, we develop the mass conservation equations in cylindrical coordinates (Appendix A).

11.3.1.1 Evaporative Regime: Compressibility Effects

The assumptions made in modeling the evaporative regime are:

1. A one dimensional (radial, homogeneous) system is assumed.
2. The temperature variation caused by Joule-Thompson cooling along the length of the system is negligible.
3. The phase behavior is described by Raoult's law.
4. The temperature is assumed constant and local thermodynamic equilibrium exists.
5. End effects are negligible and diffusion mass transfer axially is small compared to the convective mass transfer.
6. There is no flow of water/no capillarity during the evaporation regime.

With the above assumptions the conservation equations, developed in Appendix B, describing the time evolution of water saturation spatially becomes:

$$\frac{\partial S_w}{\partial \tau} + \frac{A^{1/2}(\tau)}{r^2 \lambda(S_w)} \bullet \frac{1}{\left(\frac{\Pi_1^2}{A(\tau)} + 2\int_{R_1}^{r} \frac{dr}{\lambda(S_w) r} \right)^{3/2}} = 0 \quad (1)$$

where $A(\tau) = \frac{\frac{\Pi_2{}^2}{2} - \frac{\Pi_1{}^2}{2}}{\int_{R_1}^{R_2} \frac{dr}{\lambda(S_w) r}}$, where R_1 and R_2 are the radius of wellbore and the external damage radius respectively.

The initial condition for the above equation is given by the water saturation at the end of displacement. The above equation can be solved numerically using an explicit calculation of saturation with time.

11.3.2 Fractured Gas Well: Linear Model

A mathematical model for displacement and evaporation of trapped liquid in a porous medium of linear geometry is developed in Mahadevan *et al.*[5]. One of the assumptions in the model is that the end of displacement is complete after about one hundred pore volumes of gas flow and that evaporation effects during this time are insignificant. The amount of water recovered during the displacement regime can be simulated using standard relative permeability models and capillary pressure curves.

In the evaporative regime the saturations change continuously with time, and therefore, a model is needed to calculate the time evolution of the saturation changes spatially. For a linear flow from the matrix into the fracture the saturation evolves spatially and in time according to the following equation (Mahadeva *et al.*[5]).

$$\frac{\partial S}{\partial \tau} + \frac{A^{1/2}(\tau)}{\lambda(S)} \bullet \frac{1}{\left(\frac{\Pi_0^2}{A(\tau)} - 2\int_0^x \frac{1}{\lambda(S)} dx \right)^{3/2}} = 0 \quad (2)$$

where, $A(\tau) = \frac{\Pi_0^2 - \Pi_L^2}{2\int_0^L \frac{1}{\lambda(S_w)} dx}$.

The gas mobility $\lambda(S_w)$ is calculated as a function of the local liquid saturation.

11.4 RESULTS AND DISCUSSION

Based on the model presented in the previous section, simulations are conducted to show the impact of reservoir permeability and pressure drawdown on cleanup of fractured and unfractured gas wells. To fully understand the time required for cleanup and the role played by evaporation in this cleanup process, local variations in water saturation are important.

11.5 SIMULATION OF LABORATORY EXPERIMENTS

Figure 3 shows the water saturation profile for an untreated Berea sandstone core during the injection of a wet gas at the end of the displacement regime. The saturation profile is superimposed on an X-Ray scanning result (Mahadevan *et al.*[5]). The plot shows trapped water saturation which gradually rises near the outlet end where the capillary pressure is zero. This is the so called capillary end effect where the water saturation increases to one towards the outlet (zero capillary pressure).

Figure 4 shows the time evolution of the saturation profile at a fixed pressure drop of 3 psi, during cleanup of a Berea core. The saturation profiles show a receding drying front which is due to larger drying rates near the producing face of the sample. It should be noted that gas pressure gradients are largest at the outlet end due to compressible flow and since the water saturations are high. The evaporative regime in this case occurs over long times and spans thousands of pore volumes of gas injected. The evaporation occurs purely due to the compressibility of the injected gas as the injected gas is completely saturated with water. When the pressure drop is increased to 12 psi, the drying front recedes faster (Figure 5) and, therefore, leads to faster recovery of gas relative permeabilities. Additionally, the pressure gradients become larger locally at higher drawdowns, and in the absence of effects such as film flow, leads to greater saturation changes near the outlet end.

In comparing the computed saturation profiles (Figure 6) with the experimental profiles (Mahadevan *et al.*[5]), it is seen the simulations are consistent with the experimental results. In the experiments, it is observed that the drying fronts are smeared out over the length of the core and in some cases flattens the saturation profiles. This is primarily due to the capillary induced film flow from regions of high water saturation to regions of low water saturations. It is expected that in the field film flow effects will have a smaller role as the length scale over which the drying occurs may be significantly larger.

11.6 FRACTURED CONDITIONS

We simulate the production of gas from fractured tight gas sandstone with the assumed petrophysical parameters shown in Table 1 (type TG-3). In a fractured formation, gas flow during the initial production period is mostly linear. During the cleanup, flowing gas displaces the invaded water in to the fracture and evaporation occurs over longer time scales. In this section we present results from simulation of fractured wells at drawdowns of 279 psi and 1455 psi.

11.6.1 Effect of Pressure Drop on Saturation Profiles

The model solution for saturation profile in a tight-gas sandstone formation with a typical capillary pressure curve is shown in Figure 7. Pressure drawdown affects the amount of water trapped in the formation by capillarity. At a higher pressure drawdown the end effects are also minimized. Lower drawdowns may, therefore, leave significant quantities of water trapped in addition to capillary end effects.

When fracturing a tight-gas sandstone formation, water from the fracturing fluid invades the fracture face. It is conservatively estimated that for a typical fracturing operation that produces a fracture 800 ft long and 50 ft in height, with about 5000 bbl of water lost into the formation, the water would penetrate as deep as about 2 ft into the formation. When the well is produced back, some displacement occurs initially. This is followed by an evaporation regime. Figure 8 shows the saturation profiles in the evaporation regime when the pressure drawdown is about 279 psi. The profiles show steep receding fronts which continue to change for as much as 70 days. When the pressure drop is increased to 1455 psi the saturation profiles recede faster and go to zero in about 12-13 days. This cleanup is caused entirely by the evaporation due to the compressibility of the gas. For higher drawdowns the saturation profiles are sharper and also show faster cleanup (Fig 9). Another reason for the faster cleanup during the evaporation regime for a higher drawdown case is the lower remaining water saturation at the end of displacement. The higher drawdown case clearly has lower trapped water to begin with and can, therefore, be cleaned up faster. The rate of increase of the gas flow rate is shown in Figure 10 for different pressure drawdowns. The higher drawdown case clearly starts off at a greater gas flow rate than the rest.

It has been shown in several studies (Dullien *et al.*[3], Yiotis *et al.*[7]) that liquid saturated pores are drained for long time periods due to transport through films which form on the capillary channels in the permeable medium. In the recent study by Mahadevan *et al.*[5] it was shown that, in limestone, this redistribution of liquids within the core sample occurs only until a certain time after which the saturation profiles show greater drying rates near the ends. This suggests that the liquid film flow rate is competetive with the drying rates, which depend on the pressure drop across the core (Mahadevan *et al.*[6]), near the outlet end. That is, when the drying rates are higher than the rate of transport due to redistribution, the saturations fall more rapidly. For the tight gas sandstone, used in the simulations, the film flow rates are small.

11.6.2 Effect of Temperature

The effect of higher temperature on the rate of cleanup is shown in figure 11. Higher temperatures would lead to greater vapor pressures and hence greater evaporation rates. The simulations shown here assume pure water vapor pressures as shown in table 1. The increased rate of evaporation causes rapid cleanup resulting in complete recovery of gas flow rate in about 2 days from 20 days for a temperature of 25 deg C. The cleanup time for 120 deg C goes down to almost 0.5 days.

The above simulation results show the predicted trend (Mahadevan *et al.*[6]) for the case of pure water in the damaged zone. In the presence of methanol, the volatility (and therefore the vapor pressure) is even higher and the cleanup is expected to be even faster. The presence of salts and other dissolved constituents in the damage fluid is not expected to play a significant role in the thermodynamics, although the precipitation effects on the gas relative permeability may be significant.

11.7 UNFRACTURED CONDITIONS

Various operations, such as workovers, can cause the water to invade into the formation pore space around the well. In this section, results from simulation of a well flowback after damage are presented for a radial geometry. The effect of pressure drop on the saturation evolution and the rate of cleanup are also analysed. The properties of the formation considered are shown in Table 1 (type TG-3) and it is assumed that they remain constant throughout the flowback period. The cleanup happens in two regimes, water is displaced in the first regime, and after a short time evaporation becomes significant. In the radial case, however, the amount of water that is trapped is more than that of the fractured case for a given cross sectional area of gas flow in the well. In this section, the effect of pressure drop on the saturation profile evolution and the rate of cleanup are analysed. The damage length is assumed to be around 2 ft and the formation height to be about 100ft. The drawdowns used in the simulation are 279 psi and 1455 psi.

11.7.1 Effect of Pressure Drop on Saturation Profiles

Figure 12 shows the saturation profile during the displacement at different drawdowns. The profiles show very similar trends to those observed in the fractured case, where the capillary trapping and end effects are seen at lower pressure drawdowns. The trapped saturation levels are also quite similar to that of the fractured case. Thus in an unfractured well, low drawdowns can lead to greater capillary trapping and lower gas flow rates due to relative permeability effects.

In the evaporative regime, the saturation profiles for 279 psi pressure drawdown are shown in Figure 13. The profiles show steep receding drying fronts, albeit at a much slower rate compared to the fractured case. In fact the saturations go to zero only after several hundred days of production for the same drawdown. When the drawdown is increased the saturations recede faster and the water removal is accomplished within a couple of hundred days (Figure 14). Figure 15 shows the gas recovery rates for the unfractured case at different drawdowns. Clearly the higher drawdown case produces faster cleanup and hence faster gas flow rate recovery.

11.7.2 Effect of Temperature

In the case of unfractured wells, the effect of temperature on the rate of cleanup is similar to that of the fractured wells although the absolute cleanup times are still higher than that of the fractured case. The cleanup time decreases from around 300 days at 25 deg C to about 10 days (higher than that of the fractured case, which is at 0.5 days) at 120 deg C.

11.8 EFFECT OF PERMEABILITY ON CLEANUP

When the formation permeability is varied, from 0.01 mD to 1 mD, the cleanup rates are faster for the higher permeability case. Figure 17 shows the effect of permeability on gas flow rate for a fractured case. We fix the relative permeability and the capillary pressure curve parameters for the three formations (Table 1) and the only effect is that of the greater permeability. The plot, therefore, shows the gas flow rate recovery starting from similar levels after which the higher permeability formation cleans up faster. In the case of unfractured (radial geometry) wells, the cleanup is slower for all three formations compared to the fractured case. However, the higher permeability well cleans up much faster than the lower permeability well as expected (Figure 18).

11.9 CONCLUSIONS

1. It is shown that evaporative cleaning of waterblocks in gas wells is the dominant mechanism by which the waterblock is removed over long periods of time (days to weeks).
2. All past work that address the issue of waterblocks has not adequately accounted for the effects of evaporation on the removal of waterblocks. For the first time, a complete model is presented that allows us to compute the saturation profiles in unfractured and fractured wells.
3. The impact of evaporation on increases in gas relative permeability is quite significant. It is shown that the cleanup is dependant on the reservoir permeability, drawdown, temperature and the volatility of the liquid.
4. In general, higher rates of vaporization (volatile fluids, higher temperature), higher permeability, and larger drawdowns will result in quicker cleanup. It is also shown that fractured wells tend to cleanup much quicker than unfractured wells. In some cases when drawdowns are small, it may take several weeks for the water to be completely removed and for the well productivity to build up to its undamaged value.
5. In unfractured wells the water blocks may persist for a much longer period. Thus loss of waterbased liquids in unfractured wells can be a serious detriment to the productivity of the well.

6. The results of this study shows that the evolution of the local saturation profiles can be calculated using the equations presented in this paper. These saturation profiles allow us to correctly predict the gas well deliverability and its evolution with production time.

11.10 APPENDIX A

The mass conservation, if we neglect evaporation effects (i. e. $y_w = 0$) and assuming horizontal 1-D flow, yields,

$$\phi\frac{\partial S_w}{\partial t}+\frac{1}{r}\frac{\partial r u_w}{\partial r}=0 \qquad (1)$$

$$\phi\frac{\partial}{\partial t}\left(\rho_g S_g\right)+\frac{1}{r}\frac{\partial}{\partial r}\left(\rho_g r u_g\right)=0 \qquad (2)$$

From the gas law one can get the density of the gas as,

$$\rho_g=\frac{M_g P_g}{zRT} \qquad (3)$$

Substituting this and the mass flow rate expressions into the mass conservation equation, after assuming that the water saturation is unchanging with time and also that the water phase does not flow, we get,

$$u_w = 0 \qquad (4)$$

$$\frac{1}{r}\frac{\partial}{\partial r}\left[\frac{M_g P_g}{zRT}\left(\frac{-kk_{rg}}{\mu_g}\right)r\left(\frac{\partial P_g}{\partial r}\right)\right]=0 \qquad (5)$$

The above can be re-written as below, where all the constants from the left hand side of the above equation are also combined to give,

$$\left[P_g r k_{rg}\left(\frac{dP_g}{dr}\right)\right]=-C_1 \cdot \qquad (6)$$

We know, capillary pressure

$$P_c = P_g - P_w \tag{7}$$

and,

$$\frac{dP_g}{dr} = \frac{dP_c}{dr} + \frac{dP_w}{dr} = \frac{dP_c}{dr} \tag{8}$$

therefore

$$P_g = P_c + P_{g,1} \tag{9}$$

The relative permeability function is assumed to be of the form,

$$k_{rg} = k_{rgo}\left(1 - \overline{S_w}\right)^{n_g} \tag{10}$$

where $\overline{S_w} = \dfrac{S_w - S_{wr}}{1 - S_{wr} - S_{gr}}$ is a normalized saturation of water.

Assuming the following relationship holds for the primary drainage capillary pressure,

$$\bar{S}_w = \frac{1}{\left[1 + (\alpha P_c)^n\right]^m} \text{ where } m = 1 - \frac{1}{n} \text{ and } n>1 \tag{11}$$

and,

$\alpha = \dfrac{1}{\gamma_{12}}\sqrt{\dfrac{k}{\phi}}$, where γ_{12}, k, and ϕ are the interfacial tension, permeability, and the porosity respectively.

That is,

$$P_c = \frac{1}{\alpha}\left(\left(\overline{S_w}\right)^{-\frac{1}{m}} - 1\right)^{\frac{1}{n}} \text{ if } 0 < \overline{S_w} < 1. \quad (12)$$

$$P_c = \frac{1}{\alpha}\left(\overline{S_w}\right)^{-(n-1)} \text{ if } \overline{S_w} = 0. \quad (13)$$

$$P_c = \frac{1}{\alpha}\left(\frac{\left(1-\overline{S_w}\right)}{m}\right)^{\frac{1}{n}} \text{ if } \overline{S_w} = 1. \quad (14)$$

To obtain the capillary pressure profile we solve the mass balance equation 6. The mass balance equation is solved with constraint from the capillary pressure curves. Re-writing equation 6 by using Eq. 9 and a Corey type relative permeability curve, we get,

$$\left[\left(P_c + P_{g,2}\right)k_{rgo}\left(1-\overline{S_w}\right)^{n_g} r\left(\frac{dP_c}{dr}\right)\right] = -C_1 \quad (15)$$

We non-dimensionalize the above equation, by using the following substitutions,

$$\begin{aligned} \pi_c &= \alpha P_c \\ \pi_g &= \alpha P_g \end{aligned} \quad (16)$$

Making the above substitutions and rearranging, we get,

$$\left[\left(\pi_c + \pi_{g,1}\right)k_{rgo}\left(1-\overline{S_w}\right)^{n_g} r\left(\frac{d\pi_c}{dr}\right)\right] = -\alpha^2 C_1 \quad (17)$$

Rearranging and integrating from y=0 to y,

$$\left[\pi_c\right]_y = \int_{R_1}^{r} \frac{-\alpha^2 C_1}{\left(\pi_c + \pi_{g,1}\right) k_{rgo} \left(1-\overline{S_w}\right)^{n_g}} \frac{dr}{r} \qquad (18)$$

Performing numerical integration (or calculate area under the curve represented by the integrand plotted with respect to y) gives the value of π_c at each point. To obtain an initial value, we consider the local behavior of the equation 17 near y=0. Using the asymptotic expression for the capillary pressure near Sw=0, and substituting in the equation 17 for Sw, we get,

$$\left[\left(\pi_c + \pi_{g,1}\right) k_{rgo} m^{n_g} \left(\pi_c\right)^{nn_g} r\left(\frac{d\pi_c}{dr}\right)\right] = -\alpha^2 C_1 \qquad (19)$$

Since the point in consideration is close to y=0 we neglect the the capillary pressure, π_c near y=0.

$$\left[\left(\pi_{g,1}\right) k_{rgo} m^{n_g} \left(\pi_c\right)^{nn_g} r\left(\frac{d\pi_c}{dr}\right)\right] \approx -\alpha^2 C_1 \qquad (20)$$

Integrating from y=R1 to r to obtain the local behavior near r=R1.

$$\int_0^{\pi_c} \left[\left(\pi_c\right)^{nn_g} d\pi_c\right] \approx \int_{R_1}^{r} \frac{-\alpha^2 C_1 dr}{\left(\pi_{g,1}\right) r k_{rgo} m^{n_g}} \qquad (21)$$

letting $y = \dfrac{r-R_1}{R_2-R_1}$ for transformation into dimensionless distance,

$$\pi_c \approx \left(\frac{-\alpha^2 C_1 \left(nn_g+1\right)}{\left(\pi_{g,1}\right) k_{rgo} m^{n_g}}\left(\ln\left[\frac{y(R_2-R_1)+R_1}{R_1}\right]\right)\right)^{\frac{1}{nn_g+1}} \qquad (22)$$

The above provides the value of π_c at a position near y=0 and is used as the initial value at a position near y=0. The dimensionless capillary pressure value at y=1 is already known and the numerical integration using the above equations is performed with an initial guess value of C1 to obtain the profile of π_c. If the boundary value of π_c is not satisfied at the integration at y=1, the guess value is updated to start a new integration step with the new value of C1. A constrained minimization in Matlab software is able to find the value of C1 that provides the correct solution of π_c with all boundary conditions satisfied. The known value at y=1 is given by the equation as below,

$$\pi_{c,2} = \pi_{g,2} - \pi_{g,1}$$

Knowing the dimensionless capillary pressure profile one can derive the saturation profiles and hence the pressure profile. This set of data will provide the initial condition for the evaporation phase calculations.

11.11 Appendix B

The mass conservation equations for water evaporation after displacement are given as below.

$$\phi\rho_w \frac{\partial S_w}{\partial t} + \phi\frac{\partial}{\partial t}\left(\rho_g S_g \frac{M_w y_w}{M_g}\right) + \rho_w \frac{1}{r}\left(\frac{\partial r u_w}{\partial r} + \frac{\partial}{\partial r}\left(\rho_g \frac{M_w y_w}{M_g} r u_g\right)\right) = 0 \tag{1}$$

$$\phi\frac{\partial}{\partial t}\left(\rho_g S_g \frac{M_w\left(1-y_w\right)}{M_g}\right) + \frac{1}{r}\frac{\partial}{\partial r}\left(\rho_g \frac{M_w\left(1-y_w\right)}{M_g} r u_g\right) = 0 \tag{2}$$

Where, the phase velocities are given as a fraction of the total velocity; $u_w = f_w u_T$ and $u_g = f_g u_T$. Using the following terms for concentrations, $\alpha = \frac{y_w P_g}{R_g T}$ and $\beta = \frac{\rho_w}{M_w}$, the water conservation (Eq. 1) now becomes, knowing that, $\frac{\rho_g}{M_g} = \frac{P_g}{R_g T}$,

$$\frac{\partial}{\partial t}\left(\beta S_w + \alpha\left(1-S_w\right)\right) + \frac{1}{\phi}\frac{1}{r}\frac{\partial}{\partial x} r\left(\beta f_w u_T + \alpha f_g u_T\right) = 0 \tag{3}$$

Similarly Eq. 2 for gas conservation (Nitrogen is the injected gas) becomes,

$$\frac{\partial}{\partial t}\left(\left(1-y_w\right)P_g S_g\right)+\frac{1}{\phi}\frac{1}{r}\frac{\partial}{\partial r}\left(\left(1-y_w\right)P_g f_g r u_T\right)=0 \qquad (4)$$

Raoult's law

$$y_w(x,t)=\frac{P_s}{P_g} \text{ if } S_w(x,t)>0 \qquad (5)$$

The following are limiting cases of the problem:

1. Steady State Solution assuming negligible evaporation: - The solution for S_w and P_g is obtained by solving the above set of partial differential equations assuming that the evaporation is negligible.
2. Incompressible fluids: - The total flow rate or flow velocity, u_T, is a constant and can be taken out of the spatial differential.
3. No water flow: - When the water fractional flow is set to zero. This will probably happen when the displacement part is complete and the film flow effects are neglected.

The last case is more probable in reality and therefore we can rewrite equation 3 and 4 as follows. Neglecting α, and setting $f_w = 0$, we get, after some rearrangement,

$$\frac{\partial S_w}{\partial t}+\frac{\alpha}{\phi\left(\beta-\alpha\right)}\frac{1}{r}\frac{\partial r u_T}{\partial r}=0 \qquad (6)$$

$$\frac{\partial}{\partial t}\left(\left(P_g-P_s\right)\left(1-S_w\right)\right)+\frac{1}{\phi}\frac{1}{r}\frac{\partial}{\partial r}\left(r\left(P_g-P_s\right)u_T\right)=0 \qquad (7)$$

Let $\tau=\dfrac{t\alpha}{\beta-\alpha}$ and define $\varepsilon=\dfrac{\alpha}{\beta-\alpha}<<1$. Also "pressure" $\Pi=P_g-P_s(T)$. We rescale the time axis, to introduce a "drying" time scale, $\tau=\varepsilon t$. Then, the two equations read

$$\frac{\partial S_w}{\partial t} + \varepsilon \frac{1}{\phi r} \frac{\partial r u_T}{\partial r} = 0 \tag{8}$$

$$\frac{\partial}{\partial t}\left[\Pi(1 - S_w)\right] + \frac{1}{\phi r} \frac{\partial}{\partial r}\left[r \Pi u_T\right] = 0 \tag{9}$$

To leading order, namely outside of a boundary layer in time, Eq. 9 becomes

$$\frac{1}{r} \frac{\partial}{\partial r}\left[r \Pi u_T\right] = 0 \tag{10}$$

After substituting the expression for the flow velocity $u_T = -\lambda(\bar{S}_w)\frac{\partial \Pi}{\partial r}$, where $\lambda(\bar{S}_w)$ is the gas mobility, a function of the liquid saturation, the solution of (10) is

$$\frac{\Pi^2}{2} - \frac{\Pi_1^2}{2} = A(\tau)\int_{R_1}^{r} \frac{dr}{\lambda(S_w) r} \tag{11}$$

where R_1 refers to the radius of well bore. The time-dependent variable is,

$$A(\tau) = \frac{\frac{\Pi_2^2}{2} - \frac{\Pi_1^2}{2}}{\int_{R_1}^{R_2} \frac{dr}{\lambda(S_w) r}}. \tag{12}$$

We can also write,

$$r \Pi u_T = A(\tau)$$

or

$$r u_T = \frac{A(\tau)}{\Pi} = \frac{A(\tau)}{\sqrt{\Pi_1^2 - 2A(\tau)\int_{R_1}^{r} \frac{dr}{\lambda(S_w) r}}} \tag{13}$$

Differentiating the above equation and combining with equation 8 we get,

$$\frac{\partial S_w}{\partial \tau} + \frac{A^{1/2}(\tau)}{r^2 \lambda(S_w)} \bullet \frac{1}{\left(\frac{\Pi_1^2}{A(\tau)} + 2\int_{R_1}^{r} \frac{dr}{\lambda(S_w) r} \right)^{3/2}} = 0 \tag{14}$$

This equation can be integrated numerically assuming that the second part in the LHS as known at the current time step and simply march in time. Only one initial condition is needed, which can reflect end-effects associated with the end of the forced displacement.

Nomenclature

D	*Darcy, unit of permeability, 9.8E-13m²*
f	*fractional flow.*
g	*gravitational constant, 9.8 m/s2*
k_r	*relative permeability*
k_{xro}	*end-point relative permeability*
k	*gas permeability at mean pressure, D.*
L	*length of the sample, cm.*
M	*molecular weight*
P	*pressure, atm*
P_s	*saturation pressure, atm.*
P_c	*capillary pressure, atm.*
Rg	*universal gas constant, 8.314 J/mol/°K.*
S	*saturation*
S_{xr}	*residual saturation of phase 'x'.*
$\overline{S}$	*normalized saturation*
T	*temperature, °K*
u	*velocity,cm/s.*
y_w	*mol fraction of water in the gas phase.*
y	*dimensionless length*

Subscripts

0	*inlet position of core*
L	*outlet position of core*
1	*well bore*
2	*external damage radius*
g	*gas*
w	*water*
T	*total value*
M	*mean value*

Greek letters

α'	*capillary pressure curve constant, atm.*
α	*concentration of water in gas phase, mol/m³.*
β	*concentration of water in liquid phase, mol/ m³.*

ε *drying time scaling factor.*
ϕ *porosity*
λ *gas mobility at mean pressure.*
ρ *density, kg/m^3*
π *scaled pressure, atm.*
Π *modified pressure,$P\text{-}P_s$ atm.*
τ *scaled time,($=\varepsilon t$) s.*

11.12 References:

1. Abrams, A. and Vinegar, H. J., "Impairment Mechanisms in Vicksburg Tight Gas Sands", paper SPE/DOE 13883 presented at the SPE/DOE 1985 Low Permeability Gas Reservoirs held in Denver, Colorado (May 1985).
2. Allerton, J., Brownell, L. E., Katz, D. L.: "Through-Drying of Porous Media," Chemical Engineering Progress, (October 1949), Vol. 45, No. 10, 619-635.
3. Holditch, S. A., "Factors Affecting Water Blocking and Gas Flow From Hydraulically Fractured Gas Wells," Journal of Petroleum Technology (December 1979) 1515.
4. Kamath, J. and Laroche, C., "Laboratory-Based Evaluation of Gas Well Deliverability Loss Caused by Water Blocking," Society of Petroleum Engineers Journal, (March 2003) 71-80.
5. Mahadevan, J., Sharma, M. M., and Yortsos, Y. C., "Imaging Studies of Drying in Porous Media: Effect of Film Flows," Manuscript in preparation for publication in American Institute of Chemical Engineers Journal, 2005
6. Mahadevan, J., and Sharma, M. M., "Clean up of Water Blocks in Low Permeability Formations", paper 84216 presented at the Society of Petroleum Engineers Annual Technical Conference in Denver, Colorado, U. S. A., 5-8 October 2003, accepted to 2nd review for publication in Society of Petroleum Engineers Journal.
7. McLeod, H. O. and Coulter, A. W.: "The Use of Alcohol in Gas Well Stimulation," paper SPE-AIME 1663 presented at the Eastern Regional Meeting of the Society of Petroleum Engineers of AIME, held in Columbus Ohio (November 1966).Yiotis, A. G., Boudouvis, A. G., Stubos, A. K., Tsimpanogiannis, I. N. and Yortsos, Y. C., "The effect of liquid films on the drying of porous media," American Institute of Chemical Engineers Journal, 2004.
8. Parekh, B., and Sharma, M. M.: "Cleanup of Water Blocks in Depleted Low-Permeability Reservoirs," paper SPE 89837 presented at the Society of Petroleum Engineers Annual

Technical Conference in Houston, Texas (Sep. 29 2004).

9. Tannich, J. D.: "Liquid Removal From Hydraulically Fractured Gas Wells," JPT (November 1975) 1309.

Table 1: Petrophysical properties of samples used for simulation.

Type	PPermeability, k, mD	Porosity, phi	Capillary Pressure Curve		Gas Relative permeability curve*	
			n	c	krgo	ng
Berea	97	0.17	2.6	0.4	0.45	2
Tight Gas (TG-1)	0.01	0.066	2.6	0.1	0.35	1.5
Tight Gas (TG-2)	0.1	0.066	2.6	0.1	0.35	1.5
Tight Gas (TG-3)	1	0.066	2.6	0.1	0.35	1.5
Temperature	T1	25 deg C				
	T2	70 deg C				
	T3	120 deg C				

* straight line relative permeability used for saturations less than Swr=0.5 in all cases, residual gas saturation, Sgr=0.

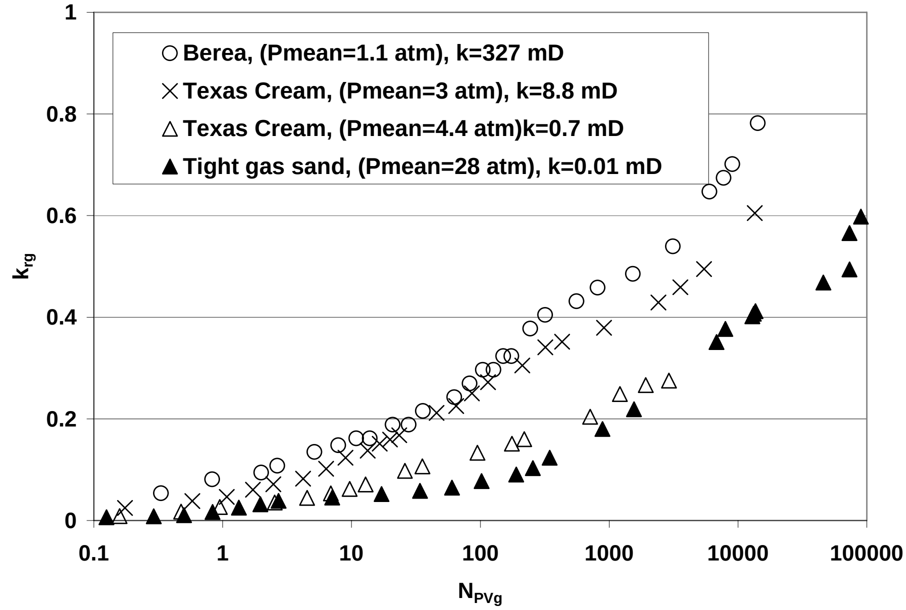

Figure 1: Effect of permeability of rock on the gas relative permeability for water-wet rock with brine as the liquid displaced.

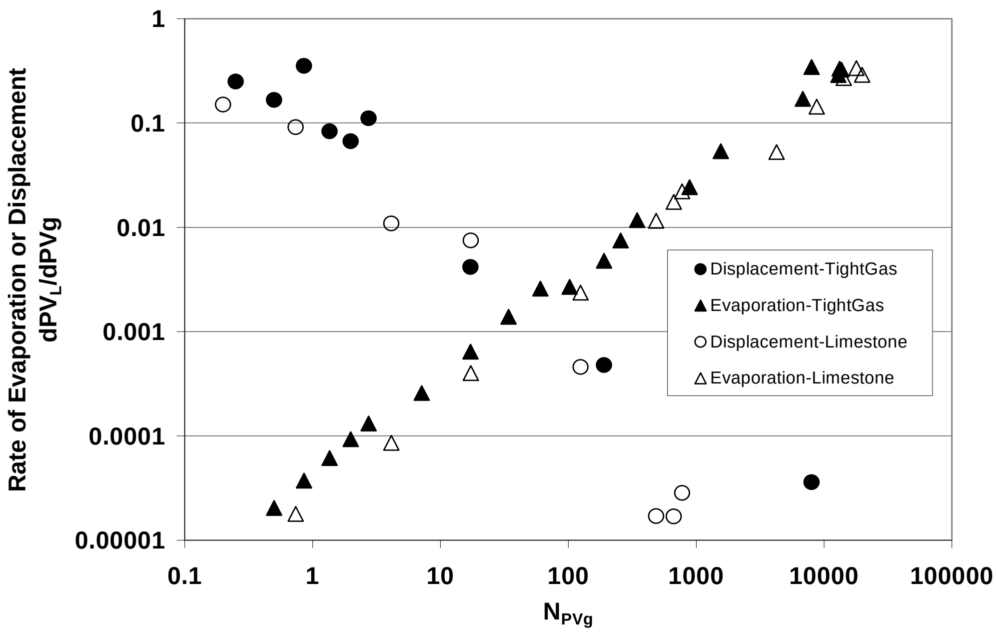

Figure 2: Rate of Liquid removal (brine) by displacement and evaporation from Texas Cream limestone (Pmean =3.0 atm, k=7.2 mD and L=15.3 cm) and tight-Gas sandstone (Pmean =28 atm, k=0.01 mD and L=6 cm).

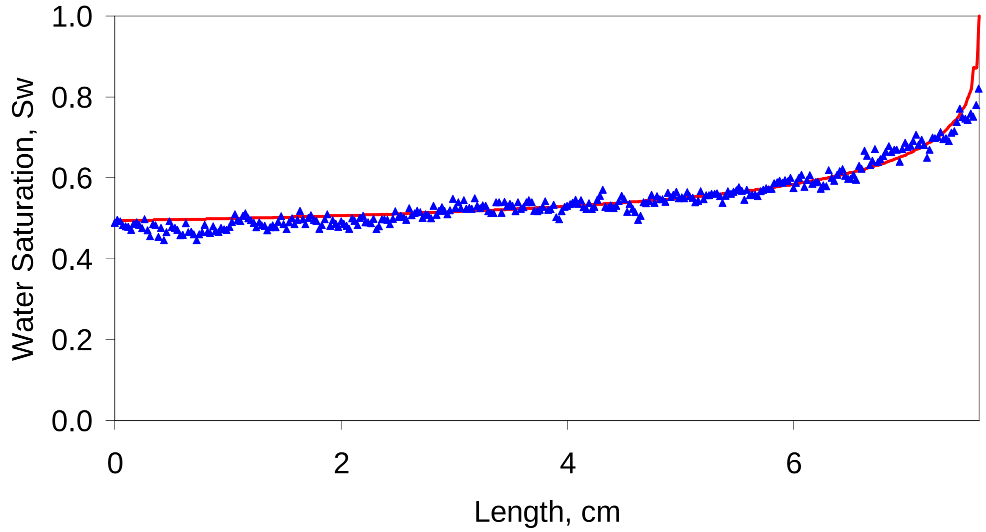

Figure 3: Brine saturation in water-wet Berea sandstone core (k=0.085 D, ΔP=0.87 atm) at the end of 30 minutes and 432 PV of gas injected. The line represents the model solution using estimated petrophysical parameters (krgo=0.3880, ng=2.4, n=6.6, α'=2).

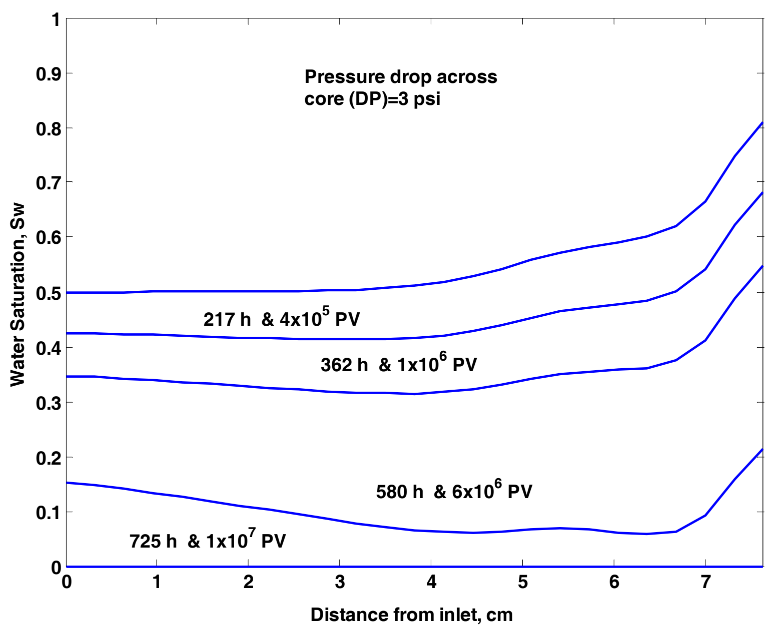

Figure 4: The time evolution of saturation profiles during the evaporative regime in a Berea sandstone at a pressure drop of 3 psi. The saturation profiles show faster evaporation near the outlet end on the right side.

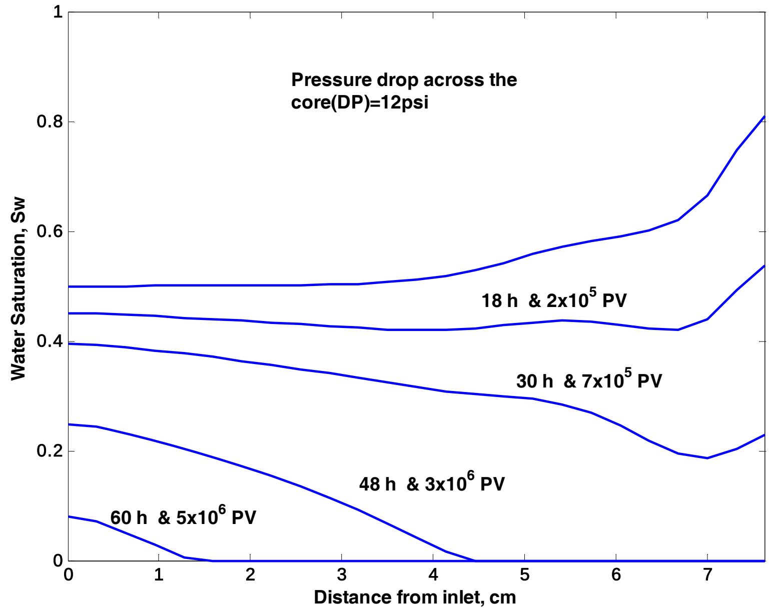

Figure 5: The effect of pressure drop on the evaporative regime in a Berea sandstone. The saturation profiles show faster overall evaporation near the outlet end on the right side at a higher pressure drop of 12 psi.

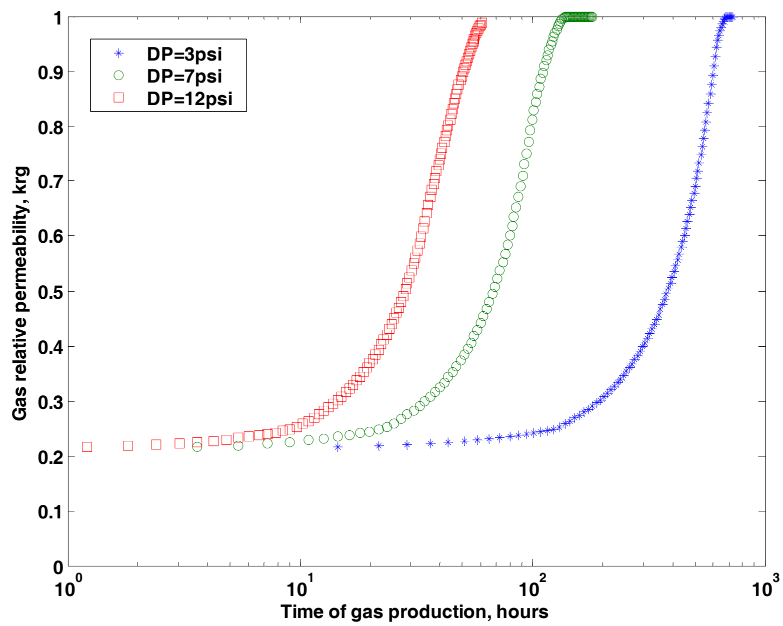

Figure 6: The effect of pressure drop on the cleanup evaporative regime in a Berea sandstone.

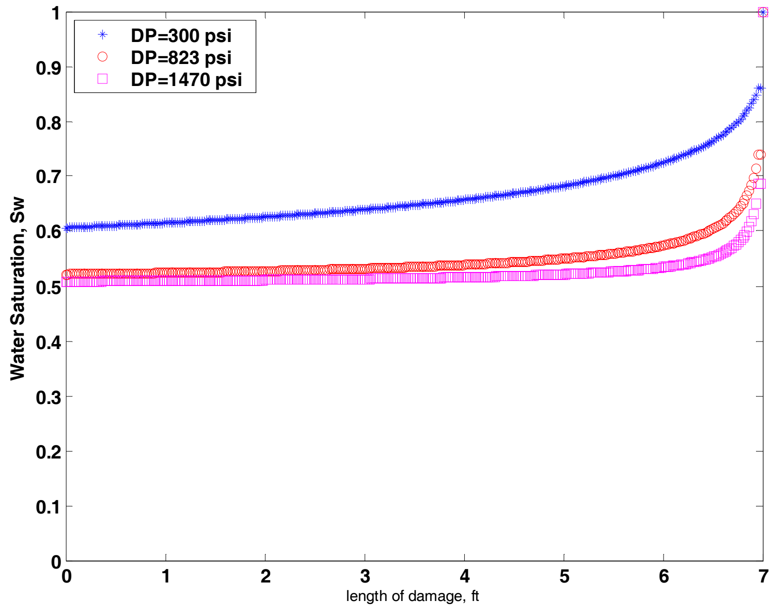

Figure 7: The effect of pressure drop on the saturation profile at the end of displacement for a fractured tight gas sandstone. The capillary pressure and relative permeability parameters are assumed to be represented by values given in table 1 (TG-3) at all pressures.

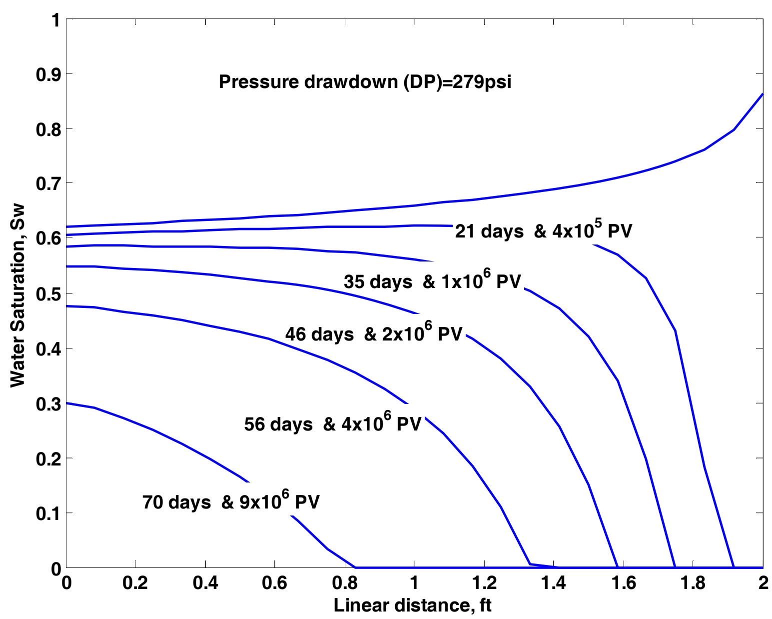

Figure 8: The time evolution of saturation profiles during the evaporative regime in a fractured tight gas sandstone (TG-3) at a pressure drop of 279 psi. The saturation profiles show faster evaporation near the outlet end on the right side.

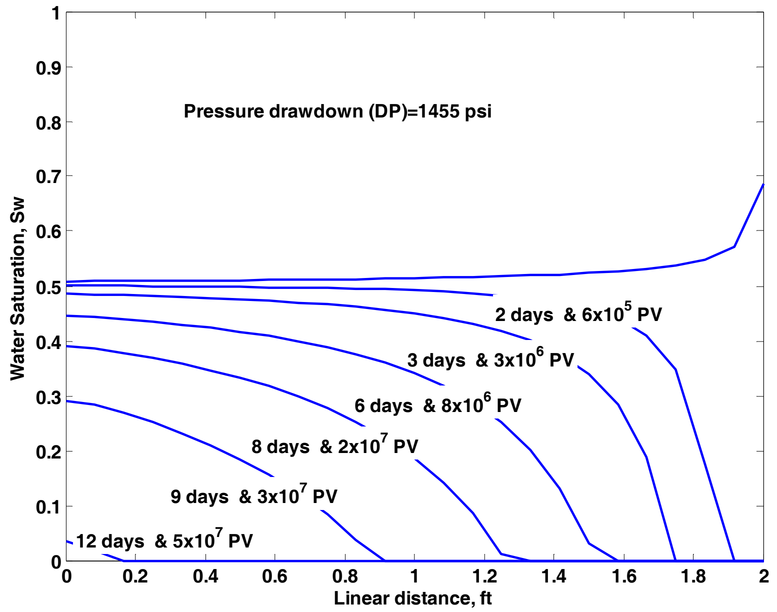

Figure 9: The effect of pressure drop on the evaporative regime in a fractured tight gas sandstone (TG-3). The saturation profiles show faster overall evaporation near the outlet end on the right side at a higher pressure drop of 1455 psi.

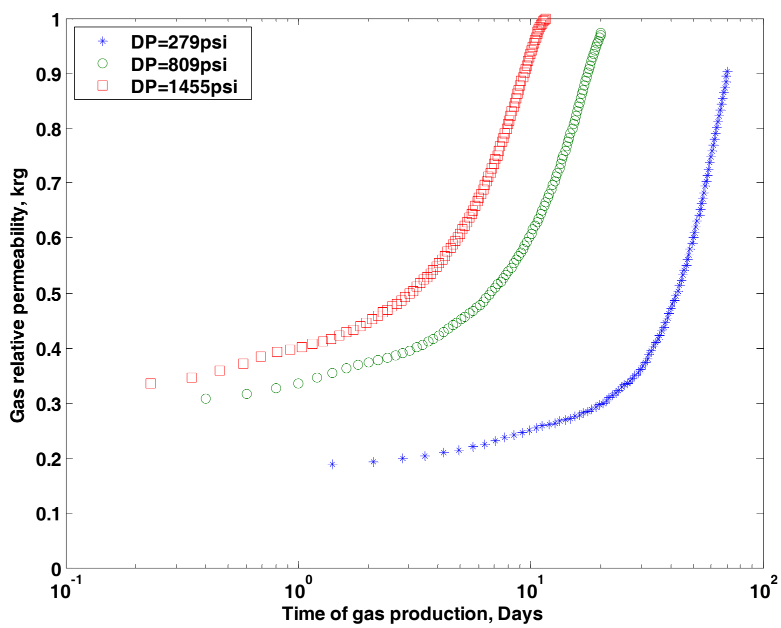

Figure 10: The effect of pressure drop on the cleanup during evaporative regime in a fractured tight gas sandstone (TG-3).

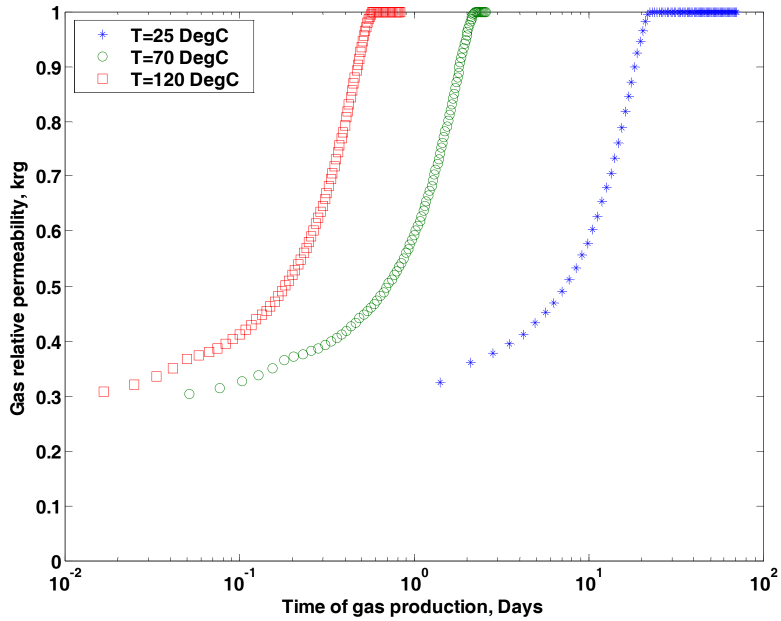

Figure 11: The effect of temperature on the cleanup during evaporative regime in a fractured tight gas sandstone (TG-3) at a pressure drop of 823 psi.

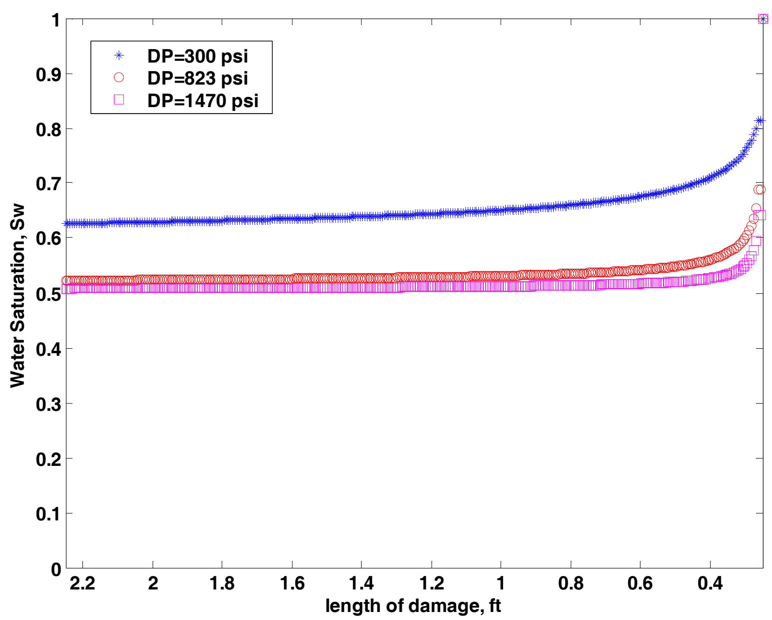

Figure 12: The effect of pressure drop on the saturation profile at the end of displacement for an unfractured tight gas sandstone (TG-3).

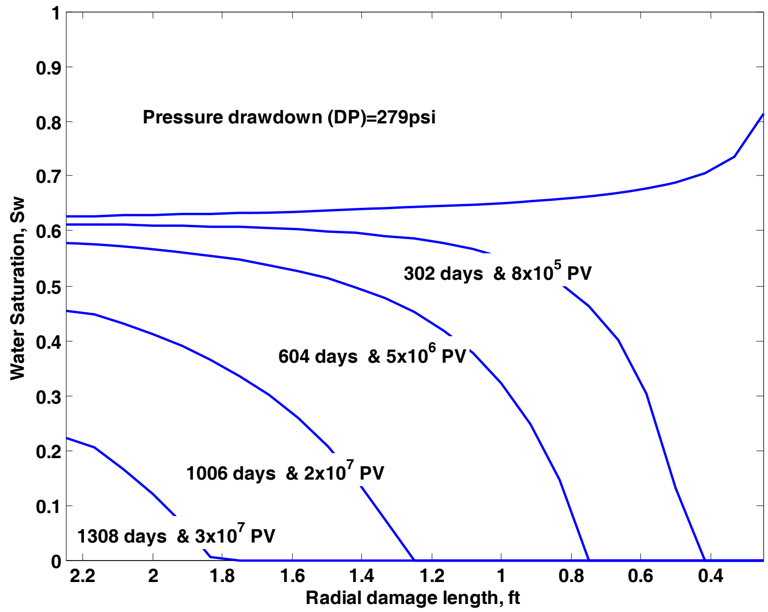

Figure 13: The time evolution of saturation profiles during the evaporative regime in a tight gas sandstone (TG-3) at a pressure drop of 279 psi in an unfractured well (radial geometry). The saturation profiles show faster evaporation near the outlet end on the right side.

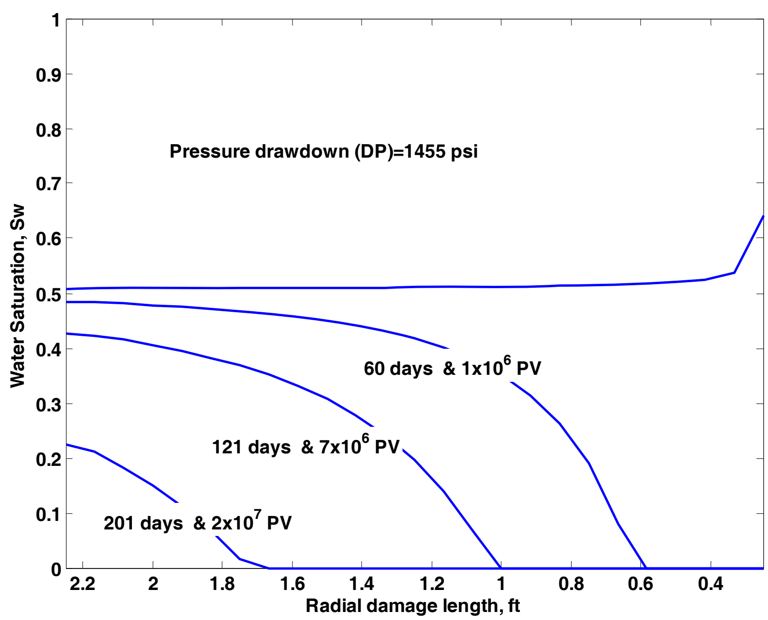

Figure 14: The effect of pressure drop on the evaporative regime in a tight gas sandstone (TG-3) in a radial geometry. The saturation profiles show faster overall evaporation near the outlet end on the right side at a higher pressure drop of 1455 psi.

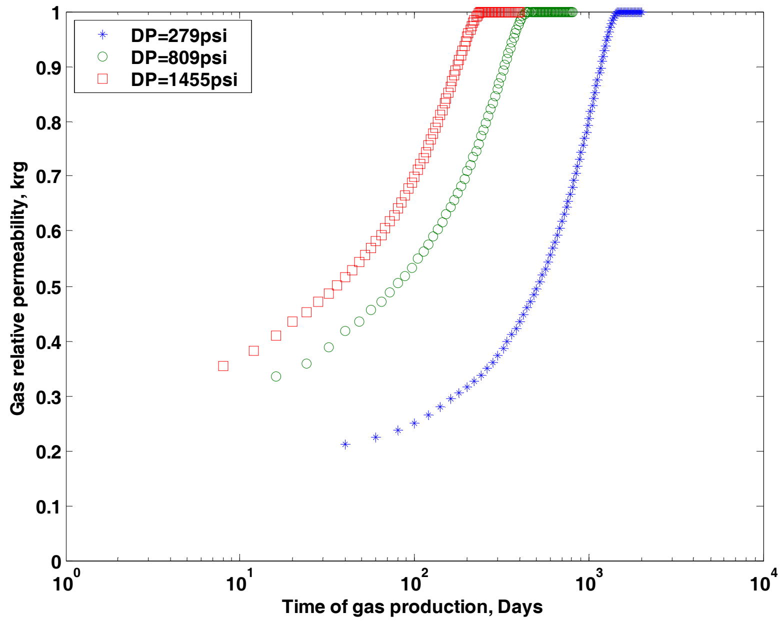

Figure 15: The effect of pressure drop on the cleanup evaporative regime in an unfractured tight gas sandstone (TG-3).

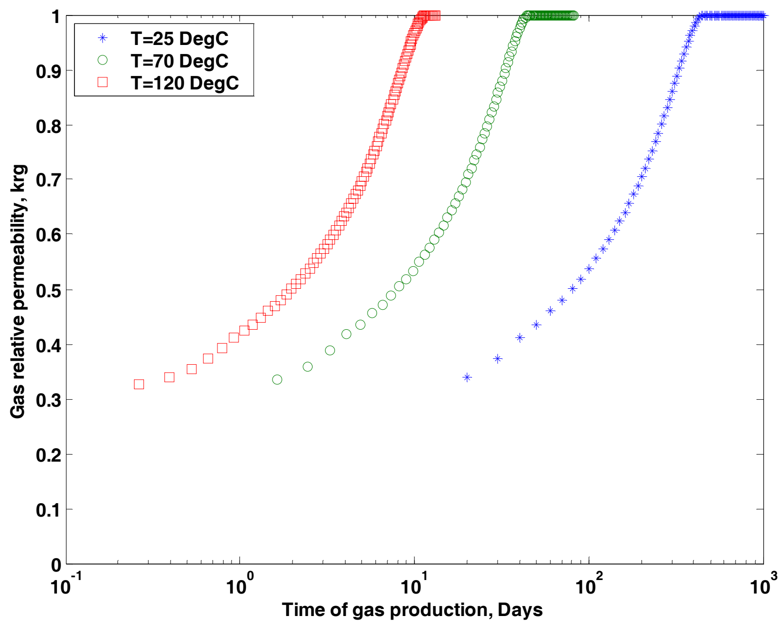

Figure 16: The effect of temperature on the cleanup during evaporative regime in an unfractured tight gas sandstone (TG-3) at a pressure drop of 823 psi.

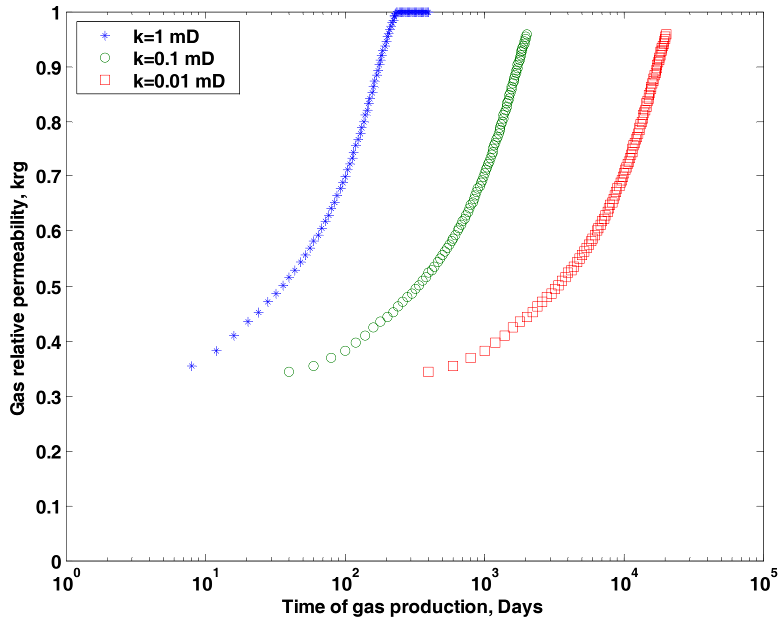

Figure 17: The effect of permeability variation on the cleanup evaporative regime in an unfractured tight gas sandstone (TG-3) at a pressure drop of 1455 psi. The petrophysical parameters used are the same for all the three simulations.

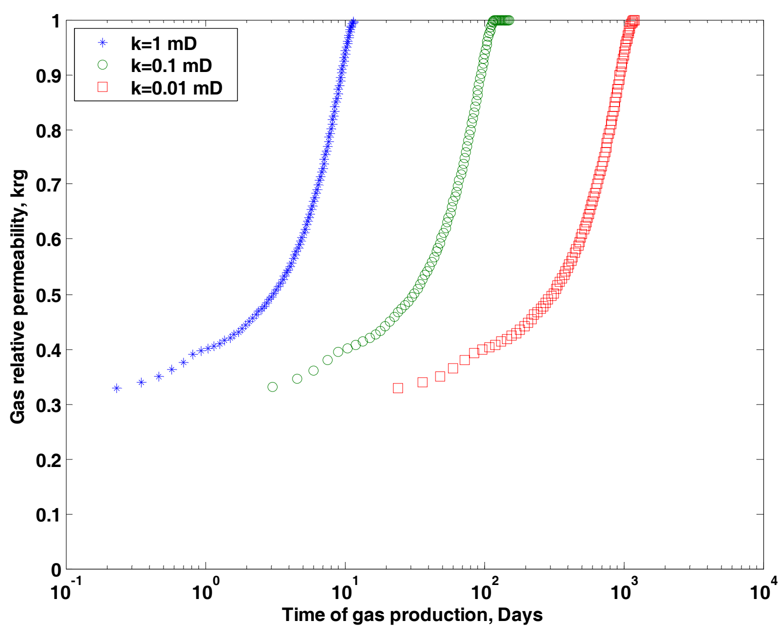

Figure 18: The effect of permeability variation on the cleanup evaporative regime in a fractured tight gas sandstone (TG-3). The petrophysical parameters used are the same for all the three simulations.

12. LIST OF PUBLICATIONS RESULTING FROM THIS DOE PROJECT:

“Clean-up of Water Blocks in Low Permeability Formations,” SPE 84216 presented at the SPE Annual Technical Conference and Exhibition held in Denver, Colorado, October 5 – 8, 2003, J. Mahadevan, M.M. Sharma.

“Productivity Impairment and Fracture Stimulation Strategies in Gas Condensate Wells”, presented at the Novel Advances in Tight Gas Completion and Production Technology Workshop, Austin, Texas, 28-30 July, 2004, M.M. Sharma.

“Cleanup of Water Blocks in Depleted Low-Permeability Reservoirs”, SPE 89837 presented at the SPE Annual Technical Conference and Exhibition, Houston, Texas, 26–29 September 2004, B. Parekh, and M.M. Sharma.

“Slick Water and Hybrid Fracs in the Bossier: Some Lessons Learnt”, SPE 89876 presented at the SPE Annual Technical Conference and Exhibition, Houston, Texas, 26-29 September 2004, M.M. Sharma, P. Gadde, R. Sullivan, R. Sigal, R. Fielder, D. Copeland, L. Griffin and L. Weilers.

“Modeling Proppant Settling in Water-Fracs”, SPE 89875 presented at the SPE Annual Technical Conference and Exhibition, Houston, Texas, 26-29 September 2004, P. Gadde, Y. Liu, J. Norman, R. Bonnecaze, and M.M. Sharma.

“Evaporative Clean-up of Water-Blocks in Gas Wells”, SPE 94215 will be presented at the 2005 SPE Production and Operations Symposium held in Oklahoma City, OK, U.S.A., 17 – 19 April 2005, J. Mahadevan, M.M. Sharma, and Y.C. Yortsos.

"The Impact of Proppant Retardation on Propped Fracture Lengths" to be presented at the SPE ATCE 2005, Gadde, P.B. and Sharma, M.M., (SPE 97106).

"Effect of Fracture Width and Fluid Rheology on Proppant Settling and Retardation: An Experimental Study" to be presented at the SPE ATCE 2005, Liu, Y and Sharma, M., (SPE-96208).